JOURNAL OF THE AERONAUTICAL SCIENCES

VOLUME 23 JULY, 1956 NUMBER 7

ST. LOUIS PUBLIC LIBRARY JUL 13 1956

CONTENTS

Aerodynamic Influence Coefficients for an Oscillating Finite Thin Wing in Supersonic Flow ..... TA LI 613

Design of Structural Models, with Application to Stiffened Panels Under Combined Shear and Compression ..... P. E. SANDORFF 623

Mechanical Stability of a Two-Bladed Cantilever Helicopter Rotor ..... PETER F. LEONE 633

Theoretical Aerodynamic Properties of Vanishing Aspect Ratio Harmonically Oscillating Rigid Airfoils in a Compressible Medium ..... BERNARD MAZELSKY 639

Eccentric Landing with Heavy Masses at the Wing Tips ..... ALEXANDER GRZEDZIELSKI 653

An Aeroelastic Parameter for Estimation of the Effects of Flexibility on the Lateral Stability and Control of Aircraft ..... WILLIAM P. RODDEN 660

Stability of a Flexible Helicopter Rotor Blade in Forward Flight ..... YECHIEL SHULMAN 663

The Compressible Flow Past an Oscillating Airfoil in a Wind Tunnel ..... JOHN W. MILES 671

Applications of Matrix Operators to the Kinematics of Airplane Motion ..... MALCOLM J. ABZUG 679

Minimum Weight Design of a Simply Supported Transversely Stiffened Plate Loaded in Shear ..... MALCOLM F. SYMONDS 685

Readers' Forum 694–708

Published by
INSTITUTE OF THE AERONAUTICAL SCIENCES, INC.

JOURNAL OF THE AERONAUTICAL SCIENCES

Editor: W. R. SEARS
Director, Graduate School of Aeronautical Engineering, Cornell University

Associate Editor: ROBERT R. DEXTER *Managing Editor:* RITA J. TURINO
Editorial Assistant: CAROLINE TAYLOR

Editorial Committee

Aerodynamics and Fluid Mechanics
Holt Ashley
H. Julian Allen
Dean R. Chapman
Francis H. Clauser
Hugh L. Dryden
John C. Evvard
Antonio Ferri
Alexander Flax
Wallace D. Hayes
R. T. Jones
Carl Kaplan
H. W. Liepmann
C. C. Lin
H. F. Ludloff
Harold Luskin
Clark B. Millikan
C. D. Perkins
H. J. E. Reid
George S. Schairer
G. B. Schubauer
John Stack
Theodore Theodorsen
Arthur N. Tifford
Th. von Kármán

Flight Testing
R. R. Gilruth
Melvin N. Gough
W. L. Howland
W. F. Milliken, Jr.

Rotating Wing Aircraft
F. B. Gustafson
K. H. Hohenemser
Bartram Kelley
R. B. Maloy
Ralph McClarren
R. H. Miller
R. H. Prewitt
Igor I. Sikorsky

Structures
John E. Duberg
N. J. Hoff
Samuel Levy
J. F. McBrearty
W. Ramberg
E. E. Sechler
F. R. Shanley
C. R. Strang
S. Timoshenko

Meteorology
C. F. Brooks
D. M. Little
F. W. Reichelderfer
K. C. Spengler

Vibration and Flutter
Lee Arnold
M. A. Biot
R. L. Bisplinghoff
Harold A. Cheilek
I. E. Garrick
Martin Goland

Aircraft Design
W. E. Beall
E. H. Heinemann
Hall L. Hibbard
Richard Hutton
C. L. Johnson
A. A. Kartveli
E. G. Stout
F. K. Teichmann
Robert J. Woods

Electronics
Welcome W. Bender
K. C. Black
M. V. Kiebert, Jr.
David S. Little
S. B. Rogers
Paul Rosenberg
L. M. Sherer

Physiologic Problems
H. G. Armstrong
Louis H. Bauer
Robert J. Benford
W. Randolph Lovelace, II
Ross A. MacFarland

Flight Propulsion
William Bollay
George W. Brady
R. P. Kroon
Frank E. Marble
Abe Silverstein
Martin Summerfield
E. S. Taylor

Instruments
Alan G. Binnie
Charles H. Colvin
Frank R. Cook
C. S. Draper
S. G. Eskin
C. F. Savage
R. C. Sylvander

SUBSCRIPTION RATES

JOURNAL OF THE AERONAUTICAL SCIENCES, Published Monthly.—United States and Possessions: 1 Year, $15.00; Single Copies, $1.50. Foreign Countries Including Canada (American Currency Rates): 1 Year, $16.00; Single Copies, $1.50.

AERONAUTICAL ENGINEERING REVIEW, Published Monthly.—United States and Possessions: 1 Year, $3.00; Single Copies, $0.50. Foreign Countries Including Canada (American Currency Rates): 1 Year, $3.50; Single Copies, $0.50.

Notices of change of address should be sent to the Institute at least 30 days prior to actual change of address.

Manuscripts for publication, proofs, and all correspondence should be addressed to the Editorial Office of the JOURNAL.

Correspondence regarding subscriptions may be addressed to the Editorial Office of the JOURNAL OF THE AERONAUTICAL SCIENCES, 2 East 64th Street, New York 21, N.Y., or to the Publication Office, 20th and Northampton Sts., Easton, Pa.

© *Copyright, 1956, by the Institute of the Aeronautical Sciences, Inc.*

Entered as Second Class Matter at the Post Office, Easton, Pa., May 1, 1937. Acceptance for mailing at a special rate of Postage provided for in the Act of August 24, 1912. Authorized April 29, 1937.

JOURNAL OF THE AERONAUTICAL SCIENCES

VOLUME 23 JULY, 1956 NUMBER 7

Aerodynamic Influence Coefficients for an Oscillating Finite Thin Wing in Supersonic Flow

TA LI*

Chance Vought Aircraft, Inc.

SUMMARY

A study, based on linearized theory, is made of the air forces of flexible thin wings oscillating harmonically in supersonic flow.

A method for calculating the aerodynamic influence coefficients is proposed. This method approximates the pressure difference by dividing the region of integration into a mesh of congruent rectangles with diagonals parallel to the Mach lines.

A set of formulas for the influence coefficients is given which can be approximated by any type of high-speed computer.

For subsonic leading edges, an imaginary diaphragm is considered to be in front of the leading edge, and linear equations expressing the condition of zero pressure difference off the wing are solved to find the corrections for the coefficients in the disturbed region. Tips are treated by a similar method.

Results for the two-dimensional case are in good agreement with those obtained by Garrick and Rubinow for $M = 10/9$, 5/4, 10/7, k up to 0.4, and are in excellent conformity with those of Temple and Jahn for $M = 1.6$, k up to 0.8.

SYMBOLS

b	=	spanwise deflection slope (roll)
c	=	velocity of sound
$C_{\mu,\nu}$	=	influence coefficients
C^*, C'	=	coefficients derived from $C_{\mu,\nu}$
$f_{q-\mu,\,s-\nu}$	=	fractions defined by Eqs. (24), (25), and (26)
h	=	deflection ratio (translation)
k	=	reduced frequency $\omega l/V$
l	=	length of a spanwise side of congruent rectangles used for approximate integration
M	=	Mach Number $= V/c$
p	=	pressure
Δp	=	pressure difference
q, s	=	integers
s^*	=	semispan
R	=	$\sqrt{(x-\xi)^2 - \beta^2(y-\eta)^2}$
S	=	region bounded by Mach lines and the leading edges
t	=	time
V	=	velocity of main stream
$w(\xi, \eta, \tau)$	=	vertical disturbance velocity at the point (ξ, η) on the wing
$W(\xi, \eta)$	=	function representing space variation of source strength
W^*	=	$W(\xi, \eta)/V$ nondimensional space variation on wing
W'^*	=	nondimensional space variation of source strength on diaphragm
x, y, ξ, η	=	rectangular coordinates attached to an airplane moving in the negative x-direction
α	=	angle of attack (pitch)
β	=	$\sqrt{M^2 - 1}$
γ	=	$M^2/(M^2 - 1)$
Λ	=	angle of sweep
μ, ν, κ, τ	=	integers
ρ	=	density of fluid
ϕ	=	disturbance velocity potential
ω	=	frequency of oscillations
$\bar{\omega}$	=	$M^2\omega/(V\beta^2)$
$\mathfrak{C}$	=	matrix
$\Im$	=	imaginary part of the influence coefficient
$\Re$	=	real part of the influence coefficient

Presented at the Aeroelasticity–II Session, Twenty-Third Annual Meeting, IAS, New York, January 24–27, 1955.

* Formerly, Lead Aeroelastic Engineer. Now, Design Specialist, Dynamics Group, Convair, A Division of General Dynamics Corp., San Diego, Calif.

(1) INTRODUCTION

S. Pines and J. Dugundji[1, 2] developed a method for calculating the aerodynamic influence coefficients in flutter analysis by assuming a wing composed of congruent square flat plates, called boxes. Since the box grid does not change with Mach Number, the significance of Mach lines could not be sufficiently observed. Consequently, subdivisions of the "nearby" boxes became necessary, and the range was thus limited to $M \geqq \sqrt{2}$.

The author[3] used rectangles with diagonals parallel to the Mach lines instead of squares, thus making it possible to obtain good results for M as small as 10/9 without any subdivision. It should be mentioned that the idea of using rectangles was a logical conse-

quence of Mach lines, if the lines of singularity should be observed.

The present paper is a revision of reference 3. Because of restrictions concerning the length of this paper, mathematical derivations of some results are necessarily omitted. However, detailed derivations may be found in reference 3.

Using the method presented in this paper, results for the two-dimensional unsteady case are in very good agreement with those presented in reference 6, which were derived from references 4 and 5. The results were checked for various choices of reduced frequency, Mach Number, and different numbers of squares. The smallest value of M checked is 10/9. The comparison is shown in charts at the end of this paper.

A step method to calculate the aerodynamic influence coefficients for the disturbed region is presented here. A direct and more rigorous approach is now being developed, and it is hoped that the results may be announced in the near future.

(2) Analysis

(2.1) *Potential and Pressure*

Under the assumption of validity of linearized theory, the equation for velocity potential may be written as

$$\frac{1}{c^2}\left[\frac{\partial}{\partial t} + V\frac{\partial}{\partial x}\right]^2 \phi = \frac{\partial^2\phi}{\partial x^2} + \frac{\partial^2\phi}{\partial y^2} + \frac{\partial^2\phi}{\partial z^2} \qquad (1)$$

In case of a swept thin wing with supersonic leading edge oscillating harmonically according to a general analytical function $f(\xi, \eta)$, the deflection at time t is

$$z = e^{i\omega t} f(\xi, \eta) \qquad (2)$$

The boundary condition thus becomes

$$\left(\frac{\partial\phi}{\partial z}\right)_{z=0} = w(\xi, \eta, t) = \frac{dz}{dt} = \frac{\partial z}{\partial t} + V\frac{\partial z}{\partial \xi} = e^{i\omega t} W(\xi, \eta) \qquad (3)$$

To avoid confusion, the strength function $W(\xi, \eta)$ is preceded by a positive sign so that the deflection h is taken positive downward. The velocity potential at any point (x, y), preceded by a positive instead of the conventional negative sign, is given by

$$\phi(x, y, t) = \frac{e^{i\omega t}}{\pi}\int_S\int W(\xi, \eta)e^{-i\omega(x-\xi)}\frac{1}{R}\cos\left(\frac{\bar{\omega}}{M}R\right)d\eta\, d\xi \qquad (4)$$

where S is the region indicated in Fig. 1 and

$$R^2 = (x - \xi)^2 - \beta^2(y - \eta)^2 \qquad (5)$$

It is obvious that ϕ is a function of the boundary.

The pressure difference at any point (x, y) may be written

$$\Delta p = -2\rho[(\partial\phi/\partial t) + V(\partial\phi/\partial x)] \qquad (6)$$

Notations Used in Figures

- $'$ = real part
- $''$ = imaginary part, damping term
- K_{11} = lift due to translation
- K_{12} = lift due to rotation
- K_{21} = moment due to translation
- K_{22} = moment due to rotation

Relations Between Symbols

Chance Vought Aircraft	Garrick-Rubinow	Temple-Jahn
K'_{11}	$\frac{4k^2}{\pi} L_1$	$\frac{1}{\pi}(l_1)$
K''	$\frac{4k^2}{\pi} L_2$	$\frac{2k}{\pi}(l_2)$
K'_{12}	$\frac{4k^2}{\pi} L'_3$	$\frac{1}{\pi}(2l_0 + l_2)$
K'_{21}	$\frac{4k^2}{\pi} M'_1$	$\frac{1}{\pi}(-2m_2 + l_1)$
K''_{21}	$\frac{4k^2}{\pi} M'_2$	$\frac{2k}{\pi}(-2m_2 + l_2)$
K'_{22}	$\frac{4k^2}{\pi} M'_3$	$\frac{1}{\pi}(-4m_0 + 2l_0 - 2m_2 + l_2)$
K''_{22}	$\frac{4k^2}{\pi} M'_4$	$\frac{2k}{\pi}(-4m_0 + 2l_0 - 2m_2 + l_2)$

(2.2) *Calculation of* $\partial\phi/\partial x$ *and* $\Delta p(x, y)$

To obtain $\partial\phi/\partial x$, we will divide S into two subregions S_1 and S_2, by the axis of the Mach cone $\eta = y$ (Fig. 1) and write

$$\phi(x, y, t) = \frac{e^{i\omega t}}{\pi}\left(\int_{S_1}\int + \int_{S_2}\int\right)\times W(\xi, \eta)e^{-i\omega(x-\xi)}\frac{1}{R}\cos\left(\frac{\bar{\omega}}{M}R\right)d\eta d\xi \qquad (7)$$

where

$$\int_{S_1}\int = \int_{(\beta y - x)/(\beta\cot\Lambda - 1)}^{y\tan\Lambda}\int_{y-(1/\beta)(x-\xi)}^{\xi\cot\Lambda} + \int_{y\tan\Lambda}^{x}\int_{y-(1/\beta)(x-\xi)}^{y}$$

and

$$\int_{S_2}\int = \int_{y\tan\Lambda}^{(\beta y + x)/(\beta\cot\Lambda + 1)}\int_{y}^{\xi\cot\Lambda} + \int_{(\beta y + x)/(\beta\cot\Lambda + 1)}^{x}\int_{y}^{y+(1/\beta)(x-\xi)}$$

One important step is the derivation of $\partial\phi/\partial x$. It can be done by either of the following methods:

(*i*) Replace the variable η by a new variable τ through the substitution

$$(y - \eta)/(x - \xi) = \tau/\beta$$

then carry out the partial differentiation of ϕ with respect to x. After this is done, express τ in terms of η.

(*ii*) Carry the operator $\partial/\partial x$ under the first integral sign by taking limits, then subtract from each integrand an appropriate quantity to make the transfer of $\partial/\partial x$ under the second integral sign possible.

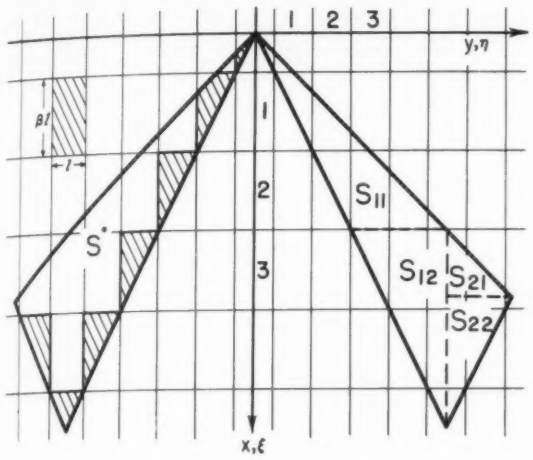

FIG. 1. Supersonic leading edges.

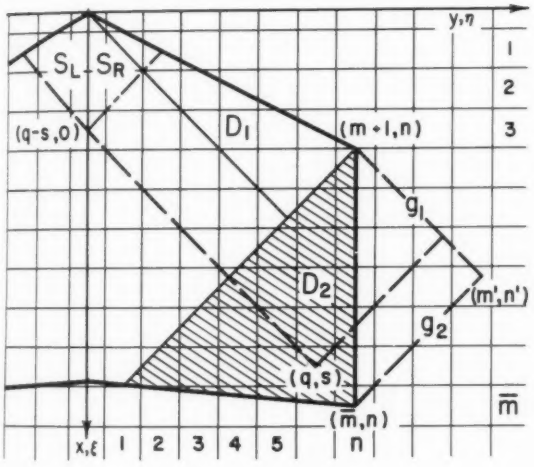

FIG. 2. Tip effect.

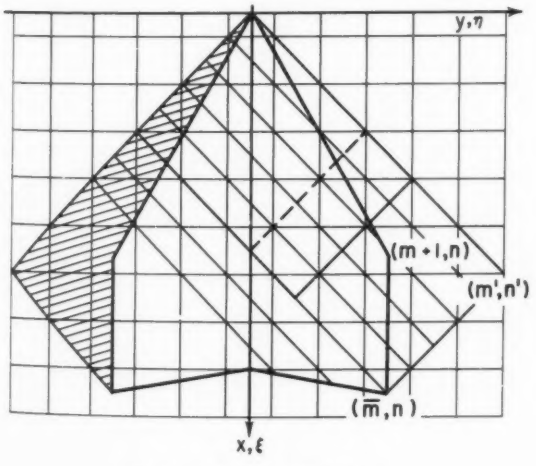

FIG. 3. Subsonic leading edges.

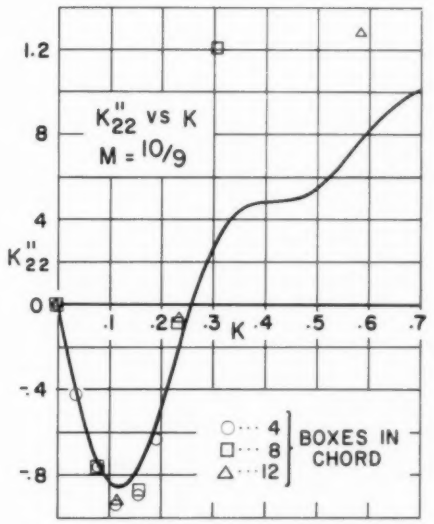

FIG. 4. K''_{22}, $M = 10/9$, comparison with Garrick and Rubinow's results.

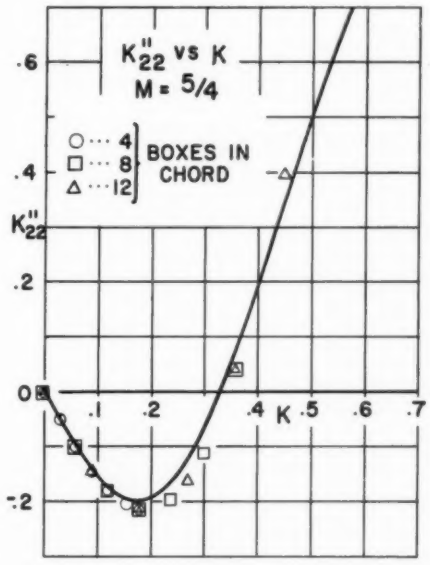

FIG. 5. K''_{22}, $M = 5/4$, comparison with Garrick and Rubinow's results.

The correct result of $\partial\phi/\partial x$ is given by

$$\pi e^{-i\omega t}\frac{\partial \phi}{\partial x} = \frac{\pi}{\beta}W(x, y) - i\bar{\omega}\pi e^{-i\omega t}\phi + \int_{S_1}\int e^{-i\omega(x-\xi)}\left\{W(\xi, \eta)\frac{\partial}{\partial x}\left[\frac{1}{R}\cos\left(\frac{\bar{\omega}}{M}R\right)\right] - W\left(\xi, y - \frac{1}{\beta}(x-\xi)\right)\left[\frac{\partial}{\partial x}\frac{1}{R}\right]\right\}d\eta d\xi + \int_{S_2}\int e^{-i\omega(x-\xi)}\left\{W(\xi, \eta)\frac{\partial}{\partial x}\left[\frac{1}{R}\cos\left(\frac{\bar{\omega}}{M}R\right)\right] - W\left(\xi, y - \frac{1}{\beta}(x-\xi)\right)\left[\frac{\partial}{\partial x}\frac{1}{R}\right]\right\}d\eta d\xi + I_1 + I_2 \quad (8)$$

where

$$\left.\begin{aligned} I_1 &= \frac{1}{\beta}\int_{(\beta y - x)/(\beta\cot\Lambda - 1)}^{y\tan\Lambda} e^{-i\bar{\omega}(x-\xi)}W\left(\xi, y - \frac{1}{\beta}(x-\xi)\right)\left[\frac{\partial}{\partial x}\cos^{-1}\left(\frac{\beta(y - \xi\cot\Lambda)}{x-\xi}\right)\right]d\xi \\ &= \int_{(\beta y - x)/(\beta\cot\Lambda - 1)}^{y\tan\Lambda} e^{-i\bar{\omega}(x-\xi)}W\left(\xi, y - \frac{1}{\beta}(x-\xi)\right)(y - \xi\cot\Lambda)(x-\xi)^{-1}[(x-\xi)^2 - \beta^2(y - \xi\cot\Lambda)^2]^{-(1/2)}d\xi \end{aligned}\right\} \quad (9)$$

$$\left.\begin{aligned} I_2 &= -\frac{1}{\beta}\int_{y\tan\Lambda}^{(\beta y + x)/(\beta\cot\Lambda + 1)} e^{-i\bar{\omega}(x-\xi)}W\left(\xi, y + \frac{1}{\beta}(x-\xi)\right)\left[\frac{\partial}{\partial x}\cos^{-1}\beta\left(\frac{\xi\cot\Lambda - y}{x-\xi}\right)\right]d\xi \\ &= \int_{y\tan\Lambda}^{(\beta y + x)/(\beta\cot\Lambda + 1)} e^{-i\bar{\omega}(x-\xi)}W\left(\xi, y + \frac{1}{\beta}(x-\xi)\right)(y - \xi\cot\Lambda)(x-\xi)^{-1}\times [(x-\xi)^2 - \beta^2(y - \xi\cot\Lambda)^2]^{-(1/2)}d\xi \end{aligned}\right\} \quad (10)$$

It is clear that $W\left(\xi, y \pm \frac{1}{\beta}(x-\xi)\right)$ denotes values of $W(\xi, \eta)$ taken along the Mach lines.

Substituting $\partial\phi/\partial x$ in Eq. (6), we find the exact expression of pressure difference $\Delta p(x, y)$ at the point (x, y):

$$-\frac{\pi e^{-i\omega t}}{2\rho}\Delta p(x, y) = \frac{V\pi}{\beta}W(x, y) + \int_{S_1}\int e^{-i\omega(x-\xi)}\left(W(\xi, \eta)\left\{-\frac{i\omega}{\beta^2}\frac{1}{R}\cos\left(\frac{\bar{\omega}}{M}R\right) + V\frac{\partial}{\partial x}\left[\frac{1}{R}\cos\left(\frac{\bar{\omega}}{M}R\right)\right]\right\} - W\left(\xi, y - \frac{1}{\beta}(x-\xi)\right)V\left[\frac{\partial}{\partial x}\frac{1}{R}\right]\right)d\eta d\xi + \int_{S_2}\int e^{-i\omega(x-\xi)}\left(W(\xi, \eta)\left\{-\frac{i\omega}{\beta^2}\frac{1}{R}\cos\left(\frac{\bar{\omega}}{M}R\right) + V\frac{\partial}{\partial x}\left[\frac{1}{R}\cos\left(\frac{\bar{\omega}}{M}R\right)\right]\right\} - W\left(\xi, y + \frac{1}{\beta}(x-\xi)\right)V\left[\frac{\partial}{\partial x}\frac{1}{R}\right]\right)d\eta d\xi + V(I_1 + I_2) \quad (11)$$

where I_1 and I_2 are defined by Eqs. (9) and (10). The pressure here is taken positive when it acts downward.

(2.3) *Transformation*

Now let us choose a suitable length, preferably $l = 2s^*/(2n+1)$, where s^* is the semispan and n a positive integer, and draw the parallels

$$y = (1/2)l,\ (3/2)l,\ (5/2)l,\ (7/2)l,\ \ldots$$

$$x = (1/2)\beta l,\ (3/2)\beta l,\ (5/2)\beta l,\ (7/2)\beta l,\ \ldots$$

so that the whole wing will be covered by a mesh of congruent rectangles.

To simplify our expressions, we will introduce non-dimensional coordinates x', y', ξ', η' by

$$\left.\begin{aligned} x &= l\beta x', \quad y = ly' \\ \xi &= l\beta\xi', \quad \eta = l\eta' \end{aligned}\right\} \quad (12)$$

and retain the notations

$$\left.\begin{aligned} W(\xi', \eta') &\quad \text{for} \quad W(l\beta\xi', l\eta') \\ W(x', y') &\quad \text{for} \quad W(l\beta x', ly') \\ p(x', y') &\quad \text{for} \quad p(l\beta x', ly') \\ R^2 &= (x' - \xi')^2 - (y' - \eta')^2 \end{aligned}\right\}$$

After the transformation is made, we will drop the prime

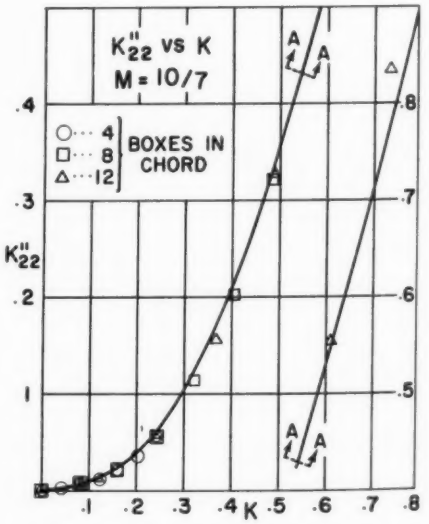

FIG. 6. K''_{22}, $M = 10/7$, comparison with Garrick and Rubinow's results.

and restrict ourselves from now on to this nondimensional coordinate system.

(2.4) Approximate Expression for Pressure

To obtain a correct expression for the pressure and to achieve uniformity of the influence coefficients, the region S is divided into four subregions—S_{11}, S_{12}, S_{21}, and S_{22}—as indicated in Fig. 1. The integrals are studied in each subregion separately.

If we denote the unshaded part of S by S^* and the shaded one by $C(S)^*$, the pressure difference Δp_{qs} can be found approximately from

$$\frac{\pi}{2\rho} e^{-i\omega t}\,\Delta p_{qs} = -\frac{V}{\beta}\,\pi W_{qs} + \frac{V\pi}{2\beta}\int_{q-(1/2)}^{q} e^{-i\beta\gamma k(q-\xi)}\left\{W_{qs}\,[\xi,\, s-(q-\xi)] + W_{qs}[\xi,\, s+(q-\xi)]\right\}\times$$
$$\left[\frac{ik}{\beta}+\frac{1}{2}\frac{M^2k^2}{\beta^2}(q-\xi)\right]d\xi + \frac{V}{\beta}\sum_{c(S^*)}(\mu\neq q)\int_{\mu-(1/2)}^{\mu+(1/2)} e^{-i\beta\gamma k(q-\xi)}\,W_{\mu,\,s\mp(q-\mu)}\,[\xi,\, s\mp(q-\xi)]\times$$
$$\left\{\left[\frac{ik}{\beta}+\frac{1}{2}\frac{M^2k^2}{\beta^2}(q-\xi)\right]\cos^{-1}\frac{q-u-(1/2)}{q-\xi} - \left(q-\mu-\frac{1}{2}\right)(q-\xi)^{-1}\left[(q-\xi)^2-\left(q-\mu-\frac{1}{2}\right)^2\right]^{-(1/2)}\right\}d\xi +$$
$$\frac{V}{\beta}\sum_{S^*}(\mu)\sum(\nu)\int_{\mu-(1/2)}^{\mu+(1/2)}\int_{\nu-(1/2)}^{\nu+(1/2)} e^{-i\beta\gamma k(q-\xi)}\,W_{\mu\nu}\,(\xi,\eta)\left[\frac{ik}{\beta}\frac{1}{R}\cos\left(\frac{Mk}{\beta}R\right)+\right.$$
$$\left.\frac{Mk}{\beta}\frac{q-\xi}{R^2}\sin\left(\frac{Mk}{\beta}R\right)+\frac{q-\xi}{R^3}\cos\left(\frac{Mk}{\beta}R\right)\right]d\eta d\xi \quad (13)$$

(3) The Influence Coefficients

(3.1) The Deflection Function

Now, let us suppose that at time $t = 0$ in the old coordinate system the z coordinate of the airfoil directly above the center of the rectangle with center $(l\beta\mu,\ l\nu)$ is $lh_{\mu\nu}$. Then that portion of the airfoil over the rectangle may be replaced by its tangent plane at $(l\beta\mu,\ l\nu,\ lh_{\mu\nu})$ as long as l is chosen small enough.

Thus, at time t, when the airfoil oscillates harmonically, the vertical deflection, positive downward, for any point $(\xi,\ \eta)$ over the rectangle mentioned above is given by

$$z_{\mu\nu} = h^*_{\mu\nu}(\xi,\eta,t) = e^{i\omega t}[lh_{\mu\nu} + \alpha_{\mu\nu}(\xi - l\beta\mu) + b_{\mu\nu}(\eta - l\nu)] \quad (14)$$

where $h_{\mu\nu}$, $\alpha_{\mu\nu}$, $b_{\mu\nu}$ are real, $h_{\mu\nu}$ the local deflection ratio or nondimensional translation, $\alpha_{\mu\nu}$ the local angle of attack or pitch, and $b_{\mu\nu}$ the spanwise deflection slope or roll.

Differentiating $z_{\mu\nu}$ with respect to t results in

$$dz_{\mu\nu}/dt = (\partial h^*_{\mu\nu}/\partial t) + V(\partial h^*_{\mu\nu}/\partial\xi) = e^{i\omega t}[(V\alpha_{\mu\nu} + i\omega l h_{\mu\nu}) + i\omega\alpha_{\mu\nu}(\xi - l\beta\mu) + i\omega b_{\mu\nu}(\eta - l\nu)] \quad (15)$$

as the approximate instantaneous vertical velocity of the airfoil above the rectangle. This gives us the local strength function

$$W_{\mu\nu}(\xi,\eta) = (V\alpha_{\mu\nu} + i\omega l h_{\mu\nu}) + i\omega\alpha_{\mu\nu}(\xi - l\beta\mu) + i\omega b_{\mu\nu}(\eta - l\nu) \quad (16)$$

After introducing nondimensional coordinates by transformation Eq. (12), the rectangle with center $(l\beta\mu,\ l\nu)$ becomes the square with center $(\mu,\ \nu)$, and the nondimensional expression for the local strength function takes the form

$$W_{\mu\nu}(\xi,\eta) = VW^*_{\mu\nu}(\xi,\eta) = V[W^*_{\mu\nu} + ik\beta\alpha_{\mu\nu}(\xi-\mu) + ikb_{\mu\nu}(\eta-\nu)] \quad (17)$$

where
$$W^*_{\mu\nu} = \alpha_{\mu\nu} + ikh_{\mu\nu} \quad (18)$$
$$k = \omega l/V \quad (19)$$

and ξ, η are nondimensional coordinates referred to the new coordinate system.

(3.2) The Formulas

In case $|\xi - \mu|$ and $|\eta - \nu|$ are small, the pressure difference can be written in the form

$$\Delta p_{qs} = -\frac{\rho V^2}{\beta} e^{i\omega t}\sum_{S}(\Re_{(q-\mu),\,(s-\nu)} + i\Im_{(q-\mu),\,(s-\nu)})\times W^*_{\mu\nu} \quad (20)$$

where $\Re$ and $\Im$ denote the real and the imaginary part of the influence coefficient.

It has been shown that

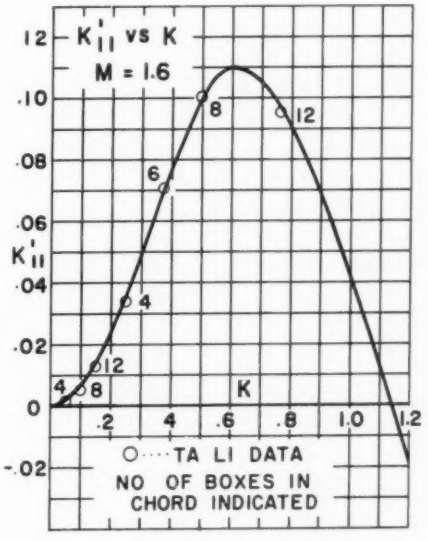

FIG. 7. K'_{11}, $M = 1.6$, comparison with Temple and Jahn's results.

(I) $\mu = q, \quad \nu = s$

$$\Re_{(q-q),\,(s-s)} = 2 - \frac{1}{M^2}\left[1 - \cos\left(\frac{1}{2}\beta\gamma k\right)\right] + \frac{1}{2}\frac{k}{\beta}\sin\left(\frac{1}{2}\beta\gamma k\right) \tag{21a}$$

$$\Im_{(q-q),\,(s-s)} = -\frac{1}{M^2}\sin\left(\frac{1}{2}\beta\gamma k\right) - \frac{1}{2}\frac{k}{\beta}\cos\left(\frac{1}{2}\beta\gamma k\right) \tag{21b}$$

(II) $\nu = s \pm (q - \mu)$

$$\Re_{(q-\mu),\,\pm(q-\mu)} = -\frac{2}{\pi}\int_0^1 \left(\frac{k}{\beta}\sin\left[\beta\gamma k\left(q-\mu-\frac{1}{2}+\theta\right)\right]\cos^{-1}\frac{q-\mu-(1/2)}{q-\mu-(1/2)+\theta} + \cos\left[\beta\gamma k\left(q-\mu-\frac{1}{2}+\theta\right)\right]\left\{\frac{1}{2}\gamma k^2\left(q-\mu-\frac{1}{2}+\theta\right)\cos^{-1}\frac{q-\mu-(1/2)}{q-\mu-(1/2)+\theta} - \frac{q-\mu-(1/2)}{[q-\mu-(1/2)+\theta]\sqrt{\theta\{2[q-\mu-(1/2)]+\theta\}}}\right\}\right)d\theta \tag{22a}$$

$$\Im_{(q-\mu),\,\pm(q-\mu)} = \frac{2}{\pi}\int_0^1 \left(-\frac{k}{\beta}\cos\left[\beta\gamma k\left(q-\mu-\frac{1}{2}+\theta\right)\right] + \sin\left[\beta\gamma k\left(q-\mu-\frac{1}{2}+\theta\right)\right]\times \left\{\frac{1}{2}\gamma k^2\left(q-\mu-\frac{1}{2}+\theta\right)\cos^{-1}\frac{q-\mu-(1/2)}{q-\mu-(1/2)+\theta} - \frac{q-\mu-(1/2)}{(q-\mu-(1/2)+\theta)\sqrt{\theta\{2[q-\mu-(1/2)]+\theta\}}}\right\}\right)d\theta \tag{22b}$$

(III) $\nu \neq s \pm (q - \mu)$

$$R = \sqrt{(q-\xi)^2 - (s-\eta)^2}$$

$$\Re_{\mu\nu} = -\frac{2}{\pi}\int_{\mu-(1/2)}^{\mu+(1/2)}\int_{\nu-(1/2)}^{\nu+(1/2)}\left\{\frac{k}{\beta}\frac{1}{R}\sin\left[\beta\gamma k(q-\xi)\right]\cos\left(\frac{Mk}{\beta}R\right) + \frac{q-\xi}{R^2}\cos\left[\beta\gamma k(q-\xi)\right]\left[\frac{Mk}{\beta}\sin\left(\frac{Mk}{\beta}\right) + \frac{1}{R}\cos\left(\frac{Mk}{\beta}\right)\right]\right\}R\,d\eta d\xi \tag{23a}$$

$$\Im_{\mu\nu} = \frac{2}{\pi}\int_{\mu-(1/2)}^{\mu+(1/2)}\int_{\nu-(1/2)}^{\nu+(1/2)}\left\{-\frac{k}{\beta}\frac{1}{R}\cos\left[\lambda\gamma k(q-\xi)\right]\cos\left(\frac{Mk}{\beta}R\right) + \frac{q-\xi}{R^2}\sin\left[\beta\gamma k(q-\xi)\right]\left[\frac{Mk}{\beta}\sin\left(\frac{Mk}{\beta}R\right) + \frac{1}{R}\cos\left(\frac{Mk}{\beta}R\right)\right]\right\}d\eta d\xi \tag{23b}$$

It may be noted that, excluding the receiving rectangle, there are two groups of uniform formulas for the influence coefficients—one group for the rectangles within the Mach lines, the other group for those on them. The fact that the groups are different becomes evident when one realizes the significance of the Mach lines. Another point worth mentioning is that the influence coefficients are obtained as functions of k and M in closed forms so that a discussion of convergence becomes unnecessary.

(3.3) *Sweep Corrections*

As shown in Fig. 1, along the leading edge there will be squares (called fractional squares) which will intersect the leading edge. The shape of the fractional squares is obviously a function of M and Λ.

It is quite natural for us to assume that the coefficient of $W^*_{\mu\nu}$ in the fractional square (μ, ν) affecting the point (q, s) is a fraction $f_{(q-\mu),\,(s-\nu)}$ of

$$C_{(q-\mu),\,(s-\nu)} = \Re_{(q-\mu),\,(s-\nu)} + i\Im_{(q-\mu),\,(s-\nu)} \tag{24}$$

This fraction can be evaluated by using the Theorem of Mean. It is given as follows:

(*i*) If the leading edge $\eta = \xi\beta \cot \Lambda$ cuts $\xi = \mu - (1/2)$ and $\eta = \nu + (1/2)$, the factor of correction is

$$f^{(i)}_{(q-\mu),\,(s-\nu)} = 1 - \int_{\mu-(1/2)}^{\frac{\nu+(1/2)}{\beta\cot\Lambda}}\int_{\xi\beta\cot\Lambda}^{\nu+(1/2)} d\eta d\xi \tag{25}$$

(*ii*) If the leading edge cuts $\eta = \nu - (1/2)$ and $\eta = \nu + (1/2)$, the factor of correction is

$$f^{(ii)}_{(q-\mu),\,(s-\nu)} = \mu - [\nu/(\beta \cot \Lambda)] + (1/2) \tag{26}$$

(*iii*) If the leading edge cuts $\eta = \nu - (1/2)$ and $\xi = \mu + (1/2)$, the factor of correction is

$$f^{(iii)}_{(q-\mu),\,(s-\nu)} = \frac{1}{2\beta\cot\Lambda}\times\left[\left(\mu+\frac{1}{2}\right)\beta\cot\Lambda - \left(\nu-\frac{1}{2}\right)\right]^2 \tag{27}$$

Eqs. (25)–(27) are formulas of sweep corrections for fractional squares on the leading edge between the Mach lines. They are independent of q and s when $(s - \nu) \neq \pm(q - \mu)$.

Along the Mach lines the situation is slightly different. There are two cases for the right-hand Mach line and two for the left-hand Mach line which will be treated separately.

Right-Hand Mach Line

(*i*) The leading edge $\eta = \xi\beta \cot \Lambda$ cuts $\xi = \mu - (1/2)$ and $\eta = s - q + \mu + (1/2)$. The factor of correction

is

$$f^{(i)}_{(q-\mu),(q-\mu)} = 1 - \frac{1}{\beta \cot \Lambda} \times \left[\left(s - q + \mu + \frac{1}{2}\right) - \left(\mu - \frac{1}{2}\right)\beta \cot \Lambda\right]^2 \quad (28)$$

(*ii*) The leading edge cuts $\eta = s - q + \mu - (1/2)$ and $\eta = s - q + \mu + (1/2)$.
The factor of correction is

$$f^{(ii)}_{(q-\mu),(q-\mu)} = \frac{1}{\beta \cot \Lambda\ (\beta \cot \Lambda - 1)} \times \left[(s - q) - \left(\mu + \frac{1}{2}\right)(\beta \cot \Lambda - 1)\right]^2 \quad (29)$$

Left-Hand Mach Line

(*i*) The leading edge $\eta = \xi\beta \cot \Lambda$ cuts $\xi = \mu - (1/2)$.
The factor of correction is

$$f^{(i)}_{(q-\mu),-(q-\mu)} = 1 - \frac{1}{\beta \cot \Lambda + 1} \times \left[(s + q) - \left(\mu - \frac{1}{2}\right)(\beta \cot \Lambda + 1)\right]^2 \quad (30)$$

(*ii*) The leading edge cuts $\eta = s + q - \mu - (1/2)$.
The factor of correction is

$$f^{(ii)}_{(q-\mu),-(q-\mu)} = \frac{1}{\beta \cot \Lambda\ (\beta \cot \Lambda - 1)} \times \left[(s + q) - \left(\mu + \frac{1}{2}\right)(\beta \cot \Lambda + 1)\right]^2 \quad (31)$$

In all cases, if (μ, ν) denotes a fractional square along the leading edge, its influence coefficient on (q, s) is found as

$$C_{(q-\mu),(s-\nu)} = f_{(q-\mu),(s-\nu)}\ C_{(q-\mu),(s-\nu)} \quad (32)$$

Eq. (32) holds true for all fractional squares along the leading edge inside the Mach lines as well as on them.

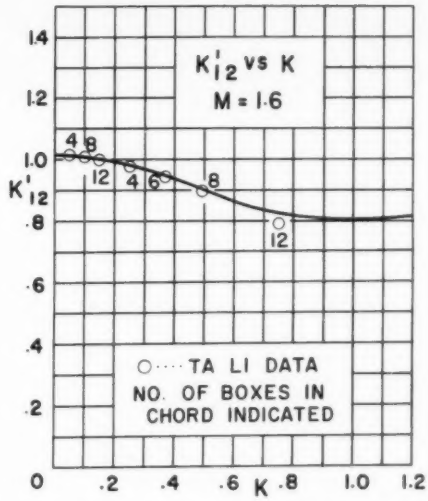

FIG. 9. K'_{12}, $M = 1.6$, comparison with Temple and Jahn's results.

(4) Finiteness Modification

In the case of a finite wing, the theory above is only valid for points lying in region D of Fig. 2. To extend its applicability to other points on the wing, say (q, s) in the shaded area D_2, modifications must be made.

Consider first the right wing, and imagine a rubber diaphragm extended beyond the tip of the wing. This diaphragm is bounded by the tip, the right-hand Mach line g_1, and the left-hand Mach line g_2 (Fig. 2).

Let us assume that the tip leading-edge point (x_1, y_1) is located in the square $(m + 1, n)$ and the tip trailing-edge point (x_2, y_2) in $(\bar{m}, n)$; then the tip of the dia-

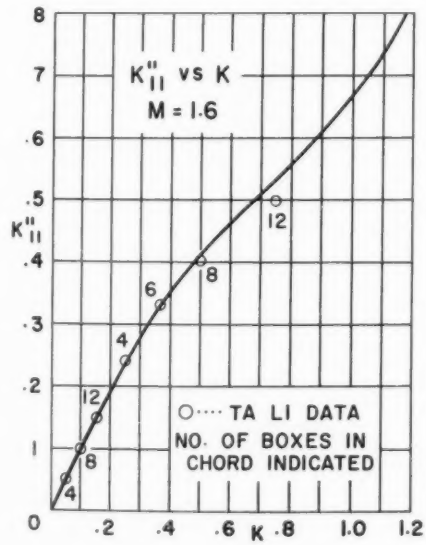

FIG. 8. K''_{11}, $M = 1.6$, comparison with Temple and Jahn's results.

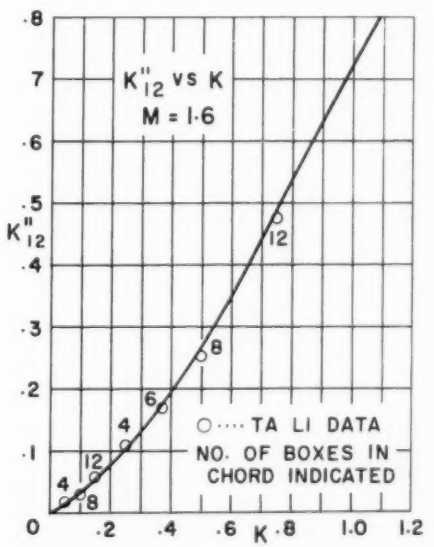

FIG. 10. K''_{12}, $M = 1.6$, comparison with Temple and Jahn's results.

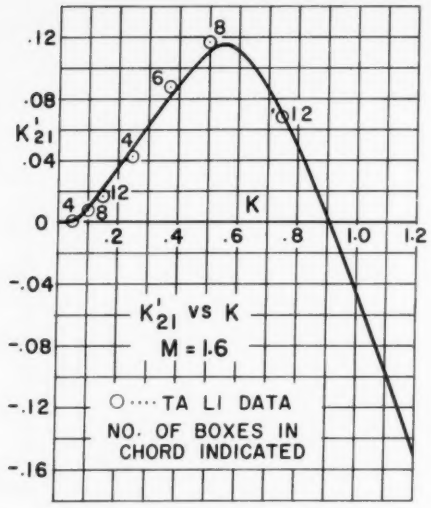

FIG. 11. K'_{21}, $M = 1.6$, comparison with Temple and Jahn's results.

phragm is located in (m', n') where m' and n' are uniquely determined by

$$\left.\begin{aligned} m' - (1/2) \leq (x_2 + x_1 + 1)/2 < m' + (1/2) \\ n' - (1/2) \leq n + [(x_2 - x_1 + 1)/2] < n' + (1/2) \end{aligned}\right\} \quad (33)$$

Thus the whole wing, including the diaphragms extended beyond the tips on both sides, can be covered by a mesh of $(\bar{m} - 1)(2n + \bar{m} + m)$ squares.

It is clear that the integer m is uniquely defined by the inequality

$$m + \frac{1}{2} \leq \frac{n + (1/2)}{\beta \cot \Lambda} < m + \frac{3}{2} \quad (34)$$

Consider now a point (q, s) in D_2 and its region of influence S. It is clear that the point (q, s) is not only influenced by the squares on the right wing within S but also by squares in S lying on the left wing. It is noted that this point is likewise affected by the squares on the diaphragm within S. Of course, there are points solely under influence of squares on the right diaphragm and the right wing, and there are other points affected by squares on the right and the left wings alone.

(4.1) *The Mutual Effect of the Wings*

To find the influence of the squares within S which lie on the left wing on points of the right wing, or vice versa, we consider the subregion S_L bounded by the fuselage center line, the left leading edge, and the right-hand Mach line through $(q, -s)$. The image of S_L with respect to the fuselage center line may be denoted by S_R.

A necessary and sufficient condition for the point (q, s) to be affected by squares in S_L is $q > s$.

Because of the symmetry of the left wing to the right wing with respect to fuselage center line, any $W^*_{\mu, -\nu}$ in S_L is identical to its counterpart $W^*_{\mu\nu}$ in S_R, while the coefficient of influence on (q, s) due to $W^*_{\mu\nu}$ is $C_{(q-\mu), (s-\nu)}$ and that due to $W^*_{\mu, -\nu}$ is $C_{(q-\mu), (s+\nu)}$. Hence, instead of considering S_L and S_R separately, we may restrict ourselves to the right wing and consider $W^*_{\mu\nu}$ in S_R alone. The combined influence coefficient of $W^*_{\mu\nu}$ in S_R on (q, s) will be

$$C''_{(q-\mu), (s-\nu)} = C_{(q-\mu), (s-\nu)} + C_{(q-\mu), (s+\nu)} \quad (35)$$

For fractional squares, sweep corrections must be made accordingly.

(4.2) *Tip Effect*

We recall that the integer n is defined by

$$2n + 1 = 2s^*/l$$

where s^* is the semispan. We notice further that $n > m$ because of the assumption of supersonic leading edge. The general situation of a tip is indicated in Fig. 2.

Since the pressure difference in each square of the diaphragm has to be zero, we can derive a set of linear equations for the $\overline{W}^*$ within the diaphragm in terms of the W^* defined in the region on the wing bounded by the tip, the leading edge or edges, and the right-hand Mach line through the right-tip trailing-edge point. In the case of fractional squares, corrections have to be made accordingly.

For the solution of $\overline{W}^*$ in terms of W^*, we will use a step method. To set up the equations for $\overline{W}^*$, two cases are considered:

(*i*) The leading edge cuts the sides $\xi = m + (1/2)$ and $\eta = n + (1/2)$ of the square $(m + 1, n)$.

Step 1. Preparatory Work.

We will first consider the diaphragm and draw the right-hand Mach line through $(m + 1, n)$.

Along this Mach line, the pressure difference at the points

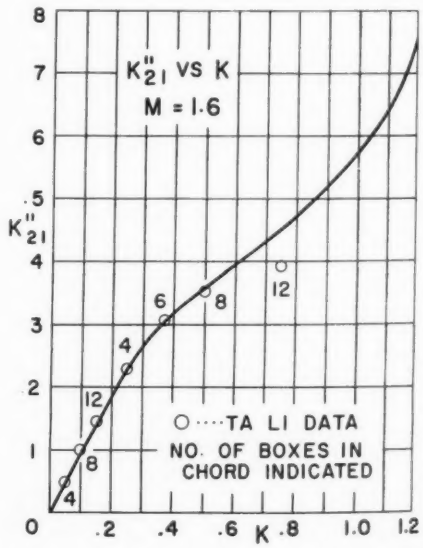

FIG. 12. K''_{21}, $M = 1.6$, comparison with Temple and Jahn's results.

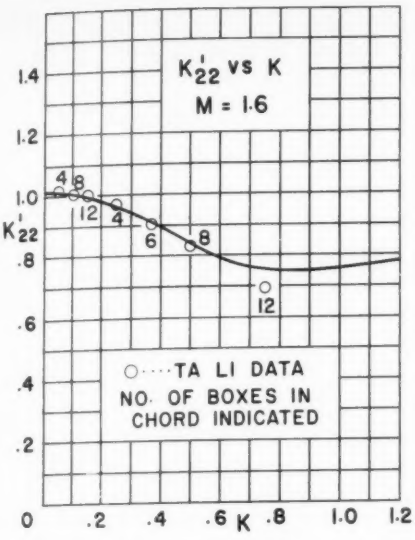

FIG. 13. K'_{22}, $M = 1.6$, comparison with Temple and Jahn's results.

$[m + (3/2), n + (1/2)]$, $[m + 2, n + 1]$,
$[m + (5/2), n + (3/2)] \ldots [m + 1 + \bar{\sigma} + (1/2),$
$n + \bar{\sigma} + (1/2)]$

where

$$\bar{\sigma} = m' - m - 1 = n' - n - 1 \qquad (36)$$

has to be zero. The factor of correction for the square (m, n) is denoted by

$$f^{(iii)}_{mn} = \frac{1}{2\beta \cot \Lambda}\left[\left(m + \frac{1}{2}\right)\beta \cot \Lambda - \left(n - \frac{1}{2}\right)\right]^2$$

Thus, we have the matrix equation

$$\begin{bmatrix} C_{00} & 0 & 0 & \ldots & 0 \\ C_{11} & C_{00} & 0 & \ldots & 0 \\ C_{22} & C_{11} & C_{00} & \ldots & 0 \\ \cdot & \cdot & \cdot & \ldots & \cdot \\ C_{\bar{\sigma}-1,\bar{\sigma}-1} & C_{\bar{\sigma}-2,\bar{\sigma}-2} & C_{\bar{\sigma}-3,\bar{\sigma}-3} & \ldots & C_{00} \end{bmatrix} \begin{bmatrix} W^*_{m+1,n+1} \\ W^*_{m+2,n+2} \\ W^*_{m+3,n+3} \\ \cdot \\ W^*_{m+\bar{\sigma},n+\bar{\sigma}} \end{bmatrix}$$
$$= -f^{(iii)}_{mn} \begin{bmatrix} C_{11} \\ C_{22} \\ C_{33} \\ \cdot \\ C_{\bar{\sigma}\bar{\sigma}} \end{bmatrix} W^*_{mn} \qquad (37)$$

which can be easily solved.

Step 2. Determination of r_λ.

Draw the right-hand Mach line through $(m + \lambda, n)$, $\lambda = 1, 2, \ldots, \bar{m} - (m + 1)$, and denote the square in which this line intersects the leading edge by $(m + \lambda - r_\lambda, n - r_\lambda)$; then the integer r_λ is uniquely determined by Λ, M, and λ.

It can be shown that r_λ satisfies the inequalities

$$\left[\frac{(\lambda - 1)\beta \cot \Lambda}{\beta \cot \Lambda - 1}\right] \leq r_\lambda \leq \min\left\{m + \lambda, \left[\frac{\lambda\beta \cot \Lambda}{\beta \cot \Lambda - 1}\right]\right\} \qquad (38)$$

where $[.]$ indicates the integral part of the number within the brackets and min $\{.,.\}$ denotes the smaller of the numbers within the braces.

Step 3. Solution for $\lambda = 1$.

After solving for r_1, we proceed to determine and solve the equations for $\overline{W}^*_{m+1+\bar{\sigma},\, n+\bar{\sigma}}$. These equations are

$$\begin{bmatrix} \overline{W}^*_{m+1+1,\,n+1} \\ \overline{W}^*_{m+1+2,\,n+2} \\ \cdot \\ \overline{W}^*_{m+1+\bar{\sigma}-1,\,n+\bar{\sigma}-1} \end{bmatrix} = -\begin{bmatrix} C_{11} & C_{22} \ldots & f_{11}C_{r_1+1,\,r_1+1} \\ C_{22} & C_{33} \ldots & f_{11}C_{r_1+2,\,r_1+2} \\ \cdot & \cdot \quad \cdot & \cdot \\ C_{\bar{\sigma}-1,\bar{\sigma}-1} & C_{\bar{\sigma}\bar{\sigma}} \ldots & f_{11}C_{r_1+\bar{\sigma}-1,\,r_1+\bar{\sigma}-1} \end{bmatrix} \begin{bmatrix} W^*_{m+1,\,n} \\ W^*_{m,n-1} \\ \cdot \\ W^*_{m+1-r_1,\,n-r_1} \end{bmatrix}$$
$$- f^{(iii)}_{mn} \begin{bmatrix} C_{10} & 0 & \ldots & 0 \\ C_{21} & C_{10} & \ldots & 0 \\ \cdot & \cdot & \ldots & \cdot \\ C_{\bar{\sigma}-1,\bar{\sigma}-1} & C_{\bar{\sigma}-2,\bar{\sigma}-3} & \ldots & C_{10} \end{bmatrix} \begin{bmatrix} C^{(1)} \\ C^{(2)} \\ \cdot \\ C^{(\bar{\sigma}-1)} \end{bmatrix} W^*_{mn} \qquad (39)$$

where f_{11} denotes the factor of correction for the squares $(m + n - r_1, n - r_1)$. The solution of equations (39) is immediate.

Repeating this process, all of the $\overline{W}^*$ can be expressed in terms of the W^*.

Thus, the pressure difference at the point (q, s) in D_2 can be found by drawing the Mach lines through this point, extending over the diaphragm, and expressing the $\overline{W}^*$ within these lines in terms of the W^* within the region.

The combined coefficient of influence of $W^*_{\mu\nu}$ on (q, s) is then the sum of $C_{q-\mu,\,s-\nu}$ and a function of C.

(*ii*) The leading edge cuts the sides $\eta = n - (1/2)$ and $\eta = n + (1/2)$ of the square $(m + 1, n)$.

In this case, the factor of correction $f^{(iii)}_{mn}$ is zero so that step 1 of case (*i*) becomes unnecessary. We can start from Eq. (39) and solve for

$$W^*_{m+1+1,\,n+1},\ \ldots,\ \overline{W}^*_{m+1+\bar{\sigma}-1,\,n-\bar{\sigma}-1}$$

and apply this process repeatedly. The rest of the work in this case is the same as step 3 of case (*i*).

(5) Subsonic Leading-Edge Adjustment

(5.1) *Evaluation of* $\Delta p(x, y)$ *at* $(0, 0)$

In the case of a subsonic leading edge, the line $\eta = \xi\beta \cot \Lambda$ is behind the Mach line $\eta = \xi$. To obtain a purely supersonic, hypothetic wing we have to add an

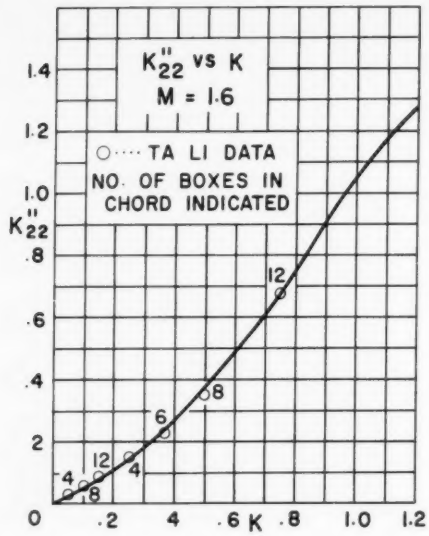

FIG. 14. K''_{22}, $M = 1.6$, comparison with Temple and Jahn's results.

imaginary diaphragm to the actual wing as indicated in Fig. 3.

Since at every point within the diaphragm the pressure difference has to be zero, we can express $\overline{W}^*_{\mu\nu}$ in terms of $W^*_{\mu\nu}$ as soon as the value of $\Delta p(x, y)$ at (0, 0) is known.

By limiting properly, it has been found that

$$\Delta p(0,0) = -\frac{4\rho V^2}{\pi} e^{i\omega t}\left\{\overline{W}^*_{00}\left(1-\pi-\beta\cot\Lambda\times[1-\beta^2\cot^2\Lambda]^{-(1/2)}\cosh^{-1}\frac{1}{\beta\cot\Lambda}\right)+W^*_{00}\left(\pi+\beta\cot\Lambda\,[1-\beta^2\cot^2\Lambda]^{-(1/2)}\times\cosh^{-1}\frac{1}{\beta\cot\Lambda}\right)\right\} \quad (40)$$

The value $\Delta p(0, 0)$ is very important for the solution of the problem of subsonic leading edge.

(5.2) *Determination of $\overline{W}^*$ on the Diaphragm*

Physically, the pressure difference on the square (0, 0) is solely induced by the existence of the square itself. It is not affected by any other square or a fractional part of it. Hence the pressure difference should be

$$(\pi e^{-i\omega t}/2\rho)\,\Delta p(0,0) = -(V^2\pi/\beta)W'(0,0)$$

where

$$W'(0,0) = (1/4)\beta\cot\Lambda W^*_{00} + (1/4)\,[1-\beta\cot\Lambda]\overline{W}^*_{00} \quad (41)$$

and $W = 0$ in front of the diaphragm. Consequently, we have

$$\Delta p(0,0) = -\rho V^2 e^{i\omega t}/(2\beta)\,(\beta\cot\Lambda\, W^*_{00} + [1-\beta\cot\Lambda]\overline{W}^*_{00}) \quad (42)$$

Comparing Eqs. (41) and (42), we find

$$\overline{W}^*_{00} = \sigma W^*_{00} \quad (43)$$

where

$$\sigma = \left\{(8-\cot\Lambda)\beta\pi\,[1-\beta^2\cot^2\Lambda]^{1/2} + 8\beta^2\cot\Lambda\left(\cosh^{-1}\frac{1}{\beta\cot\Lambda}\right)\right\}\left\{[(8-\cot\Lambda)\pi-8]\beta\times[1-\beta^2\cot^2\Lambda]^{1/2}+8\beta^2\cot\Lambda\left(\cosh^{-1}\frac{1}{\beta\cot\Lambda}\right)\right\}^{-1} \quad (44)$$

Thus, the combined strength function over (0, 0) may be replaced by $\sigma^* W^*_{00}$ where

$$\sigma^* = (1/4)\,[\sigma+\beta\cot\Lambda(1-\sigma)] \quad (45)$$

The equation for $\overline{W}^*_{11}$ is obtained by drawing the right-hand Mach line through (0, 0). It is found that

$$\overline{W}^*_{11} = \sigma_0 W^*_{11} + \sigma_1 W^*_{00} \quad (46)$$

with

$$\sigma_0 = (3\beta\cot\Lambda-1)^2\,[9\beta^2\cot^2\Lambda-10\beta\cot\Lambda+1]^{-1} \quad (47)$$

$$\sigma_1 = 2\beta\cot\Lambda[\sigma+\beta\cot\Lambda(1-\sigma)]\,[9\beta^2\cot^2\Lambda-10\beta\cot\Lambda+1]^{-1} \quad (48)$$

The combined strength function over the square (1, 1) is obviously $-C^*_{11}\sigma^* W^*_{00}$ with

$$C^*_{11} = C_{11}/C_{00} \quad (49)$$

This process will be continued until all the squares lying partly on the wing and partly on the diaphragm are exhausted.

After solving for $\overline{W}^*_{00}$ and $\overline{W}^*_{11}$, we can set up a system of equations for the other $\overline{W}^*$ along the same Mach line.

Repeating this process along each Mach line lying between $\eta = \xi$ and the leading edge, we can express $\overline{W}^*$ in terms of W^*. This solves the problem of subsonic leading edge. An additional treatment for the tip region will complete the study of a three-dimensional thin wing oscillating in supersonic flow.

REFERENCES

[1] Pines, S., and Dugundji, J., *Aerodynamic Flutter Derivatives of a Flexible Wing with Supersonic Edges*, ATC Report No. ARTC-7, February, 1954.

[2] Pines, S., and Dugundji, J., *Application of Aerodynamic Flutter Derivatives to Flexible Wings with Supersonic and Subsonic Edges*, Republic Aviation Corp, E-SAF-2.

[3] Li, Ta C. H., *Aerodynamic Influence Coefficients for an Oscillating Finite Thin Wing*, Chance Vought Aircraft, Inc., CVA Report No. 9513.

[4] Garrick, I. E., and Rubinow, S. I., *Flutter and Oscillating Airforce Calculations for an Airfoil in a Two-Dimensional Supersonic Flow*, NACA Rep. 846, 1946.

[5] Temple, T., and Jahn, H. A., *Flutter at Supersonic Speeds: Derivative Coefficients for a Thin Aerofoil at Zero Incidence*, British A.R.C. Tech. Rep. No. 8583, R&M 2140, 1940.

[6] Head, A. L., Jr., *A Compilation of Two-Dimension Aerodynamic Coefficients with a Review of Flutter Analysis Methods*, Chance Vought Aircraft, Inc. Report No. 8242, 1954.

Design of Structural Models, with Application to Stiffened Panels Under Combined Shear and Compression

P. E. SANDORFF*

Massachusetts Institute of Technology

ABSTRACT

Practical methods for the design of structural test specimens are presented, based on the principle of exploring a specific mode of failure rather than the customary indefinite investigation of structural behavior in general. This approach makes possible considerable simplification in specimen construction, through application of similitude relations, without introducing unknown restrictions on the validity of the results. Illustration is provided by application to the problem of interaction relations for stiffened-skin panels under combined compression and shear. Results of full-scale tests, under simultaneous bending and torsion, of a box beam structure incorporating machined integrally stiffened test panels substantiate the interaction curve derived by similitude relations.

INTRODUCTION

IN TESTING OF AIRCRAFT STRUCTURE, the accepted method for designing the test specimen is to make it an exact duplicate of the original in size and detail. This method has several advantages: under the correct loading there is no doubt as to the validity of the results; unsuspected weak points and deflection modes which may have been overlooked in analysis will be exposed by the test. In the case of a test program for research purposes the same philosophy is generally used; the specimen design is made as representative of typical structure as possible so that the results may be applied directly to analytical problems without danger of unknown "scale effects" or false indications of critical failure modes.

However, aircraft structures have for some time been so large and so complex that a simple proof test represents an enormous amount of cost and time, and exploratory work of the type badly needed for advancement of the art has become rare. There is therefore good reason to turn to other methods of obtaining empirical data—namely, to use specimens that do not duplicate the original either in size or in detail but which are designed by rational methods to produce the specific information desired with a minimum budget.

The laws of similitude which govern the relationship between the behavior of the test specimen (whether full-scale or reduced) and the original structure it represents are well presented in the literature.[1–3] The fundamental principle, widely recognized and accepted, is that geometric similarity of model and original is essential if a completely true test is to be obtained. Under these circumstances there is little economic advantage in using reduced scale models for aircraft structural problems: it usually costs more to duplicate complex stiffened skin structure in miniature than it does to fabricate it full scale. To reduce cost it is necessary first to achieve simplification.

In addition there exists a widespread distrust of all reduced scale models. This is unjustified if the model is a true model,[1, 2] but when does a model meet this requirement? If similitude with respect to grain structure or lattice structure of the material is significant (as it seems to be for failure in fatigue, for example), anything but the original structure itself will introduce inaccuracy. What is the size of this error? How can the importance of apparently inconsequential details of the structural design be assessed?

This state of the art in empirical structures is in contrast to that in the fields of aerodynamics and aeroelasticity, where data of practical importance are derived as a daily routine with the use of dissimilar models. In a typical low-speed wind-tunnel test, for example, true similitude is established by preserving external geometric similarity, Reynolds Number, Froude Number, Weber Number, and Mach Number. Usually only the geometric requirement is met, and a drag correction may be made for Reynolds Number. How much of the costly similitude achieved in structural test specimens could also be dispensed with as unimportant?

A rigorous method of determining such effects experimentally is treated in detail by Murphy.[1] Models that are dissimilar in some important respect from the structure they represent are called "distorted" models. The effect of distortion can be evaluated by testing additional specimens, in each of which the distorted quantity has a different value; the results can then be extrapolated to indicate the behavior of the original structure. However, this procedure leads to an expanded test program and does not offer much hope for cost reduction. Actually the method is already in widespread use in a disguised form: in many investigations such as fatigue tests, notch tests, some tension tests, etc., no specimen can represent the original with a satisfactory degree of accuracy. Unknown distortions are therefore lumped under the general term of variability. A large number of tests are conducted to evaluate the effect of these distortions, and this leads to a determination of the probable deviation or the scatter band.

Presented at the Structures Session, Twenty-Third Annual Meeting, IAS, New York, January 24–27, 1955.

* Associate Professor of Aeronautical Engineering. Formerly, Research Specialist, Lockheed Aircraft Corporation.

It seems inescapable that if a conventional type of structures test is desired which will give an answer to numerous unspecified unknowns, only two methods can be considered satisfactory: (1) a full-scale exact duplicate test model or (2) a distorted model with additional tests to evaluate the effect of the distortion.

However, a test that supplies not all the answers but merely the unknown ones may often be considered adequate. There already exist a number of different applications of what may be called "restricted structural models"; for example:

(a) "Indirect" models such as the Beggs deformator, suitable for elastic beams and truss members.[1, 23, 25]

(b) "Direct" models for individual beams and girders, and complex analogs such as those for dirigible framework constructed with such members.[1, 5, 23, 25]

(c) Simplified model techniques described by Watter for representing highly indeterminate structure by duplicating elastic properties of various portions or components.[4]

(d) Investigation of "structural principles" with transparent plastic models as described by Walker.[6]

Such model designs are possible only by excluding from consideration large portions of unimportant detail. For simpler problems the philosophy of this approach and its justification are obvious and have not been labored in the literature. For treating complex, nonlinear, possibly inelastic stiffened skin structure a firm basis is first required for delimiting the scope of the restricted investigation, and second, a systematic procedure is needed to establish for the model the minimum design specifications that guarantee the stated objectives. These considerations are discussed and implemented below.

Design of Restricted Models

Mode of Deflection as a Basis for Model Design

In order to design a restricted model it is important to recognize that similitude relations apply to a physical phenomenon. In structures testing the most useful single phenomenon to duplicate in the test of the model is the deflection response under load. Regardless of the structural detail, if the mode of deflection is duplicated and if the stress-strain relations are linear, model laws may be derived to relate loads, deflections, stresses, etc., in the model with those in the original. If plastic deformation occurs, it will in general also be necessary to duplicate the stress distribution, but for approximate purposes this may not be required particularly if two- or three-dimensional effects are negligible. In destruction tests the mode of deflection and mode of failure may usually be considered synonomous.

For unconventional structures the selection of the mode or modes of deflection to be studied may require considerable insight. For conventional structures however the critical modes are already well-recognized: in a fuselage shell, for example, the effects of inter-rivet buckling, skin buckling, stiffener crippling, joint strength, etc., can usually be provided for economically by analytical means, but test data may be desirable in connection with large-scale stress concentration effects load redistribution problems, and general instability To investigate these effects it is not necessary to test also for inter-rivet buckling, etc.; in many cases it may even be desirable to eliminate such effects in order to avoid a trivial result.

By using the test to investigate not a structure but a specific mode of deflection of that structure, all geometrical quantities and constructional details which do not affect this particular mode can be varied as desired. If these quantities can be identified, considerable simplification and economy in construction of the specimen may be expected.

Identifying the Quantities

The first step in delimiting the model design is therefore to define exactly the deflection mode to be investigated. This is in itself an explicit statement of the elements of the structure which are involved and the manner in which they deform. This leads to a statement of the physical quantities involved in the phenomenon.

For example, consider the case of a stiffener section under end-compression: several modes of deflection are possible, including direct axial compression, lateral column instability, torsional instability, crippling, and section distortions. It is decided to investigate lateral column bowing; all others are excluded. The stiffener section undergoes bending in resisting the lateral bowing, and the resisting moment is determined by the section bending rigidity EI and, for a given deflection geometry, the length L. Quantities that determine the applied moment are recognized as the end load P_{cr}, the end fixity conditions c, and again for the same deflection shape, the length L. For classical buckling the actual value of the lateral deflection itself is known to be irrelevant.

There is no specification of shape of section, thickness, height, etc. At this stage however each of the discarded quantities may be inspected to determine what type of stress it undergoes during the prescribed deflection process and to judge whether this stress contributes additionally to the action. In this way, if not earlier, it may be seen that shear deformation of the web enters into the problem, and in the case of wide flanges, shear lag effects here may significantly alter the resistance in bending. The latter can be represented by an efficiency factor η; for transverse shear deformation, the quantity GK is used to represent section shearing rigidity.

Dimensional Analysis

It is convenient to use the formality of dimensional analysis to identify the dimensionless parameters governing similitude. The procedure is well described in references 1 and 2 and is only briefly indicated here. If a total of n quantities is involved, and these involve

p fundamental measuring units, then $(n - p)$ independent Pi-terms can be formed which define completely the requirements of similitude. (There are some exceptions: see reference 1.)

For the column example there are six quantities

$$[P_{cr},\ L,\ \overline{EI},\ \overline{GK},\ c,\ \eta]$$

and these involve two dimensions, force and length. Therefore $6 - 2$ or 4 dimensionless ratios, mutually independent, suffice to express the phenomenon—if each were given a value, the set would define a family of specimens which would exhibit similar deformational characteristics. One set of four Pi-terms may readily be found as follows:

$$[P_{cr}L^2/\overline{EI},\quad \overline{GK}L^2/\overline{EI},\quad c,\quad \eta]$$

Any other four independent nondimensional ratios would be equally definitive, and alternates may be investigated to select the most convenient. Alternates can be formed by multiplying or dividing any of the original terms together; $P_{cr}/\overline{GK}$, for example, may be used in place of either $P_{cr}L^2/\overline{EI}$ or $\overline{GK}L^2/\overline{EI}$. Writing the Pi-term containing the dependent variable as some function of the others,

$$P_{cr}L^2/\overline{EI} = \phi[\overline{GK}L^2/\overline{EI},\ c,\ \eta]$$

or

$$P_{cr} = (\overline{EI}/L^2) \times \phi[\overline{GK}L^2/\overline{EI},\ c,\ \eta]$$

Thus for similitude between any two laterally buckling columns it is only necessary that the values of $\overline{GK}L^2/\overline{EI}$, c, and η be unchanged from one to the other. This expression is considerably less restrictive than that derived by considering such quantities as merely appear to be significant, such as area A, radius of gyration ρ, E and I separately, etc. By regarding the deflection mode systematically and excluding the irrelevant mode of pure axial deflection, dimensional analysis produces a result almost as explicit as the Engesser column formula.

Eliminating Parameters

It is sometimes possible to demonstrate by analytical or other means that some of the Pi-terms are mutually related in the manner in which they affect the phenomenon. As shown in reference 1, the related Pi-terms in such cases may be replaced with a single parameter formed by combining the original terms. In the column example cited, a more general type of similitude is established by combining the terms $P_{cr}L^2/\overline{EI}$ and c, since it is known that the dependent quantity P_{cr} is influenced to the same degree by c and by $\overline{EI}/L^2$. The necessary parameters then become

$$[P_{cr}L^2/(c\ \overline{EI}),\ \overline{GK}L^2/\overline{EI},\ \eta]$$

The same result could have been achieved by selecting the pin-end length $L/\sqrt{c}$ as an original quantity instead of L because of its greater generality.

In addition parameters that can be shown to have negligible effect on the test results may be cast out; the question of validity of the test then becomes a matter of the degree of accuracy desired. Obviously in the column problem, violation of the $\overline{GK}L^2/\overline{EI}$ requirement will have little effect on a long column of solid section. On a very thin-webbed section, however, or on a sandwich-core section that has low shear rigidity the relation may not be ignored, and for wide-flanged sections, stiffened-skin panels, etc., the flange effectiveness denoted by η must be considered. Thus empirically derived column relationships often reflect more than just stress-strain properties of the material.[7]

Detail Design

Similitude is established by keeping the values of the Pi-terms in the brackets unchanged between any two tests:

$$P_{cr} = (c\ \overline{EI}/L^2) \times \phi[\overline{GK}L^2/\overline{EI},\ \eta]$$

or if the shear deflection quantities can be ignored,

$$P_{cr} = (c\ \overline{EI}/L^2) \times \phi[\text{Unity}]$$

In the former case, if plasticity is involved, a simplification of detail appears impractical due to the difficulty of evaluating $\overline{GK}$ and $\overline{EI}$. In the elastic case however any column that fails in the specified mode is a satisfactory design for a test specimen. In this case the model-to-original relationships are:

$$\left[\frac{P_{cr}L^2}{c\ \overline{EI}}\right]_{\text{model}} = \phi\left[\frac{\overline{GK}L^2}{\overline{EI}},\ \eta\right] = \left[\frac{P_{cr}L^2}{c\ \overline{EI}}\right]_{\text{original}}$$

Dividing through by section area and making use of $\rho^2 = I/A$ and $\sigma_{cr} = P_{cr}/A$,

$$\left[\frac{\sigma_{cr}}{E}\left(\frac{L}{\rho\sqrt{c}}\right)^2\right]_{\text{model}} = \left[\frac{\sigma_{cr}}{E}\left(\frac{L}{\rho\sqrt{c}}\right)^2\right]_{\text{original}}$$

This is the Euler hyperbola, which is defined by a single test if shear deformations are neglected. When shearing deformations are considered, a similar entire family is defined for each combination of $\overline{GK}L^2/\overline{EI}$ and η.

Application to Integrally Stiffened Skin Panels Under Compression and Shear

In wing surfaces, and also in certain regions in fuselage shells, stiffened skin structure frequently carries a critical combination of end-wise compression and in-plane shear. In the wing, for example, this loading arises as a result of simultaneous wing bending and wing torsion. Margins of safety under such conditions are usually computed by the interaction method,[8, 9] with the shape of the interaction curve determined by empirical methods.

Previous Experimental Work

Four previous test investigations to determine the shear-compression interaction relations for stiffened structure are known,[10–13] and while margins of safety for all types of structural detail have been based on these results, the original tests are actually limited

in scope. A serious difficulty arises in interpreting early test data because information regarding the manner of failure is usually incomplete.

Of these four sources, reference 10 is generally not used because of the unusual character of the data, which is attributed to irregular end conditions. Reference 11 is concerned only with flat corrugation-stiffened panels which fail in crippling action. Effects of inter-rivet buckling and forced crippling due to local loads are noted in several cases. Five test points, including those for pure compression and shear, establish an interaction curve of $R_s^{1.7} + R_c = 1$. Reference 12 treats curved fuselage panels with inverted hat section stiffeners (i.e., open sections) and flat wing-surface panels with round-topped hats (i.e., closed section stiffeners); the interaction relations were determined as $R_s^{1.75} + R_c = 1$ and $R_s^2 + R_c^2 = 1$, respectively. In these tests the compression mode was of a column nature, while shear failures involved either stiffener crippling, skin tearing, or rivet failure. In many cases stiffener flange rolling was appreciable and inter-rivet buckling can be inferred. Reference 13 presents results of torsion-compression tests on stiffened cylinders; an interaction relation of $R_T^{1.5} + R_c = 1$ is shown for the stiffener crippling mode, where these ratios pertain to cylinder loads. On the basis of shear stress and stiffener compressive stress, derived from strain-gage data presented in the report, reference 13 appears to confirm the paradoxical results of reference 10—namely, that a small amount of shear buckling in the skin may markedly improve the performance of the stiffeners in compression.

These studies are each valid for the specific structure under investigation, but because of the diversity of failure modes the usefulness of the data is limited. A notable attempt to generalize these results is made in reference 14 in defining interaction relations for the stiffener crippling and skin rupture modes in curved panels with open section stiffeners.

Current Investigation

The studies described below were undertaken to establish the interaction relation under compression and shear for flat, machined, integrally stiffened skin. In this type of structure the stiffeners are characteristically a simple rectangular cross section, as shown in Fig. 1, and are usually closely spaced, since the cost of manufacture no longer hinges on the number of stiffeners or number of attachments and it is therefore economically feasible to design for nonbuckling skin. However, the fact that the entire panel must be machined from plate places a heavy price on deep sections, and therefore surface structure under compression is typically critical in column action rather than in crippling, as is the case for conventional built-up skin-and-stiffeners.

Possible Failure Modes

Because of the nature of the structure as indicated above, overall panel instability is a critical failure mode. In this mode a large wave pattern forms, extending (in a wing panel, for example) from rib to rib and from chord to chord; the stiffeners and skin do not act individually but rather the panel behaves as uniform orthotropic sheet material. This type of instability may occur as a result of pure compression, pure shear, or a combination of the two. For a wide structure, panel instability under pure compression is for practical purposes equivalent to column failure and collapse, but under shear, panel instability would not necessarily mean collapse. The use of the panel instability mode as the basis for a design allowable therefore may embody some conservatism.

A crippling mode, in the case of open-section stiffeners, would be primarily a compression effect: an interaction effect under compression and shear would be expected only in extreme ranges of design as a result of secondary effects of shear-buckling skin on stiffener behavior, etc. (For closed-section stiffeners that can pick up shear, the interaction effects would be more important.) Since the structure to be studied when under pure compression is critical column-wise, crippling is excluded from further consideration.

The two elementary in-plane deformation modes of straight axial compression and simple shear deformation of the skin are of minor importance to stability modes, because insofar as buckling is concerned the structure may for practical purposes be assumed to have the same in-plane dimensions up to the critical load. However, the elementary strains do produce conditions that are critical for skin rupture, and the skin rupture mode would in general show an interaction effect. A reasonable test specimen for investigating this mode would be quite different, possibly much smaller and simpler, from that for the panel instability problem.

The manufacture of machined integrally stiffened sheet permits the use of heavy edges on the test panels, as in airplane usage, so that there is no attachment failure mode in either case. Since the stringers are integral with the skin, there is no inter-rivet buckling or rivet deformation, and skin buckling can be placed beyond the range of test stresses. Even if the subject for investigation were conventional skin-and-stiffeners, it would be desirable to investigate such special problems with auxiliary tests and to eliminate them from large panel tests.

Only the panel instability mode is considered further here.

Analysis for Similitude Requirements

A detailed study of the structural quantities and their effect on the phenomenon of large panel buckle deformation [see Appendix (A)] indicates that the following are of major significance:

Panel length between ribs (parallel to stiffeners) L_y, in.
Panel width between chords, L_x, in.
Bending rigidity lengthwise, per unit width, $\overline{EI}_y$, lb. in.

Bending rigidity chordwise, per unit width, $\overline{EI}_x$, lb. in.
End-fixity conditions in compression, K_c
End-fixity conditions in shear, K_s

It is convenient to introduce the loading in terms of the nondimensional load ratios R_c and R_s and to select one of these as the dependent variable. Dimensional analysis leads to

$$R_s = \phi[R_c, L_x/L_y, \overline{EI}_x/\overline{EI}_y, K_c, K_s]$$

Therefore, every experimentally determined point on the R_c, R_s plane is applicable to any other stiffened-skin structure of the same aspect ratio (L_x/L_y), the same degree of orthotropy of bending rigidity $(\overline{EI}_x/\overline{EI}_y)$, and the same end- and edge-fixity conditions.

For structure of ordinary proportions, the requirements can be simplified further by combining the length and bending rigidity terms into a generalized aspect ratio, $(L_x/\overline{EI}_x)/(L_y/\overline{EI}_y)$. The justification for this step is presented in Appendix (B). Then for engineering purposes and for panels of customary proportions, similitude is expressed by

$$R_s = \phi[R_c, (L_x/\overline{EI}_x)/(L_y/\overline{EI}_y), K_c, K_s]$$

Isotropic Plate as a Model for Stiffened Skin Panel

In Appendix (B) it is shown that the critical combinations of shear and compression for an orthotropic panel are computed the same as those for an isotropic plate if the generalized aspect ratio $(L_x/\overline{EI}_x)/(L_y/\overline{EI}_y)$ is substituted for a/b and if $(L_x/\overline{EI}_x)/(L_y/\overline{EI}_y)$ is large—that is, of the order of 1,000. In all practicable design variations of the integrally stiffened skin construction under consideration, $(L_x/\overline{EI}_x)/(L_y/\overline{EI}_y)$ is very large. The isotropic plate of infinite aspect ratio therefore may be considered as a model for the stiffened skin panel.

Various solutions for the interaction curve for flat isotropic plates under various end and edge conditions are presented in references 15 and 16. In view of the complexity of the boundary fixity conditions for a stiffened panel [discussed in detail in Appendix (A)], a correlation with those for isotropic plate is not attempted, but it is noted that the shape of the interaction curve is appreciably affected by fixity effects only in the region of large R_c. In terms of the stiffened panel this indicates that, in an approximate fashion, K_c is important to the shape of the interaction curve but K_s is not.

In applying the charts for isotropic plate to stiffened panels, the abscissas and ordinates must be considered as load ratios, not stiffener stress ratios, since the stress distributions are not necessarily identical.

Experimental Confirmation

Results of a full-scale study of a typical machined integrally stiffened surface conducted at Lockheed Aircraft Corporation[17] confirm the use of the isotropic plate as a model in determining the interaction curve. The machined panel was tested as the upper surface of a box beam that was placed under various combinations of bending and torsional load. Load was applied by hydraulic means, and the ratio of compression to shear was held approximately constant throughout any one test. Details are given in Figs. 1 to 4 and in Appendix (A).

Because of specimen cost the box beam tests were not carried to destruction but only to the point of imminent failure. By observation of strain data from gages placed on extreme fibers in the central regions of the panel it was possible to approach with assurance to within 95 per cent of the panel instability point; an extrapolation of the bifurcation data, as in Fig. 5, could then be made to indicate actual strength within one or two per cent. With the dimensions of the panel such as to produce column failure at less than 30,000 psi and using 75S-T6 aluminum alloy plate with a proportional limit of 60,000 psi, it was possible to conduct a number of tests on each surface specimen without inflicting permanent damage, provided the shear-to-compression ratio was not too high.

The strength of the structure under pure shear was greater than anticipated due to unexpectedly favorable end-fixity effects. In the box beam the stiffener elements were continuous from bay to bay and in addition a local reinforcement was added for rib-attachment purposes. This raised the panel instability stress in pure shear to a value greater than that for skin rupture so that an end-point to the interaction curve was not obtainable. However, two test points were obtained with the ratio of shear to compressive stress of about 5. Under this combined-stress condition the proportional limit for the 75S-T6 material was approximately 35,000 psi shear, 7,000 psi compression. Test stresses exceeded these values, and the strain-gage data were therefore analyzed assuming stress-strain relations in accordance with the deformation theory of plasticity.[24]

The generalized aspect ratio of the box beam surface in the elastic range is computed as

$$\frac{L_x/I_x}{L_y/I_y} = \frac{34.7/2.86 \times 10^{-6}}{16.0/0.005} = 3{,}800$$

For cases affected by plasticity, $\overline{EI}_y$ would be expected to fall off more rapidly than $\overline{EI}_x$ so that $(L_x/\overline{EI}_x) \div (L_y/\overline{EI}_y)$ would be somewhat less than 3,800 but nevertheless large.

End-fixity for the box beam panel under pure compression was about 1.15, where 1.0 corresponds to pinned ends and 4.0 to full-fixity. The simply supported isotropic plate with $a/b = \infty$ therefore appears to be a good model for the machined box beam surface. The corresponding interaction curve taken from Fig. 5 of reference 16 is reproduced in Fig. 6 of the current paper, and on the same figure are plotted the experimental data for machined stiffened skin panels from reference 17.

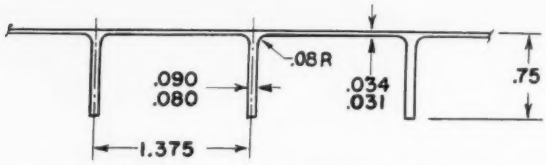

FIG. 1. Section of machined integrally stiffened skin.

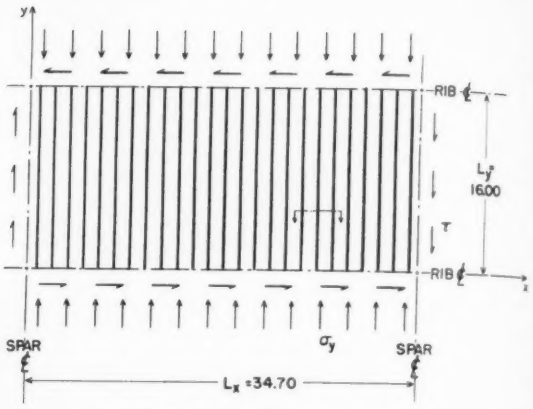

FIG. 2. Box beam test panel.

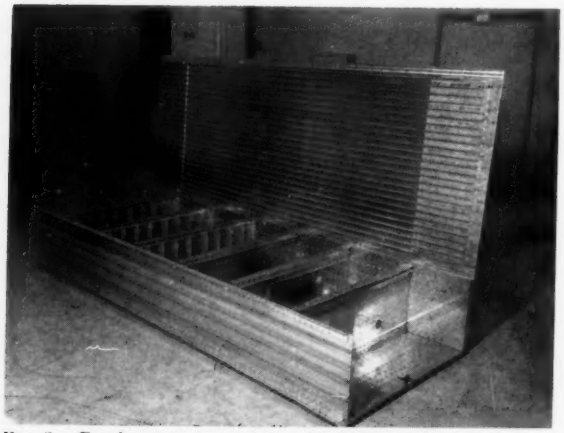

FIG. 3. Box beam test structure with upper surface test panel ready for installation.

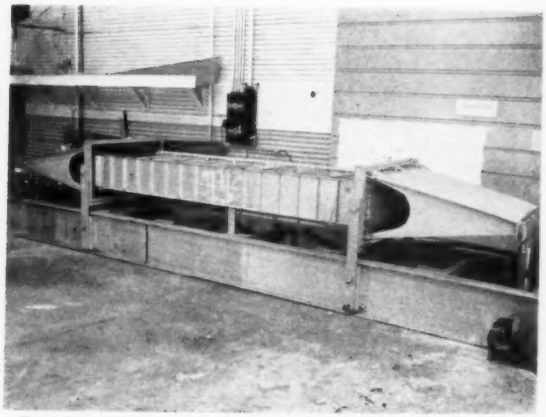

FIG. 4. General view of test arrangement for pure bending.

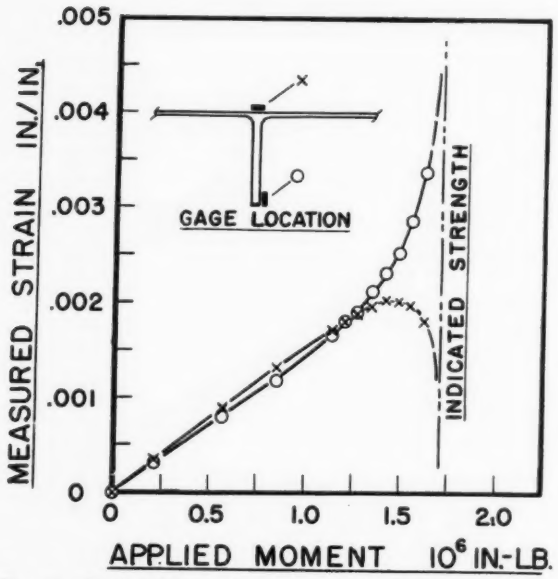

FIG. 5. Typical bifurcation plot to indicate probable failure point.

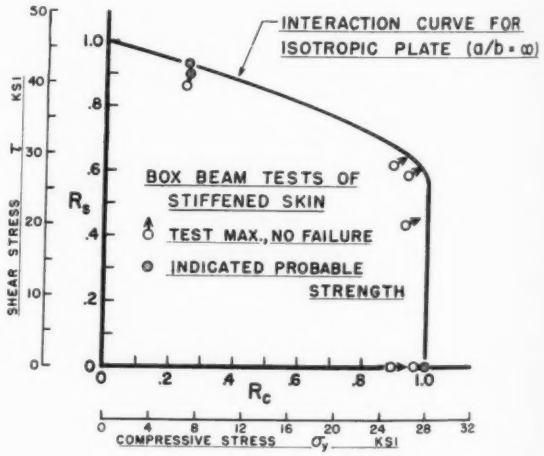

FIG. 6. Interaction data.

Other Applications

Some of the potentialities and limitations of the proposed methods are indicated by the preliminary studies described below.

Cut-Out and Diffusion Problems

In the problem of build-up and decay of axial stresses around cut-outs and at points of concentrated loading in shell structure, the investigation may as a first approximation be restricted to in-plane deformations of skin and stiffeners, excluding all other effects such as attachment deflections, shear transfer over the depth of the stiffener, warping out of plane, etc.

The mode of deflection in this case is defined by the equations of equilibrium and compatibility. For the approximate case of "unidirectional shear lag," in which transverse stringer forces are neglected, a uniform stiffened skin structure may be represented by a model of isotropic plate with suitable scale factors.

For precise studies and for structures in which skin and stiffener areas vary, the model must be made with discrete stiffener and skin elements. However, these need represent only section areas and thicknesses, not shape. A reduced scale model could be used to advantage to obtain stress distribution data.

General Instability of Stiffened Shells

If by definition of general instability all localized effects are excluded and consideration is restricted to wave forms large compared to stiffener and ring spacing, then the surface of a stiffened shell behaves as an orthotropic sheet.

The problem of simplifying and yet adequately representing the behavior of the shell surface depends on the detail structure (whether sandwich, stiffeners and skin, plywood, etc.), the type of load and the accuracy desired.

For the case of torsional load, the critical stress of an orthotropic shell is derived in reference 18 in an approximate form identical with Donnell's[19] for unstiffened cylinders. The same charts are then shown to be applicable to both problems when proper scale factors are introduced. Thus the unstiffened shell becomes a model for the stiffened structure.

For general instability in compression and bending, classical theory shows solutions that also lead to generalized parameters suitable for both stiffened and unstiffened shells. This type of analysis, as well as notable experimental work using simplified models is shown in the GALCIT studies of general instability.[20] It is to be expected that stiffened shells in compression or bending will show the same sensitivity and erratic behavior due to inherent nonlinearities and initial irregularities as is found[21] for unstiffened cylinders. An experimental program is now needed not to develop a theory but to evaluate the effect of irregularities occurring in typical fabrication, and for this problem only exact full-scale specimens appear suitable.

Thermal Stress Problems

A field in which economical test procedures are badly needed is that of stresses due to thermal heating. Transient thermal differences from point to point in the structure arise as a result of an influx of heat at the bounding surface. Duplication of these effects in geometrically similar models is governed by the parameters $qL\beta/K$ and Kt/CL^2 where

q = heat inflow per unit area, B.t.u./ft.^{2}/sec.
L = characteristic length of specimen, in.
β = coefficient of thermal expansion, strain/°F.
K = conductivity, B.t.u./sec./ft.^{2}/°F./in.
C = specific heat, B.t.u./in.^{3}/°F.
t = time from initiation of heating, sec.

A serious difficulty which arises in the use of scaled models is that, in order to hold the prescribed value of $qL\beta/K$, q must be increased as L is reduced. The value of q required for full-scale work is already often impossible to achieve. On the other hand, if an oversize model were used, not only must the surface area of the heat source be increased as L^2 but in order to maintain the value of Kt/CL^2 unchanged, the duration of heating to achieve any particular desired transient condition must also be increased as L^2. Therefore, though heat intensity requirements would be reduced in an oversize model, the total energy required would increase as L^3, and total energy supply often represents as much of a problem as intensity.

In the general case, the thermal stress problem involves elastic and plastic properties of the material as a function of both temperature and time, and these will be involved in deformation, stress, and stability effects. The time constant in transient thermal response for each element of a complex structure must be the same as in the original, or they must all bear the same scale factor, if the behavior of the original is to be duplicated. As for any structures test, the general requirements offer little hope for use of models that differ in material of construction or which violate geometric similarity.

But just as for static strength tests, if the problems are approached individually, considerable simplification may be made for each study. The mode of deflection may again be used as the basis for the design of restricted-purpose test specimens. In many cases, such as the determination of elastic stress distribution, use of a material having a large ratio of β/K, such as stainless steel or a nonmetal, would be indicated to reduce q requirements.

Rupture Phenomena

Rupture includes a number of failure phenomena for which the developing stress distribution may be significant on a microscopic scale. While Barba's law regarding the similarity in behavior and failure of geometrically similar tension coupons is well established,[26] it is recognized that in the case of the ordinary tension coupon the necking effect is large compared to the

microstructure of the material. This is not so when severe notch conditions exist, such as in fatigue, so-called brittle fracture, and some cases of stress concentration. It is believed that this may be the cause of many legitimate scale effects as well as the source of the large scatter observed in such test data.

If this is true it does not necessarily preclude the use of scaled models for studies of rupture effects; however, the possible effect of scale distortions should be investigated.

Conclusion

The fundamental thesis presented here is that geometric similarity between the test specimen and the original is not always a requirement for a valid structures test, much less for one of only engineering accuracy. That this is true is demonstrated by experimental data on the interaction curve under compression and shear for machined integrally stiffened skin; these data confirm the relationship established by a model of isotropic plate.

In order to take such liberties in the design of models or test specimens, it is necessary at the outset to sacrifice the complete generality of the usual structures test and investigate only specified failure modes. This is the same approach as used in ordinary stress analysis work, and it suffers the same disadvantage—something may be overlooked. In spite of this disadvantage much use is made of analytical methods, and considerable usefulness will also be found in the application of restricted models.

The common denominator between the model and the original is the mode of deflection. In the design of restricted models, similitude analysis provides a means for delimiting the scope of the investigation and assuring a test that represents the original problem with suitable accuracy. Reduced scale testing can be safely used for a variety of problems; certain modes and quantities however are recognized as being reproducible with accuracy only in full-scale specimens. Similitude relations for restricted models can be used not only for designing simplified test specimens but also for generalizing the application of data already at hand.

For proof testing it seems improbable that a test of a restricted model can ever be as satisfying as a test of a full-scale replica. But both size and performance requirements are expanding to the point where ordinary proof tests may become inadequate as well as exorbitant. It may then be necessary to consider a different approach to the proof test philosophy, such as substituting a number of relatively inexpensive restricted tests, the results of which are superimposed on paper.

A somewhat neglected field of structural theory is the study of deflection modes as specific physical phenomena. Of the many parameters that govern the various deflection modes in various types of structure, the significance of only a few is now known, yet these parameters may prove to be as useful to the structures engineer as Reynolds Number, Mach Number, etc., now are to the aerodynamicist.

Acknowledgment

The author expresses his thanks to the Structures Research Department, Lockheed Aircraft Corporation, for their generosity and assistance in the work described here.

APPENDIX (A)

Properties of Machined Panel

Elastic Constants

If local effects can be ignored and the effect of concentrated stiffening elements can be considered as uniformly distributed, the surface may be treated as a homogeneous orthotropic plate. The behavior of an orthotropic plate is established by the values of 15 "elastic constants" (in the list of 17 below two of the Poisson's ratios may be evaluated through the Maxwell-Betti relations $\nu_x E t_y = \nu_y E t_x$ and $\mu_x D_y = \mu_y D_x$):

Extensional stiffnesses, average per inch width	$Et_x/(1 - \nu_x\nu_x)$	lb./in.
	$Et_y/(1 - \nu_x\nu_y)$	lb./in.
In-plane shear stiffness	Gt_s	lb./in.
Bending rigidities	$D_x = EI_x/(1 - \mu_x\mu_y)$	in.lb.
	$D_y = EI_y/(1 - \mu_x\mu_y)$	in.lb.
Torsional rigidity	$2GI_t$	in.lb.
Poisson's ratios associated with stretching	ν_x, ν_y	
Poisson's ratios associated with bending	μ_x, μ_y	
Transverse shear stiffnesses	D_{Qx}, D_{Qy}	lb./in.
Coupling elastic constants	C_{xx}	per lb.
Curvature $\partial^2 w/\partial x^2$ per unit of N_x applied		
Curvature $\partial^2 w/\partial x^2$ per unit of N_y applied	C_{xy}	per lb.
Curvature $\partial^2 w/\partial y^2$ per unit of N_y applied	C_{yy}	per lb.
Curvature $\partial^2 w/\partial y^2$ per unit of N_x applied	C_{yx}	per lb.
Twist $\partial^2 w/\partial x\partial y$ per unit of N_{xy} applied	T	per lb.

The coupling constants depend on section details and Poisson effects; a thorough treatment for some types of orthotropic stiffened surface is given in reference 22.

For the integrally stiffened skin panel of Fig. 1, computation of the coupling constants indicates that these are negligible for the purpose at hand; the largest, C_{yz}, is approximately 4.0×10^{-6} per lb. Poisson's ratios in bending (μ_x, μ_y) are also seen to be negligible. Because of the overall proportions of the panel, beam shear deformations are small compared to bending, and therefore D_{Q_x} and D_{Q_y} are unimportant.

The other constants are determinable from the section properties that are as follows:

$t = t_x = 0.0325$ in.^{2}/in.
$t_y = 0.080$ in.^{2}/in. average
$I_x = 2.86 \times 10^{-6}$ in.^{4}/in.
$I_y = 0.005$ in.^{4}/in.
$I_t = I_x$ (torsional rigidity of stiffener elements considered negligible)

Boundary Restraint Conditions

Along each of the boundaries of the panel, external conditions may impose forces in three directions and moments in three directions. Certain of these are responsible for the applied load. The remaining may exist as restraints against linear and angular displacements. A summary of these conditions is presented in Table A1. A number of the restraint effects can be excluded from practical problems. There remain, however, five different important restraints against compression buckling and eight against shear buckling. Some of these may be overlooked without noticeable error, but several have not yet been individually evaluated, it being customary to lump all restraint effects into two nondimensional fixity factors—one for compression buckling and one for shear. This practice is followed in the analytical work presented here. When designing a test specimen the complexity of the problem cannot be dismissed so easily.

APPENDIX (B)

Approximate Derivation of Interaction Curve for Orthotropic Plate by Energy Method

Critical buckling of the orthotropic plate may be computed for different combinations of shear and compression in the same manner as is done in reference 16 for isotropic plates. The energy relation for the simply supported orthotropic plate corresponding to Eq. (B1) of reference 16 is, with stiffener torsional rigidity neglected,

$$\frac{EI_x}{2}\int_0^{L_y}\int_0^{L_x}\left[\left(\frac{\partial^2 w}{\partial x^2}\right)^2 + 2\nu\frac{\partial^2 w}{\partial x^2}\frac{\partial^2 w}{\partial y^2} + 2(1-\nu)\times\left(\frac{\partial^2 w}{\partial x \partial y}\right)^2\right]dx\,dy + \frac{EI_y}{2}\int_0^{L_y}\int_0^{L_x}\left(\frac{\partial^2 w}{\partial y^2}\right)^2 dx\,dy = \sigma_{ycr}\,t_y\int_0^{L_y}\int_0^{L_x}\frac{1}{2}\left(\frac{\partial w}{\partial y}\right)^2 dx\,dy + \tau_{cr}t_s\int_0^{L_y}\int_0^{L_x}\frac{1}{2}\frac{\partial w}{\partial x}\frac{\partial w}{\partial y}\,dx\,dy$$

Here the first term is identical with the classical energy expression for an isotropic plate in compound bending, except that the portion due to $\partial^2 w/\partial y^2$ bending is omitted. The second term accounts for $\partial^2 w/\partial y^2$ bending of stiffener and skin together, assuming that $\mu_x = \mu_y = 0$. In this case relations for the critical stresses may be written as follows:

$$\tau_{cr}t_s = k_s(\pi^2/L_y^2)EI_s; \quad I_s = I_x = t_s^3/12$$

$$\sigma_{y\,cr}\,t_y = k_y(\pi^2/L_y^2)EI_y$$

and substituting for w the general form, as in Eq. (B3) of reference 16:

$$w = \sum_{m=1}^{\infty}\sum_{n=1}^{\infty} a_{mn}\sin\frac{m\pi x}{L_x}\sin\frac{n\pi y}{L_y}$$

TABLE A1
Boundary Restraint Conditions for Orthotropic Stiffened Plate

Applied restraint	Resultant boundary condition: Under end compression, At ends ($y = 0, L_y$)	Under end compression, At edges ($x = 0, L_x$)	Under shear, At ends	Under shear, At edges
Normal force	N_y = applied load; edge either straight or free to warp in plane	$N_x = 0$ or specified; edge either straight or free to warp in plane	Edges free-shifting ($N_y = 0$) or restrained ($N_y \neq 0$); may be straight or free to warp	Same as at ends
In-plane shear	Excluded: $N_{xy} = 0$, $\partial v/\partial x = 0$	Excluded: $N_{xy} = 0$, $\partial u/\partial y = 0$	N_{xy} = applied load	N_{xy} = applied load
Transverse shear	$Q_y(x)$ adjusts to straight-line edge $\partial^2 w/\partial x^2 = 0$*	$Q_x(y)$ adjusts to straight-line edge $\partial^2 w/\partial y^2 = 0$*	Same as for compression*	Same as for compression*
Transverse moment	Ordinary end fixity: $M_y = 0$: pinned; $\partial^2 w/\partial y^2 = 0$: clamped	Ordinary edge fixity: $M_x = 0$: pinned; $\partial^2 w/\partial x^2 = 0$: clamped	Same as for compression	Same as for compression
Twisting moment	$M_{yx} = 0$, $\partial^2 w/(\partial x\,\partial y) = 0$ except for unsymmetrical stiffeners that roll when bowing occurs	$M_{xy} = 0$, $\partial^2 w/(\partial x\,\partial y) = 0$ for all practical purposes	May produce important fixity for all except symmetrical open section stiffeners	Same as at ends
Warping moment	Appears unimportant	Appears unimportant	May produce stiffener fixity for all types of sections	Same as at ends

* Boundaries are usually considered as not shifting out of the original plane.

the following relation is obtained:

$$\sum_{m=1}^{\infty}\sum_{n=1}^{\infty} a_{mn}{}^2 \frac{L_x L_y}{4}\left(\frac{m^4\pi^4}{L_x{}^4} + 2\frac{m^2n^2\pi^4}{L_x{}^2L_y{}^2} + \frac{EI_y}{EI_x}\frac{n^4\pi^4}{L_y{}^4} - k_y\frac{EI_y}{EI_x}\frac{n^2\pi^4}{L_y{}^4}\right) - 2k_s\frac{\pi^2}{L_y{}^2}\sum_{m=1}^{\infty}\sum_{n=1}^{\infty}\sum_{p=1}^{\infty}\sum_{q=1}^{\infty} a_{mn}\,a_{pq}\frac{4L_xL_y}{\pi^2}\frac{m\pi}{L_x}\frac{n\pi}{L_y}\frac{pq}{(p^2-m^2)(n^2-q^2)} = 0$$

where $m \pm p$ and $n \pm q$ are odd numbers. Minimizing k_s with respect to a_{mn} leads to a set of homogeneous equations which can be represented by the following equation, which is similar to Eq. (B5) of reference 16, but where $\beta = L_x/L_y$ and $\beta' = (L_x/EI_x)/(L_y/EI_y)$

$$a_{mn}(m^4 + 2m^2n^2\beta^2 + n^4\beta^4\beta' - k_yn^2\beta^3\beta') + \frac{32}{\pi^2}k_s\beta^3\sum_{p=1}^{\infty}\sum_{q=1}^{\infty} a_{pq}\frac{mnpq}{(m^2-p^2)(n^2-q^2)} = 0$$

The solution by matrix iteration may proceed just as in reference 16 where for the orthotropic plate the off-diagonal terms of the matrix are the same as those for the isotropic plate solution, but the diagonal terms become

$$L_{mn} = \frac{\pi^2}{32\,k_s}\left[\frac{m^4}{\beta^3} + 2\frac{m^2n^2}{\beta} + n^4\beta' - k_yn^2\beta'\right]$$

as compared with the values for isotropic plate

$$L_{mn} = \frac{\pi^2}{32\,k_s}\left[\frac{m^4}{\beta^3} + 2\frac{m^2n^2}{\beta} + n^4\beta - k_yn^2\beta\right]$$

For either case, if the quantities β and β' are sufficiently large, the last two terms in the brackets predominate. Thus for reasonable values of β, m, and n, the solution for the orthotropic plate where $\beta' = (L_x/EI_x)/(L_y/EI_y)$ is of the order of 1,000 becomes numerically equivalent to the isotropic plate solution where $\beta = a/b$ is similarly large. Since the type of structure under consideration is characterized by very large values of β', it can be suitably represented by the infinite aspect ratio isotropic plate.

Under the assumed condition that $\mu_x = \mu_y = 0$ for the orthotropic panel, the above approximation is suitable regardless of whether orthotropy is due to differences in modulus or in section properties. The same solution is therefore applicable to an orthotropic plate under stresses exceeding the elastic limit, if $\beta' = (L_x/\overline{EI_x})/(L_y/\overline{EI_y})$ is large. Evaluation of the $\overline{EI}$ quantities is difficult but an exact evaluation is not necessary.

References

[1] Murphy, G., *Similitude in Engineering*, Ronald Press Co., New York, 1950.

[2] Goodier, J. N., and Thomson, W. T., *Applicability of Similarity Principles to Structural Models*, NACA TN 933, July, 1944.

[3] Langhaar, H. L., *Dimensional Analysis and Theory of Models*, John Wiley & Sons, Inc., New York, 1951.

[4] Watter, M., *Design Through Testing*, Proceedings of the Society for Experimental Stress Analysis, Vol. VII, No. 2, p. 73, 1950.

[5] Loudenslager, O. W., *Structural Model Testing*, SAE Journal (Transactions), Vol. 54, No. 1, p. 18, January, 1946.

[6] Walker, P. B., *The Experimental Approach to Aircraft Structural Research*, Journal of the Aeronautical Sciences, Vol. 19, No. 5, p. 145, March, 1952.

[7] Sandorff, P. E., *Bending Rigidity and Column Strength of Thin Sections*, Transactions ASME, Vol. 69, p. 833, 1947.

[8] Shanley, F. R., and Ryder, E. I., *Stress Ratios, the Answer to the Combined Loading Problem*, Aviation, Vol. 36, No. 6, June, 1937.

[9] Anon., *Strength of Metal Aircraft Elements*, ANC-5, Army-Navy-Civil Committee on Aircraft Design Criteria, 1951.

[10] Grady, C. P., *Flat-Bottom Corrugations Under Combined Loading of Compression and Torsional Shear*, Journal of the Aeronautical Sciences, Vol. 6, No. 6, p. 255, April, 1939.

[11] Sanderson, P. A., and Fischel, J. R., *Corrugated Panels Under Combined Compression and Shear Load*, Journal of the Aeronautical Sciences, Vol. 7, No. 4, p. 148, February, 1940.

[12] Anderson, P. N., Douglas Aircraft Company Data, January, 1941.

[13] Peterson, J. P., *Experimental Investigation on Stiffened Circular Cylinders Subjected to Combined Torsion and Compression*, NACA TN 2188, September, 1950.

[14] Melcon, M. A., and Ensrud, A. F., *Analysis of Stiffened Curved Panels Under Shear and Compression*, Journal of the Aeronautical Sciences, Vol. 20, No. 2, p. 111, February, 1953.

[15] Batdorf, S. B., and Houbolt, J. C., *Critical Combinations of Shear and Transverse Direct Stress for an Infinitely Long Flat Plate with Edges Elastically Restrained Against Rotation*, NACA Wartime Report L-183 (ARR L4L14), January, 1945.

[16] Batdorf, S. B., and Stein, M., *Critical Combinations of Shear and Direct Stress for Simply Supported Rectangular Flat Plates*, NACA TN 1223, March, 1947.

[17] Foster, L. E., and Sandorff, P. E., *Shear, Compression, and Combined Load Tests of Machined Integrally Stiffened Surface*, Lockheed Aircraft Corporation Report No. 9265, July 15, 1953.

[18] Hayashi, T., *Torsional Buckling of Orthogonal-Anisotropic Cylinders*, Eighth International Congress on Theoretical and Applied Mechanics, Istanbul, August, 1952.

[19] Donnell, L. H., *Stability of Thin Walled Tubes under Torsion*, NACA Report No. 479, 1933.

[20] Guggenheim Aeronautical Laboratory, California Institute of Technology, *Some Investigations of the General Instability of Stiffened Metal Cylinders*, NACA TN 909, 1943.

[21] von Karman, T., and Tsien, H. S., *The Buckling of Thin Cylindrical Shells Under Axial Compression*, Journal of the Aeronautical Sciences, Vol. 8, No. 8, p. 303, June, 1941.

[22] Libove, C., and Hubka, R. E., *Elastic Constants for Corrugated Core Sandwich Panels*, NACA TN 2289, 1951.

[23] Norris, C. H., *Model Analysis of Structures*, Proceedings for the Society for Experimental Stress Analysis, Vol. 1, No. 2, July, 1944.

[24] Jelinek, J. J., Latter, A. J., Thomsen, E. G., and Dorn, J. L., *Study of the Forming Problems of Aluminum Alloy Sheet—Plastic Flow in Metals*, University of California, O.P.R.D. Report No. W-200, May, 1945.

[25] Hetneyi, M., *Handbook of Experimental Stress Analysis*, John Wiley & Sons, Inc., New York, 1950.

[26] Sachs, G., *Some Fundamentals of the Flow and Rupture of Metals*, Trans. Am. Inst. of Mining and Metallurgical Engrs., Vol. 143, Institute of Metals Division, p. 13, 1941.

Mechanical Stability of a Two-Bladed Cantilever Helicopter Rotor*

PETER F. LEONE†

Kellett Aircraft Corporation

SUMMARY

A theoretical analysis of the mechanical stability of a two-bladed cantilever helicopter rotor, whose hub is mounted upon isotropic elastic supports in the horizontal plane and whose elastic blades employ fixed root attachments, has been made and is reported here. This case is a generalization of a problem treated by Feingold in reference 1 where the blades are assumed inelastic and attached to the hub by means of vertical hinges. It is found that Feingold's solution remains applicable also to the general case if the Coleman parameters Λ_1, Λ_2, and Λ_3 are appropriately defined by using the natural frequencies and modal shapes of the free uncoupled lag bending vibrations of the blades. The numerical determination of Coleman's parameters for a typical nonuniform two-bladed cantilever rotor are given in Appendix A. The effects of root tension straps are treated in Appendix B.

MATHEMATICAL ANALYSIS

Consider a two-bladed cantilever rotor whose hub is mounted upon isotropic elastic supports in the horizontal plane to be executing undamped coupled natural vibrations, as shown in Fig. 1. In this figure of the horizontal plane, the Cartesian coordinate system $o_f x_f y_f$ is fixed in space, whereas the system $o_f x_r y_r$ rotates with the rotor at an angular velocity Ω where ψ measures the angular displacement of $o_f x_r y_r$ with respect to $o_f x_f y_f$. The rotating coordinates of the rotor hub center, whose mass is m and whose radial linear isotropic spring constant is K, are x_0 and y_0. The rotating coordinates of an elemental mass dm_1 of the first blade, whose azimuth angle is ψ, are $x_1 - \Delta x_1$ and y_1 measured with respect to the rotor hub center, where Δx_1 is the apparent shortening in blade length due to blade curvature during bending. Similarly, the rotating coordinates of an elemental mass dm_2 of the second blade, whose azimuth angle is $\psi + \pi$, are $x_2 - \Delta x_2$ and y_2. The apparent shortening in blade length during bending is found to be

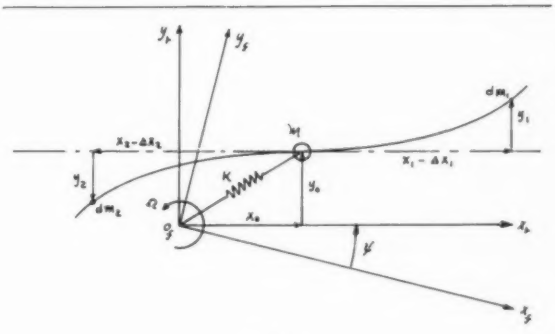

FIG. 1.

$$\Delta x = \frac{1}{2}\int_0^x \left(\frac{\partial y}{\partial x}\right)^2 dx \tag{1}$$

Now the fixed coordinates of the rotor hub center are seen to be

$$\left.\begin{aligned} x_{f_0} &= x_0 \cos\psi - y_0 \sin\psi \\ y_{f_0} &= x_0 \sin\psi + y_0 \cos\psi \end{aligned}\right\} \tag{2}$$

Similarly, the fixed coordinates of the elemental masses of each blade are seen to be

$$\left.\begin{aligned} x_{f_1} &= (x_0 + x_1 - \Delta x_1)\cos\psi - (y_0 + y_1)\sin\psi \\ y_{f_1} &= (x_0 + x_1 - \Delta x_1)\sin\psi + (y_0 + y_1)\cos\psi \end{aligned}\right\} \tag{3}$$

$$\left.\begin{aligned} x_{f_2} &= (x_0 - x_2 + \Delta x_2)\cos\psi - (y_0 - y_2)\sin\psi \\ y_{f_2} &= (x_0 - x_2 + \Delta x_2)\sin\psi + (y_0 - y_2)\cos\psi \end{aligned}\right\} \tag{4}$$

Since the kinetic energies of the hub mass and blades are defined to be

$$\left.\begin{aligned} T_0 &= (1/2)m\,(\dot{x}_{f_0}{}^2 + \dot{y}_{f_0}{}^2) \\ T_1 &= (1/2)\int (\dot{x}_{f_1}{}^2 + \dot{y}_{f_1}{}^2)dm_1 \\ T_2 &= (1/2)\int (\dot{x}_{f_2}{}^2 + \dot{y}_{f_2}{}^2)dm_2 \end{aligned}\right\} \tag{5}$$

Then upon substitution, T_0, T_1, and T_2 become

$$\left.\begin{aligned} T_0 &= (1/2)m\{\dot{x}_0{}^2 + \dot{y}_0{}^2 + \Omega^2(x_0{}^2 + y_0{}^2) + 2\Omega(x_0\dot{y}_0 - y_0\dot{x}_0)\} \\ T_1 &= (1/2)\int \{[\dot{x}_0 - \Delta\dot{x}_1 - \Omega(y_0 + y_1)]^2 + [\dot{y}_0 + \dot{y}_1 + \Omega(x_0 + x_1 - \Delta x_1)]^2\}\, dm_1 \\ T_2 &= (1/2)\int \{[\dot{x}_0 - \Delta\dot{x}_2 - \Omega(y_0 + y_2)]^2 + [\dot{y}_0 - \dot{y}_2 + \Omega(x_0 - x_2 + \Delta x_2)]^2\}\, dm_2 \end{aligned}\right\} \tag{6}$$

Finally, the elastic potential energies of the hub mass and blades are defined to be

$$\left.\begin{aligned} V_0 &= (1/2)K(x_0{}^2 + y_0{}^2) \\ V_1 &= (1/2)\int (EI)_1\,(\partial^2 y_1/\partial x_1{}^2)^2\, dx \\ V_2 &= (1/2)\int (EI)_2\,(\partial^2 y_2/\partial x_2{}^2)^2\, dx \end{aligned}\right\} \tag{7}$$

Received April 28, 1955. Revised and received August 11, 1955.

* This study was initiated by N. M. Stefano in 1946 and completed by the author in 1947.

† Chief of Vibrations.

Employing now generalized coordinate theory, the solutions for the blade deflections are assumed to be of the form

$$\left.\begin{aligned} y_1 &= \xi_1\, y(x) \\ y_2 &= \xi_2\, y(x) \end{aligned}\right\} \tag{8}$$

where ξ_1 and ξ_2 are generalized coordinates which are functions of time and where $y(x)$ is the blade uncoupled lag bending modal shape assumed common to both blades by virtue of the assumption that both blades have identical structural and mass properties. It follows then upon substitution that Δx_1 and Δx_2 become

$$\left.\begin{aligned} \Delta x_1 &= \frac{1}{2}\,\xi_1^2 \int_0^x \left(\frac{\partial y(x)}{\partial x}\right)^2 dx \\ \Delta x_2 &= \frac{1}{2}\,\xi_2^2 \int_0^x \left(\frac{\partial y(x)}{\partial x}\right)^2 dx \end{aligned}\right\} \tag{9}$$

The rotor blade static mass parameters are defined now as

$$\left.\begin{aligned} m_\xi &= \int dm \\ \sigma_\xi &= \int x\,dm \\ I_\xi &= \int x^2 dm \end{aligned}\right\} \tag{10}$$

The rotor blade dynamic mass and stiffness parameters are defined as

$$\left.\begin{aligned} f_1 &= \int y(x)\,dm \\ f_2 &= \int y^2(x)\,dm \\ f_3 &= \int x \left\{\int_0^x \left(\frac{\partial y(x)}{\partial x}\right)^2 dx\right\} dm \\ f_4 &= \int EI \left(\frac{\partial^2 y(x)}{\partial x^2}\right)^2 dx \end{aligned}\right\} \tag{11}$$

Employing the foregoing definitions and letting

$$M = m + 2m_\xi \tag{12}$$

then the total kinetic and potential energies of the hub mass and blades, ignoring variable products above the second order, become

$$\left.\begin{aligned} T = \Omega^2 I_\xi + (1/2)M\{\dot{x}_0^2 + \dot{y}_0^2 + \Omega^2(x_0^2 + y_0^2) + 2\Omega(x_0\dot{y}_0 - y_0\dot{x}_0)\} + f_1\{\Omega^2(y_0 - \dot{x}_0/\Omega)\,(\xi_1 - \xi_2) + \\ \Omega(\dot{y}_0/\Omega + x_0)\,(\dot{\xi}_1 - \dot{\xi}_2)\} + (1/2)\Omega^2(f_2 - f_3)\,(\xi_1^2 + \xi_2^2) + (1/2)f_3\,(\dot{\xi}_1^2 + \dot{\xi}_2^2) \end{aligned}\right\} \tag{13}$$

$$V = (1/2)K(x_0^2 + y_0^2) + (1/2)f_4\,(\xi_1^2 + \xi_2^2) \tag{14}$$

Lagrange's equations of motion for generalized coordinates are now employed as follows:

$$\frac{d}{dt}\left(\frac{\partial T}{\partial \dot{q}_k}\right) - \frac{\partial T}{\partial q_k} + \frac{\partial V}{\partial q_k} = 0 \tag{15}$$

where

$$q_K = x_0,\ y_0,\ \xi_1,\ \xi_2 \tag{16}$$

Now letting

$$w_r^2 = K/M \tag{17}$$

where w_r is defined as the pylon reference natural frequency, then, upon substitution, the equations of motion become the following:

$$\left.\begin{aligned} x_0\text{:}\quad & M\{\ddot{x}_0 + x_0(w_r^2 - \Omega^2)\} - 2M\Omega\dot{y}_0 - 2f_1\Omega(\dot{\xi}_1 - \dot{\xi}_2) = 0 \\ y_0\text{:}\quad & M\{\ddot{y}_0 + y_0(w_r^2 - \Omega^2)\} + 2M\Omega\dot{x}_0 + f_1\{\ddot{\xi}_1 - \ddot{\xi}_2 - \Omega^2(\xi_1 - \xi_2)\} = 0 \\ \xi_1\text{:}\quad & f_1\{\ddot{y}_0 - \Omega^2 y_0 + 2\Omega\dot{x}_0\} + f_2\ddot{\xi}_1 + \xi_1\{f_4 + \Omega^2(f_3 - f_2)\} = 0 \\ \xi_2\text{:}\quad & -f_1\{\ddot{y}_0 - \Omega^2 y_0 + 2\Omega\dot{x}_0\} + f_2\ddot{\xi}_2 + \xi_2\{f_4 + \Omega^2(f_3 - f_2)\} = 0 \end{aligned}\right\} \tag{18}$$

Solutions for the variables are assumed of the form

$$x_0 = \bar{x}_0 e^{iw_a w_r t} \tag{19}$$

and similarly for y_0, ξ_1, and ξ_2, where w_a is the dimensionless coupled natural frequency referred to w_r. Referring now the rotor angular velocity to w_r by the relation

$$w = \Omega/w_r \tag{20}$$

and defining the parameters,

$$\left.\begin{aligned}\mu_1 &= f_1/M\\ \mu_2 &= f_1/f_2\end{aligned}\right\} \tag{21}$$

$$\left.\begin{aligned}\Lambda_1 &= f_3/f_2 - 1\\ \Lambda_2 &= f_4/f_2 w_r^2\end{aligned}\right\} \tag{22}$$

then upon substitution, the equations of motion reduce to

$$\left.\begin{aligned}
x_0:&\quad \bar{x}_0(1 - w^2 - w_a^2) - \bar{y}_0(i\,2ww_a) - (\bar{\xi}_1 - \bar{\xi}_2)\,(i\,2ww_a)\mu_1 = 0\\
y_0:&\quad \bar{x}_0(i\,2ww_a) + \bar{y}_0(1 - w^2 - w_a^2) - (\bar{\xi}_1 - \bar{\xi}_2)\,(w^2 + w_a^2)\mu_1 = 0\\
\xi_1:&\quad \bar{x}_0(i\,2ww_a)\mu_2 - \bar{y}_0(w^2 + w_a^2)\mu_2 + \bar{\xi}_1(\Lambda_1 w^2 + \Lambda_2 - w_a^2) = 0\\
\xi_2:&\quad -\bar{x}_0(i\,2ww_a)\mu_2 + \bar{y}_0\,(w^2 + w_a^2)\mu_2 + \bar{\xi}_2(\Lambda_1 w^2 + \Lambda_2 - w_a^2) = 0
\end{aligned}\right\} \tag{23}$$

Addition of the last two equations above yields the solution

$$\bar{\xi}_2 = -\bar{\xi}_1 \tag{24}$$

Defining now the parameter

$$\Lambda_3 = \mu_1\mu_2 \tag{25}$$

and making use of the above solution, then the frequency equation derived from Eqs. (23) becomes:

$$2\Lambda_3(w_a^2 + w^2 - 1) + \{4w^2w_a^2 - (w_a^2 + w^2 - 1)^2\} \times \{-2\Lambda_3(w_a^2 + w^2 + 1) + w_a^2 - \Lambda_1 w^2 - \Lambda_2\} = 0 \tag{26}$$

where the parameters Λ_1, Λ_2, and Λ_3 are defined to be

$$\left.\begin{aligned}
1 + \Lambda_1 &= \int x\left\{\int_0^x [\partial y(x)/\partial x]^2\,dx\right\}dm \Big/ \int y^2(x)dm\\
\Lambda_2 &= \int EI\,[\partial^2 y(x)/\partial x^2]^2\,dx \Big/ w_r^2 \int y^2(x)dm\\
\Lambda_3 &= \left\{\int y(x)dm\right\}^2 \Big/ M\int y^2(x)dm
\end{aligned}\right\} \tag{27}$$

The foregoing frequency equation is seen to be identical with the corresponding Eq. (7) of reference 1, where a similar analysis was made for a two-bladed rotor having a hub mounted upon isotropic elastic supports and having inelastic blades employing vertical hinges offset from the rotor center. The Λ_1, Λ_2, and Λ_3 parameters were defined in reference 1 for the inelastic pin-free rotor blade to be

$$\left.\begin{aligned}\Lambda_1 &= abm_b/I\\ \Lambda_2 &= K_\beta/w_r^2 I\\ \Lambda_3 &= (bm_b)^2/MI\end{aligned}\right\} \tag{28}$$

where a is the vertical hinge offset from the rotor center, b is the radial distance from the vertical hinge to the blade mass center, m_b is the total blade mass, I is the total blade mass moment of inertia about the vertical hinge, K_β is the angular mechanical spring constant acting about the vertical hinge, and M and w_r are defined as herein. The Coleman parameters, Λ_1, Λ_2, and Λ_3, derived in reference 1 are associated with the inelastic pin-free rotor blade whose modal shape is by definition

$$y(x) = x \tag{29}$$

Hence, if this solution for $y(x)$ be substituted into the generalized Coleman parameters derived in the present analysis with the additional substitution of $a + x$ for x in the equation for Λ_1 (since that particular x is measured from the rotor center), and noting further that the numerator of Λ_2 is an equivalent angular spring constant, then the following are obtained:

$$\left.\begin{aligned}
1 + \Lambda_1 &= (a\int xdm + \int x^2dm) \Big/ \int x^2dm\\
\Lambda_2 &= K_\beta/w_r^2 \int x^2dm\\
\Lambda_3 &= (\int xdm)^2/M\int x^2dm
\end{aligned}\right\} \tag{30}$$

Since by definition,

$$\left.\begin{aligned}\int xdm &= bm_b\\ \int x^2dm &= I\end{aligned}\right\} \tag{31}$$

then it follows that Eqs. (28) and (30) are identical.

The Coleman parameters derived herein for a two-bladed elastic rotor are applicable to rotors having three or more blades if the coefficient $n/2$, where n is the number of blades per rotor, be applied to Λ_3, and further if M be defined as:

$$M = m + nm_\xi \tag{32}$$

Although the proof for the foregoing is not presented here, it follows from a comparison of these parameters derived in references 1 and 2 that this is true. Using now the generalized solutions for the Coleman parameters, a comparison will now be made between the fundamental modes of the pin-free and cantilever rotor blades. Defining now the mass ratio μ to be

$$\mu = nm_\xi/M \tag{33}$$

then the Coleman parameters for the uniform pin-free rotor blade are found to be the following:

$$\left.\begin{aligned}\Lambda_1 &= (3/2)\epsilon/(1 - \epsilon)\\ \Lambda_2 &= K_\beta/Iw_r^2\\ \Lambda_3 &= 0.375\,\mu\end{aligned}\right\} \tag{34}$$

where ϵ is the dimensionless lag axis offset referred to the rotor tip radius. For the uniform cantilever rotor blade, the solution of its partial differential equation for stationary uncoupled bending free vibrations yields $y(x)$ to be of the form

$$y(x) = (\sin\beta x - \sinh\beta x) + \lambda\,(\cos\beta x - \cosh\beta x) \tag{35}$$

where for the fundamental mode

$$\left.\begin{aligned}\beta &= 1.8750\\ \lambda &= -1.3621\end{aligned}\right\} \tag{36}$$

Assuming the stationary solution for $y(x)$ to be identical with the corresponding rotating solution, then the Coleman parameters for the uniform cantilever rotor

TABLE 1

Top, Myklestad Vibration Parameters for Typical Non-Uniform Rotor Blade. *Bottom*, Solution for Rotating Modal Shape.

R = 210 IN

Ω = 34.87 RAD/SEC

n	x IN	m LBS.SEC²/IN	l IN	EI.10⁻⁶ LBS.IN²
1	199.46	.01822350	21.00	174.90
2	178.46	.01876748	21.00	192.75
3	157.46	.01920267	21.00	211.11
4	136.46	.01963786	20.87	231.29
5	115.58	.01975184	21.10	254.95
6	94.48	.01952906	21.02	281.01
7	73.46	.01990985	21.00	308.60
8	52.46	.02039944	21.74	336.70
9	30.72	.01987100	20.63	365.86
10	10.09	.05295824	10.09	370.00
b	0	0		

n	y IN
1	1.0
2	.8475621
3	.6972797
4	.5521469
5	.4166215
6	.2923544
7	.1852799
8	.09892450
9	.03549322
10	.003857949
b	0

blade are found to be

$$\left.\begin{aligned} \Lambda_1 &= 0.19336 \\ \Lambda_2 &= 12.36\ (EI/\mu_b l^4)/w_r^2 \\ \Lambda_3 &= 0.30663\ \mu \end{aligned}\right\} \tag{37}$$

where EI is the bending stiffness, μ_b the mass per unit length, and l the blade length. It is interesting to note from a comparison of the foregoing solutions for Λ_1 that the uniform cantilever rotor blade is equivalent to a uniform pin-free rotor blade whose lag axis offset is 11.42 per cent of the rotor tip radius, considering, of course, zero EI and zero K_β. Also, for the same mass ratio μ the coupling parameter Λ_3, which dictates the strength of the instability region, for the uniform cantilever rotor blade is 18.23 per cent less than that for the uniform pin-free rotor blade. As a final note, the value of $\Lambda_1 = 0.187$ suggested by Deutsch in reference 3 for a cantilever rotor is in fairly close agreement with the corresponding value given here.

For a rigorous determination of the Coleman parameters of a nonuniform cantilever rotor blade, the Myklestad method of structural vibration analysis[4] should be employed. The procedure would be to calculate the fundamental mode stationary and rotating natural frequencies, w_{s_0} and w_0, respectively. Now since

$$w_0^2 = w_{s_0}^2 + \Lambda_1\Omega^2 \tag{38}$$

Then it follows that

$$\Lambda_1 = (w_0^2 - w_{s_0}^2)/\Omega^2 \tag{39}$$

Also, by definition,

$$\Lambda_2 = w_{s_0}^2/w_r^2 \tag{40}$$

The parameter Λ_3 may be found from the solution for the rotating mode shape obtained from the Myklestad analysis. Accordingly, if the nonuniform rotor blade is assumed to consist of a finite number of discrete masses m_i whose individual bending deflection amplitudes are y_i, then Λ_3 becomes

$$\Lambda_3 = \frac{n}{2M}\left\{\Sigma\, y_i m_i\right\}^2/\Sigma y_i^2 m_i \tag{41}$$

The Myklestad tabular calculations for the fundamental cantilever mode stationary and rotating natural frequencies and the resulting solutions for the Coleman parameters for a typical two-bladed rotor are presented in the Appendix A here. Also, the effects of root tension straps on the fundamental cantilever mode stationary natural frequency of a uniform rotor blade are considered in the Appendix B.

In concluding the present analysis, it is to be noted that the criterion for the nonexistence of the second instability region given in reference 1, namely,

$$\Lambda_3 \geq 1/4 \tag{42}$$

is believed to be in error. This criterion should be:

$$\Lambda_3 \geq (1/4)\ (1 - \Lambda_1) \tag{43}$$

The revised criterion was derived from the frequency equation, Eq. (26), wherein the substitution $w = w_s$ was made to obtain the frequency equation governing the rotor speeds at which a constant force in the horizontal plane can excite a resonant vibration. This equation reduces to the following:

$$w^4(16\Lambda_3 + 4\Lambda_1 - 4) + w^2(4\Lambda_2 - \Lambda_1 + 1) - \Lambda_2 = 0 \tag{44}$$

If one of the roots w^2 is infinite, then the second constant force resonant speed exists at infinity and hence the second instability region likewise exists at infinity. For this to be true, the above criterion must be satisfied.

REFERENCES

[1] Feingold, A. M., *Theory of Mechanical Oscillations of Rotors with Two Hinged Blades*, NACA ARR 3I13, September, 1943.

[2] Coleman, R. P., *Theory of Self-Excited Mechanical Oscillations of Hinged Rotor Blades*, NACA ARR 3G29, July, 1943.

[3] Deutsch, M. L., *Ground Vibrations of Helicopters*, Journal of the Aeronautical Sciences, Vol. 13, No. 5, p. 223, May, 1946.

[4] Leone, P. F., *Theory of Rotor Blade Uncoupled Lag Bending Aero-Elastic Vibrations*, Proceedings, Eleventh Annual Forum, American Helicopter Society, April, 1955.

[5] Hohenemser, K. H., *Attachment of Rotor Blades by Laminated Elastic Straps*, Readers' Forum, Journal of the Aeronautical Sciences, Vol. 19, No. 5, p. 350, May, 1952.

APPENDIX A

Determination of Coleman Parameters for a Typical, Nonuniform Two-Bladed Cantilever Rotor

The Myklestad method of structural vibration analysis, as presented in reference 4, is employed here to determine the Coleman parameters for a typical nonuniform two bladed cantilever rotor. Specifically, the Myklestad method is used to calculate the fundamental cantilever mode stationary and rotating natural frequencies and modal shapes of the nonuniform rotor blade for free uncoupled lag bending vibrations. These results then are employed in the formulas derived in the paper to yield the Coleman parameters.

For the typical rotor blade considered here, the Myklestad tabular calculations (see Table 1) yield the stationary and rotating uncoupled lag bending natural frequencies for the fundamental cantilever mode to be as follows:

$$w_{s_0} = 48.5 \text{ rad. per sec.}$$
$$w_0 = 51.4 \text{ rad. per sec.}$$

Now, since the rotor angular velocity employed in the calculations was

$$\Omega = 34.87 \text{ rad. per sec.}$$

then Λ_1 and Λ_2 become

$$\Lambda_1 = 0.23826$$
$$\Lambda_2 = (48.5)^2/w_r^2$$

From the solutions for the rotating modal shapes, the following are obtained:

$$\Sigma\, y_i m_i = 0.07891765 \qquad \Sigma\, y_i^2 m_i = 0.05303509$$
$$\{\Sigma\, y_i m_i\}^2/\Sigma\, y_i^2 m_i = 0.1174316$$

Now, since $\Sigma m_i = 0.2285094$

then Λ_3 becomes $\Lambda_3 = 0.5139027\mu$

Finally, the critical mass ratio for the elimination of the second instability region becomes

$$\mu \geq 0.370564$$

APPENDIX B

Effects of Root Tension Straps on the Fundamental Cantilever Mode Stationary Natural Frequency of a Uniform Rotor Blade

Consider a uniform cantilever rotor blade employing root tension straps to be executing free uncoupled bending vibrations in the horizontal plane for the stationary condition, as shown in Fig. B-1. In this figure of the horizontal plane, x and y measure the longitudinal and lateral coordinates, respectively, of a point on the rotor blade neutral bending axis, x_s is the root offset of the two tension straps, and l_s is the strap length for no blade bending. The offsets of the straps with respect to the blade neutral axis permit them to experience both compressive and tensile forces during blade bending by virtue of their fixed attachments. As a consequence, the rotor blade enjoys an

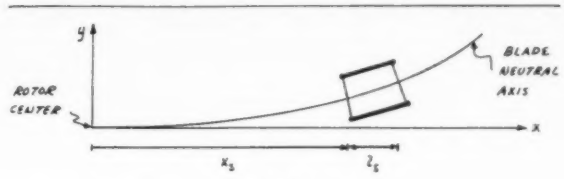

FIG. B-1.

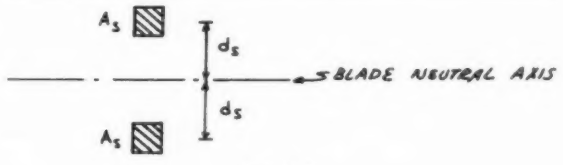

FIG. B-2.

increase in its total elastic potential energy during bending. The contribution of the straps to the total elastic potential energy may be seen in Fig. B-2. A_s is the strap cross-sectional area and d_s is the strap offset with respect to the blade neutral bending axis. Now, if E_s be the strap modulus of elasticity and I_s be the strap area moment of inertia with respect to the blade neutral axis, namely,

$$I_s = 2A_s d_s^2 \tag{B-1}$$

then the strap elastic potential energy becomes

$$V_s = \frac{1}{2} E_s I_s \int_{x_s}^{x_s+l_s} (\partial^2 y/\partial x^2)^2 dx \tag{B-2}$$

Assuming now a fundamental cantilever mode deflection curve of the form

$$y = \xi\{1 - \cos [(\pi/2)\,(x/R)]\} \tag{B-3}$$

where R is the rotor tip radius and ξ is a generalized time coordinate, and defining the dimensionless quantities,

$$\left.\begin{aligned} \epsilon_s &= x_s/R \\ \lambda_s &= l_s/R \end{aligned}\right\} \tag{B-4}$$

then the final form of the strap elastic potential energy becomes

$$V_s = \frac{1}{2}\xi^2 E_s I_s \left(\frac{\pi^4}{32R^3}\right) \times \left\{\lambda_s + \frac{1}{\pi}[\sin \pi(\epsilon_s + \lambda_s) - \sin \pi\epsilon_s]\right\} \tag{B-5}$$

The total rotor blade kinetic energy is defined to be

$$T = (1/2)\int \dot{y}^2 dm \tag{B-6}$$

Defining now the constant mass per unit length,

$$\mu_\xi = dm/dx \tag{B-7}$$

then upon substitution, T becomes

$$T = (1/2)\dot{\xi}^2\, \mu_\xi R[(3/2) - (4/\pi)] \tag{B-8}$$

Assuming a solution for ξ of the form

$$\xi = \delta e^{i\Delta w_s t} \tag{B-9}$$

TABLE 2
The Variations of γ_s with ϵ_s and λ_s

γ_s

ϵ_s \ λ_s	.05	.10	.15	.20	.25
0	1.3396	2.6628	3.9535	5.1964	6.3775
.05	1.3232	2.6139	3.8568	5.0379	6.1446
.10	1.2907	2.5336	3.7147	4.8214	5.8761
.15	1.2653	2.4240	3.5306	4.5854	5.4799
.20	1.1811	2.2877	3.3426	4.2370	5.0647
.25	1.1067	2.1614	3.0560	3.8837	4.6075

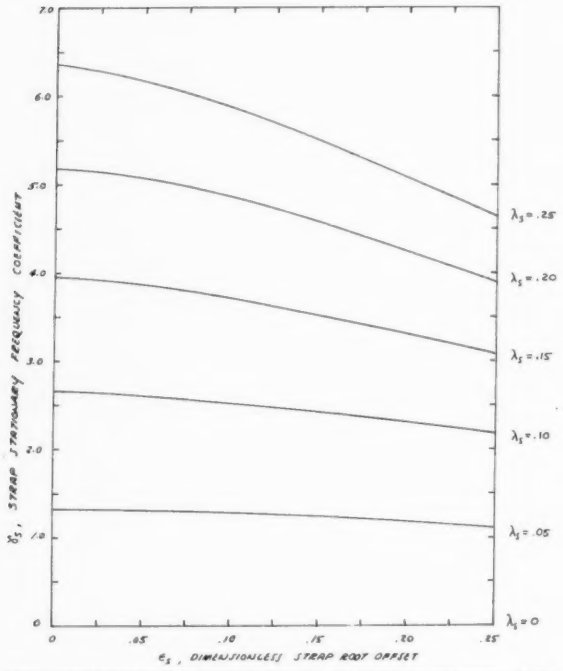

where Δw_s is the rotor blade stationary natural frequency due to the strap elastic potential energy only, then employing Lagrange's equations of motion, the solution of the resulting equation of motion for ξ yields Δw_s to be as follows:

$$\Delta w_s^2 = \gamma_s (E_s I_s / \mu_\xi R^4) \tag{B-10}$$

where

$$\gamma_s = 13.424 \left\{ \lambda_s + \frac{1}{\pi} [\sin \pi(\epsilon_s + \lambda_s) - \sin \pi \epsilon_s] \right\} \tag{B-11}$$

The frequency coefficient γ_s is seen to be proportional to both the strap root offset and strap length. Now the fundamental cantilever mode stationary natural frequency of a uniform rotor blade due to blade elasticity only is given to be

$$w_s^2 = 12.36 \, (E_\xi I_\xi / \mu_\xi R^4) \tag{B-12}$$

where $E_\xi I_\xi$ is the rotor blade bending stiffness. The assumption of linear vibrations permits the addition of these two results, giving the total stationary natural frequency due to both strap and blade elasticity to be

$$w_s'^2 = w_s^2 + \Delta w_s^2 \tag{B-13}$$

It is this total stationary natural frequency which must be employed to determine the A_2 Coleman parameter of rotor ground resonance theory for a uniform cantilever rotor blade employing root tension straps. Because of their equal offsets from the blade neutral bending axis, the two straps nullify the effects of centrifugal potential energy and hence the A_1 Coleman parameter is not affected by the straps (see Table 2).

As a final note, Hohenemser in reference 5 presents a discussion citing why care must be taken in designing the straps in order to avoid rotor mechanical instability.

IAS Twenty-Fifth Annual Meeting

Hotel Sheraton-Astor, New York City, January 28-31, 1957

The Meetings Committee plans to schedule sessions on Aerodynamics, Aeroelasticity, Design, Electronics, Flight Propulsion, Instruments, Rotating Wing Aircraft, Safety in Flight, Structures, Air Transportation, etc.

Members or organizations wishing to have papers considered for presentation at this meeting should submit outlines or short abstracts to the Meetings Committee, 2 East 64th St., New York 21, N.Y., no later than August 15, 1956.

Theoretical Aerodynamic Properties of Vanishing Aspect Ratio Harmonically Oscillating Rigid Airfoils in a Compressible Medium

BERNARD MAZELSKY*

Lockheed Aircraft Corporation

SUMMARY

Theoretical solutions are given in terms of tabulated Mathieu functions for the aerodynamic properties of rigid vanishing aspect ratio harmonically oscillating airfoils in a compressible medium for the complete range of reduced frequencies. The significant variable introduced in defining the oscillatory coefficients when the flow is compressible is the single entity, k_0M, and Mach Number variations enter only through this quantity. Numerical coefficients are tabulated for use in evaluating the expressions for lift, pitching, and rolling moment for the rectangular and triangular plan forms. Comparisons of the oscillatory coefficients based on compressible and incompressible flow indicate that, for the range of reduced frequencies applicable for flutter, the effects of compressibility can be considered negligible.

SYMBOLS

X, Y, Z	=	Cartesian coordinates [see Sketch (a)]
U	=	free-stream velocity
a	=	speed of sound
M	=	Mach Number
φ	=	velocity potential
t	=	time
ω	=	frequency of oscillation
$b\,(x)$	=	local half span
c	=	root chord
w	=	vertical velocity
ζ, η	=	elliptic coordinates
$k_0(x)$	=	reduced frequency in local half spans, $k_0(x) = \omega b(x)/U$
k_1	=	reduced frequency in root chords, $k_1 = \omega c/U$
$se_n(\zeta)$	=	odd Mathieu function of order n
B_r^n	=	coefficients in series expansion of $se_n(\zeta)$
$N_{e_n}^{(2)}(\eta)$	=	modified Mathieu function
$N_{e_n}^{(2)\prime}(\eta)$	=	derivative of $N_{e_n}^{(2)}(\eta)$ (with respect to η)
α_n	=	coefficients dependent upon downwash [see Eq. (22)]
X_0	=	axis of rotation
θ	=	angle of pitch (positive nose up)
β	=	angle of roll (positive right wing down)
Δp	=	pressure difference
ρ_0	=	free-stream air density
$l(x)$	=	section lift (positive up)
$p(x)$	=	section rolling moment (positive right wing up)
A	=	aspect ratio
S	=	wing area
L	=	total lift (positive up)
M	=	total pitching moment (positive nose up)
$\mathfrak{R}$	=	total rolling moment (positive right wing up)

$P\,(k_0M) + iQ(k_0M)$ defined by Eq. (45)
$P_0[(\omega b_{max}/U)M] + iQ_0[(\omega b_{max}/U)M]$ defined by Eq. (46)
$P_n(k_1AM/4) + iQ_n(k_1AM/4)$ defined by Eq. (59)
$J\,(k_0M) + iN(k_0M)$ defined by Eq. (48)
$J_0[(\omega b_{max}/U)M] + iN_0[(\omega b_{max}/U)M]$ defined by Eq. (49)
$J_n(k_1AM/4) + iN_n(k_1AM/4)$ defined by Eq. (60)

NOTE: Bar over variable denotes modulus, for example, $\varphi = \bar{\varphi}\, e^{i\omega t}$. In Figures modulus of complex functions is denoted by $|\ |$, while Φ refers to phase angle, and R and I refer, respectively, to the real and imaginary parts.

INTRODUCTION

THE MILLENIUM to a theoretical aerodynamicist will have arrived (or at least be very near) when he can describe the transient aerodynamic properties of any finite aspect ratio wing at all speeds and frequencies in a compressible medium. In the interim, he must resort to a sufficient number of restrictions with respect to plan form, Mach Number, frequency, etc., to arrive at a simplified mathematical model that is amenable to solution with the present state of knowledge. Except for special cases in the supersonic regime, most solutions, in general, have been restricted (due to mathematical expediency) such that effects due to compressibility and finite aspect ratio are not considered simultaneously. For example, complete solutions in closed form have been obtained for the infinite aspect ratio wing in incompressible flow as well as in a compressible medium for both the subsonic and supersonic regimes. The investigations of finite span effects are usually handled as extensions (employing modified strip analysis techniques) of the infinite aspect ratio results.

In addition to these studies, investigators have successfully made use of Munk's airship theory to determine the aerodynamic properties of wings which presume to be of such low aspect ratio that the flow is essentially two-dimensional in planes perpendicular to the free-stream direction. This assumption is equivalent to neglecting the streamwise derivatives in the potential flow equation. The wake behind the wing is assumed to have a minor effect on the flow over the wing. On this basis, the solution to the problem simplifies to determining the aerodynamic properties of a

Based on a paper presented at the Aeroelasticity II Session, Twenty-Second Annual Meeting, IAS, New York, January 25–29, 1954. Revised and received December 22, 1955.

* Group Engineer, Flight Dynamics Research.

The author is indebted to F. H. Nuernberg for assistance in the computations and the preparation of the Figures.

spanwise strip perpendicular to the streamwise direction. Once the properties of the strip are determined, the total forces and moments can be determined by integration of the spanwise strips in a chordwise direction with proper consideration of variations in span. For the steady planar case, Jones[1] first made use of this concept while Garrick[2] extended the results obtained by Jones to the transient incompressible case. This paper presents an extension of Garrick's results to the compressible case. This work was begun by the author while at the NACA Dynamic Loads Division, Langley Field. The extension differs basically in only one respect from the solutions obtained by Garrick, in that solutions of the velocity potential are determined from the two-dimensional wave equation instead of the Laplace equation. Fortunately, closed form solutions are available for the required boundary conditions in terms of Mathieu functions; all the required functions for determining the aerodynamic properties are tabulated for the complete range of the parameter, reduced frequency times Mach Number. Due to the availability of the complete mathematics it was felt that a formulation of the problem as well as the interesting numerical results that would be obtained would be desirable.

Apparently, at the time the present theoretical study was undertaken, Merbt and Landahl of the Royal Institute of Technology in Sweden were also considering this problem and recently published their results.[3] The theoretical considerations in the present paper are similar to their paper. The present study, however, contains more extensive numerical results than that given in reference 3. A comparison of the numerical results obtained by the two investigations is given. The numerical computations given herein cover the complete reduced frequency range such that the indicial lift and moment functions (response to a sudden change in angle of attack) can be readily determined. These indicial functions have wide applicability in the gust problem.

Theoretical Considerations

The theoretical considerations of the present paper follow closely those given by Merbt and Landahl and are included herein for the purpose of clarity and continuity. The linearized equation for the velocity potential for three-dimensional time-dependent flow is

$$(1 - M^2)\varphi_{XX} + \varphi_{YY} + \varphi_{ZZ} - (2M/a)\varphi_{Xt} = (1/a^2)\varphi_{tt} \quad (1)$$

If the aspect ratio of the wing is sufficiently small that the disturbed flow over the wing is essentially two-dimensional in planes perpendicular to the streamwise direction (X direction), then the X derivatives of the velocity potential may be neglected. The resulting equation under this condition is

$$\varphi_{YY} + \varphi_{ZZ} = (1/a^2)\varphi_{tt} \quad (2)$$

Solutions to Eq. (2) represent the velocity potential on

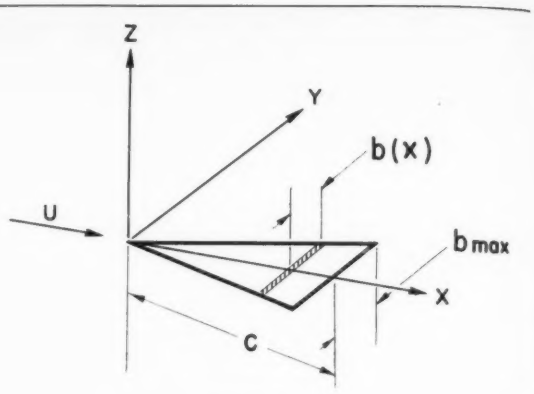

Sketch (a).

a spanwise strip of length 2b on a low aspect ratio wing [see Sketch (a)]. Each spanwise section is assumed to act independently of the others, but, when the total forces and moments on the wing are determined, the effects of span variation in the chordwise direction should be properly accounted for.

In order to obtain closed form solutions to Eq. (2) it is first necessary to assume harmonic oscillations of the spanwise strip. Letting

$$\varphi = \bar{\varphi}e^{i\omega t} \quad (3)$$

Eq. (2) becomes

$$\bar{\varphi}_{YY} + \bar{\varphi}_{ZZ} + (\omega^2/a^2)\bar{\varphi} = 0 \quad (4)$$

Associated with Eq. (4) are the following boundary conditions.

(a) The boundary condition of no relative normal flow at the lifting surface is [in accordance with the original linearizations made in obtaining Eq. (1)] for $|y| \leq b$, $Z = \pm 0$,

$$w = dZ/dt = (\partial Z/\partial t) + U(\partial Z/\partial X) \quad (5)$$

Noting that the downwash can be obtained from the velocity potential

$$W = \partial\varphi/\partial Z$$

and since harmonic motion is assumed, Eq. (5) becomes

$$\frac{\partial\bar{\varphi}(X, Y, 0)}{\partial Z} = i\omega\bar{Z}(X, Y) + U\frac{\partial\bar{Z}(X, Y)}{\partial X} \quad \text{for} \quad -b(x) \leq Y \leq b(x) \quad (6)$$

(b) The second boundary condition arises from the assumption that the velocity potential must be continuous everywhere in the Y, Z plan outside the spanwise strip. This requirement is satisfied if for $|Y| \geq b$ and $Z = \pm 0$

$$\bar{\varphi}(X, Y, 0) = 0 \quad (7)$$

Examination of Eqs. (5) and (7) suggests that $\bar{\varphi}$ on the spanwise strip must be an odd function of Z, while $\partial\bar{\varphi}/\partial Z$ must be an even function of Z.

(c) The final boundary condition is one requiring no radiation energy reflection at infinity. As Z approaches plus or minus infinity, the velocity potential must as-

sume the form

$$\bar{\varphi} \approx f(y, Z)e^{-(i\omega^2/a^2)(Y^2 + Z^2)} \tag{8}$$

where $f(Y, Z)$ tends to zero as Z tends to plus or minus infinity. (Note that the waves must radiate away from the surface.)

Explicit solutions to Eq. (4) for the required boundary conditions previously described are possible through the introduction of elliptic coordinates η and ζ, defined as follows:

$$\left.\begin{aligned} Y &= b \cdot \cosh \eta \cdot \cos \zeta \\ Z &= b \cdot \sinh \eta \cdot \sin \zeta \end{aligned}\right\} \tag{9}$$

In Sketch (b) a geometrical interpretation of the coordinate transformation given by Eq. (9) is indicated. The $\eta = \eta_0$ curve represents a particular ellipse while $\zeta = \zeta_0$ represents the hyperbolic branch which lies in the first quadrant. The values of ζ for the branches of the same hyperbola which lie in the second, third, and fourth quadrants are $\pi - \zeta_0$, $\pi + \zeta_0$, and $2\pi - \zeta_0$. Note that, when $\eta = 0$, the ellipse degenerates to a line extending from $Y = -b$ to $Y = +b$. This line represents a strip perpendicular to the X direction; a particular point on the strip is determined by the variable ζ.

Partial derivatives with respect to the Y and Z coordinates in terms of the η and ζ coordinates are given as follows:

$$\left.\begin{aligned} \frac{\partial}{\partial Y} &= \frac{(\partial/\partial\eta)(\sinh \eta \cos \zeta) - (\partial/\partial\zeta)(\cosh \eta \sin \zeta)}{b(\cosh^2 \eta - \cos^2 \zeta)} \\ \frac{\partial}{\partial Z} &= \frac{(\partial/\partial\eta)(\cosh \eta \sin \zeta) + (\partial/\partial\zeta)(\sinh \eta \cos \zeta)}{b(\cosh^2 \eta - \cos^2 \zeta)} \end{aligned}\right\} \tag{10}$$

The result obtained in applying this coordinate transformation of the partial derivatives on Eq. (4) is

$$(\partial^2\bar{\varphi}/\partial\eta^2) + (\partial^2\bar{\varphi}/\partial\zeta^2) + k_0^2M^2(\cosh^2 \eta - \cos^2 \zeta)\bar{\varphi} = 0 \tag{11}$$

where $$k_0(X) = \omega b(x)/U$$

The boundary conditions (a), (b), and (c) under this coordinate transformation result in the following expressions: for boundary condition (a)

for $\eta = 0$,

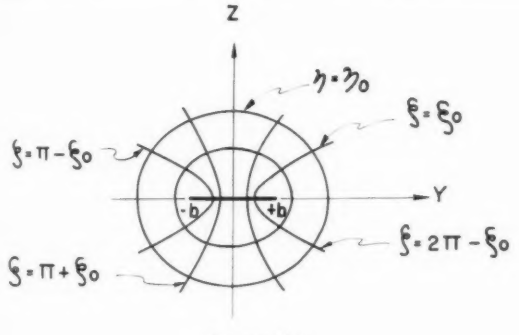

SKETCH (b).

$$\frac{\partial\bar{\varphi}(X, 0, \zeta)}{\partial\eta} = b(x)\left[\frac{\partial\bar{Z}(X, \zeta)}{\partial t} + U\frac{\partial\bar{Z}(X, \zeta)}{\partial X}\right]\sin \zeta \tag{12a}$$

or

$$\frac{\partial\bar{\varphi}(X, 0, \zeta)}{\partial\eta} = b(x)\,\bar{w}(X, \zeta)\sin \zeta \tag{12b}$$

and for boundary condition (b) at the tips of the strip—that is, $\zeta = n\pi$ where $h = 0, 1, 2, \ldots$.—the velocity potential is described as

$$\bar{\varphi}(X, \eta, n\pi) = 0 \tag{13}$$

Before discussing boundary condition (c), the radiation condition, it is desirable first to discuss suitable solutions to Eq. (11) by separation of variables.

Let $$\bar{\varphi}(\eta, \zeta) = \bar{\varphi}_1(\eta)\bar{\varphi}_2(\zeta) \tag{14}$$

then Eq. (11) becomes

$$\frac{\partial^2\bar{\varphi}_1(\eta)/\partial\eta^2}{\bar{\varphi}_1(\eta)} + k_0^2M^2\cosh^2\eta + \frac{\partial^2\bar{\varphi}_2(\zeta)/\partial\zeta^2}{\bar{\varphi}_2(\zeta)} - k_0^2M^2\cos^2\zeta = 0 \tag{15}$$

With a separation constant d, the following two equations result from Eq. (15):

$$[\partial^2\bar{\varphi}_1(\eta)/\partial\eta^2] + (k_0^2M^2\cosh^2\eta - d)\,\bar{\varphi}_1(\eta) = 0 \tag{16a}$$

$$[\partial^2\bar{\varphi}_2(\zeta)/\partial\zeta^2] - (k_0^2M^2\cos^2\zeta - d)\,\bar{\varphi}_2(\zeta) = 0 \tag{16b}$$

Eq. (16a) is referred to as the Mathieu equation while Eq. (16b) is referred to as the modified Mathieu equation. Values of the separation constant d are determined by the requirement that the functions $\bar{\varphi}_2(\zeta)$ are periodic. According to the boundary condition given by Eq. (13), then $\bar{\varphi}_2(\zeta)$ must be an odd function of ζ with period 2π. Thus, the solutions to Eq. (16a) which meet this requirement should assume the form of the elliptic sine function, as follows:

$$\bar{\varphi}_2(\zeta) = se_n(\zeta) \tag{17}$$

The constant of separation, d, is determined from the characteristic values associated with the function $se_n(\zeta)$. (Note that the notation used herein for the Mathieu functions is that of McLachlan.[4])

Solutions which correspond to Eq. (16a) require additional consideration involving the no radiation-energy reflection at infinity given by Eq. (8). Functions which have this property are the modified Mathieu functions of the third kind. Although two forms are possible, if it is specified that the waves must travel away from the wing, then the only solutions to Eq. (16a) must take the form

$$\bar{\varphi}_1(\eta) \sim Ne_n^{(2)}(\eta) \tag{18}$$

Substitution of Eqs. (17) and (18) into Eq. (14) leads to the following solution of Eq. (11):

$$\bar{\varphi}(X, \eta, \zeta) = \sum_{n=1}^{\infty} \alpha_n Ne_n^{(2)}(\eta, k_0M)se_n(\zeta, k_0M) \tag{19}$$

The coefficients α_n are specified by the boundary condi-

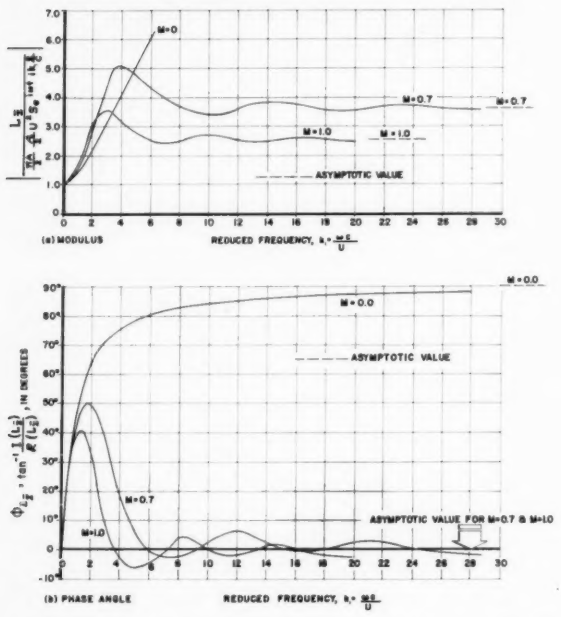

FIG. 1. Modulus and phase of complex lift functions due to plunge for rectangular plan form of unit aspect ratio at several Mach Numbers.

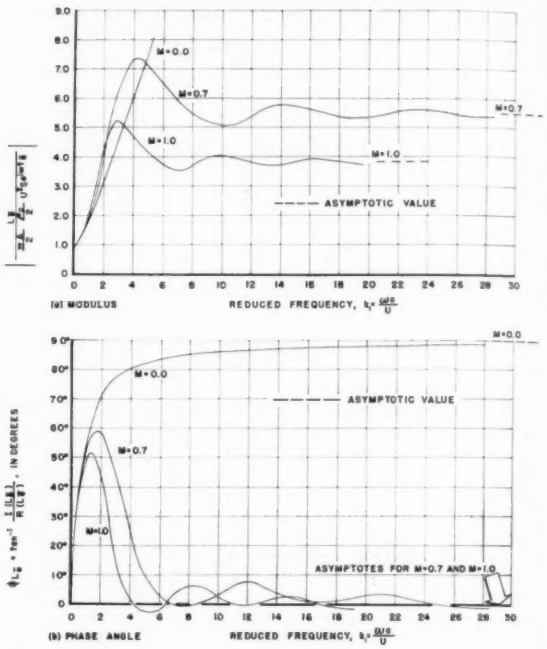

FIG. 3. Modulus and phase of complex lift functions due to pitch for rectangular plan form of unit aspect ratio at several Mach Numbers ($X_0/c = 1/2$).

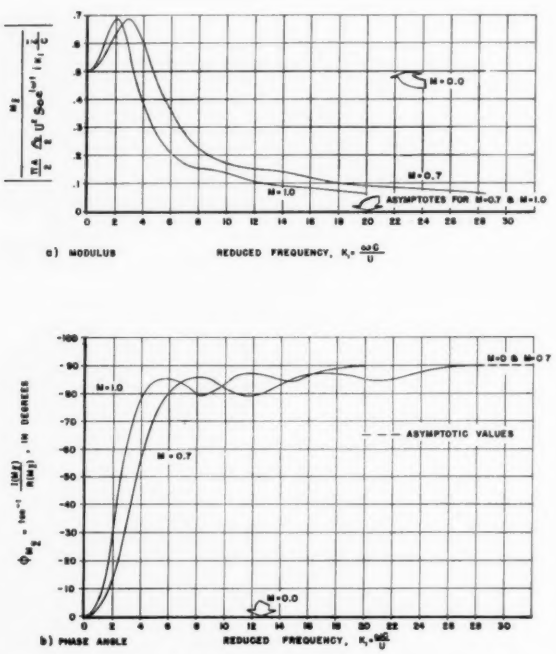

FIG. 2. Modulus and phase of complex pitching moment functions due to plunge for rectangular plan form of unit aspect ratio at several Mach Numbers ($X_0/c = 1/2$).

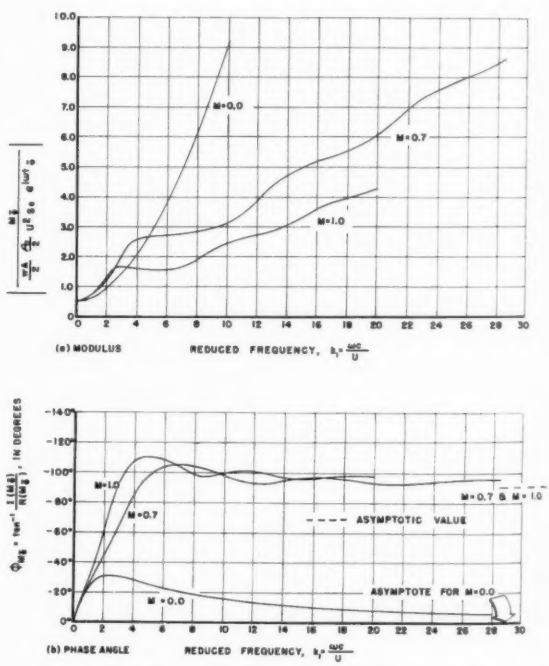

FIG. 4. Modulus and phase of complex pitching moment functions due to pitch for rectangular plan form of unit aspect ratio at several Mach Numbers ($X_0/c = 1/2$).

tion given by Eq. (12). Differentiation of Eq. (19) with respect to η and setting $\eta = 0$ results in an expression for α_n in terms of the downwash $\bar{w}(X, \zeta)$, as follows:

$$\sum_{n=1}^{\infty} \alpha_n N_{en}^{(2)\prime}(0, k_0M) se_n(\zeta, k_0M) = b(x)\bar{w}(X, \zeta) \sin \zeta \quad (20)$$

An explicit solution for α_n is due to the following orthogonality properties of the Mathieu functions. Using Goldstein's normalization the following relations can be shown to exist.

$$\int_0^{\pi} se_n(\zeta, k_0M)\, se_m(\zeta, k_0M) d\zeta = \begin{cases} \pi/2 & \text{if } m = n \\ 0 & \text{if } m \neq n \end{cases} \quad (21)$$

If both sides of Eq. (20) are multiplied by $se_m(\zeta, k_0M)$ and then each side integrated from zero to π, the following expression for α_n is obtained:

$$\alpha_n = \frac{2}{\pi} \frac{b(x)}{N_{en}^{(2)\prime}(0, k_0M)} \int_0^{\pi} \bar{w}(X, \zeta) \sin \zeta\, se_n(\zeta, k_0M) d\zeta \quad (22)$$

For rigid body motions the expression $\bar{w}(X, \zeta)$ assumes the following forms:

(1) plunge

$$\bar{w}(X, \zeta) = -i\omega \bar{Z} \quad (23)$$

(2) pitch about the point X_0 (positive when rearward of the leading edge)

$$\bar{w}(X, \zeta) = U\bar{\theta} + (X - X_0) i\omega\bar{\theta} \quad (24)$$

where $\bar{\theta}$ is maximum angle of pitch.

(3) roll about the root chord

$$\bar{w}(X, \zeta) = i\omega\bar{\beta}\, b(x) \cos \zeta \quad (25)$$

and $\bar{\beta}$ is maximum angle of roll.

Substitution of Eq. (23) into Eq. (22) gives the following result for α_n due to plunge:

$$\alpha_n = \frac{-2i\omega\bar{Z}b(x)}{\pi N_{en}^{(2)\prime}(0, k_0M)} \int_0^{\pi} \sin \zeta\, se_n(\zeta, k_0M) d\zeta \quad (26)$$

but the elliptic sine function, $se_n(\zeta, k_0M)$, can be written

$$se_n(\bar{\theta}, k_0M) = \sum_{r=1}^{\infty} B_r^{n}(k_0M) \sin r\zeta \quad (27)$$

Substitution of Eq. (27) into Eq. (26) leads to the result

$$\alpha_n = -\frac{2b(x)\, i\omega\bar{Z}}{\pi N_{en}^{(2)\prime}(0, k_0M)} \sum_{r=1}^{\infty} B_r^{n}(k_0M) \times \int_0^{\pi} \sin \zeta \sin r\zeta\, d\zeta \quad (28)$$

but

$$\int_0^{\pi} \sin \zeta \sin r\zeta\, d\zeta = \begin{cases} \pi/2 & \text{for } r = 1 \\ 0 & \text{for } r \neq 1 \end{cases}$$

Thus the final result for α_n due to plunge becomes

$$\alpha_{n\bar{z}} = -\frac{i\omega\, b(x)\, \bar{Z}}{N_{en}^{(2)\prime}(0, k_0M)} B_1^{n} \quad (29)$$

In a similar fashion to that shown for the plunge the results for α_n due to pitch and roll become, respectively,

$$\alpha_{n\bar{\theta}} = \frac{b(x)\, [U\bar{\theta} + (X - X_0) i\omega\bar{\theta}]}{N_{en}^{(2)\prime}(0, k_0M)} B_1^{n} \quad (30)$$

$$\alpha_{n\bar{\beta}} = \frac{b(x)^2\, i\omega\bar{\beta}}{2N_{en}^{(2)\prime}(0, k_0M)} B_2^{n} \quad (31)$$

Now that the α_n coefficients are specified, the velocity potential $\bar{\varphi}(X, \eta, \zeta)$ given by Eq. (19) can be used to calculate the pressures, lifts, and moments on the airfoil. The pressure difference, Δp, between the lower and upper surface of the wing is in terms of the velocity potential

$$\Delta p = -2\rho_0 e^{i\omega t} \times \left[i\omega\, \bar{\varphi}(X, Y, 0, k_0M) + \frac{U\, d\bar{\varphi}(X, Y, 0, k_0M)}{dX} \right] \quad (32)$$

Substitution of Eq. (19) into Eq. (32) for $\eta = 0$ leads to the following expression for Δp.

$$\Delta p = -2\rho_0 e^{i\omega t} \times \left[i\omega \sum_{n=1}^{\infty} \alpha_n N_{en}^{(2)}(0, k_0M) se_n(\zeta, k_0M) + U \frac{d\left(\sum_{n=1}^{\infty} \alpha_n N_{en}^{(2)}(0, k_0M) se_n(\zeta, k_0M) \right)}{dX} \right] \quad (33)$$

Detailed examination of the second term appearing in Eq. (33)—where a differentiation with respect to due X direction is required—indicates that, due to this operation, a closed form solution for the pressure, Δp, is not feasible. This unfortunate circumstance can be avoided when calculating the total lifts and moments on the airfoil.

Consider the equation for lift.

$$L = \int_0^{c} \int_{-b}^{b} \Delta p(X, Y, 0, k_0M) dY dX \quad (34)$$

Substitution of Eq. (32) into Eq. (34) gives

$$L = -2\rho_0 e^{i\omega t} \times \left[i\omega \int_0^{c} \int_{-b}^{b} \bar{\varphi} dY dX + U \int_0^{c} \int_{-b}^{b} \frac{d\bar{\varphi}}{dX} dY dX \right] \quad (35)$$

The integration with respect to X in the second integral is relatively simple. Noting that one of the boundary conditions requires $\bar{\varphi}(0)$—at the leading edge—to be zero, Eq. (35) becomes

$$L = -2\rho_0 e^{i\omega t} \times \left[i\omega \int_0^{c} \int_{-b}^{b} \bar{\varphi} dY dX + U \int_{-b_{max}}^{b_{max}} \bar{\varphi}(c) dY \right] \quad (36)$$

(where $\bar{\varphi}(c)$ denotes the potential at the largest span).

The corresponding expressions for the pitching moment can be determined from the relation

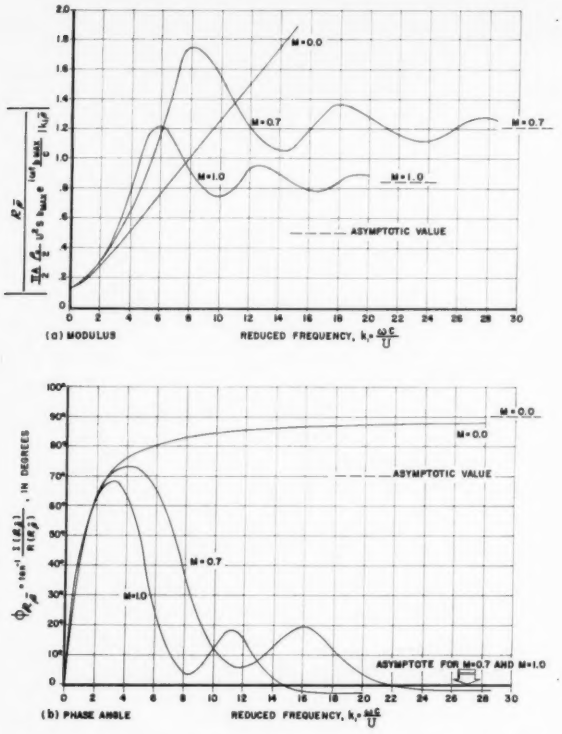

FIG. 5. Modulus and phase of complex rolling moment functions due to roll for rectangular plan form of unit aspect ratio at several Mach Numbers.

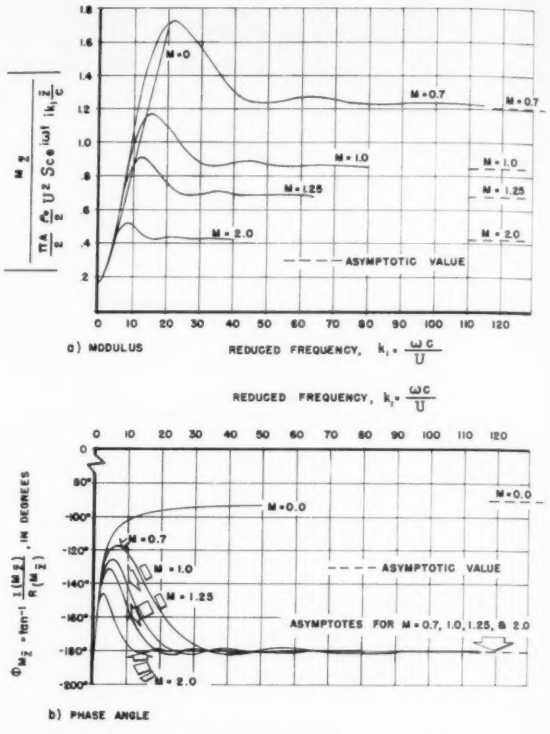

FIG. 7. Modulus and phase of complex moment functions due to plunge for delta plan form of one-half aspect ratio at several Mach Numbers ($X_0/c = 1/2$).

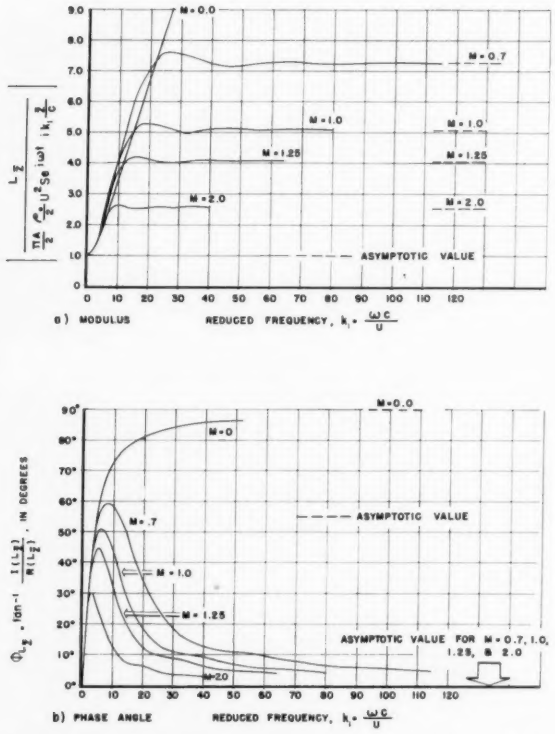

FIG. 6. Modulus and phase of complex lift functions due to plunge for delta plan form of one-half aspect ratio at several Mach Numbers.

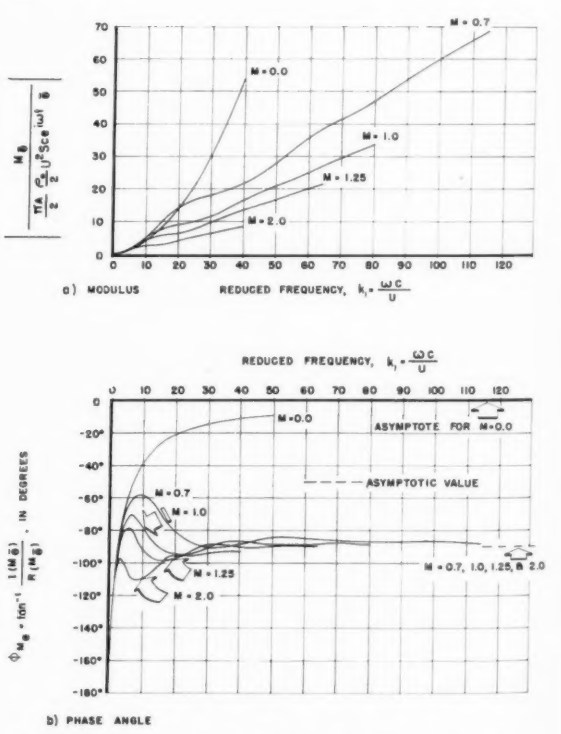

FIG. 8. Modulus and phase of complex lift functions due to pitch for delta plan form of one-half aspect ratio at several Mach Numbers ($X_0/c = 1/2$).

$$M = \int_0^c \int_{-b}^{b} (X_0 - X)\Delta p(X, Y, 0, k_0 M) dY dX \quad (37)$$

Substitution of Eq. (32) into Eq. (37) once again leads to an expression such that the differentiation of the potential with respect to the X direction is required. An additional step involving integration by parts is required for this evaluation. The desired equation for the pitching moment is

$$M = -2\rho_0 e^{i\omega t}(X_0 i\omega + U)\int_0^c \int_{-b}^{b} \bar{\varphi} dY dX + 2\rho_0 e^{i\omega t} U(c - X_0)\int_{-b_{max}}^{b_{max}} \bar{\varphi}(c) dY + 2\rho_0 e^{i\omega t} i\omega \int_0^c \int_{-b}^{b} X\bar{\varphi} dY dX \quad (38)$$

The expression for rolling moment due to roll is determined as follows:

$$\mathfrak{R}_{\bar{\beta}} = \int_0^c \int_{-b}^{b} \Delta p_{\bar{\beta}}(X, Y, 0, k_0 M) Y dY dX \quad (39)$$

or, in terms of the velocity potential,

$$\mathfrak{R}_{\bar{\beta}} = -2\rho_0 e^{i\omega t}\left[i\omega \int_0^c \int_{-b}^{b} \bar{\varphi}_{\bar{\beta}} Y dY dX + U\int_{-b_{max}}^{b_{max}} \bar{\varphi}_{\bar{\beta}}(c) Y dY\right] \quad (40)$$

Eqs. (36) and (38) were evaluated for rigid body motions, plunge, and pitch, as well as Eq. (40) for rigid body roll. The expressions are given for arbitrary plan forms.

Lift due to plunge:

$$L_z = \rho_0 \pi e^{i\omega t}\bar{Z}\left\{-\omega^2 \int_0^c b(x)^2 [p(k_0 M) + iQ(k_0 M)] dX + b_{max}{}^2 i\omega U\left[p_0\left(\frac{\omega b_{max}}{U} M\right) + iQ_0\left(\frac{\omega b_{max}}{U} M\right)\right]\right\} \quad (41)$$

Lift due to pitch:

$$L_\theta = \pi\rho_0 e^{i\omega t}\bar{\theta}\left\{-i\omega U\int_0^c b(x)^2 [P(k_0 M) + iQ(k_0 M)] dX + \omega^2 \int_0^c b(x)^2 (X - X_0)[P(k_0 M) + iQ(k_0 M)] dX - b_{max}{}^2 (U^2 + (c - X_0) i\omega U)\left[p_0\left(\frac{\omega b_{max}}{U} M\right) + iQ_0\left(\frac{\omega b_{max}}{U} M\right)\right]\right\} \quad (42)$$

Pitching moment due to plunge:

$$M_z = \pi\rho_0 e^{i\omega t}\bar{Z}\left\{i\omega(X_0 i\omega + U)\int_0^c b(x)^2 [P(k_0 M) + iQ(k_0 M)] dX - i\omega U(c - X_0) b_{max}{}^2 \times \left[P_0\left(\frac{\omega b_{max}}{U} M\right) + iQ_0\left(\frac{\omega b_{max}}{U} M\right)\right] + \omega^2 \int_0^c b(x)^2 X[P(k_0 NM) + iQ(k_0 M)] dX\right\} \quad (43)$$

Pitching moment due to pitch:

$$M_{\bar{\theta}} = \pi\rho_0 e^{i\omega t}\bar{\theta}\left\{(X_0 i\omega + U)\int_0^c b(x)^2 \left(U + (X - X_0) i\omega\right)[P(k_0 M) + iQ(k_0 M)] dX + b_{max}{}^2 U(c - X_0)\left(U + i\omega(c - X_0)\right)\left[P_0\left(\frac{\omega b_{max}}{U} M\right) + iQ_0\left(\frac{\omega b_{max}}{U} M\right)\right] + i\omega \int_0^c b(x)^2 X[U + (X - X_0) i\omega][P(k_0 M) + iQ(k_0 M)] dX\right\} \quad (44)$$

where the complex quantities $P(k_0 M) + iQ(k_0 M)$ and $P_0\left(\frac{\omega b_{max}}{U} M\right) + iQ_0\left(\frac{\omega b_{max}}{U} M\right)$ are defined, respectively, by Eqs. (45) and (46)

$$P(k_0 M) + iQ(k_0 M) \equiv \sum_{n=1}^{\infty} [B_1{}^n(k_0 M)]^2 \frac{N_{e_n}{}^{(2)}(0, k_0 M)}{N_{e_n}{}^{(2)\prime}(0, k_0 M)} \quad (45)$$

$$P_0\left(\frac{\omega b_{max}}{U} M\right) + iQ_0\left(\frac{\omega b_{max}}{U} M\right) \equiv \sum_{n=1}^{\infty}\left[B_1{}^n\left(\frac{\omega b_{max}}{U} M\right)\right]^2 \frac{N_{e_n}{}^{(2)}[0, (\omega b_{max}/U) M]}{N_{e_n}{}^{(2)\prime}[0, (\omega b_{max}/U) M]} \quad (46)$$

Note that since the reduced frequency k_0 is a function of X (it contains the half span as the reference distance) the $P(k_0 M) + iQ(k_0 M)$ functions must appear inside the integral.

The general equation for arbitrary plan form which describes the rolling moment due to roll is

$$\mathfrak{R}_{\bar{\beta}} = +\pi\rho_0 e^{i\omega t}\bar{\beta}\left\{\frac{\omega^2}{4}\int_0^c b(x)^4 [J(k_0 M) + iN(k_0 M)] dX - \frac{i\omega U b_{max}{}^4}{4}\left[J_0\left(\frac{\omega b_{max}}{U} M\right) + iN_0\left(\frac{\omega b_{max}}{U} M\right)\right]\right\} \quad (47)$$

where the complex quantities $J(k_0 M) + iN(k_0 M)$ and $J_0\left(\frac{\omega b_{max}}{U} M\right) + iN_0\left(\frac{\omega b_{max}}{U} M\right)$ are defined, respectively,

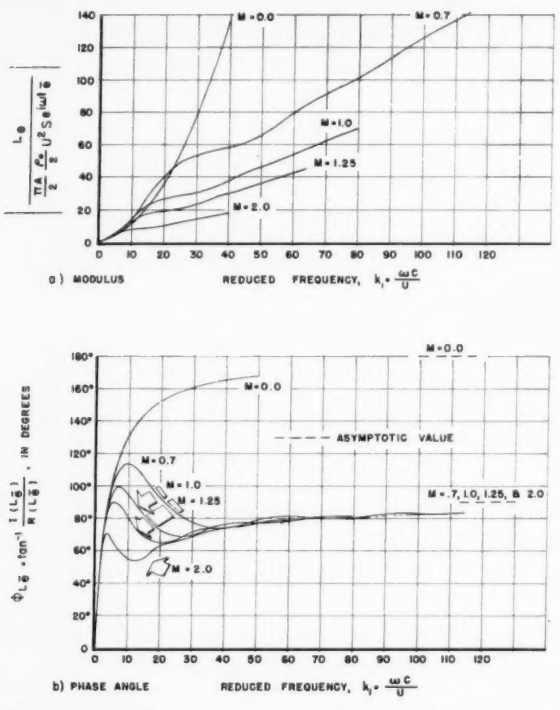

FIG. 9. Modulus and phase of complex pitching moment functions due to pitch for delta plan form of one-half aspect ratio at several Mach Numbers ($X_0/c = 1/2$).

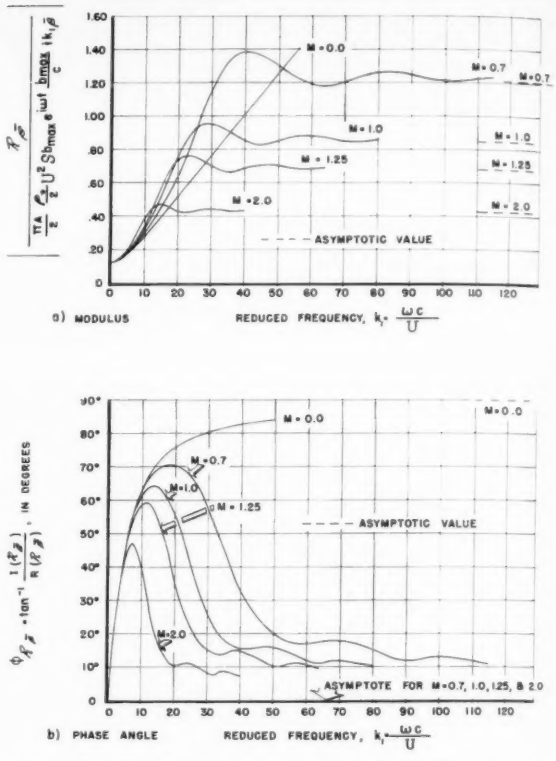

FIG. 10. Modulus and phase of complex rolling moment functions due to roll for delta plan form of one-half aspect ratio for several Mach Numbers.

$$(k_0M) + iN(k_0M) \equiv \sum_{n=1}^{\infty} [B_2{}^n(k_0M)]^2 \frac{N_{en}{}^{(2)}(0, k_0M)}{N_{en}{}^{(2)\prime}(0, k_0M)} \tag{48}$$

$$J_0\left(\frac{\omega b_{max}}{U} M\right) + iN_0\left(\frac{\omega b_{max}}{U} M\right) \equiv \sum_{n=1}^{\infty} \left[B_2{}^n\left(\frac{\omega b_{max}}{U} M\right)\right]^2 \frac{N_{en}{}^{(2)}[0, (\omega b_{max}/U) M]}{N_{en}{}^{(2)\prime}[0, (\omega b_{max}/U) M]} \tag{49}$$

For the rectangular wing, Eqs. (41), (42), (43), (44), and (47) can be evaluated in closed form since for this configuration the reduced frequency, k_0, is independent of the X direction, thus permitting the removal of the Mathieu functions given by Eqs. (45) and (48) from under the integral sign. The reduced frequency when expressed in terms of the more familiar reference distance, the wing chord, c, is related to the parameter, k_0, as follows:

$$k_0 = k_1A/2 \tag{50}$$

where A is the aspect ratio and k_1 is defined as

$$k_1 = \omega c/U \tag{51}$$

(Note that this differs from present usage where $\omega c/2U$ is normally used.) Eqs. (41), (42), (43), (44), and (47), when evaluated for the rectangular plan form, became, respectively,

$$L_{\bar{z}} = (\pi A/2)\ (\rho_0/2) U^2 S(\bar{Z}/c) e^{i\omega t}\ (-k_1{}^2 + ik_1)\ [P(k_1AM/2) + iQ(k_1AM/2)] \tag{52}$$

$$L_{\bar{\theta}} = (\pi A/2)\ (\rho_0/2) U^2 S e^{i\omega t}\bar{\theta}\ [-2ik_1 + k_1{}^2((1/2) - (X_0/c)) - 1 + ik_1(X_0/c)]\ [P(k_1AM/2) + iQ(k_1AM/2)] \tag{53}$$

$$M_{\bar{z}} = (\pi A/2)\ (\rho_0/2)\ ScU^2 e^{i\omega t}\ (\bar{Z}/c)\ [k_1{}^2((1/2) - (X_0/c)) + ik_1(X_0/c)]\ [P(k_1AM/2) + iQ(k_1AM/2)] \tag{54}$$

$$M_{\bar{\theta}} = (\pi A/2)\ (\rho_0/2) S' cU^2 e^{i\omega t}\ \bar{\theta}\{ik_1[1 - (2X_0/c) + (X_0/c)^2] - (X_0/c) + k_1{}^2[(X_0/c) - (1/3) - (X_0/c)^2]\}\ \{P(k_1AM/2) + iQ(k_1AM/2)\} \tag{55}$$

$$\mathfrak{R}_{\bar{\beta}} = (\pi A/2)\ (\rho_0/2) U^2 Sb_{max} e^{i\omega t}\bar{\beta}\ [(k_1{}^2/4)\ (b_{max}/c) - (ik_1/4)\ (b_{max}/c)]\ [J(k_1AM/4) + iN(k_1AM/4)] \tag{56}$$

A more interesting plan form, and, admittedly, much more applicable to the zero aspect ratio concepts, is the delta

wing. Unfortunately, closed form evaluation of the integrals appearing in the expressions for lift and moment are not possible. As a result, it was first necessary to evaluate certain integrals containing the $P(k_0M) + iQ(k_0M)$ and $J(k_0M) + iN(k_0M)$ functions. Once again it is desirable to describe the lift and moment functions in terms of a reduced frequency based on chord lengths rather than span lengths. If the wing root chord, c, is chosen as the reference distance, then

$$k_0 = (k_1A/4)\,(X/c) \tag{57}$$

where

$$k_1 = \omega c/U \tag{58}$$

The following notation is adapted for describing the required integrations:

$$P_n\left(\frac{k_1AM}{4}\right) + iQ_n\left(\frac{k_1AM}{4}\right) = \int_0^1 \left(\frac{X}{c}\right)^n \left[P\left(\frac{k_1AM}{4}\frac{X}{c}\right) + iQ\left(\frac{k_1AM}{4}\frac{X}{c}\right)\right] d\left(\frac{X}{c}\right) \tag{59}$$

$$J_n\left(\frac{k_1AM}{4}\right) + iN_n\left(\frac{k_1AM}{4}\right) = \int_0^1 \left(\frac{X}{c}\right)^n \left[J\left(\frac{k_1AM}{4}\frac{X}{c}\right) + iN\left(\frac{k_1AM}{4}\frac{X}{c}\right)\right] d\left(\frac{X}{c}\right) \tag{60}$$

Evaluation of Eqs. (41), (42), (43), (44), and (47) for the delta plan form leads to the following results:

$$L_z = \frac{\pi A}{2}\frac{\rho_0}{2} U^2 S e^{i\omega t}\frac{\bar{Z}}{c}\left\{-k_1^2\left[P_2\left(\frac{k_1AM}{4}\right) + iQ_2\left(\frac{k_1AM}{4}\right)\right] + ik_1\left[P_0\left(\frac{k_1AM}{4}\right) + iQ_0\left(\frac{k_1AM}{4}\right)\right]\right\} \tag{61}$$

$$L_{\bar{\theta}} = \frac{\pi A}{2}\frac{\rho_0}{2} U^2 S e^{i\omega t}\bar{\theta}\left\{-\left(1 + \left(1 - \frac{X_0}{c}\right)ik_1\right)\left[P_0\left(\frac{k_1AM}{4}\right) + iQ_0\left(\frac{k_1AM}{4}\right)\right] - \left(k_1^2\left(\frac{X_0}{c}\right) + ik_1\right)\left[P_2\left(\frac{k_1AM}{4}\right) + iQ_2\left(\frac{k_1AM}{4}\right)\right] + k_1^2\left[P_3\left(\frac{k_1AM}{4}\right) + iQ_3\left(\frac{k_1AM}{4}\right)\right]\right\} \tag{62}$$

$$M_z = \frac{\pi A}{2}\frac{\rho_0}{2} U^2 S c e^{i\omega t}\frac{\bar{Z}}{c}\left\{\left(ik_1 - \left(\frac{X_0}{c}\right)k_1^2\right)\left[P_2\left(\frac{k_1AM}{4}\right) + iQ_2\left(\frac{k_1AM}{4}\right)\right] - ik_1\left(1 - \frac{X_0}{c}\right)\left[P_0\left(\frac{k_1AM}{4}\right) + iQ_0\left(\frac{k_1AM}{4}\right)\right] + k_1^2\left[P_3\left(\frac{k_1AM}{4}\right) + iQ_3\left(\frac{k_1AM}{4}\right)\right]\right\} \tag{63}$$

$$M_{\bar{\theta}} = \frac{\pi A}{2}\frac{\rho_0}{2} U^2 S c e^{i\omega t}\bar{\theta}\left\{\left[1 - \frac{X_0}{c} + ik_1\left(1 - \frac{X_0}{c}\right)^2\right]\left[P_0\left(\frac{k_1AM}{4}\right) + iQ_0\left(\frac{k_1AM}{4}\right)\right] - \left(1 + k_1^2\left(\frac{X_0}{c}\right)^2\right)\left[P_2\left(\frac{k_1AM}{4}\right) + iQ_2\left(\frac{k_1AM}{4}\right)\right] + 2k_1^2\frac{X_0}{c}\left[P_3\left(\frac{k_1AM}{4}\right) + iQ_3\left(\frac{k_1AM}{4}\right)\right] - k_1^2\left[P_4\left(\frac{k_1AM}{4}\right) + iQ_4\left(\frac{k_1AM}{4}\right)\right]\right\} \tag{64}$$

$$Q_{\bar{\beta}} = \frac{\pi A}{2}\frac{\rho_0}{2} U^2 S b_{max} e^{i\omega t}\bar{\beta}\left\{\frac{k_1^2}{4}\frac{b_{max}}{c}\left[J_4\left(\frac{k_1AM}{4}\right) + iN_4\left(\frac{k_1AM}{4}\right)\right] - \frac{ik_1}{4}\frac{b_{max}}{c}\left[J_0\left(\frac{k_1AM}{4}\right) + iN_0\left(\frac{k_1AM}{4}\right)\right]\right\} \tag{65}$$

If incompressible flow is assumed, the preceding expressions for the lift and moment on the rectangular and delta plan forms simplify considerably. The first simplification to be noted is in the expressions containing the Mathieu functions. It can be shown from McLachlan[4] that

$$\left.\begin{aligned} P(0) + iQ(0) &= -1.0 + i0 \\ P_0(0) + iQ_0(0) &= -1.0 + i0 \end{aligned}\right\} \tag{66}$$

$$\left.\begin{aligned} J(0) + iN(0) &= -(1/2) + i0 \\ J_0(0) + iN_0(0) &= (1/2) + i0 \end{aligned}\right\} \tag{67}$$

$$P_n(0) + iQ_n(0) = -[1/(n+1)] + i0 \tag{68}$$

$$J_n(0) + iN_n(0) = -\{1/[2(n+1)]\} - i0 \tag{69}$$

For the incompressible case, the lift and moment equations for the rectangular wing become

$$L_{\bar{z}} = \frac{\pi A}{2}\frac{\rho_0}{2} U^2 S e^{i\omega t}\frac{\bar{Z}}{c}\left[-ik_1 + k_1^2\right] \tag{70}$$

$$L_{\bar{\theta}} = \frac{\pi A}{2}\frac{\rho_0}{2} U^2 S e^{i\omega t}\bar{\theta}\left[1 + 2ik_1 - ik_1\frac{X_0}{c} + k_1^2\left(\frac{X_0}{c} - \frac{1}{2}\right)\right] \tag{71}$$

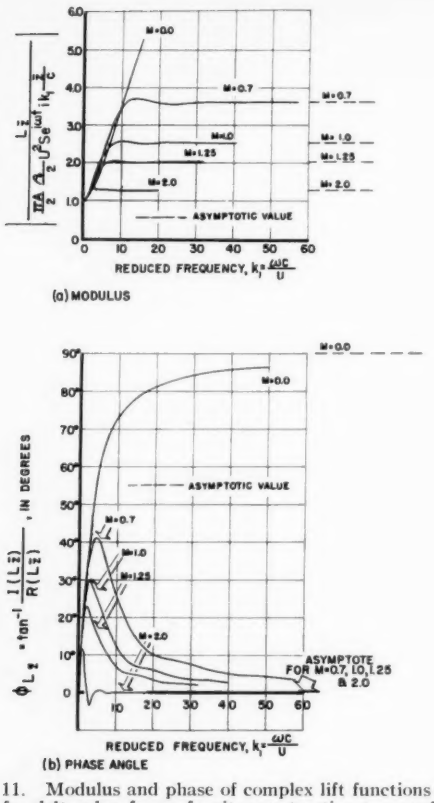

FIG. 11. Modulus and phase of complex lift functions due to plunge for delta plan form of unit aspect ratio at several Mach Numbers.

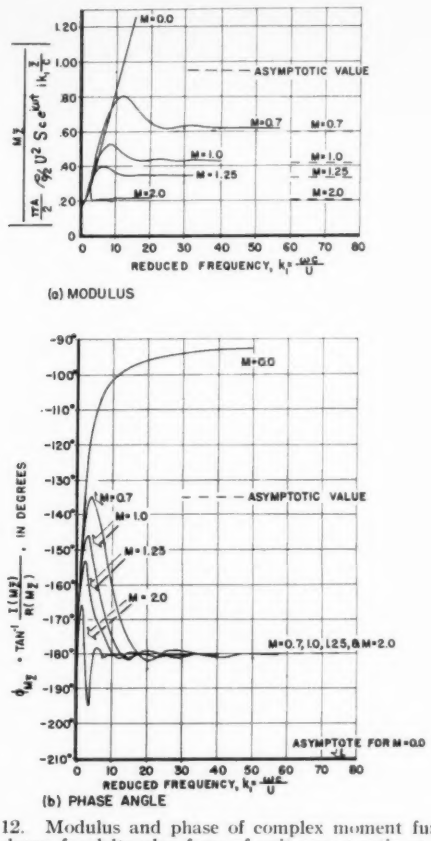

FIG. 12. Modulus and phase of complex moment functions due to plunge for delta plan form of unit aspect ratio at several Mach Numbers ($X_0/c = 1/2$).

$$M_{\bar{z}} = \frac{\pi A}{2}\frac{\rho_0}{2} U^2 Sce^{i\omega t}\frac{\bar{Z}}{c}\left[ik_1\frac{X_0}{c} + k_1^2\left(\frac{X_0}{c} - \frac{1}{2}\right)\right] \tag{72}$$

$$M_{\bar{\theta}} = \frac{\pi A}{2}\frac{\rho_0}{2} U^2 Sce^{i\omega t}\,\bar{\theta}\left[\frac{X_0}{c} + k_1^2\left(\frac{1}{3} - \frac{X_0}{c} + \left(\frac{X_0}{c}\right)^2\right) - ik_1\left(\left(\frac{X_0}{c}\right)^2 - 2\frac{X_0}{c} + 1\right)\right] \tag{73}$$

$$\Re_{\bar{\beta}} = \frac{\pi A}{2}\frac{\rho_0}{2} U^2 Sbe^{i\omega t}\,\bar{\beta}\left[+\frac{ik_1}{8}\frac{b}{c} - \frac{k_1^2}{8}\frac{b}{c}\right] \tag{74}$$

Similarly, the lift and moment equations for the delta wing in incompressible flow become:

$$L_{\bar{z}} = \frac{\pi A}{2}\frac{\rho_0}{2} U^2 Se^{i\omega t}\frac{\bar{Z}}{c}\left[\frac{k_1^2}{3} - ik_1\right] \tag{75}$$

$$L_{\bar{\theta}} = \frac{\pi A}{2}\frac{\rho_0}{2} U^2 Se^{i\omega t}\,\bar{\theta}\left[1 + ik_1\left(\frac{4}{3} - \frac{X_0}{c}\right) + k_1^2\left(\frac{X_0}{3c} - \frac{1}{4}\right)\right] \tag{76}$$

$$M_{\bar{z}} = \frac{\pi A}{2}\frac{\rho_0}{2} U^2 Sce^{i\omega t}\frac{\bar{Z}}{c}\left[-ik_1\left(\frac{X_0}{c} - \frac{2}{3}\right) - k_1^2\left(\frac{1}{4} - \frac{X_0}{3c}\right)\right] \tag{77}$$

$$M_{\bar{\theta}} = \frac{\pi A}{2}\frac{\rho_0}{2} U^2 Sce^{i\omega t}\,\bar{\theta}\left[\frac{X_0}{c} - \frac{2}{3} - ik_1\left(\frac{X_0}{c} - 1\right)^2 + k_1^2\left(\frac{1}{3}\left(\frac{X_0}{c}\right)^2 - \frac{1}{2}\left(\frac{X_0}{c}\right) + \frac{1}{5}\right)\right] \tag{78}$$

$$\Re_{\bar{\beta}} = \frac{\pi A}{2}\frac{\rho_0}{2} U^2 Sb_{max}\, e^{i\omega t}\,\bar{\beta}\left[\frac{ik_1}{8}\frac{b_{max}}{c} - \frac{k_1^2}{40}\frac{b_{max}}{c}\right] \tag{79}$$

The preceding equations for the lift and pitching moment on the two plan forms in incompressible flow agree with those obtained in previous investigations. (See references 2 and 3).

It appears desirable to mention at this point the range of validity of the theory. The limitations on the theoretical results obtained depend primarily on two approximations: the linearization of the velocity

TABLE 1
Correspondence of Notation

Present Paper	Ref. (7) (National Bureau of Standards)
k_0M	$\sqrt{s}$
n	r
$B_1^n(k_0M)$	$B(s)\ D_{0_1}{}^r\ (s)$
$B_2^n(k_0M)$	$B(s)\ D_{0_2}{}^r\ (s)$
$\frac{Ne_n^{(2)}(0,k_0M)}{Ne_n^{(2)'}(0,k_0M)}$	$\frac{-(g_{0,r}(s))^2 f_{0,r}(s)+i(g_{0,r}(s))^2}{(f_{0,r}(s))^2+1}$

potential equation which resulted in the formulation of Eq. (1), and the disregard of the X derivatives in Eq. (1) which resulted in Eq. (2). Two excellent discussions can be found in the literature covering the implications of these two approximations. Miles in reference 5 considers the first approximation as a function of reduced frequency k_1, Mach Number M, aspect ratio A, and the thickness ratio δ, of the wing. He sets forth the following conditions.

In the neighborhood of the wing all of these conditions must be satisfied:

$$\left.\begin{aligned} \delta &\ll 1 \\ M\cdot\delta &\ll 1 \\ k_1\cdot\delta &\ll 1 \\ k_1\cdot M\cdot\delta &\ll 1 \end{aligned}\right\} \tag{80}$$

In addition, one or more of the following conditions must be satisfied, also in the neighborhood of the wing:

$$\left.\begin{aligned} |M-1| &\gg (\delta)^{2/3} \\ k &\gg (\delta)^{2/3} \\ \frac{1}{A} &\gg (\delta)^{1/3} \end{aligned}\right\} \tag{81}$$

The second approximation (neglect of the X derivatives) which implies that

$$|(1-M^2)\varphi_{XX}| \ll |\varphi_{YY}+\varphi_{ZZ}| \tag{82}$$

$$|(2M/c)\varphi_{Xt}| \ll (1/a^2)\varphi_{tt} \tag{83}$$

is treated by Merbt and Landahl.[3] Briefly summarizing their results, they find that relation (82) is satisfied if

$$(1-M^2)\ [db(X)/dX]^2 \ll 1 \tag{84}$$

Examination of relation (84) implies that, for the rectangular wing, the only region of validity is at sonic speeds since $db(X)/dX$ is an impulse at the leading edge. However, for the delta wing, relation (82) is satisfied if

$$|1-M^2|A^2 \ll 16 \tag{85}$$

In their study of the implications of relation (83) it was found that precise limitations could not be set forth since they depend to a large extent on the type of motion as well as the plan form. However, they do conclude that the solutions obtained from the wave equation are much more restricted than those obtained from steady-state considerations. For example, at very low aspect ratios (say for the delta configuration), the neglect of the X derivatives of the velocity potential may be valid for all reduced frequencies, k_1, while for larger aspect ratios at $M = 1.0$ the validity may be restricted to only very low or very high reduced frequencies. One may also note that the validity of the results obtained at infinite reduced frequency are independent of plan form and Mach Number and would agree precisely with the results obtained if Eq. (1) had been used instead of Eq. (2).

NUMERICAL COMPUTATION OF AERODYNAMIC COEFFICIENTS AND SIGNIFICANCE OF RESULTS

Rectangular Plan Form

The successful numerical evaluation of the expressions for lift and moment developed in the present paper depends largely on the numerical tabulation of the Mathieu functions given in Eqs. (45) and (48). Fortunately, complete tabulations of these functions are available in reference 7. Since the notation used in this reference is completely different from that used by McLachlan, Table 1 is provided to indicate the correspondence of the two.

In Table 2, listings of the complex functions $P(k_0M) + iQ(k_0M)$ and $J(k_0M) + iN(k_0M)$ are given (as computed by the information given in reference 6) for values of k_0M ranging from 0.0 to 10.0. The values are accurate to four significant figures. Note that these tabulations are sufficient for evaluating the lift and moment expressions for the rectangular plan form where the values of k_0M correspond to $k_1AM/2$. The expressions for lift and moment were evaluated for a rectangular wing of unit aspect ratio for three Mach Numbers, $M = 0.0$, $M = 0.7$, and $M = 1.0$ at $X_0/c = 1/2$. The results are plotted as the modulus and phasing as a function of reduced frequency, k_1, in Figs. 1 through 5. Although it is realized that these results

TABLE 2
Values of Complex Functions
$P(k_0M) + iQ(k_0M)$ and $J(k_0M) + iN(k_0M)$

k_0M	$P(k_0M)$	$Q(k_0M)$	$J(k_0M)$	$N(k_0M)$
0.0	-1.0000	0.0	-.5000	0.0
.5000	-1.1473	.1289	-.5111	.0003924
1.0000	-1.1811	.6944	-.5498	.006831
1.5000	-.5309	1.0039	-.6275	.04091
2.0000	-.1491	.7539	-.7394	.1638
2.5000	-.05091	.5418	-.7500	.4565
2.8284	-.03537	.4498	-.5770	.6374
3.4641	-.04132	.3398	-.1948	.5922
4.0000	-.05617	.3000	-.08649	.4386
4.4721	-.05039	.2895	-.07214	.3418
4.8990	-.03168	.2729	-.08604	.2883
5.2915	-.01859	.2503	-.1070	.2684
5.6569	-.01243	.2291	-.1169	.2752
6.0000	-.01047	.2113	-.1033	.2892
6.3246	-.01094	.1970	-.07519	.2902
6.6332	-.01281	.1860	-.04896	.2771
6.9282	-.01511	.1782	-.03060	.2582
7.2111	-.01660	.1733	-.01903	.2390
7.4833	-.01623	.1701	-.01193	.2218
7.7460	-.01406	.1669	-.007583	.2075
8.0000	-.01109	.1629	-.004882	.1965
8.2462	-.008257	.1580	-.003182	.1889
8.4853	-.005978	.1529	-.002098	.1851
8.7178	-.004281	.1478	-.001397	.1847
8.9443	-.003061	.1429	-.0009384	.1863
9.1652	-.002195	.1384	-.0006358	.1879
9.3808	-.001581	.1343	-.0004341	.1878
9.5917	-.001144	.1307	-.0002985	.1856
9.7980	-.0008326	.1276	-.0002066	.1815
10.0000	-.0006088	.1251	-.0001439	.1762

TABLE 3
Values of Complex Functions
$P_n\left(\frac{k_1AM}{4}\right) + iQ_n\left(\frac{k_1AM}{4}\right)$ and $J_n\left(\frac{k_1AM}{4}\right) + iN_n\left(\frac{k_1AM}{4}\right)$

$\frac{k_1AM}{4}$	$P_0(\frac{k_1AM}{4})$	$P_1(\frac{k_1AM}{4})$	$P_2(\frac{k_1AM}{4})$	$P_3(\frac{k_1AM}{4})$	$P_4(\frac{k_1AM}{4})$	$Q_0(\frac{k_1AM}{4})$	$Q_1(\frac{k_1AM}{4})$	$Q_2(\frac{k_1AM}{4})$	$Q_3(\frac{k_1AM}{4})$	$Q_4(\frac{k_1AM}{4})$	$J_0(\frac{k_1AM}{4})$	$J_1(\frac{k_1AM}{4})$	$N_0(\frac{k_1AM}{4})$	$N_1(\frac{k_1AM}{4})$
0	-1.000	-.333	-.250	-.200	.000	.000	.000	.000	.000	.000	-.500	-.100	.000	.000
.10	-1.009	-.334	-.250	-.200	.009	.003	.002	.002	.002	.002	-.501	-.100	.000	.000
.20	-1.038	-.337	-.253	-.203	.024	.006	.005	.004	.004	.004	-.502	-.100	.000	.000
.40	-1.105	-.353	-.267	-.214	.075	.017	.015	.013	.013	.013	-.507	-.101	.000	.000
.70	-1.228	-.386	-.293	-.237	.200	.056	.048	.042	.041	.041	-.513	-.103	.002	.000
1.00	-1.380	-.432	-.305	-.245	.404	.118	.112	.097	.097	.096	-.550	-.108	.007	.001
1.20	-1.955	-.382	-.284	-.226	.925	.193	.163	.141	.141	.141	-.575	-.112	.017	.002
1.40	-1.660	-.343	-.258	-.208	1.644	.281	.221	.191	.191	.191	-.611	-.117	.032	.004
1.50	-.531	-.333	-.250	-.197	1.004	.341	.254	.224	.221	.221	-.630	-.118	.041	.005
1.70	-.330	-.296	-.174	-.127	.915	.288	.225	.186	.186	.186	-.672	-.122	.075	.008
2.00	-.169	-.188	-.218	-.082	.754	.280	.217	.176	.176	.176	-.760	-.135	.154	.017
2.20	-.094	-.151	-.093	-.060	.654	.269	.204	.163	.163	.163	-.773	-.142	.258	.026
2.40	-.060	-.122	-.069	-.044	.576	.254	.189	.148	.148	.148	-.787	-.146	.385	.040
2.60	-.044	-.100	-.054	-.033	.510	.238	.174	.135	.135	.135	-.780	-.147	.515	.057
2.80	-.036	-.082	-.043	-.025	.451	.223	.160	.123	.123	.123	-.990	-.142	.633	.075
3.00	-.037	-.069	-.036	-.020	.402	.209	.147	.112	.112	.112	-.435	-.136	.720	.092
3.20	-.039	-.059	-.030	-.015	.355	.197	.136	.098	.098	.098	-.285	-.127	.646	.107
3.60	-.045	-.045	-.021	-.012	.328	.176	.117	.087	.087	.087	-.150	-.083	.560	.112
4.00	-.056	-.038	-.018	-.012	.300	.158	.104	.077	.077	.077	-.097	-.058	.438	.106
4.30	-.055	-.034	-.017	-.011	.292	.142	.096	.072	.072	.072	-.073	-.045	.370	.099
4.60	-.065	-.031	-.016	-.011	.285	.133	.091	.068	.068	.068	-.078	-.037	.323	.090
5.00	-.088	-.027	-.014	-.010	.269	.124	.086	.064	.064	.064	-.091	-.030	.270	.080
5.30	-.017	-.024	-.012	-.008	.250	.118	.082	.060	.060	.060	-.108	-.027	.240	.073
5.60	-.013	-.021	-.011	-.007	.230	.112	.078	.058	.058	.058	-.119	-.026	.216	.069
6.00	-.010	-.018	-.009	-.006	.211	.105	.073	.054	.054	.054	-.103	-.025	.199	.065
6.30	-.011	-.016	-.008	-.005	.198	.100	.069	.051	.051	.051	-.080	-.024	.190	.064
6.60	-.013	-.014	-.007	-.004	.186	.095	.066	.048	.048	.048	-.050	-.022	.180	.062
7.00	-.0155	-.012	-.006	-.004	.177	.090	.060	.045	.045	.045	-.030	-.020	.170	.060
7.30	-.0163	-.011	-.005	-.004	.170	.086	.058	.043	.043	.043	-.016	-.017	.221	.058
7.60	-.015	-.011	-.005	-.003	.169	.083	.056	.042	.042	.042	-.013	-.015	.218	.056
8.00	-.011	-.010	-.005	-.003	.163	.079	.053	.040	.040	.040	-.005	-.013	.196	.053
8.30	-.008	-.009	-.004	-.003	.153	.076	.050	.038	.038	.038	-.002	-.013	.181	.049
9.00	-.003	-.008	-.004	-.003	.141	.070	.047	.035	.035	.035	-.001	-.012	.186	.046
9.50	-.001	-.007	-.003	-.002	.132	.067	.045	.034	.034	.034	-.000	-.011	.186	.044
10.00	-.001	-.006	-.003	-.002	.125	.063	.042	.032	.032	.032	-.000	-.010	.176	.042

are not entirely applicable over the complete reduced frequency range, they are presented with the purpose of indicating the trends of the coefficients with reduced frequency as well as the effects of Mach Number. Also plotted on these figures are the asymptotic values at infinite reduced frequency which were determined independently of the Mathieu functions by physical considerations. In some cases the asymptotes for the incompressible case are infinite, as is the modulus of the moment due to pitch for the compressible case. For the incompressible case, these infinite values are attributable to the assumed incompressibility of the fluid—i.e., at infinite frequency infinite forces are required to move the airfoil. For the modulus of the moment due to pitch the infinite asymptotic value is a result of normalizing the contributions of the moment due to angular position and angular velocity both with respect to $\bar{\theta}$. If these contributions were normalized with respect to $\bar{\theta}$ for moment due to angular position and with $ik_1\bar{\theta}$ for the moment due to angular velocity, finite asymptotes would have been obtained for each. This procedure is actually necessary for evaluating the indicial functions in pitch.

Detailed examination of Figs. 1–5 indicate that, in general, for the region of reduced frequencies for practical flutter problems (say between $k_1 = 0$ to $k_1 = 1.0$) the effects of Mach Number are small. The only instance where they become somewhat appreciable for this frequency range is in the moment due to plunge (see Fig. 2). For the range of reduced frequencies, $1 < k_1 < \infty$, the effects of Mach Number become quite significant, suggesting that the associated indicial functions (the response to a step input) would vary appreciably with Mach Number in the initial region of chord lengths traveled. It should also be noted that solutions obtained by the Mathieu functions approach their respective asymptotic values very closely in all cases, indicating that the numerical evaluation of the Mathieu functions used is correct and that the evaluation of the indicial functions from the harmonically oscillating coefficients using the well known reciprocal relations (see reference 7) would be relatively simple and accurate.

Delta Plan Form

In addition to the tabulated functions given in Table 2, the numerical computation of the integrals given by Eqs. (59) and (60) are required for determining the aerodynamic coefficients for the delta plan form. These integrations were performed numerically; unfortunately, the four-place accuracy of the functions appearing inside the integral could not be retained in the evaluation of the integrals. However, sufficient care was taken in the numerical computation that the evaluation of the aerodynamic coefficients is within plotting accuracy. In Table 3 a listing is provided of the functions $P_0(k_1AM/4) + iQ_0(k_1AM/4)$ and $P_n(k_1AM/4) + iQ_n(k_1AM/4)$ for $n = 2$, 3, and 4 as well as $J_0(k_1AM/4) + iN_0(k_1AM/4)$ and $J_n(k_1AM/4) + iN_n(k_1AM/4)$ for $n = 4$. On the basis of these values, the expressions for lift and moment due to plunge, pitch, and roll [see Eqs. (61) through (65)] were evaluated for two aspect ratios, $A = 0.5$ and $A = 1.0$, and for a wide range of Mach Numbers, $M = 0.0$, 0.7, 1.0, 1.25, and 2.0. The axis of rotation for pitch as well as the point where the moments are evaluated was taken at the root mid-chord—i.e., $X_0/c = 1/2$. The results of these calculations are shown in Figs. 6–15. Also plotted are the asymptotic values at infinite reduced frequency which were determined by physical considerations. As was similarly shown for the rectangular

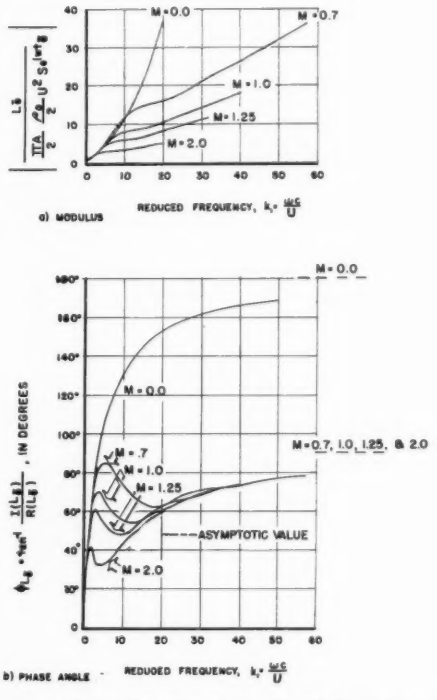

FIG. 13. Modulus and phase of complex lift functions due to pitch for delta plan form of unit aspect ratio at several Mach Numbers ($X_0/c = 1/2$).

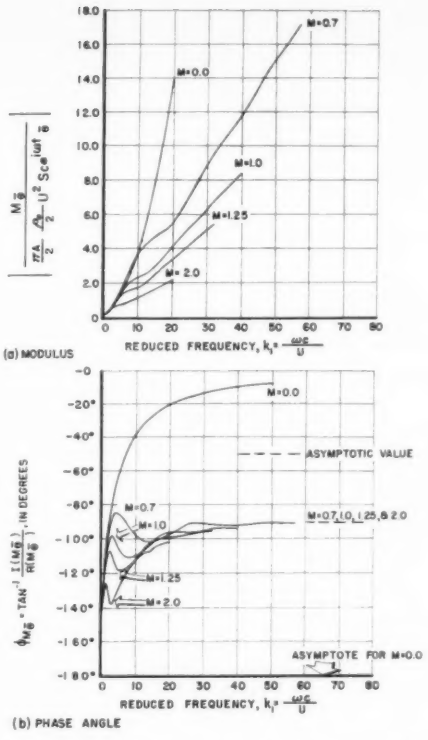

FIG. 14. Modulus and phase of complex moment functions due to pitch for delta plan form of unit aspect ratio at several Mach Numbers ($X_0/c = 1/2$).

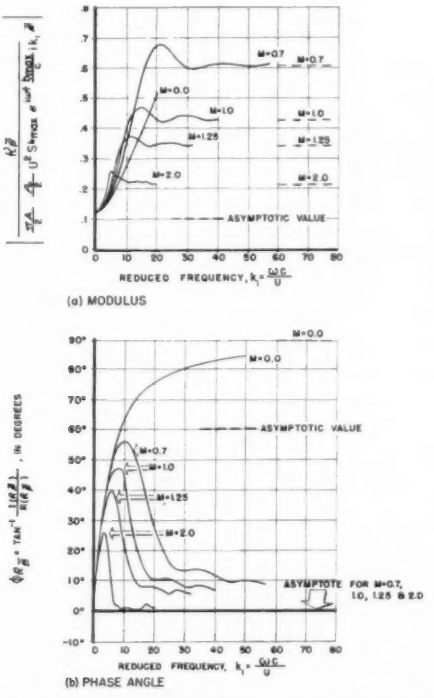

FIG. 15. Modulus and phase of complex rolling moment functions due to roll for delta plan form of unit aspect ratio at several Mach Numbers.

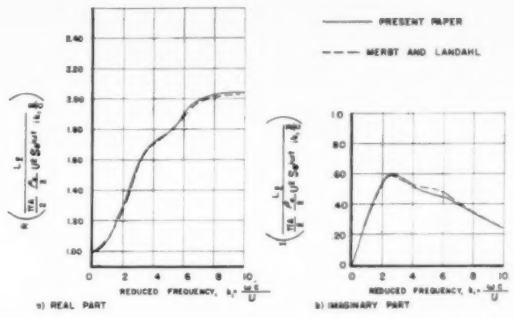

FIG. 16. Comparison of complex lift due to plunge for $A = 1$ delta plan form at $M = 1.25$ determined by present paper and Merbt and Landahl.

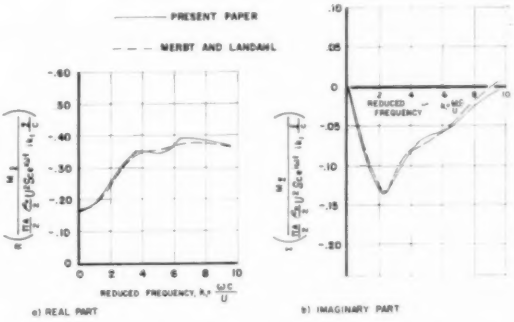

FIG. 17. Comparison of complex moment due to plunge ($X_0/c = 1/2$) for $A = 1$ delta plan form at $M = 1.25$ determined by present paper and Merbt and Landahl.

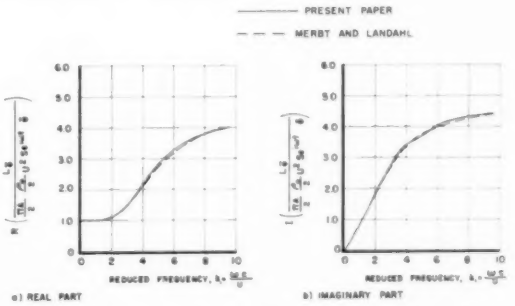

FIG. 18. Comparison of complex lift due to pitch ($X_0/c = 1/2$) for $A = 1$ delta plan form at $M = 1.25$ determined by present paper and Merbt and Landahl.

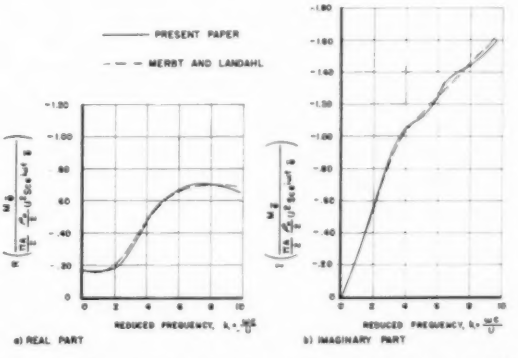

FIG. 19. Comparison of complex moment due to pitch ($X_0/c = 1/2$) for $A = 1$ delta plan form at $M = 1.25$ determined by present paper and Merbt and Landahl.

plan form, the asymptotes for the moduli associated with the delta plan form are infinite at infinite reduced frequency for $M = 0.0$ due to the assumed incompressibility of the medium; for the compressible case the moduli for lift and moment due to pitching motion also possess infinite asymptotes for reasons previously mentioned for the rectangular plan form.

Examination of the aerodynamic coefficients indicates that for the low reduced frequency range, $0 \leq k_1 \leq 1$, the effects of Mach Number are small and can perhaps be assumed negligible in flutter calculations. For the high reduced frequency range, the effects of Mach Number once again become important, thus implying that the associated indicial functions would vary considerably in the initial region of chord lengths traveled. The solutions at highest reduced frequencies are shown to agree very well with their respective independently determined asymptotes.

Aerodynamic Coefficients Determined by Present Paper Compared with Those of Merbt and Landahl

A comparison of the oscillatory coefficients determined in the present study with those obtained by Merbt and Landahl appears desirable in view of the fact that the coefficients are based on the same physical considerations but were evaluated independently. Such a comparison is made in Figs. 16 through 19 of the lift and pitching moment due to plunge and pitch of an $A = 1$ delta plan form at $M = 1.25$. The real and imaginary parts of the lift and moment are plotted versus reduced frequency, k_1.

Inspection of Figs. 16 through 19 indicates that, in general, the aerodynamic coefficients compare favorably. The same order of agreement was found to exist for the aerodynamic coefficients at other Mach Numbers. The slight differences that do exist are perhaps a result of a combination of the Mathieu functions used and the required numerical integration containing these functions.

Comparison of the analytical expressions obtained by Merbt and Landahl with the present paper for the delta wing indicates that agreement is obtained for all the lift and pitching moment expressions provided (in the notation of Merbt and Landahl) the functions $F'(k)$ and $F''(k)$ defined in their paper by Eqs. (50) and (51) are modified such that $k = \lambda$. The functions $F'(\lambda u)$ and $F''(\lambda u)$ which appear in Eqs. (52) and (53) are defined correctly by Eqs. (50) and (51) with no modification.

For the incompressible case, the analytical expressions agree exactly.

Concluding Remarks

The theoretical aerodynamic properties of low aspect ratio harmonically oscillating rigid airfoils have been extended to include the effects of compressibility. These effects enter only through a single parameter, k_0M. Closed form solutions are obtained for the rectangular plan form. The delta plan form does not, unfortunately, lend itself to closed form solutions since integrations in a chordwise direction must be evaluated numerically due to the presence of Mathieu functions in the integrand which vary with the parameter, k_0M. Complete numerical evaluation of the required Mathieu functions and integrations are tabulated. Plots of the aerodynamic coefficients are given for the rectangular and delta plan form for a range of Mach Numbers.

Examination of the plots of aerodynamic coefficients indicates that, for the region of reduced frequencies used in flutter calculations, the effects of compressibility are found to be negligible; however, at high reduced frequencies the effects of compressibility are significant. The coefficients are computed at sufficiently large reduced frequencies such that the indicial functions (Fourier transform of the oscillatory functions) can be determined readily and accurately by use of the well known reciprocal relations.

References

[1] Jones, R. T., *Properties of Low-Aspect-Ratio Pointed Wings at Speeds Below and Above the Speed of Sound*, NACA TN 1032, 1946.

[2] Garrick, I. E., *Some Research on High Speed Flutter*, Proceedings of the Third Anglo-American Aeronautical Conference, Appendix B, R.Ae.S–I.A.S. 1951.

[3] Merbt, H., and Landahl, M., *Aerodynamic Forces on Oscillating Low Aspect Ratio Wings in Compressible Flow*, Royal Institute of Technology, Division of Aeronautics, Stockholm, Sweden, KTH Aero TN 30.

[4] McLachlan, N. W., *Theory and Application of Mathieu Functions*, Clarendon Press, Oxford, England, 1947.

[5] Miles, J. W., *On Linearized Theory*, Readers' Forum, Journal of the Aeronautical Sciences, Vol. 20, No. 1, p. 64, January, 1953.

[6] *Tables Relating to Mathieu Functions*, National Bureau of Standards, Columbia University Press, New York, 1951.

[7] Garrick, I. E., *On Some Fourier Transforms in the Theory of Non-Stationary Flows*, Proc. Fifth Int. Cong. Appl. Mech. (Cambridge, Mass., 1938) John Wiley & Sons, Inc., pp. 590–593, New York, 1939.

Eccentric Landing with Heavy Masses at the Wing Tips*

ALEXANDER GRZEDZIELSKI†
Avro Aircraft Ltd.

SUMMARY

An eccentric landing of a conventional aircraft carrying heavy masses at the wing tips is investigated. The landing gears make contact with the ground one after the other, the second contact taking place before the shock absorbing process of the first gear is completed. The following results are of interest.

(a) In eccentric landing with heavy tip masses the effective mass acting on (or the drop mass of) one shock absorbing unit may be larger than one half of the total mass of the aircraft.

(b) The magnitude of this mass depends on the ratio, radius of gyration of the aircraft in roll to the undercarriage tread, on the initial roll angle, and on the roll velocity at the moment of the first contact.

(c) Since the time span between two impacts and the magnitude of each impact depend on the initial roll angle and roll velocity and both can have any values, within certain statistical limits of course, an asymmetric wing vibration can be generated and have larger effects on wing stresses than the symmetric vibration due to the symmetric landing.

(d) Parameters defining the landing gear strength are in general three: (1) sinking velocity, (2) roll angle, and (3) roll velocity.

(e) Available information concerning the shock absorber characteristics is insufficient to bring the subject to a conclusion. It appears, however, that for large tip masses the shock absorption capacity of the gear should be checked in two cases at least; (1) in the case corresponding to symmetric landing shock (small drop mass and large sinking velocity), and (2) in the case of eccentric landing shock (large drop mass and small sinking velocity).

SYMBOLS

$F(t)$	=	forcing function of the vertical gear reaction
$G(t/T)$ $H(t/T)$	=	defined by Eq. (7)
M	=	mass of the aircraft
T	=	deceleration time
F_1, F_2	=	maxima of the forcing function for the first and second contact, respectively
e	=	undercarriage semitread
i	=	radius of gyration in roll
m_e	=	effective mass factor. Mm_e = effective mass
k	=	t_1/T = time lag factor
t, s	=	time coordinate
$u(t)$	=	vertical displacement of the aircraft
$\phi(t)$	=	angular displacement of the aircraft
x	=	span coordinate
y	=	vertical coordinate
u_0, ϕ_0	=	initial values of the above
$\dot{u}(t)$, $\dot{\phi}(t)$	=	dots indicate the time derivatives

Received May 24, 1955.

* This paper is based on an investigation connected with practical design problems. The writer is indebted to Avro Aircraft Ltd. for releasing the above material for publication. Acknowledgment is due to F. P. Mitchell, Chief Stress Engineer, for suggesting the problem and for his helpful comments in preparation of the paper. Drawings and computations are the work of R. N. Shearly, Stress Engineer. Opinions represented in the paper are not necessarily those of Avro Aircraft Ltd.

† Senior Stress Engineer.

INTRODUCTION

THERE ARE FEW references on the subject of eccentric landings. The most important work is reference 6, which is unfortunately restricted to landings in which impact on the gear first to contact the ground is largely completed prior to the next impact. Thus, the analysis presumes that either the initial roll angle is large or the duration of the first shock is short. With heavy loads at the tips neither may represent a practical case. Since the effective drop masses in eccentric landing can be quite large, restrictions may be imposed in practice on the allowable roll angle, with the result that the two impacts may overlap considerably. An exact solution of the problem would involve examination of the interaction of the shock absorbers, and would probably be a forlorn undertaking without an electronic computer. Therefore only an approximate solution is offered at this time.

If the lag factor of the second gear—i.e., the time lag of the second impact divided by the shock absorbing time of the first gear—is not too large, it can be assumed as a first approximation that the characteristics of both landing gears are the same but for a constant factor and as found in the symmetric drop test. If so, then by integration of the equations of motion for certain selected initial conditions the impact on each gear can be found analytically, together with the corresponding velocity changes. Thus, an effective mass can be estimated to be used in a new drop test, conducted, if necessary, with a conveniently modified drop velocity. With this new information, the integration of the equations of motion can be repeated and the value of the effective mass corrected again. One is allowed to expect that the outlined procedure would provide a sound basis for a compromise between the restrictions imposed on landing conditions and the improvement of the design offered by tip masses (whatever they are).

By neglecting the fine detail of the landing gear characteristic and using a simple impulse momentum theory, it is possible to gain an insight into the behavior of the aircraft with heavy loads at the wing tips. Here are a few noteworthy facts and definitions:

Equivalent Mass

An aircraft represented in Fig. 1 in full lines has a total mass given by

$$M = \sum m_i$$

and a roll moment of inertia, in close approximation,

$$I = \sum x_i^2 m_i$$

The quantity

$$i = \sqrt{I/M}$$

is the radius of gyration in roll. One can see that two masses of the magnitude $M/2$ spaced $2i$ in. apart represent the aircraft as far as concerns its behavior in the plane perpendicular to the axis of rolling. This is the concept of the equivalent concentrated masses.

Center of Rotation

If a force F, representing landing gear reaction, is applied as shown in Fig. 2, the initial movement of the aircraft is a rotation around a point O such that

$$er = i^2$$

Point O is called the instantaneous center of rotation. In the case $e = i$, we have $r = i$. Hence the following important statement. If the landing gears are placed where the equivalent masses are located, a vertical impact on one gear does not alter the sinking velocity of the other gear.

Effective Mass

If the force F (see Fig. 2) acts during a short time t, the point of application of the force is displaced upwards by a distance

$$y = [(1 + e^2/i^2)Ft^2]/2M$$

and the quantity

$$M_e = M/(1 + e^2/i^2)$$

is called the effective mass or the percussion mass. This concept is introduced since a force F acting on a mass M_e during the time t would produce a displacement

$$y = Ft^2/2M_e$$

If $i > e$, which is likely to happen with heavy loads at the tips,

$$M_e > (1/2)M$$

In many aircraft with good landing qualities the landing gear semitread is not much different from the radius of gyration in roll. In such a case the eccentric landing does not overload either landing gear.

Rocking of the Aircraft with Heavy Tip Loads

If i is much greater than e the aircraft may rock even when the landing gear is built for a complete dissipation of energy. (No rebound shock absorbers and tires.) Assume two aircraft—Fig. 3, $i < r$, and Fig. 4, $i > r$. Let the aircraft be represented by their equivalent masses. Suppose that each aircraft while air-borne has contacted the ground with a gear denoted as R. Since no rebound is assumed the aircraft rotates around the point R until the other gear, denoted as L, contacts the ground. At this moment, inertia forces, denoted by double arrows, are generated. In the case of Fig. 3, both inertia forces act down and inboard of the landing gear tread, hence both ground reactions act upwards. In the case of Fig. 4, inertia forces are outboard of the landing gear tread and are directed so that the R reaction has to act down if the gear is not to lose contact with the ground. This is not possible, however, and the gear R will lift up. Thus in the case of $i > r$ the sum of the impulses produced by the landing gears is larger than the momentum of the aircraft. In other words, in eccentric landing the gear strength cannot be derived from consideration of the symmetric case.

Beam Analogy

The motion of a mass under the action of a given force which is variable in time can be followed easily by means of a beam analogy. According to this analogy

displacement	corresponds to	bending moment
velocity		shear force
acceleration		running load
time variable		beam axis station

Displacement due to a given load time variability can be found by means of a funicular polygon.

Suppose that an aircraft having the mass M moves toward the ground with a velocity v. At the time $t = 0$ the ground contact is made and the shock absorber starts to compress. Denote the travel of the center of gravity of the aircraft by y and the landing gear reaction by $F(t)$. The differential equation of the motion, in terms of the coordinates of Fig. 5 and with the aircraft weight supported by wings, is

$$M(d^2y/dt^2) = -F(t)$$

subject to the boundary conditions

$$\text{at} \quad t = 0, \quad y = 0, \quad dy/dt = v$$

$$\text{at} \quad t = T, \quad dy/dt = 0$$

whereby the momentum principle

$$M v = \int_0^T F(t)\, dt$$

It is not necessary that for $t > T$, $F(t)$ becomes zero, because of the rebound occurring in most undercarriages.

The solution of the above elementary problem is given by

$$\frac{dy}{dt} = -\frac{1}{M}\int_0^t F(s)\, ds + v$$

$$y = -\frac{1}{M}\int_0^t F(s)\,(t - s)\, ds + v\, t$$

Note that the last formula when differentiated yields

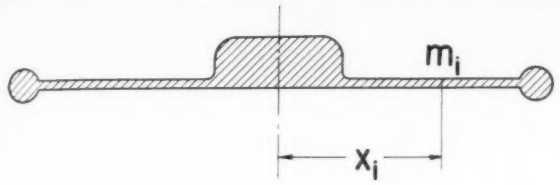

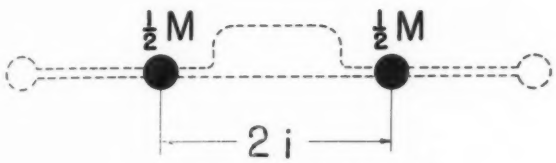

FIG. 1. Equivalent mass distribution.

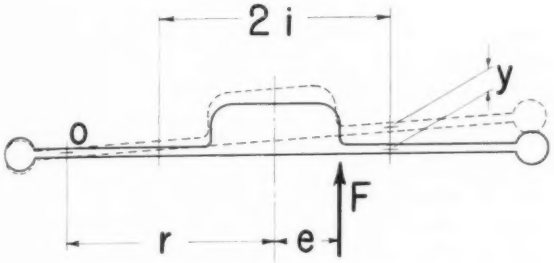

FIG. 2. Center of rotation.

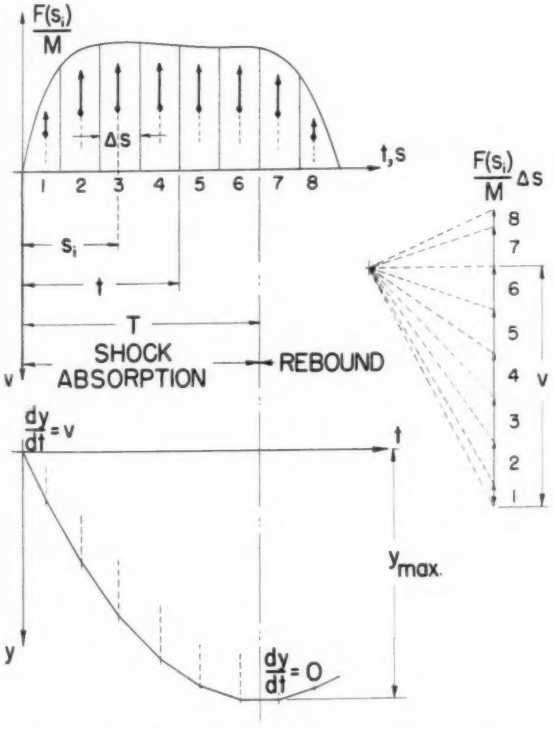

FIG. 5. Determination of displacement by beam analogy.

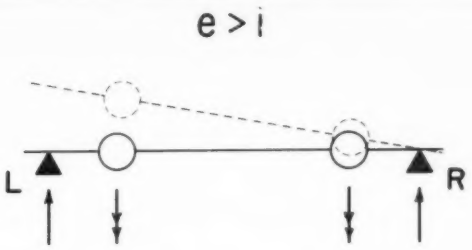

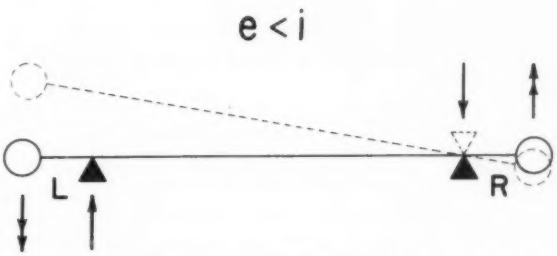

FIG. 3 (*top*). Inertia forces and gear reaction in the case $e>i$.
FIG. 4 (*bottom*). Inertia forces and gear reactions in the case $e<i$.

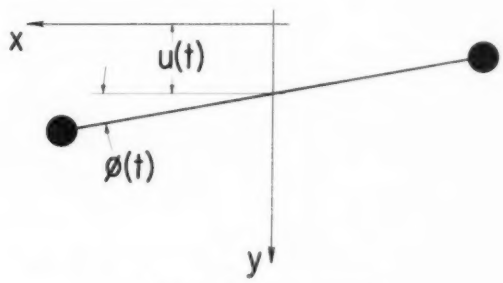

FIG. 6. Reference drawing.

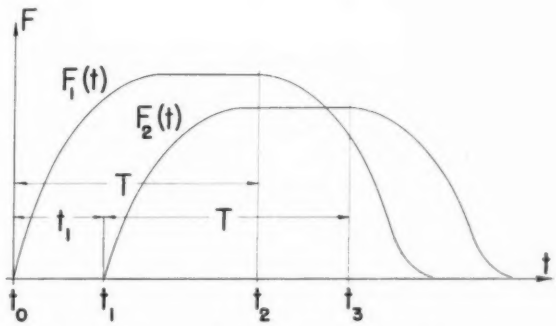

FIG. 7. Gear reactions in nonsimultaneous impact.

$$\frac{dy}{dt} = -\frac{1}{M}F(t)\ (t-t) - \frac{1}{M}\int_0^t F(s)\ ds + v$$

It appears that y is analogous to the bending moment generated in a cantilever beam at a station t from the tip by a concentrated load v at the tip and a running load $-[F(s)/M]$ at a station s from the tip; see Fig. 5.

Integrals such as

$$\int_0^t F(s)\ (t-s)\ ds$$

will have to be computed in the work below. The above beam analogy is intended to bring their meaning nearer to other familiar concepts of engineering analysis.

Eccentric Landing

Let Fig. 6 represent the aircraft. The masses, $M/2$, are the equivalent masses each located at i in (radius of gyration) from the center plane of the craft. $F_1(t)$ and $F_2(t)$ are the landing gear reactions. The gear designated as 1 is supposed to contact the ground first. Position of the aircraft with respect to the ground coordinates is defined by the center of gravity displacement $u(t)$ and by the rotation (roll) angle $\phi(t)$. In this notation the displacement of a reference line M—M, connected with the aircraft and passing through its center of gravity parallel to the ground in the unloaded state, is given by

$$y(x, t) = u(t) + x\phi(t) \tag{1}$$

Up to the moment of the first contact the aircraft moves as a free body and its motion can be described by an expression

$$y(x, t) = (\dot{u}_0 + x\dot{\phi}_0)t + u_0 + x\phi_0 \tag{2}$$

$\dot{u}_0$, $\dot{\phi}_0$, u_0, and ϕ_0 are the four constants characterizing the initial conditions providing that the roll angle is assumed small so that any horizontal displacement of the points of the reference line due to rotation can be disregarded.

The dynamic equations for an air-borne landing are

$$\left.\begin{aligned} M\ddot{u}(t) &= -F_2(t) - F_1(t) \\ Mi^2\ddot{\phi}(t) &= -[F_2(t) - F_1(t)]e \end{aligned}\right\} \tag{3}$$

Hence, by substitution of Eq. (3) in the second time derivative of Eq. (1),

$$M\,[\partial^2 y(x, t)/\partial t^2] = -F_2(t)\ (1 + xe/i^2) - F_1(t)\ (1 - xe/i^2) \tag{4}$$

This is the equation of motion of the aircraft reference line to be integrated with the initial condition that at the time $t = 0$ the motion is such as given by Eq. (2). The first integral is

$$M\,\partial y/\partial t = -(1 + ex/i^2)\int_0^t F_2(s)ds - (1 - ex/i^2)\int_0^t F_1(s)ds + M(\dot{u}_0 + x\dot{\phi}_0) \tag{5}$$

The second integral is

$$My = -(1 + xe/i^2)\int_0^t F_2(s)\ (t-s)ds - (1 - ex/i^2)\int_0^t F_1(s)\ (t-s)ds + M(\dot{u}_0 + x\dot{\phi}_0)t + M(u_0 + x\phi_0) \tag{6}$$

The difficulty now is with the landing gear reactions $F_2(t)$ and $F_1(t)$. Primarily, the landing gear reaction is not defined as a function of time but as a function of displacement and of velocity. The time relation is obtained by a long integration process and this method is not practicable for the present purpose. Therefore, the form of a suitable forcing function $F(t)$ can only be estimated from experimental data obtained in similar conditions.

It is assumed in the first approximation that the gear reactions are as shown in Fig. 7, and that i is always greater than e; this means that the motion of the aircraft is largely a rocking, as explained in the Introduction. In the figure, $T = t_2 = t_3 - t_1$ is the deceleration time while the rebound is produced over the remaining range. $t_1/T = k$ is the lag factor. It is assumed that T and the whole shape of the forcing function is about the same for both landing gears, which probably is true for small k and for i/e not too much in excess of 1. The maxima F_1 and F_2 are left undetermined for the time being. For any $k < 1$ the following holds:

at $t = 0$, first gear contacts the ground,

$$y(-e, 0) = 0$$

at $t = t_1$, second gear contacts the ground,

$$y(e, t_1) = 0$$

at $t = t_2$, first gear compressed to the end,

$$[\partial y(-e, t_2)]/\partial t = 0$$

at $t = t_3$, second gear compressed to the end,

$$[\partial y(e, t_3)]/\partial t = 0$$

It is understood that the above conditions are approximate and that the last condition may not even be true—in other words, after the first gear has absorbed most of the shock, there may not be enough momentum left to compress the second gear to the end. With this reservation we introduce two nondimensional functions

$$\left.\begin{aligned} G(t/T) &= \frac{1}{F_{max}T}\int_0^t F(s)ds \\ H(t/T) &= \frac{1}{F_{max}T^2}\int_0^t F(s)(t-s)ds \end{aligned}\right\} \tag{7}$$

for an assumed gear characteristic of Fig. 8. $G(\ )$ and $H(\ )$ are given in Fig. 9. Then Eqs. (5) and (6) become, respectively,

$$M\,\partial y/\partial t = -(1 + xe/i^2)F_2TG(t/T - k) - (1 - xe/i^2)F_1TG(t/T) + M(\dot{u}_0 + x\dot{\phi}_0) \tag{8}$$

$$My = -(1 + ex/i^2)F_2T^2H(t/T - k) - (1 - ex/i^2)F_1T^2H(t/T) + M(\dot{u}_0 + x\dot{\phi}_0)t + M(u_0 + x\phi_0) \quad (9)$$

The four initial conditions become:

at $t = 0$, first contact,

$$u_0 - e\,\phi_0 = 0 \quad (a)$$

at $t = t_1$, second contact,

$$+(1 - e^2/i^2)F_1T^2H(k) + M(\dot{u}_0 + e\dot{\phi}_0)t_1 + M(u_0 + e\phi_0) = 0 \quad (10)$$

at $t = t_2 = T$, first gear compressed to the end,

$$-(1 - e^2/i^2)F_2TG(1 - k) - (1 + e^2/i^2)F_1TG(1) + M(\dot{u}_0 - e\dot{\phi}_0) = 0 \quad (11)$$

at $t = t_3 = T + t_1$, second gear compressed to the end,

$$-(1 + e^2/i^2)F_2TG(1) - (1 - e^2/i^2) \times F_1TG(1 + k) + M(\dot{u}_0 + e\dot{\phi}_0) = 0 \quad (12)$$

The above represents a set of three simultaneous equations from which three unknowns F_1, F_2, k can be determined for any u_0, ϕ_0, $\dot{u}_0$, $\dot{\phi}_0$ given.* Mathematically, however, it appears to be much simpler to start with a given k.

The analysis can be brought to some conclusion in three cases: (A) symmetric landing, (B) landing with gears receiving equal impact $F_1 = F_2$ but not at the same time, and (C) eccentric landing.

Case (A)—This is a limit case: $k = 0$, $F_1 = F_2$, $H(0) = 0$. Eqs. (11) and (12) yield

$$\dot{u}_0 = \frac{2F_1T}{M}\,G(1), \qquad e\dot{\phi}_0 = 0 \quad (13)$$

Case (B)—Equal impact, $F_1 = F_2$. If a value for the lag factor is assumed, Eqs. (11) and (12) yield $\dot{u}_0$ and $\dot{\phi}_0$; then Eq. (9) yields $-y_2 = u_0 + e\phi_0$. The last quantity defines the elevation of the second wheel above the ground at the moment of the first contact. One obtains

$$\dot{u}_0 = (2F_1T/Mm_e)G(1) \quad (14)$$

where Mm_e is the effective mass. The nondimensional factor m_e is given by Eq. (15) and contains the assumed value of k.

$$1/m_e = \frac{2(1 + e^2/i^2)G(1) + (1 - e^2/i^2)\,[G(1 - k) + G(1 + k)]}{4G(1)} \quad (15)$$

Then

$$e\dot{\phi}_0/\dot{u}_0 = (1 - e^2/i^2)m_e\,\frac{G(1 + k) - G(1 - k)}{4G(1)} \quad (16)$$

* u_0 and ϕ_0 being related by Eq. (a).

$$-y_2/\dot{u}_0T = m_e \times [(1 + e^2/i^2)G(1) + (1 - e^2/i^2)G(1 + k)]k - \frac{(1 - e^2/i^2)H(k)}{2G(1)} \quad (17)$$

For $i > e$ and because $G(1 + k) > G(1 - k)$ the initial roll, velocity is positive (see Fig. 6). This implies that the condition of equal impact reduces the sinking velocity of the wheel first to contact to the amount

$$\dot{u}_{01} = \dot{u}_0 - e\dot{\phi}_0$$

at the same moment, the velocity of the wheel second to contact is increased to

$$\dot{u}_{02} = \dot{u}_0 + e\dot{\phi}_0$$

At the moment of the second contact, however, the velocity $\dot{u}_{2c}$ of the second wheel is reduced to an amount comparable with $\dot{u}_{01}$. It can be shown that

$$\dot{u}_{2c} = \dot{u}_{01} + \delta\dot{u}_0 \quad (18)$$

where

$$\delta\dot{u}_0 = m_e(1 - e^2/i^2)\,\frac{G(1 + k) - G(1 - k) - G(k)}{2G(1)}\,\dot{u}_0$$

This correction vanishes in the extreme cases, if there is no overlapping of the shock absorbing processes, $k > 1.4$; or if the overlapping is complete, $k = 0$. It vanishes also if $e = i$, of course.

Case (C)—Eccentric landing, $k \neq 0$, $F_2 \neq F_1$, $\dot{\phi}_0 = 0$. Here Eqs. (11) and (12) yield the maxima of the gear reactions in terms of the sinking velocity. Then Eq. (9) yields y_2. One obtains

$$\dot{u}_0 = (2F_1T/Mm_e)\,G(1) \quad (19)$$

where Mm_e is the effective mass particular to this case. m_e is given by

$$1/m_e = \frac{1}{2} \times \frac{(1 + e^2/i^2)^2G(1) - (1 - e^2/i^2)^2G(1 + k)G(1 - k)}{(1 + e^2/i^2)G(1) - (1 - e^2/i^2)G(1 - k)} \quad (20)$$

The impact ratio is

$$F_2/F_1 = \frac{(1 + e^2/i^2)G(1) - (1 - e^2/i^2)G(1 + k)}{(1 + e^2/i^2)G(1) - (1 - e^2/i^2)G(1 - k)} \quad (21)$$

Finally,

$$-y_2/\dot{u}_0T = k - (1/2)\,(1 - e^2/i^2)m_eH(k)/G(1) \quad (22)$$

It appears that for $i > e$, $F_2 < F_1$.

Numerical Example and Discussion

Assume the following data:

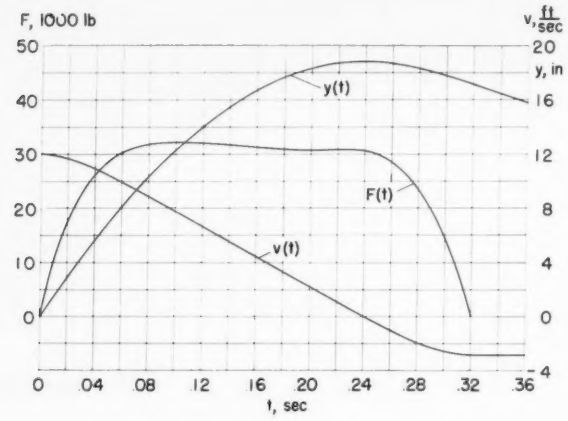

FIG. 8. Assumed landing gear characteristic.

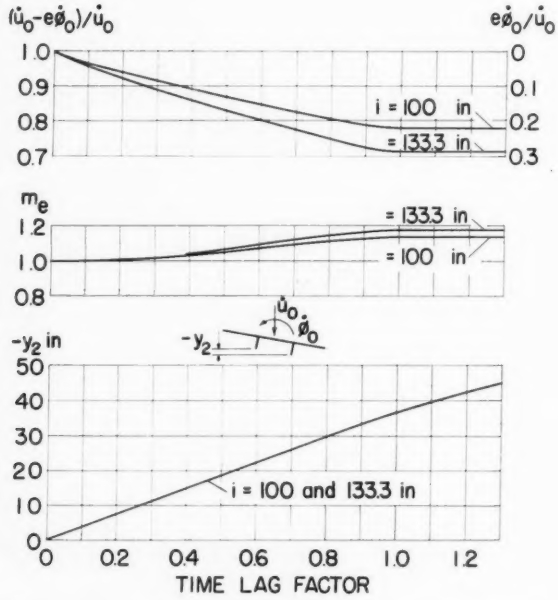

FIG. 10. Effective mass, initial roll angle, and initial roll velocity in the case of equal impacts, Case (B).

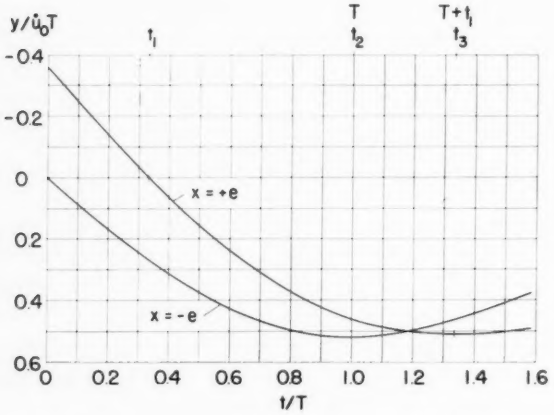

FIG. 12. Displacement of points $x = \pm e$ in Case (B).

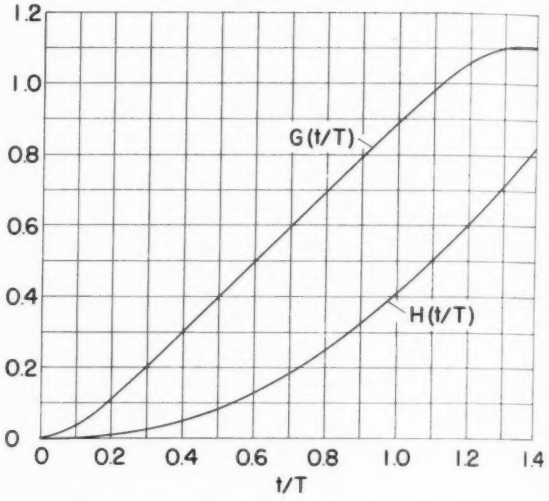

FIG. 9. Nondimensional gear functions, Eq. (7).

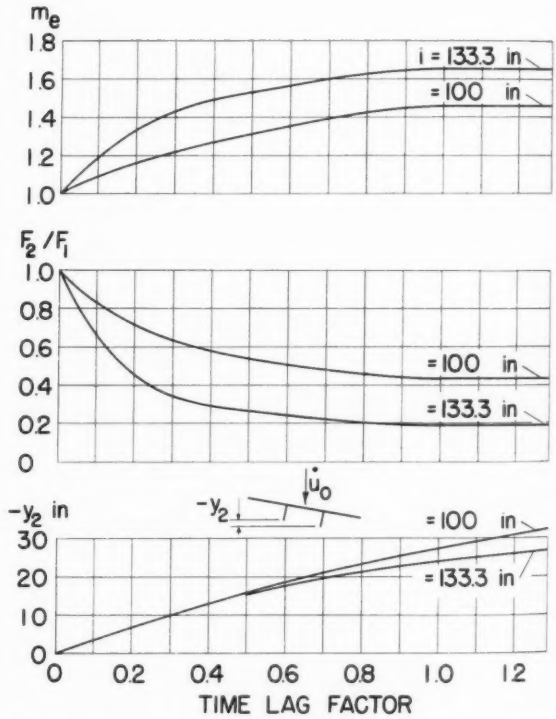

FIG. 11. Effective mass, initial roll angle, and impact ratio in the case of eccentric landing, Case (C).

Landing gear half tread	e	= 61 in.
Radius of gyration in roll	i	= 100.0 in.
		133.3 in.
Sinking velocity	$\dot{u}_0$	= 12.0 ft./sec.
Deceleration time	T	= 0.24 sec.

Gear characteristic, Fig. 8, air-borne landing

Fig. 10 presents the equal impact Case (B). Effective mass, initial roll angle, and initial roll velocity are plotted against the time lag factor. Fig. 11 presents the eccentric landing Case (C). Effective mass, initial roll angle, and impact ratio are plotted against the time lag factor. Fig. 12 shows displacement of the points $x = \pm e$ of the aircraft reference line in the case of equal impact. Note that at the time $t = 1.6T$ approx., both wheels have lifted from the ground, the aircraft moving up and rolling. Clearly, the initial angular momentum could not be altered by two equal impacts. (See also the paragraph on rocking in the Introduction.)

Figs. 10, 11, and 12, supported by the qualitative analysis at the beginning of the paper, seem to demonstrate conclusively that the most favorable condition for a conventional undercarriage is

$$e = i$$

If the above is satisfied, the landing gear is subjected to the same impact in an eccentric landing as in a symmetric one, assuming the same sinking velocity. With heavy masses at the wing tips, i is greater than e and, therefore, the impact on the wheel first to contact may be quite severe. For instance, for an initial roll angle corresponding to $-y_2 = 10$ in. and for $i = 133.3$ in. the effective mass is up to 1.44 times the mass carried in the symmetric landing (see Fig. 11). Yet if the assumed magnitude of initial rolling is such that the second impact equals the first, the effective mass is only 1.03 of the mass in the symmetric case. Unfortunately, the pilot has no means of controlling the required amount of rolling velocity, although an experienced pilot may always attempt to ease the shock by leveling the aircraft in the last moment. Hence, Case (C) should be considered as critical.

In the light of the above, the shock absorbing unit that contacts the ground first develops the impulse of Eq. (19)

$$F_1TG(1) = (1/2)Mm_e\dot{u}_0$$

equal to the momentum of a fictitious mass $(1/2)Mm_e$ moving with the velocity $\dot{u}_0$. Since for $i > e$, m_e is always greater than 1, therefore $\dot{u}_0$ must be assumed smaller in all cases of eccentric landing than in the symmetric ones if the required impulse is not to exceed the capacity of the unit. Thus, by Fig. 11, the permissible sinking velocity would appear as a function of the lag factor k and, consequently, as a function of the initial roll angle defined by $y_2/2e$. However, the problem is not as simple as that. Any change in the sinking velocity $\dot{u}_0$ affects the shape of the forcing function $F(t)$ and the values $G(1)$ and T. Therefore, although $\dot{u}_0$ may be reduced in the presence of y_2 so as to have the impact $F_1TG(1)$ the same as in the symmetric case, it does not follow that F_1 will remain unchanged. Because the strength of the landing gear and the adjacent structure is directly affected by F_1, the proof should be provided that the latter quantity remains on the conservative side for all values of $\dot{u}_0$ and y_2. This can be done by a numerical analysis or by a drop test. In doing so new information could be obtained as to the shape of the forcing function and a better estimate could be made of the required impulse.

As regards wing vibration excited by the landing impact, it is always possible that the aircraft receives two shocks of the same magnitude timed so that the effects of the second shock add to the effects of the first shock. Fig. 13 shows an example of a wing tip acceleration computed for a symmetric landing and for a single eccentric shock on one wheel. One can deduce easily that when the second shock lags about $t_1/T = 0.35$ behind the first one, the wing tip acceleration on the side of the wheel second to contact becomes larger than the acceleration in the symmetric case.

(*Continued on page 678*)

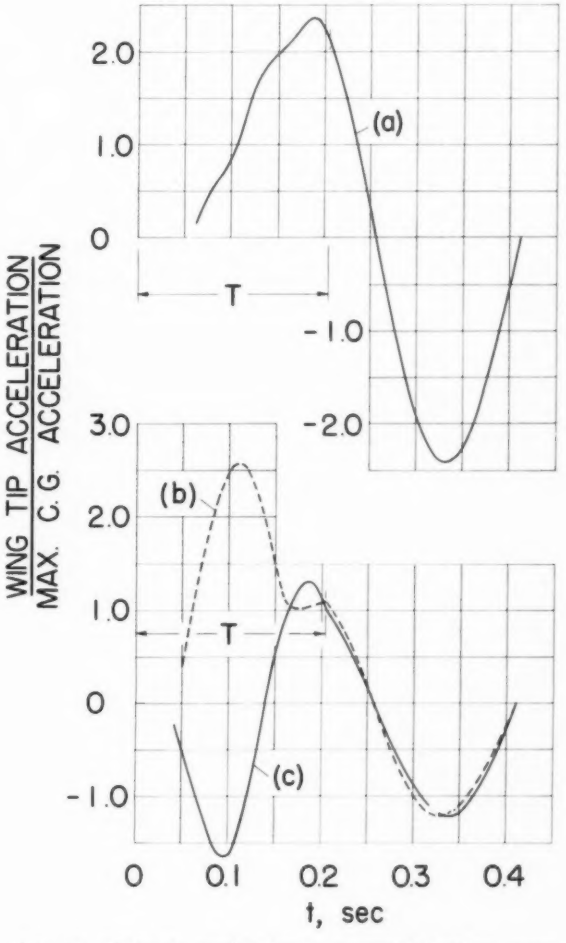

FIG. 13. Wing tip acceleration in symmetric landing, curve (a); wing tip acceleration in asymmetric impact on one gear; on the side of the shock, curve (b); on the opposite side, curve (c).

An Aeroelastic Parameter for Estimation of the Effects of Flexibility on the Lateral Stability and Control of Aircraft

WILLIAM P. RODDEN*
The RAND Corporation

SUMMARY

The importance of the estimation of flexibility effects on the maneuvering performance of an aircraft is known from the losses in lateral control and stability at high speeds.

In this paper an aeroelastic parameter is introduced in a quasi-steady analysis which separates the effects of Mach Number from those of altitude on the lateral motion of a flexible wing. Its use is demonstrated by an application to a wing with one degree of freedom in roll and it is shown that the conventional stability derivatives can be modified to include the steady-state effects of flexibility.

The determination of aileron reversal speed and applications for preliminary design are discussed.

SYMBOLS

P_h = ambient air pressure at altitude, lbs. per sq.ft.
P_0 = ambient air pressure at sea level, lbs. per sq.ft.
M = Mach Number
q = dynamic pressure, lbs. per sq.ft.; $q = 0.7\ P_h M^2$
b = wing span, ft.
S = wing plan-form area, sq.ft.
V = airplane forward velocity, ft. per sec.
p = rolling angular velocity, rad. per sec.
L = rolling moment, ft.lbs.
I_x = rolling moment of inertia, slug-ft.^{2}
δ_a = total aileron deflection, deg.
ϵ = twist at wing tip, deg.
k = ratio of successive twists, defined in Eq. (4)
C_l = rolling moment coefficient, $C_l = L/qSb$
C_{I_x} = inertia coefficient, $C_{I_x} = I_x/qSb$, sec.^{2}
C_{l_δ} = $\partial C_l/\partial \delta_a$
C_{l_p} = $\partial C_l/\partial(pb/2V)$
C_{l_ϵ} = $\partial C_l/\partial \epsilon$
$(\dot{})$ $\equiv d(\ )/dt$

INTRODUCTION

With the increasing speeds of modern airplanes the aerodynamic problems presented by structural deformations have become more and more important. One of the most serious problems encountered has been the loss of lateral control at high speeds. The corresponding losses in lateral stability are also of considerable interest.

In this analysis the assumption of linearity in all aerodynamic coefficients is made which is sufficiently accurate for the low angles of attack encountered in high-speed flight. It is further assumed that the aerodynamic loads are applied slowly with respect to the fundamental period of vibration of the structure so that a quasi-steady analysis may be made—that is, the aircraft as a whole may be considered to follow the laws of rigid body mechanics and the effects of unsteady aerodynamic forces may be neglected.

On the basis of these assumptions the basic stability derivatives may easily be modified to include flexibility effects by the introduction of an aeroelastic parameter denoted by $\partial\epsilon/\partial L$. This parameter is an influence coefficient which allows the separation of the effects of Mach Number from those of altitude on the lateral motion of an aircraft.

DISCUSSION

The effects of flexibility can be included in the one degree of freedom rolling moment equation by the addition of a term of the form $C_{l_\epsilon}\epsilon$. The rolling equation becomes

$$C_{I_x}\dot{p} = C_{l_\delta}\,\delta_a + C_{l_p}\,(pb/2V) + C_{l_\epsilon}\epsilon \qquad (1)$$

The twist at the wing tip, ϵ, can be written as an infinite series of twists;

$$\epsilon = \epsilon_1 + \epsilon_2 + \epsilon_3 + \ldots \qquad (2)$$

in which ϵ_1 is the twist resulting from the applied aerodynamic forces and the wing inertia, ϵ_2 is the twist caused by the load due to ϵ_1, ϵ_3 is caused by the load from ϵ_2, and so on. ϵ_1 can be expressed as a linear combination of the various angles of attack and accelerations.

$$\epsilon_1 = \epsilon_\delta\delta_a + \epsilon_p\,(pb/2V) + \epsilon_{\dot{p}}\,\dot{p} \qquad (3)$$

The twist coefficients are discussed later. If the approximation is made that each succeeding twist is proportional to the preceding one in the series,

$$\epsilon_2/\epsilon_1 = \epsilon_3/\epsilon_2 = \epsilon_4/\epsilon_3 = \ldots = -k \qquad (4)$$

then the series for ϵ becomes a geometric series whose sum is

$$\epsilon = \epsilon_1/(1 + k) \qquad (5)$$

This approximation is justified by the fact that the loads due to aileron, damping-in-roll, rolling inertia, and twist all have similar spanwise distributions and is similar to the approximation made in reference 1.

The twist rolling moment coefficient, $C_{l_\epsilon}\epsilon$, can be expanded as a series of terms corresponding to each twisting mode using Eqs. (3) and (5).

Received May 24, 1955.

* Formerly, Assistant Engineer, Missiles Division. Now, Senior Aerodynamics Engineer, North American Aviation, Inc., Los Angeles, Calif.

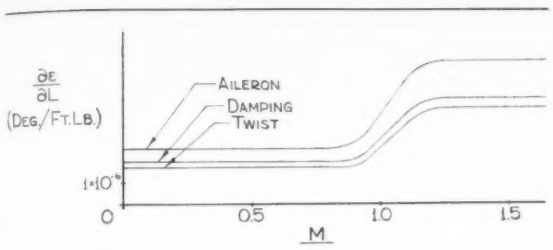

FIG. 1. Typical variations of the aeroelastic parameters of a sweptback wing.

$$C_{l_\epsilon}\epsilon = [1/(1+k)]\,[(C_{l_\epsilon})_\delta \epsilon_\delta \delta_a + (C_{l_\epsilon})_p\,\epsilon_p\,(pb/2V) + (C_{l_\epsilon})_{\dot{p}}\epsilon_{\dot{p}}\,\dot{p}] \quad (6)$$

A mean twisting mode can be used to determine k. For conventional wings with sweptback elastic axes this term is usually positive and of order unity so that an error in $1/(1+k)$ is small compared to an error in k. The rolling moment coefficient due to this mean mode is denoted by $(C_{l_\epsilon})_\epsilon$.

Substituting Eq. (6) into Eq. (1) yields an equation equivalent to the rigid rolling moment equation with modified stability derivatives

$$C_{I_x}'\dot{p} = C_{l_\delta}'\,\delta_a + C_{l_p}'\,(pb/2V) \quad (7)$$

where

$$C_{I_x}' = C_{I_x} - [1/(1+k)]\,(C_{l_\epsilon})_{\dot{p}}\,\epsilon_{\dot{p}} \quad (8)$$

$$C_{l_\delta}' = C_{l_\delta} + [1/(1+k)]\,(C_{l_\epsilon})_\delta\,\epsilon_\delta \quad (9)$$

$$C_{l_p}' = C_{l_p} + [1/(1+k)]\,(C_{l_\epsilon})_p\,\epsilon_p \quad (10)$$

It remains to discuss the form of the coefficients, C_{l_ϵ}, and to derive the twist coefficients ϵ_δ, ϵ_p, $\epsilon_{\dot{p}}$ and an expression for k. The twist rolling moment derivatives, C_{l_ϵ}, are obtained from the spanwise twist variation caused by the corresponding loadings considered as a variable spanwise angle of attack. Various methods are available for these calculations such as the Weissinger method for subsonic speeds and three-dimensional linearized theory for supersonic speeds.

Aeroelastic Parameters

We now define the aeroelastic parameter as $\partial\epsilon/\partial L$. This expression represents the twist at the wing tip corresponding to a unit rolling moment. It is an influence coefficient independent of the magnitude of the applied forces which relates the wing elastic properties to the spanwise distribution of aerodynamic load. For a given wing rigidity it therefore depends only on the load distribution and, hence, is only a function of Mach Number. Since load distributions are fairly constant in the subsonic and supersonic regimes, the variation of the aeroelastic parameter can be found from a subsonic and supersonic value and faired through the transonic region. Fig. 1 shows typical variations of the aeroelastic parameters of a sweptback wing for different loadings. The twist coefficients are obtained from these aeroelastic parameters.

$$\epsilon_\delta = (\partial\epsilon/\partial L_\delta)\,C_{l_\delta}\,qSb \quad (11)$$

$$\epsilon_p = (\partial\epsilon/\partial L_p)\,C_{l_p}\,qSb \quad (12)$$

$$k = -(\epsilon_2/\epsilon_1) = -(\partial\epsilon/\partial L_\epsilon)\,(C_{l_\epsilon})_\epsilon\,qSb \quad (13)$$

The inertia coefficient, $\epsilon_{\dot{p}}$, is merely a constant corresponding to the given rigidity and mass distribution and is the value of tip twist for a unit rolling acceleration. The use of Eqs. (11), (12), and (13) in Eqs. (8), (9), and (10) completely separates the effects of Mach Number from those of altitude—since $q = 0.7\,P_h M^2$—on the stability derivatives of flexible wings.

Calculation of the Aeroelastic Parameters

The basic information required to determine the aeroelastic parameters is both aerodynamic and structural data. The basic aerodynamic data are the spanwise load distribution and the chordwise center of pressure distribution for the aileron and damping-in-roll types of loading for several values of Mach Number sufficient to cover the speed range. The necessary structural data consist of bending and torsional rigidities and a wing weight distribution. The rigidities can be given either as spanwise variations of moments of inertia or as a matrix of structural influence coefficients.

From this information not only the twist at the wing tip can be found but also the spanwise variation of twist for each type of loading. The aeroelastic parameter for each loading is then given as the ratio of wing tip twist to the corresponding rolling moment.

$$\partial\epsilon/\partial L = \epsilon/L \quad (14)$$

As mentioned previously, the twist rolling moment coefficients, C_{l_ϵ}, are calculated from the spanwise variation of twist considered as a variable spanwise angle of attack for each twisting mode by some three-dimensional wing theory. Two-dimensional strip theory could be sufficiently accurate in some cases if appropriate tip corrections were made.

Steady Roll

The steady rolling helix angle is obtained by combining Eqs. (9), (10), (11), (12), and (13) with (7) and setting the rolling acceleration to zero.

$$\left.\begin{aligned}\frac{pb}{2V} &= -\frac{C_{l_\delta}'\,\delta_a}{C_{l_p}'} \\ &= \left(\frac{pb}{2V}\right)_0 \times \\ &\frac{1 + [(\partial\epsilon/\partial L_\delta)\,(C_{l_\epsilon})_\delta - (\partial\epsilon/\partial L_\epsilon)\,(C_{l_\epsilon})_\epsilon]\,qSb}{1 + [(\partial\epsilon/\partial L_p)\,(C_{l_\epsilon})_p - (\partial\epsilon/\partial L_\epsilon)\,(C_{l_\epsilon})_\epsilon]\,qSb}\end{aligned}\right\} \quad (15)$$

Eq. (15) shows the reduction in rolling rate as a function of Mach Number and altitude.

Aileron Reversal Speed

Setting the numerator of Eq. (15) to zero gives the condition for aileron reversal.

$$1 + [(\partial\epsilon/\partial L_\delta)\,(C_{l_\epsilon})_\delta - (\partial\epsilon/\partial L_\epsilon)\,(C_{l_\epsilon})_\epsilon]\,qSb = 0 \quad (16)$$

For a given altitude this is an equation only in Mach

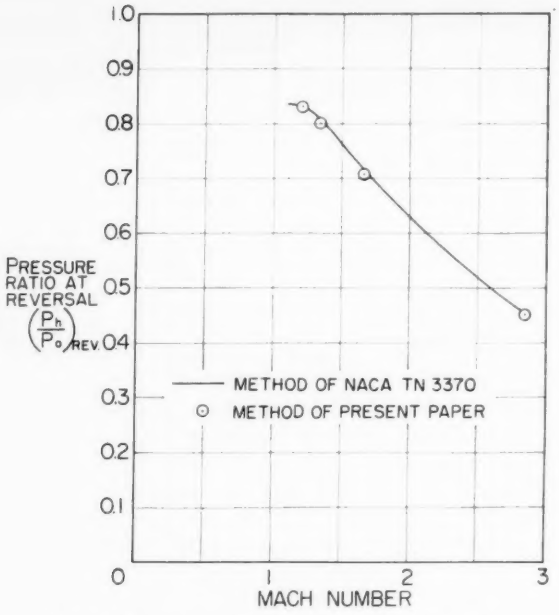

FIG. 2. Pressure ratio at reversal vs. Mach Number.

Number and can be solved for the reversal Mach Number by trial and error. The variation of reversal Mach Number with altitude can then be determined.

APPLICATIONS TO PRELIMINARY DESIGN

For preliminary design purposes, certain approximations can be made to facilitate the estimation of requirements for rigidity to avoid reversal and aileron deflections to provide adequate rates of roll. First, the twisting modes can all be assumed similar. Hence, the twist rolling moment coefficients are approximately equal for each mode.

$$(C_{l_\epsilon})_\delta = (C_{l_\epsilon})_p = (C_{l_\epsilon})_{\dot{p}} = (C_{l_\epsilon})_\epsilon \qquad (17)$$

An extension of this approximation is to assume that not only the modes are similar but are approximately linear functions of span. On this basis the twist rolling moment coefficients can be replaced by the damping-in-roll coefficient. That is, all of the quantities of Eq. (17) can be approximated by C_{l_p}. Variations in C_{l_p} with plan form and Mach Number are given in the literature. Consistent with this extension is the assumption that the spanwise loading distribution due to twist is the same as the damping-in-roll load distribution. From this the aeroelastic parameter for twist is equal to the aeroelastic parameter for damping.

$$\partial\epsilon/\partial L_\epsilon = \partial\epsilon/\partial L_p \qquad (18)$$

The result of these simplifications is to reduce Eq. (15) to the form

$$\frac{pb}{2V} = \left(\frac{pb}{2V}\right)_0 \left\{1 + \left[\frac{\partial\epsilon}{\partial L_\delta} - \frac{\partial\epsilon}{\partial L_p}\right] C_{l_p}\, qSb\right\} \qquad (19)$$

which shows a relatively simple flexibility correction to the rigid rate of roll.

ACCURACY

Reference 2 presents another method for the analysis of this problem based on a Galerkin type procedure. One of its statements is that the results of aileron-reversal calculations provide an adequate test of the accuracy of the method. It also presents a comparison of pressure ratio at reversal ($P_h/P_0 = q_{rev.}/0.7\ P_0M^2$) with an earlier work by the same authors.

An estimate of the accuracy of the present method is made by a comparison with the results of reference 2. The pressure ratio at reversal calculated by each method is shown in Fig. 2 based on the structural and aerodynamic characteristics of Model 2 of reference 2. Since both Models 1 and 2 are straight wings, the second one is chosen because it has a more typical airfoil section. The agreement is seen to be satisfactory.

CONCLUDING REMARKS

The consideration of one degree of freedom given here gives a good approximation of the rolling motion at high speeds where aeroelastic effects are important. The three degree of freedom motion of the aircraft can be analyzed if the additional aeroelastic effects on the wing dihedral and on the vertical stabilizer and fuselage are included. The dihedral effect of a flexible wing is discussed by the author in reference 3. In that note only the effect of wing deflection is considered and wing twist is neglected. The wing twist caused by sideslip also modifies the dihedral effect and can be included in the equations of reference 3 by replacing the rigid damping-in-roll coefficient by the modified value of Eq. (10) of the present paper. The losses in vertical stabilizer effectiveness due to stabilizer and fuselage flexibility can be estimated by any of the longitudinal aeroelastic techniques used for horizontal stabilizer effectiveness. The wing twist caused by rate of yaw and the effect of wing twist on the yawing equation of motion have generally been found to be negligible.

This method offers the advantage of separating the variations of aeroelastic effects with Mach Number and altitude and also separating the estimation of the aeroelastic parameters from the stability derivatives by not imposing restrictions on mode shapes or load estimation techniques. It further allows the application of conventional stability and control analyses using modified stability derivatives.

The reasonably accurate simplifications that can be made in this method indicate its value as a reliable technique for use in preliminary design.

REFERENCES

[1] Benun, D., *A Universal Solution to the Steady State Aeroelastic Problem*, Curtiss-Wright Corp. (Airplane Division) Report No. H49-5, October, 1949.

[2] Hedgepeth, John M., Waner, Paul G., Jr., and Kell, Robert J., *A Simplified Method for Calculating Aeroelastic Effects on the Roll of Aircraft*, NACA TN 3370, March, 1955.

[3] Rodden, W. P., *A Simplified Expression for the Dihedral Effect of a Flexible Wing*, Readers' Forum, Journal of the Aeronautical Sciences, Vol. 22, No. 8, pp. 579–580, August, 1955.

Stability of a Flexible Helicopter Rotor Blade in Forward Flight

YECHIEL SHULMAN*

Massachusetts Institute of Technology

SUMMARY

The problem of the stability of the transient motion in the flapping plane of a flexible helicopter rotor blade in forward flight is considered. The formulation of the problem considers two degrees of freedom—rigid flapping and elastic bending. A new method of determining the transient stability of the motion is developed, using the concept of Stability Number. It is shown that the results obtained by inclusion of the elastic degree of freedom agree with experimental results to a much larger extent than was achieved by analyses neglecting blade flexibility. Numerical solutions of the equations of motion using the M.I.T. "Whirlwind" high-speed computer are given for a number of cases, for both the rigid and the flexible blades.

SYMBOLS

a	= three-dimensional lift curve slope
a_n	= coefficient of cos $n\psi$ in Eq. (18)
b_n	= coefficient of sin $n\psi$ in Eq. (18)
c	= blade chord
c_n	= coefficient of cos $n\psi$ in Eq. (19)
C_1 to C_5	= certain constants, defined in Eq. (16)
d_n	= coefficient of sin $n\psi$ in Eq. (19)
e	= flapping hinge offset
EI	= bending stiffness
F	= external force distribution
g	= acceleration of gravity
I_b	= mass moment of inertia of blade about flapping hinge
L	= lift force per unit span
m	= blade mass distribution
M_r	= rth generalized mass
r	= radial coordinate of blade section
R	= radius of blade
$[SN] = \frac{\kappa}{-\lvert\kappa_{ref}\rvert}$	= Stability Number
t	= time
U	= resultant velocity at blade section
U_P	= velocity component normal to blade section
U_T	= velocity component tangential to blade section
v	= inflow velocity through rotor disc
V	= forward velocity of helicopter
$w = z/R$	= nondimensional vertical coordinate of blade section
$x = r/R$	= nondimensional radial coordinate of blade section
X, Y, Z	= orthogonal reference axes
z	= vertical coordinate of blade section
$\alpha = (\theta + \varphi)$	= angle of attack of blade section
β	= normal coordinate representing flapping angle
$\gamma = \frac{\rho c a R^4}{I_b}$	= Lock's blade mass constant
δ_3	= angle of pitch-flap coupling hinge
ζ	= running variable in direction of r
θ	= blade pitch angle
κ	= exponent of assumed solution
$\lambda = v/\Omega R$	= inflow velocity ratio, positive upward
$\mu = V/\Omega R$	= advance ratio
ξ	= normal coordinate representing bending deflection
ξ_r	= rth normal coordinate
Ξ_r	= rth generalized force
ρ	= air density
φ	= induced angle of attack
$\Phi(r)$	= rth principal mode shape of blade
Φ	= natural mode shape of first bending mode of blade
$\psi = \Omega t$	= blade azimuth position
ω_r	= frequency of rth natural mode
ω	= natural frequency of first bending mode of rotating blade
ω_{NR}	= natural frequency of first bending mode of stationary blade
Ω	= rotor angular velocity

Presented at the Helicopter Dynamics Session, Twenty-Third Annual Meeting, IAS, New York, January 24–27, 1955.

* Research Engineer, Aeroelastic and Structures Research Laboratory.

INTRODUCTION

IT HAS BEEN OBSERVED[1] that the stability of the transient flapping motion of helicopter rotor blades is not constant but varies with the advance ratio of the rotor. The relative transient stability decreases while μ increases until, at some "critical" μ, instability occurs. This flapping instability is an important problem from the practical standpoint for a helicopter operating in an unloaded rotor condition.

Various authors, notably Glauert and Shone,[2] Bennett,[3] Horvay,[4] Parkus,[5] and Hohenemser,[1] have tackled this problem. Their simplifying assumptions and methods differed so that, in some early papers, contradictory conclusions were reached.[2, 3] Investigations conducted since World War II[1, 4, 5] have reached the same basic conclusion—namely, that a decrease in relative transient stability occurs with high μ. However, a significant difference still exists between the theoretical predictions and the experimental findings of "critical" μ for various values of γ, the blade mass constant.

All past investigations have had one common underlying assumption—the blade is infinitely rigid. No allowance has been made for the blade's flexibility in bending and/or in torsion. Lately, opinions were raised that the blade bending and torsional elasticities may have a significant effect on the flapping stability—i.e., that the problem is aeroelastic in nature. The present investigation is an attempt to bring the problem into the realm of aeroelasticity—i.e., to include elastic

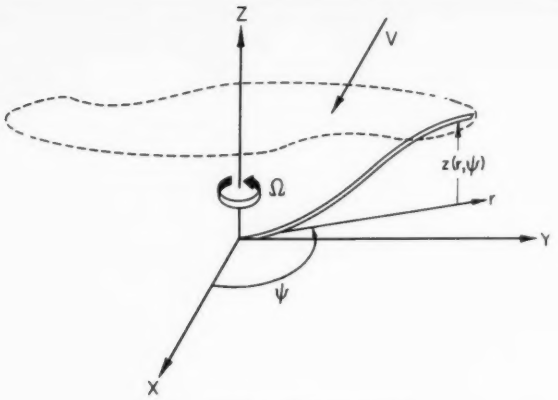

FIG. 1. Blade coordinate system.

effects; hence, the methods of structural dynamics are used to formulate the problem. This approach is contrary to that of the previous investigations, where a single equation of motion was derived using the methods of rigid-body dynamics. To the best of the author's knowledge, the following paper is the first such analysis, and, therefore, it is to be regarded as a preliminary investigation rather than a complete work.

DISCUSSION

A helicopter rotor, moving at a forward speed V experiences alternating aerodynamic moments because of the difference between the resultant velocities of the advancing and retreating blades. In an articulated rotor, the blades are hinged at the rotor shaft in such a manner as to allow them to flap out of the rotor plane. By this means, no moments are transmitted to the shaft.

Control of the blades is effected by varying the collective and cyclic pitch of the blades. In some rotors, a coupling between flapping and pitching is afforded by a cocked (at a δ_3 angle) flapping hinge. In this analysis, however, no pitch-flap coupling is included. The blade is considered free to flap in a plane passing through the rotor shaft and perpendicular to the XY plane. It moves so as to reach equilibrium at all values of the azimuth position ψ. This condition of equilibrium is expressed by the requirement that the sum of the moments about the flapping hinge shall vanish. Using D'Alembert's principle, these moments are Inertia moment, Centrifugal moment, Gravity moment, and Lift moment. When the assumption of rigid blades is discarded and blade flexibility is introduced, the number of degrees of freedom of the blade is essentially increased to infinity. This is so because the blade is a continuous beam which has an infinite number of vibration modes both in bending and in torsion. However, in order to simplify the analysis and make it manageable within the limited scope of this investigation, only one vibration degree of freedom is added—namely, the first natural bending mode of the blade.

Since the introduction of blade bending means crossing the boundary into the aeroelastic domain, methods of analysis used in structural dynamics are utilized to derive the equations of motion. Specifically, this means use of normal equations of motion in normal coordinates.

It should be noted that, by starting out with the bending moment equation for a rotating blade,[6]

$$EI\frac{\partial^2 z(r)}{\partial r^2} = \int_r^R \left(\left\{ L(\zeta) - m(\zeta)\left[g + \frac{\partial^2 z(\zeta)}{\partial t^2} \right] \right\} \times [\zeta - r] - m(\zeta)\zeta\Omega^2[z(\zeta) - z(r)] \right) d\zeta \quad (1)$$

Then, by assuming z, the blade deflection, to be composed of the sum of the blade's natural modes and by using the orthogonality relations between these modes, the same two equations that are derived below could be obtained. Essentially, the same is done in the ensuing analysis, only it is simplified by use of results already known from the theory of free vibrations in normal coordinates.

A list of assumptions on which the analysis is based is now in order:

Physical conditions:

(1) Blade is untwisted and untapered. (θ, c are constant.)
(2) Blade mass distribution m is constant.
(3) Blade is infinitely rigid in torsion.
(4) Flapping hinge is perpendicular to shaft and is located on center of rotation. ($\delta_3 = e = 0$.)

Operating conditions:

(5) Angular velocity of rotor Ω is constant.
(6) Forward velocity V is constant.

Aerodynamic conditions:

(7) Induced velocity through rotor disc λ is constant over the disc.
(8) Radial flow is neglected.
(9) Lift force is quasi-stationary. Apparent mass effects are neglected.
(10) All angles are small.
(11) Lift coefficient slope a is constant.
(12) Effect of reversed flow region is neglected.

Of all the assumptions, the last three are the least accurate, especially when high-advance ratios are to be considered. However, introduction of reverse-flow effects and blade stall complicates the expressions appreciably. Since this paper is of an exploratory nature only, these factors are left out.

ANALYSIS

Equilibrium Equations

The equations of motion of the system are derived by considering the deflection of a blade section relative

to a system of orthogonal reference axes fixed to the helicopter with their origin at the hub. The axis system is shown in Fig. 1. The Z axis is along the rotor shaft positive up; the X axis is horizontal so that the axes form a right-hand system. The location of a blade section is best described by a system of cylindrical coordinates, where, at any time t, r denotes radial distance measured from the hub in the XY plane, $\psi = \Omega t$ denotes angular displacement measured from the X axis, and z denotes displacement of a blade section from the XY plane.

The forces per unit span acting on a blade section are resolved in Z and r (vertical and radial) directions and are shown in Fig. 2. Using assumption (10) of small angles, they are:

External Forces

(a) In Z direction
lift force $= L(r, t)$
gravity force $= -m(r)g$

(b) In r direction—none

Inertia Forces

(a) In Z direction

$$\text{inertia force} = -m(r)\frac{\partial^2 z(r, t)}{\partial t^2}$$

(b) In r direction
centrifugal force $= m(r)r\Omega^2$

Since all functions of time are periodic, the relations

$$\psi = \Omega t \qquad d\psi = \Omega\, dt \tag{2}$$

are used to transform derivatives with respect to time (t) to derivatives with respect to azimuth angle (ψ). The coordinates r and z are now nondimensionalized by dividing them by R, the blade radius; thus

$$x = r/R \qquad w(x, \psi) = [z(r, t)]/R \tag{3}$$

The blade displacement w is assumed to consist of the sum of two of its principal modes:

$$w(x, \psi) = \sum_{r=1}^{2} \Phi^{(r)}(x)\xi_r(\psi) \tag{4}$$

where

$\Phi^{(1)}(x) = x$ = rigid body mode shape
$\Phi^{(2)}(x) = \Phi(x)$ = first normalized natural bending mode shape
$\xi_1(\psi) = \beta(\psi)$ = normal coordinate for rigid body mode
$\xi_2(\psi) = \xi(\psi)$ = normal coordinate for first elastic bending mode

The bending mode shape Φ is normalized on its value at the blade tip ($x = 1$)—i.e., $\Phi(1) = 1$.

Strictly, the deflection w is composed of the sum of an infinite number of natural mode shapes, both in bending and in torsion, the amplitude of each being given by ξ_r. However, as stated above, just one vibration mode is included in this analysis. In more precise analyses, additional modes may be included, notably

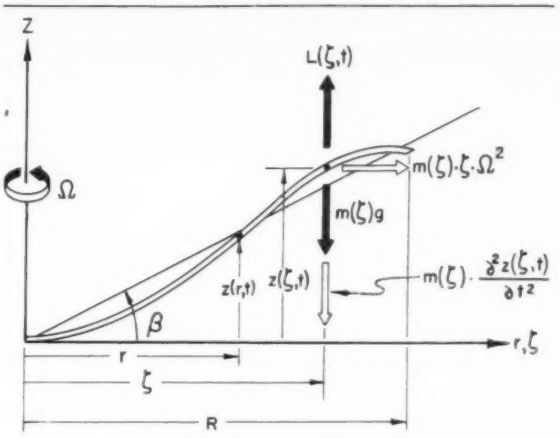

FIG. 2. Force diagram.

first torsion mode. It is self-evident that this will increase the complexity of the problem.

The normal equations of motion are

$$M_r(d^2\xi_r/dt^2) + M_r\omega_r^2\,\xi_r = \Xi_r \tag{5}$$

where

$M_r = \int_0^1 m(x)[\Phi^{(r)}(x)]^2\, R\, dx$ = generalized mass of the rth mode
ω_r = frequency of rth mode
$\Xi_r = \int_0^1 F(x, \psi)\Phi^{(r)}(x)\, dx$ = generalized force of rth mode
$F(x, \psi) = L(x, \psi) - m(x)g$ = external force in Z direction

Since $r = 1, 2$, there are two equations of motion.

Eq. (5) defines the response of the rth mode of motion to an applied force $F(x, \psi)$. If the external force $F(x, \psi)$ is independent of the motion, the equations for the two modes are uncoupled, but, as in this case, if $F(x, \psi)$ is dependent on the motion, then the two equations of motion are coupled and have to be solved simultaneously.

Evaluating the quantities M_r, Ξ_r, the equations of motion are obtained:

$$\ddot{\beta} + \beta = \frac{3}{mR\Omega^2}\int_0^1 L(x, \psi)x\, dx - \frac{3g}{2R\Omega^2} \tag{6}$$

$$\ddot{\xi} + \left(\frac{\omega}{\Omega}\right)^2 \xi = \left\{1 \Big/ \left[mR\Omega^2\int_0^1 [\Phi(x)]^2\, dx\right]\right\} \times \left[\int_0^1 L(x, \psi)\Phi(x)\, dx - mg\int_0^1 \Phi(x)\, dx\right] \tag{7}$$

(A dot denotes differentiation with respect to ψ.)

The lift per unit span in the Z direction is

$$L = a\alpha(\rho/2)cU^2\cos\varphi \tag{8}$$

where

a = average lift coefficient slope over blade
α = local angle of attack

ρ = air density
c = blade chord
U = local resultant velocity
$\cos\varphi$ = U_T/U
$\alpha \simeq \sin\alpha$ = $\sin(\theta + \varphi)$

Then

$$\left.\begin{aligned} L &= (\rho/2)ac\sin(\theta+\varphi)UU_T \\ &= (\rho/2)ac(U_T^2\sin\theta + U_PU_T\cos\theta) \end{aligned}\right\} \quad (9)$$

Following assumption (10),

$$L = (\rho/2)ac(\theta U_T^2 + U_PU_T) \quad (10)$$

The expressions for the velocity components are

$$U_T = \Omega r + V\sin\psi = \Omega R(x + \mu\sin\psi) \quad (11)$$

$$U_P = v - \frac{\partial z}{\partial t} - \frac{\partial z}{\partial r}V\cos\psi = \Omega R(\lambda - \dot{w} - w'\mu\cos\psi) \quad (12)$$

(A prime denotes differentiation with respect to x.) Substituting Eqs. (4), (11), and (12) into Eq. (10), the expression for the lift finally becomes

$$L(x, \Phi, \beta, \xi, \psi) = (\rho/2)ac(\Omega R)^2\{\theta[x + \mu\sin\psi]^2 + [x + \mu\sin\psi][\lambda - x\dot{\beta} - \Phi\dot{\xi} - (\beta + \Phi'\xi)\mu\cos\psi]\} \quad (13)$$

Note that the lift force is dependent on the motion (β and ξ appear in the expression); therefore, as stated above, the two equations of motion will be coupled and will have to be treated and solved simultaneously.

On the right-hand side of the equations of motion the lift force is multiplied by the natural mode shapes x, Φ and is integrated over the blade. Since the lift is a function of the motion, and thus of the mode shapes, the integral will contain terms composed of products of the mode shapes. Since these are natural modes, they are orthogonal to each other. This orthogonality condition between the natural mode shapes, for constant mass distribution, is expressed as

$$\int_0^1 \Phi(x)x\,dx = 0 \quad (14)$$

Substituting Eq. (13) into Eqs. (6) and (7), using Eq. (14), and transposing, the equations of motion of the system are obtained:

$$\ddot{\beta} + \frac{\gamma}{8}\left[1 + \frac{4}{3}\mu\sin\psi\right]\dot{\beta} + \left[1 + \frac{\gamma}{6}\mu\cos\psi + \frac{\gamma}{8}\mu^2\sin 2\psi\right]\beta + \frac{\gamma}{2}C_2\ddot{\xi} + \left[\frac{\gamma}{2}C_5\mu\cos\psi + \frac{\gamma}{4}C_6\mu^2\sin 2\psi\right]\xi = \frac{\gamma}{8}\left\{\theta[1+\mu^2] + \frac{4}{3}\lambda + \left[\frac{8}{3}\theta + 2\lambda\right]\mu\sin\psi - \theta\mu^2\cos 2\psi\right\} - \frac{3g}{2R\Omega^2} \quad (15)$$

$$\ddot{\xi} + \frac{\gamma}{8}\left[\frac{4C_4}{3C_3} + \frac{4}{3}\mu\sin\psi\right]\dot{\xi} + \left[\frac{\omega^2}{\Omega^2} + \frac{\gamma}{6}\frac{C_8}{C_3}\mu\cos\psi + \frac{\gamma}{8}\frac{2C_7}{3C_3}\mu^2\sin 2\psi\right]\xi + \frac{\gamma}{6}\frac{C_2}{C_3}\ddot{\beta} + \left[\frac{\gamma}{12}\frac{C_1}{C_3}\mu^2\sin 2\psi\right]\beta = \frac{\gamma}{8}\left\{\theta\left[\frac{4}{3}\frac{C_2}{C_3} + \frac{2}{3}\frac{C_1}{C_3}\mu^2\right] + \frac{4C_1}{3C_3}\lambda\mu\sin\psi - \frac{2C_1}{3C_3}\theta\mu^2\cos 2\psi\right\} - \frac{C_1 g}{C_3R\Omega^2} \quad (16)$$

where $\gamma = (\rho acR^4)/I_b$

and

$$C_1 = \int_0^1 \Phi\,dx \qquad C_4 = \int_0^1 \Phi^2 x\,dx \qquad C_7 = \frac{1}{2}(C_5)^2$$

$$C_2 = \int_0^1 \Phi x^2\,dx \qquad C_5 = \Phi(1) = 1 \qquad C_8 = \frac{1}{2}[(C_5)^2 - C_3]$$

$$C_3 = \int_0^1 \Phi^2\,dx \qquad C_6 = C_5 - C_1$$

are constants dependent on the mode shape in bending.

The two equations of motion, Eqs. (15) and (16), are a set of simultaneous linear ordinary differential equations in β and ξ with periodic coefficients, of period 2π. The general solution to this class of differential equations cannot be expressed in closed form and in terms of the constants of the equation.[7] Furthermore, the techniques available when dealing with a single equation of this form, such as were used by Horvay[4] and Parkus,[5] have not yet been extended to a treatment of a set of simultaneous equations. One could eliminate one of the variables by careful pre- or post-multiplication of the differential operators; but then one would end up with a fourth-order differential equation with highly complex variable coefficients, in only one variable, say β, whose solution cannot be easily obtained either. Since a mathematical treatise on the theory of sets of equations with periodic coefficients is not the purpose of this work, a relatively simple solution is assumed so that some engineering results can be obtained.

In order to determine the values of the constants C_i ($i = 1, 2, \ldots 8$), the mode shape Φ must be known as a function of x. Since this is a hinged blade, one must use the expression for the first bending mode shape of a hinged, rotating beam with constant properties. However, an expression that closely approximates the actual mode shape may also be used without losing much accuracy. The chosen expression must also be orthogonal to x, the rigid-body mode, and must be normalized on its value at $x = 1$. An expression that satisfies all these requirements is

$$\Phi(x) = x - (\pi/3) \sin \pi x \tag{17}$$

This expression, then, is used to determine the C_i's.

Analytical Solution

The equations of motion as obtained contain a forcing function dependent on the parameters of the blade and on μ and ψ. This function, which appears on the right-hand side of the equations, determines the steady-state response of β and ξ. This response is usually assumed to be a Fourier expansion in ψ. However, when the blade motion is started or is disturbed by an external source, such as a gust or a sudden variation in pitch, a free motion of the blade is superimposed on the steady-state motion. The stability of this transient motion is of concern here. Since the equations are linear, the transient solution is obtained by letting the right-hand side of Eqs. (15) and (16) vanish and solving for β and ξ from the homogeneous equations. If the coefficients of the equations were constant, this would be a simple matter since the methods of operational calculus are available for such cases. Here, as mentioned above, one could also use operational methods to eliminate one of the variables from the equations and to obtain an equation in a single variable; however, no visible advantage is gained thereby. Another approach is to try and predict the form of the solution as best possible and substitute the assumed solution into the equations, thus obtaining algebraic expressions for the constants of the solution containing the parameters of the equations. When these expressions are satisfied (for certain values of the constants), then the assumed solution is a solution of the equations.

Since the solution sought is a transient solution to a set of equations with periodic coefficients, a logical assumption in this case is one of the form

$$\beta = e^{\kappa\psi} \sum_{n=1}^{\infty} (a_n \cos n\psi + b_n \sin n\psi) \tag{18}$$

$$\xi = e^{\kappa\psi} \sum_{n=1}^{\infty} (c_n \cos n\psi + d_n \sin n\psi) \tag{19}$$

Upon substitution of these expressions for the variables β and ξ into the equations of motion, the expressions that are obtained are for κ, a_n, b_n, c_n, d_n, in terms of γ and μ.

The absolute stability of the system is determined by the sign of κ.

When $\kappa < 0$, the system is absolutely stable.

When $\kappa > 0$, the system is absolutely unstable.

The relative stability, on the other hand, is determined by the Stability Number $[SN]$, which is defined as $[SN] = (\kappa/-|\kappa_{ref}|)$, κ_{ref} being chosen arbitrarily, depending on the nature of the problem. (See reference 8 for a complete discussion of the concept of Stability Number.)

When $[SN] = 1$, the system has a complete relative stability.

When $0 < [SN] < 1$, the system is relatively partially destabilized.

When $[SN] < 0$, the system is absolutely and relatively unstable.

Strictly, in the assumed solutions, Eqs. (18) and (19), n should extend to infinity. However, the choice of the number of harmonics retained in the expansion is contingent upon the nature of the equations and practical expedience. When a choice is made and a result obtained, a refinement to this result may be achieved by adding another harmonic. Comparing successive results, one may determine the number of harmonics required for a given level of accuracy in the results.

Since the first and second harmonics of the trigonometric functions in ψ only appear in the equations of motion, one is led, as a first step, to choose the first two harmonics in the Fourier expansion also, assuming rapid convergence. However, such a choice results in a formidable 8×8 determinant; therefore, for practical considerations, the assumed solutions are

$$\beta = e^{\kappa\psi}(a_1 \cos \psi + b_1 \sin \psi) \tag{20a}$$

$$\xi = e^{\kappa\psi}(c_1 \cos \psi + d_1 \sin \psi) \tag{20b}$$

It can be easily seen that this assumption results in a neglect of those terms in the equations which are proportional to μ. Substituting Eqs. (20a) and (20b) into the "homogenized" Eqs. (15) and (16) and recognizing that, in order for the relations to hold at any value of ψ, all coefficients of the various trigonometric functions ($\sin \psi$, $\cos \psi$) should vanish, one obtains a set of four linear homogeneous algebraic equations in the constants a_1, b_1, c_1, d_1 (two for each equation of motion). In order for a nontrivial solution to exist, the following determinant of the coefficients of a_1, b_1, c_1, d_1 must vanish.

$$\begin{vmatrix}
\kappa^2 + \frac{\gamma}{8}\kappa & 2\kappa + \frac{\gamma}{8} + \frac{\gamma}{16}\mu^2 & \frac{\gamma}{2}C_2\kappa & \frac{\gamma}{2}C_2 + \frac{\gamma}{8}C_6\mu^2 \\
-2\kappa - \frac{\gamma}{8} + \frac{\gamma}{16}\mu^2 & \kappa^2 + \frac{\gamma}{8}\kappa & -\frac{\gamma}{2}C_2 + \frac{\gamma}{8}C_6\mu^2 & \frac{\gamma}{2}C_2\kappa \\
\frac{\gamma}{6}\frac{C_2}{C_3}\kappa & \frac{\gamma}{6}\frac{C_2}{C_3} + \frac{\gamma}{24}\frac{C_1}{C_3}\mu^2 & \kappa^2 + \frac{\gamma}{6}\frac{C_4}{C_3}\kappa + \left(\frac{\omega^2}{\Omega^2} - 1\right) & 2\kappa + \frac{\gamma}{6}\frac{C_4}{C_3} + \frac{\gamma}{24}\frac{C_7}{C_3}\mu^2 \\
-\frac{\gamma}{6}\frac{C_2}{C_3} + \frac{\gamma}{24}\frac{C_1}{C_3}\mu^2 & \frac{\gamma}{6}\frac{C_2}{C_3}\kappa & -2\kappa - \frac{\gamma}{6}\frac{C_4}{C_3} + \frac{\gamma}{24}\frac{C_7}{C_3}\mu^2 & \kappa^2 + \frac{\gamma}{6}\frac{C_4}{C_3}\kappa + \left(\frac{\omega^2}{\Omega^2} - 1\right)
\end{vmatrix} = 0 \tag{21}$$

Evaluating the integrals appearing in Eq. (16), the following values for the C_i's, as they appear in the stability determinant, are obtained:

$$\begin{array}{llll} C_2 = 0.05 & C_6 = 1.10 \\ C_1/C_3 = -0.80 & C_2/C_3 = 0.25 \\ C_4/C_3 = 0.60 & C_7/C_3 = 2.50 \end{array} \tag{22}$$

The ratio $(\omega/\Omega)^2$, which is the ratio of the natural frequency of the first bending mode of a hinged, rotating blade with constant properties to the angular velocity of the blade, is given[9] as

$$(\omega/\Omega)^2 = (\omega_{NR}/\Omega)^2 + 6.05 \tag{23}$$

where ω_{NR} = natural frequency of the first bending mode of the nonrotating blade.

The value of (ω_{NR}/Ω) depends on the geometrical and elastic properties of the blade.

For a typical rotor blade under normal operating conditions, the value of $(\omega_{NR}/\Omega)^2$ equals 0.95; then,

$$(\omega/\Omega)^2 = 0.95 + 6.05 = 7.00 \tag{24}$$

Upon substitution of Eqs. (23) and (24) into the stability determinant, Eq. (21), expanding it, and collecting terms with equal powers of κ, the final eighth-order characteristic equation is obtained

$$\begin{aligned} &\kappa^8 \\ &+ \kappa^7[0.450\gamma] \\ &+ \kappa^6[0.0735416\gamma^2 + 20.0] \\ &+ \kappa^5[0.00515624\gamma^3 + 6.90\gamma] \\ &+ \kappa^4[0.000131293\gamma^4 + 0.796875\gamma^2 - 0.00559039\gamma^2\mu^4 + 100.0] \\ &+ \kappa^3[0.0326562\gamma^3 + 0.00020049\gamma^3\mu^4 + 23.40\gamma] \\ &+ \kappa^2[0.000262656\gamma^4 + 0.000047591\gamma^4\mu^4 + 1.60667\gamma^2 - 0.0142365\gamma^2\mu^4 + 144.0] \\ &+ \kappa[0.02750\gamma^3 + 0.062604\gamma^3\mu^4 + 18.0\gamma] \\ &+ [0.000131293\gamma^4 + 0.000047591\gamma^4\mu^4 + 0.000123072\gamma^4\mu^8 + 0.56250\gamma^2 - 0.140625\gamma^2\mu^4] = 0 \end{aligned} \tag{25}$$

The coefficients in Eq. (25) are functions of γ and μ; therefore, the roots of the equation depend on the values of γ and μ. Physically, this means that the stability of the blade motion varies with changes in μ and/or γ. It is well known that, for polynomials of order larger than four, the roots cannot be obtained in terms of the coefficients. It is, therefore, necessary to resort to approximate methods of factoring in order to obtain the roots of this polynomial. Lin's method may be used to factor out a real root or a pair of conjugate complex roots for a particular combination of γ and μ. However, the roots so obtained are the closest to the imaginary axis in the complex plane; they are not the most positive ones. Hitchcock's method affords another way of factoring high-order polynomials. However, since the purpose of this analysis is to determine the (relative) stability of the motion, it is the most positive root (or real part of a complex root) of the characteristic equation that is of importance since it characterizes the stability of the solution. A method of obtaining the most positive root for each combination of γ and μ in the characteristic equation is by the use of the Routh-Hurwitz criteria for positive roots in conjunction with the Polynomial Transformation theorem. By employing this method, the magnitude and sign of the most positive root in each case is obtained. Use is then made of the concept of Stability Number of the Equation to measure the relative degree of stability of equations with different values of γ and μ.

Computations were carried out by the "Whirlwind" high-speed electronic digital computer at M.I.T. for four values of γ (γ = 4, 10, 13, 16) which span the entire range of γ's characteristic to current helicopters; the results are shown in Fig. 3 which is a plot of $[SN]$ vs. μ for different values of γ. The value of κ_{ref} is chosen as the most stable of all vlaues of κ found—namely, for the case of γ = 16, μ = 0, where its value is -0.758.

Numerical Integration

The method described above for solution of the differential Eqs. (15) and (16) is a rather crude one. A much more exact solution can be obtained by numerical integration of the equations. This method is feasible, however, only when high-speed computing devices are available since the amount of arithmetic computation is very large. A machine capable of performing these integrations economically is the M.I.T. high-speed electronic digital computer "Whirlwind" which was used in this case.

Eqs. (15) and (16) were integrated, using the fourth-order Runge-Kutta method, for various γ and μ combinations. So that the results of the two degrees of freedom (flexible) case could be compared with the single degree of freedom (rigid) case, Eq. (15), the flapping equation, with the ξ variable omitted, was also integrated using the same method and the same $\Delta\psi$ increment (15°). As a matter of interest, it should be noted that the time required for the step-by-step

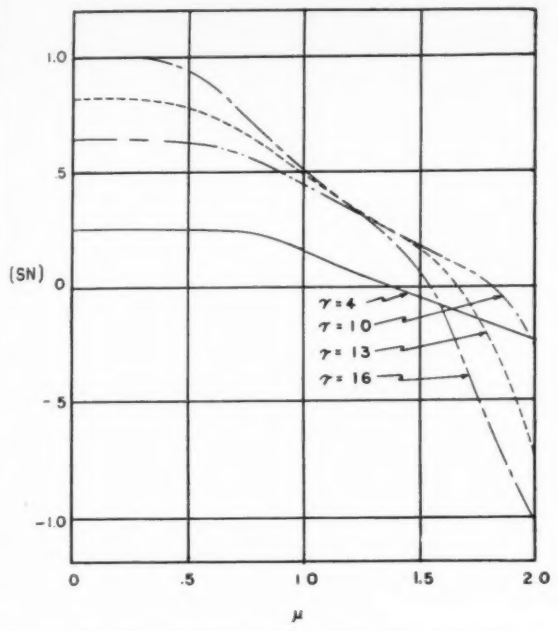

FIG. 3. Stability Number vs. advance ratio at various values of γ.

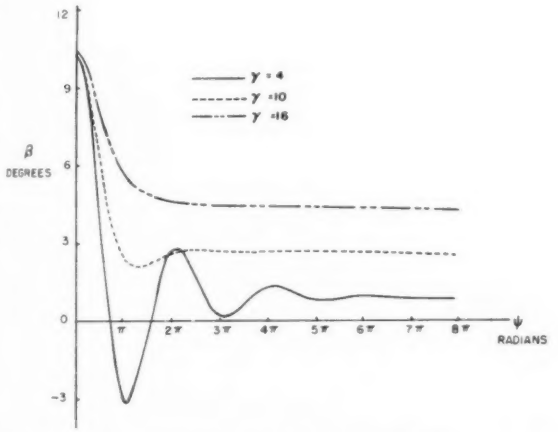

FIG. 4. Digital computer results of blade flapping at $\mu = 0$ (hovering) for $\gamma = 4, 10, 16$ (two degrees of freedom).

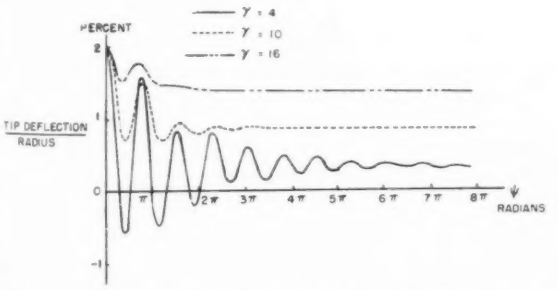

FIG. 5. Digital computer results of elastic tip deflection at $\mu = 0$ (hovering) for $\gamma = 4, 10, 16$.

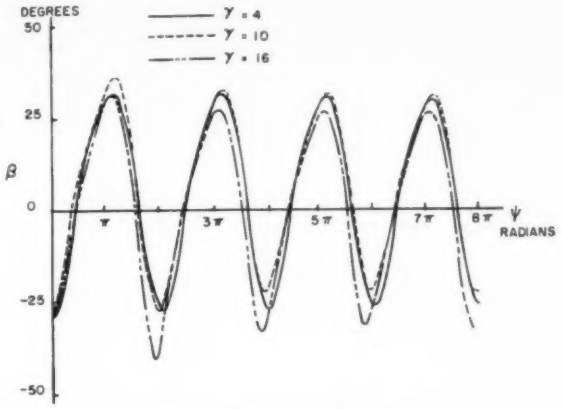

FIG. 6. Digital computer results of blade flapping at $\mu = 1.0$, for $\gamma = 4, 10, 16$ (two degrees of freedom).

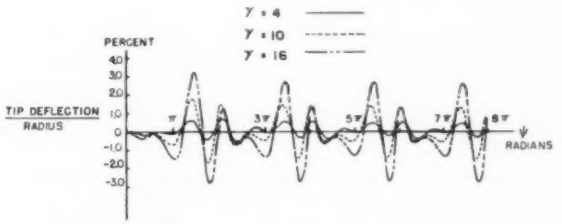

FIG. 7. Digital computer results of elastic tip deflection at $\mu = 1.0$, for $\gamma = 4, 10, 16$.

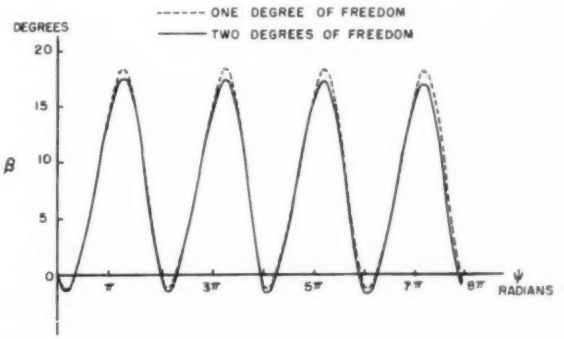

FIG. 8. Comparison of digital computer results of blade flapping at $\mu = 0.5$, for $\gamma = 16$.

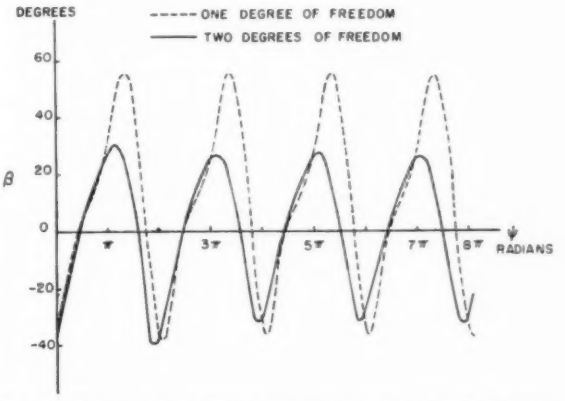

FIG. 9. Comparison of digital computer results of blade flapping at $\mu = 1.0$, for $\gamma = 16$.

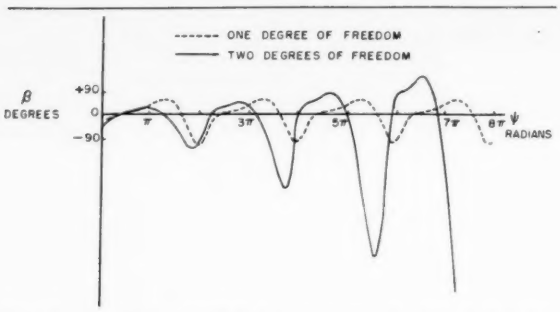

FIG. 10. Comparison of digital computer results of blade flapping at $\mu = 1.2$, for $\gamma = 16$ (stability limit).

calculations was approximately 1 sec. per azimuth position, so that, for a typical run of 96 steps ($0 \leq \psi \leq 8\pi$), it took approximately $1^1/_2$ min. to obtain the time history of β and ξ. The results were plotted directly by the computer on the screen of an oscilloscope, and a photograph of the two curves was obtained.

The results of the calculations are shown in Figs. 4–10. Figs. 4 and 5 show β and ξ, respectively, for the hovering case. It is evident that γ in this case is a damping factor. Figs. 6 and 7 show the same variables for the case of $\mu = 1.0$. The motion is stable with β little affected by γ, whereas an interesting result is seen for ξ—the lower the γ, the smaller the amplitude. The predominant frequency is three per rev. Fig. 8 shows the comparison of the β motion, for $\mu = 0.5$, as calculated from the rigid case and the flexible case. In Fig. 9, the same is shown for $\mu = 1.0$. It is seen that the difference in the β motion is largest for the higher μ. It should be noted, of course, that the large amplitudes in both cases indicate that the small angle assumption should be revised in future calculations. This means that the equations would be nonlinear with variable coefficients so that numerical methods only could be used for their solution. Fig. 10 shows the motion of β for the two cases for $\mu = 1.2$. It is seen that, for the flexible case β diverges, whereas for the rigid case the motion is stable.

CONCLUSIONS

From Fig. 3 it is clearly seen that, for values of μ smaller than 1.0, relative stability decreases for decreasing values of γ. Since in this region γ is essentially an aerodynamic damping term, this seems plausible. On the other hand, for μ greater than the "critical" μ, the interesting fact is that greater relative stability results from smaller γ. The physical reasoning behind this might possibly be that, for larger advance ratios, γ ceases to play the role of a damping coefficient as it did for the hovering and low μ cases and becomes a destabilizing factor.

Fig. 3 establishes the fact that the region of instability is reached at values of μ between 1.5 and 1.8, depending on γ. This result compares favorably with the result obtained experimentally,[1] which showed that, for $\gamma = 5.0$, instability occurred at μ between 1.5 and 1.6. Although in that particular case a δ_3 angle was included, it is safe to assume that the "critical" μ is in the same region as obtained here for a wide range of γ, as is borne out by Fig. 3.

The analyses presented previously[4, 1] had predicted instability at values of μ greater than 2.0.

Hence, it can safely be stated that a prediction of "critical" μ's based on the approximate analysis outlined in this paper will compare with experimental values closer than any of the previous methods developed thus far. A comparison of the results for the "critical" μ obtained by the approximate theoretical analysis with the one obtained from the numerical integration indicates a difference of 25 per cent.

It might be added that the constant relative stability zone as obtained here is stretched over a wider range of μ, for the higher γ, than was obtained previously. However, for the lower γ, relative stability starts to decrease at a lower μ than was predicted previously.

The following conclusions may be drawn from the results obtained here:

(1) The most important—elastic deformation of the blade appreciably affects the stability of the flapping motion.

(2) For helicopters operating at a range of μ up to 1.0 (true of all current models), a choice of a higher γ will result in greater transient stability. For μ greater than 1.0, this statement may have to be qualified.

(3) Except for the parameters assumed constant in this analysis (θ, λ, etc.) and those that did not enter into the analysis owing to the simplifying assumptions (δ_3, chordwise *CG* and *EA* locations, torsional stiffness, etc.), the most important parameter affecting stability is γ, the blade mass constant.

(4) The type of analysis employed in this work—namely, one using normal coordinates—is perfectly suitable for this problem since it eliminates inertia and elastic coupling among the various modes which otherwise may turn out to be quite complex.

CONCLUDING REMARKS

Since this work is of an exploratory nature, it just illustrates a method which may be followed by more precise analyses. Refinements may be added in the setting up of the equations, and ways may be sought to facilitate and speed up their solution.

The refinements are:

(1) Inclusion of at least one torsion mode, and also, perhaps, one or two more bending modes, especially those that have proved to be excited by blade vibrations. A preliminary investigation has shown that the torsional mode affects the results appreciably.

(2) Revision of assumptions (10), (11), and (12) to include reverse flow and blade stall effects, thus lending more authority to results for high advance ratios.

(3) Revision of the assumptions of constant induced velocity and blade twist.

(*Continued on page 693*)

The Compressible Flow Past an Oscillating Airfoil in a Wind Tunnel

JOHN W. MILES*

University of California, Los Angeles

SUMMARY

The disturbance produced by an oscillating airfoil in a two-dimensional supersonic wind tunnel is exhibited explicitly in terms of image fields and guided waves. The corresponding subsonic problem leads to an integral equation, the kernel of which is expanded in guided waves. The supersonic results are applied to the calculation of the longitudinal stability derivatives associated with a low-frequency pitching oscillation. It is pointed out that the guided wave formulation may be of some interest in the analysis of cascades of airfoils.

SYMBOLS

A = tunnel aspect ratio; see Eq. (4.6)
B = $(M^2 - 1)^{1/2}$
J_0 = Bessel function of first kind and order zero
L = Laplace transform operator; see Eq. (3.1)
M = Mach Number = U/a_0
N = the largest integer smaller than A^{-1}; see Eq. (7.14)
$\mathrm{R}\{\ \}$ = denotes real part of $\{\ \}$
U = speed of undisturbed flow
a_0 = speed of sound in undisturbed flow
b = height of wind tunnel
c = wing chord and characteristic length
c_l = lift coeficient = lift/$(1/2)\rho_0 U^2 c$
c_m = moment coefficient = moment/$(1/2)\rho_0 U^2 c^2$
e = base of natural logarithms
g = influence function for potential; see Eqs. (3.7) and (3.8)
h = modified influence function for pressure jump; see Eqs. (3.11) and (3.12)
i = imaginary unit
k = reduced frequency (based on wing chord) = $\omega c/U$
m = Ackeret lift curve slope = $4B^{-1}$
p = perturbation pressure
s = Laplace transform spectrum parameter
$\mathrm{sgn}\ y$ = ± 1 as $y \gtrless 0$
t = time
$u_n^{\pm}$ = group velocity of nth mode, downstream $(+)$ or upstream $(-)$
$v_n^{\pm}$ = phase velocity of nth mode, downstream $(+)$ or upstream $(-)$
x = dimensionless (with respect to c) streamwise coordinate; see Fig. 1
y = dimensionless (with respect to c) transverse coordinate; see Fig. 1
y_1 = see Eq. (2.10b)
Γ = Fourier transform of γ
Φ = Fourier transform of φ
α = complex amplitude of incidence; see Eq. (2.1)
α_0 = amplitude of pitching oscillation; see Eq. (7.1)
γ = complex amplitude of dimensionless pressure jump across airfoil; see Eqs. (2.5) and (2.6)
ϵ_n = 1 if $n = 0$; = 2 if $n \geq 1$
η = see Eq. (6.8)
κ = see Eq. (3.3b)
λ = see Eq. (3.3a)
μ_n = see Eq. (5.4)
ν = Fourier integral spectrum parameter
ξ = see Eq. (6.8)
ρ_0 = mass density of undisturbed flow
φ = dimensionless, perturbation velocity potential, see Eq. (2.2)
ω = angular frequency
$\mathbf{1}$ = unit step function; $\mathbf{1}(x) = 1$ if $x > 0$, $= 0$ if $x < 0$

Received March 24, 1955.

* Professor of Engineering.

(1) INTRODUCTION

THE TWO-DIMENSIONAL PROBLEM of an oscillating airfoil in a wind tunnel has been considered by Reissner[1] for incompressible flow and by Runyan and Woolston[2] for subsonic compressible flow. The finite oscillating wing in incompressible flow has been considered by Jones[3] for a tunnel of rectangular cross section and by Goodman[4] for a tunnel of circular cross section. A survey of the literature reveals no treatment of the supersonic problem, however, and it is toward this end that the following analysis is primarily directed.

It should be remarked at the outset that two-dimensional interference between wind-tunnel walls a distance b apart and an airfoil of chord c midway between these walls cannot take place at supersonic speeds if

$$(M^2 - 1)^{1/2}(b/c) > 1 \tag{1.1}$$

in consequence of the fact that the reflections of the leading-edge Mach waves in the wind-tunnel walls then intersect the plane of the airfoil downstream of the trailing edge. This inequality is satisfied in most practical tests, and it is perhaps for this reason that the supersonic interference problem has not received much attention. It may not always be possible to satisfy Eq. (1.1) at low supersonic Mach Numbers, however, so that it is of some value to investigate the possible effects of interference. A problem of particular interest is the effect on the possible instability of single degree of freedom, pitching oscillations, for which free-stream theory and experiment[5] have provided conflicting information (that apparently is not reconciled by providing for the nonlinear effects of thickness[6, 7]); in this respect, the results of the present investigation appear to be negative insofar as they predict an extension, rather than a contraction, of the range of Mach Numbers over which instability is possible.

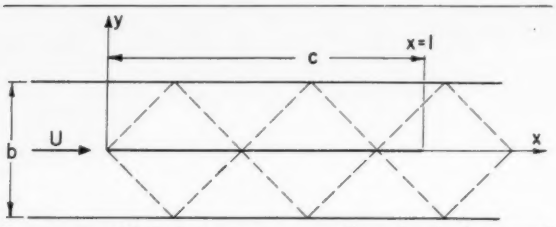

FIG. 1. An airfoil of chord c in a two-dimensional wind tunnel of height b.

The solution to the boundary value problem that is presented by an airfoil in a wind tunnel* may be exhibited either as an expansion in the fields of the images of the obstacle in the walls or in the *natural modes* (guided waves) of the tunnel. The former approach usually will be preferable at supersonic speeds, but the latter approach might prove more advantageous in some subsonic problems and would tend to be superior (for both subsonic and supersonic speeds) in the presence of very strong airfoil tunnel interference.† These two methods of viewing the solution can be unified through a Laplace transform formulation of the supersonic problem [see Sections (3)–(5)] or a Fourier formulation of the subsonic problem [see Section (6)].

(2) Formulation of Problem

Consider a thin airfoil of chord c that lies approximately parallel to and midway between the two walls of a two-dimensional supersonic wind tunnel of height b in which an otherwise undisturbed uniform flow of velocity U is directed along the positive x axis (see Fig. 1). The airfoil will be assumed to execute a harmonic motion of complex amplitude $-U\alpha(x)$ and angular frequency ω, the transverse velocity at the airfoil being given by

$$dy/dt = -U\mathrm{Rl}[\alpha(x)e^{i\omega t}] \tag{2.1}$$

The coordinates x and y are assumed dimensionless, with the airfoil chord c as the unit of length, and the origin is placed at the mean position of the leading edge of the airfoil, as shown in Fig. 1. It is required to find the pressure jump across the airfoil due to the motion prescribed by Eq. (2.1) on the assumption $|\alpha| << 1$, so that the linearized equations of flow may be regarded as adequate approximations.

The perturbation velocity vector $\mathbf{q}$ associated with the motion of the airfoil may be derived from a *dimensionless* (with reference value Uc) velocity potential φ according to

$$\mathbf{q}(x, y, t) = Uc\mathrm{Rl}[\nabla\varphi(x, y)e^{i\omega t}] \tag{2.2}$$

The perturbation pressure is related to φ through the linearized Bernoulli equation

$$p(x, y, t) = -\rho_0\mathrm{Rl}\left[\left(\frac{U}{c}\frac{\partial}{\partial x} + \frac{\partial}{\partial t}\right)Uc\varphi(x, y)e^{i\omega t}\right] \tag{2.3a}$$

$$= -\rho_0U^2\mathrm{Rl}\{[(\partial/\partial x) + ik]\varphi(x, y)e^{i\omega t}\} \tag{2.3b}$$

where ρ_0 denotes the mass density of the undisturbed flow and k the reduced frequency defined by

$$k = \omega c/U \tag{2.4}$$

The pressure jump across the airfoil may be referred to the dimensionless complex amplitude γ according to

$$p(x, 0-, t) - p(x, 0+, t) = 2\rho_0U^2\mathrm{Rl}[\gamma(x)e^{i\omega t}] \tag{2.5}$$

Substituting p in Eq. (2.5) from Eq. (2.3) and anticipating the antisymmetrical dependence of φ on y yields

$$\gamma(x) = [(\partial/\partial x) + ik]\varphi(x, 0+) \tag{2.6}$$

The velocity potential φ satisfies the wave equation (referred to a coordinate system moving with velocity U relative to the flow)

$$a_0^2\nabla^2\varphi = [(U/c)(\partial/\partial x) + i\omega]^2\varphi \tag{2.7}$$

where a_0 denotes the sonic velocity in the undisturbed flow. Expanding Eq. (2.7) and introducing the reduced frequency k from Eq. (2.4) and the Mach Number according to

$$M = U/a_0, \qquad B^2 = M^2 - 1 \tag{2.8}$$

yields $$B^2\varphi_{xx} + 2ikM^2\varphi_x - k^2M^2\varphi - \varphi_{yy} = 0 \tag{2.9}$$

It is required to solve Eq. (2.9) subject to the boundary conditions imposed by the tunnel walls and the motion of the airfoil—viz.,

$$\varphi_y = -\alpha(x), \qquad y = 0 \tag{2.10a}$$

$$= 0, \qquad y = \pm y_1 = \pm b/2c \tag{2.10b}$$

and the initial conditions (with respect to x, not t)

$$\varphi = 0, \qquad x \leq 0 \tag{2.11a}$$

$$\varphi_x = \varphi_y = 0, \qquad x < 0 \tag{2.11b}$$

Having the solution to Eqs. (2.9)–(2.11), the pressure jump across the airfoil then may be calculated from Eqs. (2.5) and (2.6).

(3) Laplace Transform Solution

The Laplace transformation of a function with respect to x will be denoted by an overbar.

$$\bar{f}(s) = Lf(x) = \int_0^\infty e^{-sx}f(x)dx \tag{3.1a}$$

$$f(x) = L^{-1}\bar{f}(s) \tag{3.1b}$$

The transformation of Eq. (2.9), subject to the conditions implied by Eq. (2.11) at $x = 0$, may be placed in the form

$$\bar{\varphi}_{yy} - \lambda^2\bar{\varphi} = 0 \tag{3.2}$$

where λ^2 is defined by

$$\lambda^2 = B^2[(s + ikM)^2 + \kappa^2] \tag{3.3a}$$

* A similar boundary value problem is presented by an unstaggered cascade of airfoils, although the problems are identical only if adjacent airfoils in the cascade are 180° out of phase.

† The guided wave approach might be particularly advantageous in treating closely spaced cascades.

$$\kappa = kM/B^2 = \omega c/B^2 a_0 \tag{3.3b}$$

The boundary conditions of Eq. (2.10) go over directly to

$$\bar{\varphi}_y = -\bar{\alpha}(s), \qquad y = 0 \tag{3.4a}$$

$$= 0, \qquad y = \pm y_1 \tag{3.4b}$$

A solution to Eq. (3.2) satisfying Eq. (3.4) is found to be

$$\bar{\varphi}(s, y) = \lambda^{-1}\bar{\alpha}(s)\,\mathrm{csch}\,(\lambda y_1)\cosh\,[\lambda(y_1 - |y|)]\,\mathrm{sgn}\,y \tag{3.5}$$

The corresponding transform of the pressure jump function γ, as defined by Eq. (2.6), then is given by (noting that $\varphi = 0$ at $x = 0$)

$$\bar{\gamma}(s) = (s + ik)\lambda^{-1}\coth\,(\lambda y_1)\bar{\alpha}(s) \tag{3.6}$$

The inverse transformation of Eq. (3.5) yields the convolution integral

$$\varphi(x, y) = \mathrm{sgn}\,y\int_0^x g\,(x - \xi, y)\alpha(\xi)d\xi \tag{3.7}$$

where g is the inverse transform of

$$\bar{g}(s, y) = \lambda^{-1}\,\mathrm{csch}\,(\lambda y_1)\cosh\,[\lambda(y_1 - |y|)] \tag{3.8}$$

The pressure jump function then is given by

$$\gamma(x) = [(\partial/\partial x) + ik]\int_0^x g\,(x - \xi, 0)\,\alpha\,(\xi)\,d\xi \tag{3.9}$$

Carrying out the differentiation and noting that

$$\lim_{x\to 0+} g(x, 0) = \lim_{s\to\infty} s\bar{g}(s, 0) = B^{-1} \tag{3.10}$$

there results the alternative form

$$\gamma(x) = B^{-1}\alpha(x) + \int_0^x h(x - \xi)\alpha(\xi)d\xi \tag{3.11}$$

where $$h(x) = [(\partial/\partial x) + ik]g(x, 0) \tag{3.12}$$

The first term in Eq. (3.11) may be identified as the *quasi-steady* result—i.e., the result calculated on the hypothesis that the flow at any instant may be calculated as if the instantaneous flow field were steady.

In many calculations [see Section (7)] it may be expedient to deal directly with $\bar{\gamma}$, as given by Eq. (3.6), rather than γ.

(4) Image Interpretation of Influence Function

The inversion of $\bar{g}$ for most practical applications is best effected through an expansion of Eq. (3.8) in exponentials. Expressing the hyperbolic functions in exponential form and expanding the denominator in a geometric series* yields

$$\bar{g}(s, y) = \lambda^{-1}\sum_{n=0}^{\infty}(\exp[-\lambda(2ny_1 + |y|)] + \exp\{-\lambda[(2n + 2)y_1 - |y|]\}) \tag{4.1}$$

Substituting λ from Eq. (3.3a) and using the results[8]

$$L^{-1}f(s + ik_M) = e^{-ik_M x}f(x) \tag{4.2}$$

$$L^{-1}(s^2 + \kappa^2)^{-1/2}e^{-\mu(s^2+\kappa^2)^{1/2}} = J_0[\kappa(x^2 - \mu^2)^{1/2}]\mathbf{1}(x - \mu) \tag{4.3}$$

where J_0 denotes a Bessel function of the first kind and order zero and $\mathbf{1}$ the unit step function, the inverse transform of Eq. (4.1) is given by

$$g(x, y) = B^{-1}e^{-ik_M x}\sum_{n=0}^{\infty}\Big[J_0\{\kappa[x^2 - B^2(2ny_1 + |y|)^2]^{1/2}\}\mathbf{1}[x - B(2ny_1 + |y|)] + J_0(\kappa\{x^2 - B^2[(2n + 2)y_1 - |y|^2]^{1/2}\}\mathbf{1}\{x - B[(2n + 2)\times y_1 - |y|]\}\Big] \tag{4.4}$$

At the wing ($y = 0$) this simplifies to

$$g(x, 0) = B^{-1}e^{-ik_M x}\sum_{n=0}^{\infty}\epsilon_n J_0[\kappa(x^2 - n^2A^2)^{1/2}]\mathbf{1}(x - nA) \tag{4.5}$$

where the *tunnel aspect ratio* A is defined by [cf. Eq. (1.1)]

$$A = 2By_1 = Bb/c \tag{4.6}$$

and ϵ_n by $$\epsilon_n = 1, \qquad n = 0 \tag{4.7a}$$

$$= 2, \qquad n \geq 1 \tag{4.7b}$$

The first term in Eq. (4.5)—viz., $B^{-1}\exp(-ik_M x)\times J_0(\kappa x)$—is the free space ($A = \infty$) influence function for the potential.[9]

The results, Eqs. (4.4) and (4.5), also might have been derived by the classical procedure of representing the effect of the wind-tunnel walls by an infinite set of images located at $y = \pm 2y_1, \pm 4y_1, \ldots$, the fields of which would bear a one to one correspondence to the terms beyond the first in Eq. (4.4). It should be remarked that only a finite number of these images affect the flow at any station x in virtue of the restriction to supersonic flow; in particular, if $A > 1$ in Eq. (4.5), none of the images can affect the flow at the airfoil ($0 \leq x \leq 1$)—as already noted in Section (1).

(5) Guided Wave Interpretation of Influence Functions

An informative, albeit less practical (at least for supersonic flow), interpretation of the influence function is afforded by the Fourier series expansion [motivated by the periodicity of the boundary condition (2.10b)] of Eq. (3.8)—viz.,

$$\bar{g}(s, y) = y_1^{-1}\sum_{n=0}^{\infty}\epsilon_n[\lambda^2 + (n\pi/y_1)^2]^{-1}\cos\,(n\pi y/y_1) \tag{5.1}$$

Substituting λ from Eq. (3.3a) and inverting Eq. (5.1) with the aid of Eq. (4.2) and the inverse transform

$$L^{-1}(s^2 + \delta^2)^{-1} = \delta^{-1}\sin\,(\delta x) \tag{5.2}$$

yields†

* $\mathrm{csch}\,z = 2e^{-z}(1 - e^{-2z})^{-1} = 2e^{-z}\sum_{n=0}^{\infty}e^{-2nz}$.

† The result [Eq. (5.3)] also might have been obtained from Eq. (3.8) by the Heaviside expansion theorem, but the intermediate step [Eq. (5.1)] appreciably simplifies the interpretation.

$$g(x, y) = B^{-2}e^{-i\kappa Mx}\sum_{n=0}^{\infty}\epsilon_n(\mu_n\kappa y_1)^{-1}\sin(\mu_n\kappa x)\times\cos(n\pi y/y_1) \quad (5.3)$$

where ϵ_n is defined by Eq. (4.7) and μ_n by

$$\mu_n = [1 + (n\pi/\kappa By_1)^2]^{1/2} \quad (5.4a)$$

$$= [1 + (2n\pi Ba_0/\omega b)^2]^{1/2} \quad (5.4b)$$

$$= [1 + (nB\lambda_0/b)^2]^{1/2} \quad (5.4c)$$

λ_0 being the *free space* wave length corresponding to the angular frequency ω.

The expansion [Eq. (5.3)] may be regarded as a superposition of *guided wave modes* of the form (restoring the time dependence factor)

$$\varphi_n^{\pm}(x, y)e^{i\omega t} = \exp[i(\omega t - \kappa Mx \mp \mu_n\kappa x)]\times\cos(n\pi y/y_1) \quad (5.5a)$$

$$= \exp\{i\omega[t - (cx/v_n^{\pm})]\}\cos(n\pi y/y_1) \quad (5.5b)$$

where $v_n^{\pm}$ denote the *phase* velocities

$$v_n^{\pm} = \frac{\omega c}{\kappa(M \mp \mu_n)} = \left(\frac{M^2 - 1}{M \mp \mu_n}\right)a_0 \quad (5.6)$$

with which the disturbances are propagated with respect to the wind tunnel. The corresponding phase velocities with respect to the fluid are

$$v_n^{\pm} - U = \pm[(\mu_n M \mp 1)/(M \mp \mu_n)]a_0 \quad (5.7)$$

In the limit $y_1 \to \infty$, Eqs. (5.6) and (5.7) yield the free space values $(M \pm 1)a_0$ and $\pm a_0$, respectively. These same limits also obtain if $n = 0$ ($\mu_0 = 1$), the result being a *plane* wave.

The group velocity u_n, i.e., the velocity with which energy is propagated, may be derived from the phase velocity v_n according to[10, 11]

$$u_n = \frac{d(v_n/\lambda_n)}{d(1/\lambda_n)} = \frac{d\omega}{d(\omega/v_n)} = v_n\left[1 - \left(\frac{\omega}{v_n}\right)\left(\frac{dv_n}{d\omega}\right)\right]^{-1} \quad (5.8)$$

where λ_n is the *guide wave length* of the disturbance in the nth mode—i.e., $\lambda_n = 2\pi v_n/\omega$, as opposed to the *free space wave length* $\lambda_0 = 2\pi a_0/\omega$. Substituting Eqs. (5.4b) and (5.6) in Eq. (5.8) yields

$$u_n^{\pm} = \frac{\mu_n(M^2 - 1)}{(\mu_n M \mp 1)}a_0 \quad (5.9)$$

$$u_n^{\pm} - U = \pm\left(\frac{M \mp \mu_n}{\mu_n M \mp 1}\right)a_0 \quad (5.10)$$

It is of interest to note that

$$(u_n^{\pm} - U)(v_n^{\pm} - U) = a_0^2 \quad (5.11)$$

—i.e., the product of the phase and group velocities *with respect to the fluid* for any particular mode is equal to the square of the free space sonic velocity.

The fact that both the phase and group velocities of the guided modes are frequency dependent (except for the plane wave $n = 0$, for which $u_0 = v_0 = a_0$) implies that the disturbance generated by an airfoil in a wind tunnel is necessarily subjected to dispersive distortion. It also should be remarked that *all* of the modes defined by Eq. (5.5) are propagated without diminution of amplitude, whereas in subsonic flow only those modes for which the frequency is inferior to the *cut off* frequency are so propagated [cf. Section (6)].

The expansion Eq. (5.3) evidently converges rather slowly for moderate values of (x/By_1) and, in this respect, compares unfavorably with the *finite* expansion, Eq. (4.4); on the other hand, Eq. (5.3) would be preferable to Eq. (4.4) for large values of (x/By_1),* especially in virtue of the analytical simplicity of the trigonometric relative to the Bessel functions. In the limit $y_1 \to \infty$ the summation of Eq. (5.3) may be converted to an integration by the substitution

$$\zeta = n\pi/\kappa By_1, \qquad y_1 \to \infty \quad (5.12a)$$

$$d\zeta = \zeta_{n+1} - \zeta_n = \pi/\kappa By_1, \qquad y_1 \to \infty \quad (5.12b)$$

whence

$$\lim_{y_1 \to \infty} g(x, y) = B^{-1}e^{-i\kappa Mx}\cdot\frac{2}{\pi}\int_0^{\infty}(1 + \zeta^2)^{-1/2}\times\sin[\kappa x(1 + \zeta^2)^{1/2}]\cos(\kappa By\zeta)d\zeta \quad (5.13)$$

The integral may be identified as of the Sonine-Gegenbauer type (reference 8, p. 38) with $\nu = 1/2$ and $\mu = -(1/2)$, with the result

$$\lim_{y_1 \to \infty} g(x, y) = B^{-1}e^{-i\kappa Mx}J_0[\kappa(x^2 - B^2y^2)^{1/2}]\times\mathbf{1}(x - B|y|) \quad (5.14)$$

in agreement with the first ($n = 0$) term in Eq. (4.4).

(6) The Subsonic Pressure Doublet

The formulation of Section (2) also is valid for the subsonic problem if the *initial* conditions of Eq. (2.11) are replaced by the appropriate *radiation* and *finiteness* conditions at $x = \mp\infty$. However, the fact that the disturbance produced by the airfoil extends over the entire x domain renders the Laplace transformation of Eq. (3.1) inadmissible, and it is expedient to introduce in its place the Fourier transformation† defined by

$$F(\nu) = \int_{-\infty}^{\infty}e^{-i\nu x}f(x)dx \quad (6.1a)$$

$$f(x) = \frac{1}{2\pi}\int_{-\infty}^{\infty}e^{i\nu x}F(\nu)d\nu \quad (6.1b)$$

* Large values of (x/By_1) probably would be more important in the cascade problem than in the wind-tunnel problem.

† The referee informed the writer that Professor Reissner had given a Fourier transform formulation of the subsonic problem in an unpublished memorandum (1951). Professor Reissner, in turn, referred the writer to: Porter, E. H., *Considerations on Oscillating Airfoils in Subsonic Compressible Flow, Two Dimensional Tunnel Wall Corrections*, B.S. Thesis, Massachusetts Institute of Technology. The writer has not been able to obtain a copy of this thesis (as of the time of correcting the galley proofs), but is under the impression that there is very little overlap with his treatment.

The path of integration for the inverse transform of Eq. (6.1b) may be deformed in the complex ν plane in any manner that is compatible with the conditions at $x = \pm\infty$ and that ensures the existence of the integrals over both ν and x [cf. discussion following Eq. (6.9) and Fig. 2].

The formulation of the subsonic boundary value problem is necessarily implicit in consequence of the nonvanishing and unknown downwash off the airfoil on $y = 0$ and the discontinuity in the velocity potential across the wake downstream of the airfoil. The pressure (or, equivalently, the acceleration potential) on the other hand, must be continuous except across the airfoil and, in virtue of symmetry considerations, must satisfy the condition*

$$\varphi_x + ik\varphi = 0, \quad y = 0, \quad x < 0 \text{ or } x \leq 1 \tag{6.2}$$

It is evident from a comparison of Eqs. (6.1a) and (3.1) that Φ, the Fourier transform of the velocity potential, must satisfy Eq. (3.2) if s is replaced by $i\nu$ in λ^2 (which remains positive and real since both B^2 and κ are negative for $M < 1$). The required solution for Φ also must satisfy Eq. (2.10b) at the tunnel walls and be related to Γ, the Fourier transform of γ, at $y = 0$ according to

$$(i\nu + ik)\Phi(\nu, 0^+) = \Gamma(\nu) \tag{6.3}$$

It is found that these conditions are satisfied by

$$\Phi(\nu, y) = -i(\nu + k)^{-1}\Gamma(\nu)\,\mathrm{sech}\,(\lambda y_1) \times \cosh\,[\lambda(y_1 - |y|)]\,\mathrm{sgn}\,y \tag{6.4a}$$

$$= \Gamma(\nu)\Phi_1(\nu, y) \tag{6.4b}$$

where $\Phi_1(\nu, y)$ is the Fourier transform of the velocity potential of a unit doublet located at the origin $x = 0$ and $y = 0$.

Given φ_1, the inverse of Φ_1, the inverse transformation of Eq. (6.4b) yields the convolution integral

$$\varphi(x, y) = \int_0^1 \varphi_1(x - \xi, y)\gamma(\xi)d\xi \tag{6.5}$$

where the range of integration is restricted in virtue of Eq. (6.2). Invoking the boundary condition [Eq. (2.10a)] at the airfoil then yields the integral equation

$$\alpha(x) = -\lim_{y \to 0+} \frac{\partial}{\partial y}\int_0^1 \varphi_1(x - \xi, y)\gamma(\xi)d\xi \tag{6.6}$$

Runyan and Watkins[2] have determined the kernel of this integral equation—i.e., $-\varphi_{1y}(x, 0+)$—by formulating the boundary value problem in terms of images. Their result, which is an extension of the Possio kernel for the free space integral equation,[12] may be obtained from Eq. (6.4) by expanding the hyperbolic functions in exponentials and inverting term by term, as in Section (4). The goal of this section, however, is the alternative representation of the doublet field in terms of guided waves.

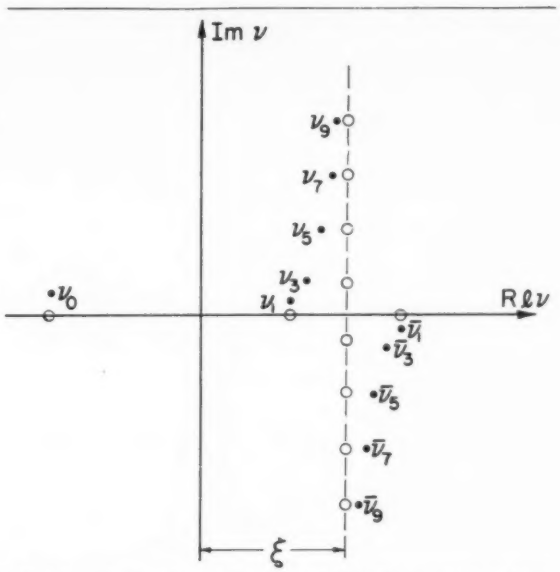

FIG. 2. The location of the poles of Φ_1 in the complex ν plane. The solid circles are based on the assumption that k has a small negative imaginary part, whereas the open circles are based on the assumption that k is real.

The transform Φ_1, as defined by Eq. (6.4), has poles (see Fig. 2) at the zeros of $\nu + k$ and $\cosh(\lambda y_1)$—viz.,

$$\nu_0 = -k \tag{6.7}$$

$$\begin{matrix}\nu_{2n+1} \\ \bar{\nu}_{2n+1}\end{matrix} = \frac{kM^2}{(1 - M^2)} \pm i\left[\frac{(2n + 1)^2}{(1 - M^2)}\left(\frac{\pi}{2y_1}\right)^2 - \left(\frac{kM}{1 - M^2}\right)^2\right]^{1/2}, \quad n = 0, 1, \ldots \tag{6.8a}$$

$$= \xi \pm i\eta_{2n+1} \tag{6.8b}$$

The orientation of the path of integration for the Fourier integral defining φ_1 [cf. Eq. (6.1b)] is expedited by assuming k to have a small negative imaginary part, corresponding to an exponential dissipation of the wake as x tends to $+\infty$. The poles ν_0 and ν_{2n+1} then have positive imaginary parts and the $\bar{\nu}_{2n+1}$ negative imaginary parts for all (positive, by definition) values of the real part of k; if the imaginary part of k tends to zero, the ν_{2n+1} will tend to limiting points on the line $\mathrm{Re}\nu = \xi$, $\mathrm{Im}\nu > 0$ or points on $\mathrm{Re}\nu < \xi$, $\mathrm{Im}\nu = 0$ as k is less or greater, respectively, than

$$k_{2n+1} = \frac{(2n + 1)\pi}{2y_1}\left(\frac{1}{M^2} - 1\right)^{1/2} \tag{6.9}$$

Similarly, the $\bar{\nu}_{2n+1}$ will tend to points on $\mathrm{Re}\nu = \xi$, $\mathrm{Im}\nu < 0$ or $\mathrm{Re}\nu > \xi$, $\mathrm{Im}\nu = 0$. These statements are illustrated in Fig. 2, where the poles are drawn as solid or open circles for the imaginary part of k slightly negative or zero, respectively, and it is assumed (by way of illustration) that the real part of k lies between 0 and k_1.

Granted the assumption that k has a small negative imaginary part, the path of integration for the integral

* The fact that Eq. (6.2) must be satisfied at the trailing edge of the airfoil ($x = 1$) as well as on the wake ($x > 1$) expresses the Kutta condition.

defining φ_1 may be made to coincide with the real axis in the ν plane. If x is positive this path may be closed by a semicircle of radius tending to infinity in the upper half plane; along this semicircle the integrand tends exponentially to zero in virtue of the factor $e^{i\nu x}$, and the application of Cauchy's residue theorem to the resulting contour integral yields

$$\varphi_1(x, y) = \frac{1}{2\pi}\int_{-\infty}^{\infty} e^{i\nu x}\Phi_1(\nu, y)d\nu \tag{6.10a}$$

$$= i\sum \text{Res. } \Phi_1(\nu, y)e^{i\nu x}\big|_{\nu=\nu_0,\ \nu_{2n+1}} \tag{6.10b}$$

Evaluating the residues leads to the end result

$$\varphi_1(x, y) = e^{-ikx}\,\text{sech}\,(ky_1)\cosh\,[k(y_1 - |y|)]\,\text{sgn}\,y - \frac{i\pi}{2y_1{}^2}\,e^{i\xi x}\sum_{n=0}^{\infty}\times \frac{(2n+1)e^{-\eta_{2n+1}x}\sin[(2n+1)(\pi y/2y_1)]}{\eta_{2n+1}[k + i(1 - M^2)\eta_{2n+1}]},\ x > 0 \tag{6.11a}$$

where the η_{2n+1} are either real or positive imaginary, as dictated by Eq. (6.8). If x is negative the ν contour may be closed in the lower half plane (thereby excluding the pole at ν_0), and the end result for φ_1 is

$$\varphi_1(x, y) = -\frac{i\pi}{2y_1{}^2}\,2y_1{}^2\,e^{i\xi x}\sum_{n=0}^{\infty}\times \frac{(2n+1)e^{\eta_{2n+1}x}\sin\,[(2n+1)(\pi y/2y_1)]}{\eta_{2n+1}[k - i(1 - M^2)\eta_{2n+1}]},\ x < 0 \tag{6.11b}$$

Finally, the imaginary part of k may be equated to zero in Eqs. (6.11a,b) without violating any of the physical constraints on the solution unless k happens to be equal to one of the k_{2n+1} (so $\eta_{2n+1} = 0$); in the latter event no *steady-state* solution exists for real k.

The first term in Eq. (6.11a) represents a wake that moves downstream from the doublet with velocity U and, therefore, remains stationary with respect to the fluid. On $y = 0\pm$ it reduces simply to the free space values $\pm\exp(ikx)$, independently of the location of the tunnel walls. The remaining terms, which vanish on $y = 0$, represent guided waves. Those modes for which η_{2n+1} is real ($k < k_{2n+1}$) are exponentially damped away from the source; if, on the other hand, η_{2n+1} is imaginary ($k > k_{2n+1}$) the particular mode is freely propagated away from the source. The points at which $\eta_{2n+1} = 0$ ($k = k_{2n+1}$) are designated as the *cutoff frequencies* or, in the terminology of reference 2, the "tunnel resonant frequencies."* The corresponding phase and group velocities may be calculated as in Section (5) (being real only for imaginary η_{2n+1}). It may be remarked that if U tends to zero (so that k tends to infinity but kM remains finite) these modes become those appropriate to an acoustic wave guide, as described by Rayleigh.[13]

* The adjective *resonant* is somewhat misleading in the present context insofar as the points $k = k_{2n+1}$ correspond to a transition from a condition of energy acceptance (η_{2n+1} imaginary) to one of energy rejection (η_{2n+1} real). A true resonance point is characterized by an abrupt phase transition of approximately 180° in the system impedance, which contrasts with the 90° transition that characterizes a *cutoff point*.

(7) Supersonic Longitudinal Stability Derivatives

The results of Sections (3) and (4) now will be applied to the calculation of the dynamic stability derivatives associated with a pitching motion of amplitude α_0 about the axis $x = x_0$, for which

$$\alpha(x) = \alpha_0[1 + ik(x - x_0)] \tag{7.1}$$

$$\bar{\alpha}(s) = \alpha_0[s^{-1} + ik(s^{-2} - x_0 s^{-1})] \tag{7.2}$$

The lift and moment coefficients may be calculated as inverse Laplace transforms according to

$$c_l = 4\int_0^1 \gamma dx \tag{7.3a}$$

$$= 4L^{-1}\{s^{-1}\bar{\gamma}(s)\}\,|_{x=1} \tag{7.3b}$$

$$c_m = 4\int_0^1 (x_0 - x)\gamma(x)dx \tag{7.4a}$$

$$= 4L^{-1}\{[(x_0 - 1)s^{-1} + s^{-2}]\bar{\gamma}(s)\}\,|_{x=1} \tag{7.4b}$$

These integrals will be evaluated in the *first-order* approximation that terms of order k^2 may be neglected. It then is convenient to write

$$c_l = \alpha_0[c_{l\alpha} + ik(c_{lq} + c_{l\dot{\alpha}}) + 0(k^2)] \tag{7.5}$$

$$c_m = \alpha_0[c_{m\alpha} + ik(c_{mq} + c_{m\dot{\alpha}}) + 0(k^2)] \tag{7.6}$$

where $c_{l\alpha}$ and c_{lq} are calculated in the *quasi-steady* approximation (that $k = 0$ in the equations of motion) from the terms 1 and $(x - x_0)$, respectively, comprised by $\alpha(x)$, while $c_{l\dot{\alpha}}$ represents the terms of order k in the equations of motion, and similarly for $c_{m\alpha}$, c_{mq}, and $c_{m\dot{\alpha}}$.

A first-order approximation to $\bar{\gamma}$, obtained by replacing λ by $B(s + i\kappa M)$ in Eq. (3.6) and neglecting terms of order k^2, is given by

$$\bar{\gamma}(s) = B^{-1}\{\coth(Bsy_1) - ikB^{-2}s^{-1}[\coth\,(Bsy_1) + M^2(Bsy_1)\,\text{csch}^2\,(Bsy_1)] + 0(k^2M^2/B^4)\}\bar{\alpha}(s) \tag{7.7a}$$

$$= B^{-1}\{1 + ikB^{-2}s^{-1}[M^2A(\partial/\partial A) - 1] + 0(k^2M^2/B^4)\}\cdot\coth\,[(1/2)As]\bar{\alpha}(s) \tag{7.7b}$$

where A is defined by Eq. (4.6). Substituting Eqs. (7.2) and (7.7) in the Laplace transforms of Eqs. (7.3b) and (7.4b) yields

$$\bar{c}_l = 4B^{-1}\alpha_0\{s^{-2} + ik(s^{-3} - x_0 s^{-2}) + ikB^{-2}s^{-3}[M^2A(\partial/\partial A) - 1]\}\coth\,[(1/2)As] \tag{7.8}$$

$$\bar{c}_m = [(x_0 - 1) + s^{-1}]\bar{c}_l \tag{7.9}$$

It is, of course, implicit that the inverse transforms of $\bar{c}_l$ and $\bar{c}_m$ are to be evaluated at $x = 1$.

The first two terms in brackets in Eq. (7.8), representing $c_{l\alpha}$ and c_{lq}, respectively, comprise the quasi-steady approximation, while the third term, which contains the terms of order k from the equations of motion, represents $c_{l\dot{\alpha}}$. Defining the functions

$$f_n(A) = L^{-1}\{s^{-n-1}\coth[(1/2)As]\}\,|_{x=1} \quad (7.10)$$

and the Ackeret lift curve slope

$$m = 4B^{-1} \quad (7.11)$$

the inverse transforms of the terms in Eq. (7.8) yield

$$c_{l\alpha} = mf_1(A) \quad (7.12a)$$

$$c_{lq} = m[f_2(A) - x_0 f_1(A)] \quad (7.12b)$$

$$c_{l\dot{\alpha}} = mB^{-2}[M^2A(\partial/\partial A) - 1]f_2(A) \quad (7.12c)$$

The corresponding moment coefficients are, from Eq. (7.9),

$$c_{m\alpha} = m[(x_0 - 1)f_1(A) + f_2(A)] \quad (7.13a)$$

$$c_{mq} = -m[x_0(x_0 - 1)f_1(A) + f_2(A) - f_3(A)] \quad (7.13b)$$

$$c_{m\dot{\alpha}} = mB^{-2}[M^2A(\partial/\partial A) - 1][(x_0 - 1)f_2(A) + f_3(A)] \quad (7.13c)$$

The inverse transform of Eq. (7.10), obtained by expanding the hyperbolic function in a series of exponentials [cf. Section (4)] and inverting term by term, is given by

$$f_n(A) = \frac{1}{n!}\sum_{r=0}^{N}\epsilon_r(1 - rA)^n, \qquad N < A^{-1} \leq N + 1 \quad (7.14)$$

where N is the largest integer smaller than A^{-1}. An alternative expression, which proves more convenient for small A (large N), may be obtained by expanding the binomial $(1 - rA)^n$ and reversing the order of summation, whence

$$f_n(A) = \sum_{s=0}^{n}\frac{(-A)^s}{s!(n-s)!}\sum_{r=0}^{N}\epsilon_r r^s \quad (7.15)$$

Setting $n = 1, 2, 3$ in Eq. (7.15) and evaluating the summations over r with the aid of Bernoulli's formula for a sum of positive powers of integers[14] yields

$$f_1(A) = (2N + 1) - N(N + 1)A \quad (7.16a)$$

$$f_2(A) = (1/2)(2N + 1) - N(N + 1)A + (1/6)N(N + 1)(2N + 1)A^2 \quad (7.16b)$$

$$f_3(A) = (1/6)(2N + 1) - (1/2)N(N + 1)A + (1/6)N(N + 1)(2N + 1)A^2 - (1/12)N^2(N + 1)^2A^3 \quad (7.16c)$$

Substituting Eq. (7.16) in Eqs. (7.12) and (7.13) yields the end results

$$c_{l\alpha} = m[(2N + 1) - N(N + 1)A] \quad (7.17a)$$

$$c_{lq} = m\{(2N + 1)[(1/2) - x_0] - N(N + 1)A \times (1 - x_0) + (1/6)N(N + 1)(2N + 1)A^2\} \quad (7.17b)$$

$$c_{l\dot{\alpha}} = m\{-[(2N + 1)/2(M^2 - 1)] - N(N + 1)A + (1/6)N(N + 1)(2N + 1)A^2[(2M^2 - 1) \div (M^2 - 1)]\} \quad (7.17c)$$

$$c_{m\alpha} = m\{(2N + 1)[x_0 - (1/2)] - N(N + 1)Ax_0 + (1/6)N(N + 1)(2N + 1)A^2\} \quad (7.18a)$$

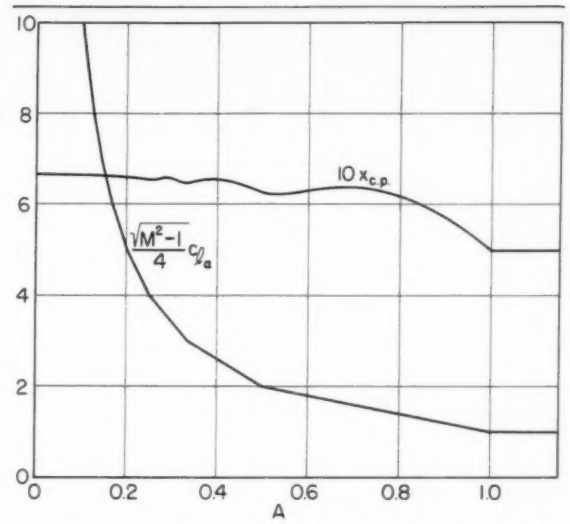

FIG. 3. $c_{l\alpha}$ and $x_{c.p.}$ as given by Eqs. (7.17a) and (7.20).

$$c_{mq} = -m\{(2N + 1)[x_0^2 - x_0 + (1/3)] - N(N + 1)A[x_0^2 - x_0 + (1/2)] + (1/12)N^2(N + 1)^2A^3\} \quad (7.18b)$$

$$c_{m\dot{\alpha}} = m\{-[(2N + 1)/(M^2 - 1)][(1/2)x_0 - (1/3)] - N(N + 1)A[x_0 - (1/2)] + (1/6)N(N + 1) \times (2N + 1)A^2[(2M^2 - 1)/(M^2 - 1)]x_0 - (1/12)N^2(N + 1)^2A^3[(3M^2 - 1)/(M^2 - 1)]\} \quad (7.18c)$$

where the value of N is determined by that of A, as in Eq. (7.14).

The lift coefficient, $c_{l\alpha}$, which is plotted in Fig. 3, has the value m for $A > 1$ and increases with A in linear increments from Nm to $(N + 1)m$ as A decreases from N^{-1} to $(N + 1)^{-1}$; thus, its asymptotic value is given by

$$c_{l\alpha} \sim A^{-1}m, \qquad A \to 0 \quad (7.19)$$

The center of pressure (as determined by $c_{m\alpha} = 0$), which also is plotted in Fig. 3, moves aft in an oscillatory fashion, according to

$$x_{c.p.} = \frac{1}{2}\left[\frac{1 - (1/3)N(N + 1)A^2}{1 - [N(N + 1)/(2N + 1)]A}\right] \quad (7.20)$$

and has the limiting value

$$\lim_{A \to 0} x_{c.p.} = \frac{2}{3} \quad (7.21)$$

It is of interest to remark that if the tunnel were of the open jet type, the results of this section could be rederived by replacing $\coth[(1/2)As]$ by $\tanh[(1/2)As]$, and the limiting values of $c_{l\alpha}$ and $x_{c.p.}$ would be $(1/2)mA = 2b/c$ and 0, respectively.*

The possibility of single degree of freedom pitching instability for a supersonic airfoil in a wind tunnel

* These results are similar to those of slender wing theory, as might have been anticipated from the similarity between the Mach wave reflections at the boundary of a free jet and a wing edge.

may be investigated by setting $c_{mq} + c_{m\dot{\alpha}} = 0$. If $A \geq 1$ the well-known result that instability may arise in the Mach Number range (1, 1.56) is recovered; but for $A < 0.54$ it is found that instability is possible (for some value of x_0) for all $M > 1$. It appears, therefore, that wind-tunnel wall interference is an improbable explanation of the discrepancy[5] between theory and experiment in respect to instability of single degree of freedom pitching oscillations.*

References

[1] Reissner, Eric, *Wind Tunnel Corrections for the Two-Dimensional Theory of Oscillating Airfoils*, Rep. No. SB-318-S-3, Cornell Aero. Lab., 1947.

[2] Woolston, D. S., and Runyan, H. L., *Some Considerations on the Air Forces on a Wing Oscillating Between Two Walls for Subsonic Compressible Flow*, Journal of the Aeronautical Sciences, Vol. 22, No. 1, pp. 41–50, January, 1955; also Runyan, H. L., and Watkins, C. E., *Considerations of the Effect of Wind Tunnel Walls on Oscillating Air Forces for Two Dimensional Subsonic Compressible Flow*, NACA Rep. 1150, 1953.

[3] Jones, W. P., *Wind Tunnel Interference Effect on the Values of Experimentally Determined Derivative Coefficients for Oscillating Airfoils*, R. & M. 1912, British A.R.C., 1943.

[4] Goodman, T. R., *The Upwash Correction for an Oscillating Wing in a Wind Tunnel*, Journal of the Aeronautical Sciences, Vol. 20, No. 6, pp. 383–386, June, 1953.

[5] Howarth, L. (Ed.), *Modern Developments in Fluid Dynamics —High Speed Flow*, Vol. 1, pp. 371–374; Oxford Univ. Press, London, 1953.

[6] Van Dyke, M. D., *On Second-Order Supersonic Flow Past a Slowly Oscillating Airfoil*, Journal of the Aeronautical Sciences, Vol. 20, No. 1, p. 61, January, 1953.

[7] Van Dyke, M. D., *Supersonic Flow Past Oscillating Airfoils Including Nonlinear Thickness Effects*, NACA TN 2982, 1953.

[8] Magnus, W., and Oberhettinger, F., *Formulas and Theorems for the Special Functions of Mathematical Physics*, pp. 123, 132; Chelsea Publ. Co., New York, 1949.

[9] Miles, J. W., *The Aerodynamic Forces on an Oscillating Airfoil at Supersonic Speeds*, Journal of the Aeronautical Sciences, Vol. 14, No. 6, pp. 351–358, June, 1947.

[10] Lord Rayleigh, *On Progressive Waves*, Proc. London Math. Soc., Vol. 9, p. 21, 1877.

[11] Lord Rayleigh, *Theory of Sound*, Vol. 1, pp. 301, 475; Dover Publications, New York, 1945.

[12] See reference 5; p. 353.

[13] Lord Rayleigh, *Theory of Sound*, Vol. 2, pp. 72–74 and 159–162; Dover Publications, New York, 1945.

[14] Whittaker, E., and Robinson, G., *The Calculus of Observations*, pp. 137, 138; Blackie and Son, Ltd., London, 1944.

* The referee has pointed out that "experiments on the single degree of freedom instability have generally avoided the conditions wherein it is necessary to take account of the reflected waves" and that "it may pay to intentionally test in these regions wherein it is necessary to consider the reflected waves in order to enhance the expected effects."

Eccentric Landing with Heavy Masses at the Wing Tips

(Continued from page 659)

Conclusions

(a) The case of equal impact landing, Case (B), may represent a critical condition for asymmetric wing vibration.

(b) The case of eccentric landing, Case (C), is most critical for the landing gear unless the sinking velocity is conveniently reduced. Therefore, for large i/e ratios, the landing gears should be designed so as to be satisfactory for two extreme conditions: (1) for a small drop mass, or about $(1/2)M$, and normal sinking velocity, and (2) for an increased drop mass and a reduced sinking velocity.

Only then could the condition for safe landing be formulated.

References

[1] von Karman, Theodore, and Biot, Maurice A., *Mathematical Methods in Engineering*, McGraw-Hill Book Company, Inc., 1949.

[2] Timoshenko, S., and Young, D. H., *Engineering Mechanics Statics*, McGraw-Hill Book Company, Inc., 1937.

[3] McPherson, A. E., Evans, J., Jr., and Levy, Samuel, *Influence of Wing Flexibility on Force-Time Relation in Shock Strut following Vertical Impact*, NACA TN 1995, 1949.

[4] Milwitzky, Ben, and Lindquist, F. A., *Evaluation of the Reduced Mass Method of Representing Wing-lift Effects in Free-Fall Drop Tests of Landing Gears*, NACA TN 2400, 1951.

[5] Walls, James H., *Investigation of the Air-Compression Process during Drop Tests of an Oleo-Pneumatic Gear*, NACA TN 2477, 1951.

[6] Yntema, Rob. T., and Milwitzky, Ben, *An Impulse-Momentum Method for Calculating Landing Gear Contact Conditions in Eccentric Landings*, NACA TN 2596, 1952.

[7] Lindquist, Dean C., *Effects of Wing Lift and Weight on Landing Gear Loads*, NACA TN 2645, 1952.

[8] Horne, Walter B., *Static Force-Deflection Characteristics of Six Aircraft Tires Under Combined Loading*, NACA TN 2926, 1953.

[9] Zahorski, Adam, *Remarks on Dynamic Loads in Landing*, Journal of the Aeronautical Sciences, Vol. 19, No. 4, pp. 258–264, April, 1952.

[10] Milwitsky, Ben., and Cook, F. E., *Analysis of Landing Gear Behaviour*, NACA Report 1153, 1953.

Applications of Matrix Operators to the Kinematics of Airplane Motion*

MALCOLM J. ABZUG†

Douglas Aircraft Company, Inc.

SUMMARY

The effects of a finite rotation of a reference frame on the projections of a vector on that frame may be represented by an orthogonal matrix. Three successive applications of this principle, corresponding to the yaw, pitch, and roll orientation angles of an airplane, yield the general matrix of transformation. This transformation is applied to the problem of projecting from earth to airplane axes, and vice versa. Using this result, the direct and inverse relationships between angular velocities and orientation angle rates are derived. The projections on earth axes of the small-disturbance motions calculated by classical airplane dynamic stability theory are then derived from the previous relationships.

Azimuth and elevation angles of a target on tracking airplane axes are conveniently derived by use of the matrix of transformation, as are the relationships between the orientation angles of NACA stability axes and arbitrarily aligned airplane body axes. Finally, the indications of free gyros (gimbal angles) are obtained by equating the matrix of transformation to gyro matrices formed by considering successive finite rotations about the spin, inner gimbal, and outer gimbal axes. The variations of inner and outer gimbal angles with airplane orientation angles for two typical gyros show that large discrepancies in indicated orientation angles and possible ambiguous readings are present for large values of bank and pitch angles.

REFERENCE AXES AND SYMBOLS

Orthogonal reference axes fixed in the airplane (body axes), having their origins at the center of gravity are used, defined as follows:

The X-axis lies within the plane of symmetry and is positive forward. The X-axis orientation is arbitrary, but it is often chosen parallel to a wing or fuselage reference line or to the thrust line.

The Y-axis is perpendicular to the plane of symmetry and is positive towards the right wing.

The Z-axis is perpendicular to the X- and Y-axes and is positive towards the bottom of the airplane.

NACA stability axes are a special case of these airplane body axes, oriented so that the Z-axis is perpendicular to the relative wind in steady flight or at the start of a disturbed motion.

A, E = azimuth and elevation angles (in succession) of sight-line with respect to airplane axes

G_i, G_o = inner and outer gimbal angles of a free gyro, measured as the departure from orthogonality of the gimbal frames and base

$[L]$ = matrix of transformation

P, Q, R = angular velocities about the X-, Y-, and Z-airplane axes

p, q, r = disturbance angular velocities about the X-, Y-, and Z-airplane axes

U, V, W = velocities along the X-, Y-, and Z-airplane axes

u, v, w = disturbance velocities along the X-, Y-, and Z-airplane axes

V_X, V_Y, V_Z = velocities along the X-, Y-, and Z-earth axes

u' = disturbance air-speed variable $u/\mathcal{U}_1$

$\mathcal{U}$ = total velocity

X, Y, Z = generalized projections along X-, Y-, and Z-earth axes

x, y, z = generalized projections along X-, Y-, and Z airplane axes

α, β = disturbance angles of attack and sideslip, $w/\mathcal{U}_1$ and $v/\mathcal{U}_1$

γ = flight path angle

ψ, θ, ϕ = yaw, pitch, and roll orientation angles (in succession) of airplane body (or stability) axes with respect to earth axes, as defined by Durand.[4]

ψ_s, θ_s = yaw and pitch angle orientation angles (in succession) of sight-line with respect to earth axes.

$[\ ]$ = matrix

$[\ ]^{-1}$ = inverse matrix

Subscripts

1 = steady flight

B = body axes

V = conventional vertical gyro (defined in Section 8—Results)

D = conventional directional gyro (defined in Section 8—Results)

INTRODUCTION

SOLUTIONS OF THE general equations of airplane motion for large disturbances have been of interest to stability and control researchers for over 30 years, mainly in connection with motions in spins and following complete stalls. In recent years, the more easily manageable small-disturbance equations of airplane motion have been more widely used, yielding results of sufficient accuracy for most engineering purposes. The study of large-disturbance airplane motions is still of interest,[1, 2] however, due to the use of automatic flight control equipment in extreme maneuvers and to the availability of analog and digital techniques for the solution of simultaneous nonlinear differential equations.

Matrix transformations may be applied to derive airplane kinematical relationships of the type encountered in large-disturbance problems, and several of these applications are developed in this paper. The use of matrix transformations to represent finite rotations is fundamental to this paper. This concept was developed by Frazer, Duncan, and Collar.[3]

Received April 11, 1955.

* The majority of this paper consists of excerpts from Douglas Aircraft Company Report No. ES 16144, *Kinematics and Dynamics of Fully-Maneuvering Airplanes*, dated June 23, 1952.

† Head, Stability and Control Group, El Segundo Division.

Results

(1) *Orthogonal Matrix of Transformation*

An orthogonal matrix, called the matrix of transformation, may be used to represent the effects of a finite reference frame rotation on the projections of a vector on that frame. Thus, if x, y, 0 and x', y', 0 are vector projections on the X-, Y-, and Z-airplane axes before and after a finite rotation ψ from X to Y, then

$$\begin{bmatrix} x' \\ y' \\ z' \end{bmatrix} = \begin{bmatrix} \cos\psi & \sin\psi & 0 \\ -\sin\psi & \cos\psi & 0 \\ 0 & 0 & 1 \end{bmatrix} \begin{bmatrix} x \\ y \\ z \end{bmatrix} = [\psi] \begin{bmatrix} x \\ y \\ z \end{bmatrix} \tag{1}$$

In Eq. (1), the orthogonal matrix of transformation $[\psi]$ is an operator on the x, y, z column matrix to obtain the x', y', z' column matrix.

By making three successive applications of Eq. (1) corresponding to the successive rotations ψ, θ, and ϕ defining an arbitrary airplane orientation with respect to the earth, the complete matrix of transformation $[L]$ is obtained as

$$\left.\begin{aligned} [L] &= [\phi]\,[\theta]\,[\psi] \\ &= \begin{bmatrix} 1 & 0 & 0 \\ 0 & \cos\phi & \sin\phi \\ 0 & -\sin\phi & \cos\phi \end{bmatrix} \begin{bmatrix} \cos\theta & 0 & -\sin\theta \\ 0 & 1 & 0 \\ \sin\theta & 0 & \cos\theta \end{bmatrix} \begin{bmatrix} \cos\psi & \sin\psi & 0 \\ -\sin\psi & \cos\psi & 0 \\ 0 & 0 & 1 \end{bmatrix} \\ &= \begin{bmatrix} \cos\theta\cos\psi & \cos\theta\sin\psi & -\sin\theta \\ \sin\phi\sin\theta\cos\psi - \sin\psi\cos\phi & \sin\psi\sin\theta\sin\phi + \cos\psi\cos\phi & \sin\phi\cos\theta \\ \cos\psi\cos\phi\sin\theta + \sin\psi\sin\phi & \sin\psi\cos\phi\sin\theta - \cos\psi\sin\phi & \cos\phi\cos\theta \end{bmatrix} \end{aligned}\right\} \tag{2}$$

The property of the $[L]$ matrix is defined by the equation

$$\begin{bmatrix} x \\ y \\ z \end{bmatrix} = [L] \begin{bmatrix} X \\ Y \\ Z \end{bmatrix} \tag{3}$$

where X, Y, and Z are projections of a vector on earth coordinates and x, y, and z are projections of the same vector on the airplane reference frame in any arbitrary attitude.

(2) *Projecting from Earth to Airplane Axes*

Eq. (3) may be expanded to obtain the generalized projections on the airplane reference frame x, y, z of any vector with projections X, Y, Z on earth coordinates, as

$$\left.\begin{aligned} x &= X\cos\theta\cos\psi + Y\cos\theta\sin\psi - Z\sin\theta \\ y &= X(\cos\psi\sin\phi\sin\theta - \sin\psi\cos\phi) + \\ &\quad Y(\sin\psi\sin\phi\sin\theta + \cos\psi\cos\phi) + \\ &\quad Z\sin\phi\cos\theta \\ z &= X(\cos\psi\cos\phi\sin\theta + \sin\psi\sin\phi) + \\ &\quad Y(\sin\psi\cos\phi\sin\theta - \cos\psi\sin\phi) + \\ &\quad Z\cos\theta\cos\phi \end{aligned}\right\} \tag{3A}$$

As an example of the application of Eqs. (3A), the components on airplane axes of the acceleration of gravity vector $g = Z$ are

$$\left.\begin{aligned} x &= -g\sin\theta \\ y &= g\sin\phi\cos\theta \\ z &= g\cos\phi\cos\theta \end{aligned}\right\} \tag{4}$$

(3) *Projecting from Airplane to Earth Axes*

Premultiplying both sides of Eq. [3] by the inverse orientation matrix $[L]^{-1}$ leads to

$$\begin{bmatrix} X \\ Y \\ Z \end{bmatrix} = [L]^{-1} \begin{bmatrix} x \\ y \\ z \end{bmatrix} \tag{5}$$

Since the matrix $[L]$ is orthogonal, its inverse is identical with its transpose[3] and

$$[L]^{-1} = \begin{bmatrix} \cos\theta\cos\psi & \sin\phi\sin\theta\cos\psi - \cos\phi\sin\psi & \cos\phi\sin\theta\cos\psi + \sin\phi\ \sin\psi \\ \cos\theta\sin\psi & \sin\phi\sin\theta\sin\psi + \cos\phi\cos\psi & \cos\phi\sin\theta\sin\psi - \sin\phi\ \cos\psi \\ -\sin\theta & \sin\phi\cos\theta & \cos\phi\cos\theta \end{bmatrix}$$

Expanding Eq. (5),

$$\left.\begin{aligned} X &= x\cos\theta\cos\psi + \\ &\quad y(\cos\psi\sin\phi\sin\theta - \sin\psi\cos\phi) + \\ &\quad z(\cos\psi\cos\phi\sin\theta + \sin\psi\sin\phi) \\ Y &= x\cos\theta\sin\psi + \\ &\quad y(\sin\psi\sin\phi\sin\theta + \cos\psi\cos\phi) + \\ &\quad z(\sin\psi\cos\phi\sin\theta - \cos\psi\sin\phi) \\ Z &= -x\sin\theta + \\ &\quad y\sin\phi\cos\theta + \\ &\quad z\cos\theta\cos\phi \end{aligned}\right\} \quad (5A)$$

As an example of the application of Eqs. (5A), the components on earth coordinates of the airplane's linear velocities measured along airplane axes may be found by substituting U, V, and W for x, y, and z, respectively, and V_X, V_Y, and V_Z for X, Y, and Z, respectively, where V_X, V_Y, and V_Z represent the components of airplane velocity in earth coordinates. This application has been made by Hall.[1]

(4) *Angular Velocities About Airplane Axes and Orientation Angle Rates*

The relationships between angular velocities measured on the moving airplane axes and the rates of change of the orientation angles ψ, θ, and ϕ may be derived from the preceding equations. First, the projections of the orientation angle rates of change on earth axes are found from Eqs. (5A) and simple projection as

$$\left.\begin{aligned} X &= (d\phi/dt)\cos\theta\cos\psi - (d\theta/dt)\sin\psi \\ Y &= (d\phi/dt)\cos\theta\sin\psi + (d\theta/dt)\cos\psi \\ Z &= -(d\phi/dt)\sin\theta + d\psi/dt \end{aligned}\right\} \quad (6)$$

Then, using Eqs. (3A), these components may be resolved along airplane axes (after some reduction) as

$$\left.\begin{aligned} P &= d\phi/dt - (d\psi/dt)\sin\theta \\ Q &= (d\theta/dt)\cos\phi + (d\psi/dt)\sin\phi\cos\theta \\ R &= -(d\theta/dt)\sin\phi + (d\psi/dt)\cos\theta\cos\phi \end{aligned}\right\} \quad (7)$$

The inverse solution is

$$\left.\begin{aligned} d\phi/dt &= P + Q\sin\phi\tan\theta + R\cos\phi\tan\theta \\ d\theta/dt &= Q\cos\phi - R\sin\phi \\ d\psi/dt &= Q\sin\phi\sec\theta + R\cos\phi\sec\theta \end{aligned}\right\} \quad (7A)$$

Eqs. (7) or (7A) have been given previously by Frazer, Duncan, and Collar,[3] Goldstein,[5] and Hall.[1]

(5) *Small-Disturbance Motion Projections on Earth Axes*

Eqs. (7A) may be used together with Eqs. (5A) to obtain the components of airplane linear velocity in earth coordinates, starting from motions calculated by small-disturbance dynamic stability theory, using stability axes. Making the necessary assumptions,

$$\begin{aligned} U &= \mathfrak{V}_1 + u = \mathfrak{V}_1(1+u') & \psi_1 &= 0 \\ V &= v = \mathfrak{V}_1\beta & \theta_1 &= \gamma_1 \\ W &= w = \mathfrak{V}_1\alpha & \phi_1 &= 0 \end{aligned}$$

From Eq. (7A),

$$\left.\begin{aligned} \phi &= \int p\,dt + (\tan\gamma_1)\int r\,dt \\ \theta &= \gamma_1 + \int q\,dt \\ \psi &= (\sec\gamma_1)\int r\,dt \end{aligned}\right\} \quad (8)$$

With the usual approximations for sines, cosines, and products of infinitesimals, Eqs. (5A) give

$$\left.\begin{aligned} V_X/\mathfrak{V}_1 &= (1+u')\cos\gamma_1 + (\alpha - \textstyle\int q\,dt)\sin\gamma_1 \\ V_Y/\mathfrak{V}_1 &= \textstyle\int r\,dt + \beta \\ V_Z/\mathfrak{V}_1 &= -(1+u')\sin\gamma_1 + (\alpha - \textstyle\int q\,dt)\cos\gamma_1 \end{aligned}\right\} \quad (9)$$

For the special case where $\gamma_1 = 0$, the quantity $\int r\,dt$ is not necessarily infinitesimal for small disturbances, and

$$\left.\begin{aligned} V_X/\mathfrak{V}_1 &= (1+u')\cos\textstyle\int r\,dt - \beta\sin\int r\,dt \\ V_Y/\mathfrak{V}_1 &= (1+u')\sin\textstyle\int r\,dt + \beta\cos\int r\,dt \\ V_Z/\mathfrak{V}_1 &= \alpha - \textstyle\int q\,dt \end{aligned}\right\} \quad (10)$$

(6) *Azimuth and Elevation Angles*

One of the airplane kinematics problems which may be treated conveniently with the matrix of transformation is that of the relationship between a maneuvering airplane and a line-of-sight having an arbitrary space orientation. If the angles between the sight-line (or sight-line-plus-lead) and fixed earth axes are ψ_s and θ_s (in succession), then the projections of a unit sight-line vector on the earth axes are, from Eq. (5A),

$$\left.\begin{aligned} X &= \cos\theta_s\cos\psi_s \\ Y &= \cos\theta_s\sin\psi_s \\ Z &= -\sin\theta_s \end{aligned}\right\} \quad (11)$$

Similarly, if the angles between the sight-line and the airplane axes are A and E (in succession), then the projections of the unit sight-line vector on airplane axes are

$$\left.\begin{aligned} x &= \cos E\cos A \\ y &= \cos E\sin A \\ z &= -\sin E \end{aligned}\right\} \quad (12)$$

Using Eqs. (3A), (11), and (12),

$$\left.\begin{aligned} A &= \tan^{-1}\left[\frac{\cos\theta_s\cos\psi_s(\cos\psi\sin\phi\sin\theta - \sin\psi\cos\phi) + \cos\theta_s\sin\psi_s(\sin\psi\sin\phi\sin\theta + \cos\psi\cos\phi) - \sin\theta_s\sin\phi\cos\theta}{\cos\theta_s\cos\psi_s\cos\theta\cos\psi + \cos\theta_s\sin\psi_s\cos\theta\sin\psi + \sin\theta_s\sin\theta}\right] \\ E &= -\sin^{-1}\left[\cos\theta_s\cos\psi_s(\cos\psi\cos\phi\sin\theta + \sin\psi\sin\phi) + \cos\theta_s\sin\psi_s(\sin\psi\cos\phi\sin\theta - \cos\psi\sin\phi) - \sin\theta_s\cos\theta\cos\phi\right] \end{aligned}\right\} \quad (13)$$

Results

(1) *Orthogonal Matrix of Transformation*

An orthogonal matrix, called the matrix of transformation, may be used to represent the effects of a finite reference frame rotation on the projections of a vector on that frame. Thus, if x, y, 0 and x', y', 0 are vector projections on the X-, Y-, and Z-airplane axes before and after a finite rotation ψ from X to Y, then

$$\begin{bmatrix} x' \\ y' \\ z' \end{bmatrix} = \begin{bmatrix} \cos\psi & \sin\psi & 0 \\ -\sin\psi & \cos\psi & 0 \\ 0 & 0 & 1 \end{bmatrix} \begin{bmatrix} x \\ y \\ z \end{bmatrix} = [\psi] \begin{bmatrix} x \\ y \\ z \end{bmatrix} \tag{1}$$

In Eq. (1), the orthogonal matrix of transformation $[\psi]$ is an operator on the x, y, z column matrix to obtain the x', y', z' column matrix.

By making three successive applications of Eq. (1) corresponding to the successive rotations ψ, θ, and ϕ defining an arbitrary airplane orientation with respect to the earth, the complete matrix of transformation $[L]$ is obtained as

$$\left.\begin{aligned} [L] &= [\phi]\,[\theta]\,[\psi] \\ &= \begin{bmatrix} 1 & 0 & 0 \\ 0 & \cos\phi & \sin\phi \\ 0 & -\sin\phi & \cos\phi \end{bmatrix} \begin{bmatrix} \cos\theta & 0 & -\sin\theta \\ 0 & 1 & 0 \\ \sin\theta & 0 & \cos\theta \end{bmatrix} \begin{bmatrix} \cos\psi & \sin\psi & 0 \\ -\sin\psi & \cos\psi & 0 \\ 0 & 0 & 1 \end{bmatrix} \\ &= \begin{bmatrix} \cos\theta\cos\psi & \cos\theta\sin\psi & -\sin\theta \\ \sin\phi\sin\theta\cos\psi - \sin\psi\cos\phi & \sin\psi\sin\theta\sin\phi + \cos\psi\cos\phi & \sin\phi\cos\theta \\ \cos\psi\cos\phi\sin\theta + \sin\psi\sin\phi & \sin\psi\cos\phi\sin\theta - \cos\psi\sin\phi & \cos\phi\cos\theta \end{bmatrix} \end{aligned}\right\} \tag{2}$$

The property of the $[L]$ matrix is defined by the equation

$$\begin{bmatrix} x \\ y \\ z \end{bmatrix} = [L] \begin{bmatrix} X \\ Y \\ Z \end{bmatrix} \tag{3}$$

where X, Y, and Z are projections of a vector on earth coordinates and x, y, and z are projections of the same vector on the airplane reference frame in any arbitrary attitude.

(2) *Projecting from Earth to Airplane Axes*

Eq. (3) may be expanded to obtain the generalized projections on the airplane reference frame x, y, z of any vector with projections X, Y, Z on earth coordinates, as

$$\left.\begin{aligned} x &= X\cos\theta\cos\psi + Y\cos\theta\sin\psi - Z\sin\theta \\ y &= X(\cos\psi\sin\phi\sin\theta - \sin\psi\cos\phi) + \\ &\quad Y(\sin\psi\sin\phi\sin\theta + \cos\psi\cos\phi) + \\ &\quad Z\sin\phi\cos\theta \\ z &= X(\cos\psi\cos\phi\sin\theta + \sin\psi\sin\phi) + \\ &\quad Y(\sin\psi\cos\phi\sin\theta - \cos\psi\sin\phi) + \\ &\quad Z\cos\theta\cos\phi \end{aligned}\right\} \tag{3A}$$

As an example of the application of Eqs. (3A), the components on airplane axes of the acceleration of gravity vector $g = Z$ are

$$\left.\begin{aligned} x &= -g\sin\theta \\ y &= g\sin\phi\cos\theta \\ z &= g\cos\phi\cos\theta \end{aligned}\right\} \tag{4}$$

(3) *Projecting from Airplane to Earth Axes*

Premultiplying both sides of Eq. [3] by the inverse orientation matrix $[L]^{-1}$ leads to

$$\begin{bmatrix} X \\ Y \\ Z \end{bmatrix} = [L]^{-1} \begin{bmatrix} x \\ y \\ z \end{bmatrix} \tag{5}$$

Since the matrix $[L]$ is orthogonal, its inverse is identical with its transpose[3] and

$$[L]^{-1} = \begin{bmatrix} \cos\theta\cos\psi & \sin\phi\sin\theta\cos\psi - \cos\phi\sin\psi & \cos\phi\sin\theta\cos\psi + \sin\phi\ \sin\psi \\ \cos\theta\sin\psi & \sin\phi\sin\theta\sin\psi + \cos\phi\cos\psi & \cos\phi\sin\theta\sin\psi - \sin\phi\ \cos\psi \\ -\sin\theta & \sin\phi\cos\theta & \cos\phi\cos\theta \end{bmatrix}$$

Expanding Eq. (5),

$$\left.\begin{aligned} X &= x\cos\theta\cos\psi + \\ &\quad y(\cos\psi\sin\phi\sin\theta - \sin\psi\cos\phi) + \\ &\quad z(\cos\psi\cos\phi\sin\theta + \sin\psi\sin\phi) \\ Y &= x\cos\theta\sin\psi + \\ &\quad y(\sin\psi\sin\phi\sin\theta + \cos\psi\cos\phi) + \\ &\quad z(\sin\psi\cos\phi\sin\theta - \cos\psi\sin\phi) \\ Z &= -x\sin\theta + \\ &\quad y\sin\phi\cos\theta + \\ &\quad z\cos\theta\cos\phi \end{aligned}\right\} \quad (5A)$$

As an example of the application of Eqs. (5A), the components on earth coordinates of the airplane's linear velocities measured along airplane axes may be found by substituting U, V, and W for x, y, and z, respectively, and V_X, V_Y, and V_Z for X, Y, and Z, respectively, where V_X, V_Y, and V_Z represent the components of airplane velocity in earth coordinates. This application has been made by Hall.[1]

(4) *Angular Velocities About Airplane Axes and Orientation Angle Rates*

The relationships between angular velocities measured on the moving airplane axes and the rates of change of the orientation angles ψ, θ, and ϕ may be derived from the preceding equations. First, the projections of the orientation angle rates of change on earth axes are found from Eqs. (5A) and simple projection as

$$\left.\begin{aligned} X &= (d\phi/dt)\cos\theta\cos\psi - (d\theta/dt)\sin\psi \\ Y &= (d\phi/dt)\cos\theta\sin\psi + (d\theta/dt)\cos\psi \\ Z &= -(d\phi/dt)\sin\theta + d\psi/dt \end{aligned}\right\} \quad (6)$$

Then, using Eqs. (3A), these components may be resolved along airplane axes (after some reduction) as

$$\left.\begin{aligned} P &= d\phi/dt - (d\psi/dt)\sin\theta \\ Q &= (d\theta/dt)\cos\phi + (d\psi/dt)\sin\phi\cos\theta \\ R &= -(d\theta/dt)\sin\phi + (d\psi/dt)\cos\theta\cos\phi \end{aligned}\right\} \quad (7)$$

The inverse solution is

$$\left.\begin{aligned} d\phi/dt &= P + Q\sin\phi\tan\theta + R\cos\phi\tan\theta \\ d\theta/dt &= Q\cos\phi - R\sin\phi \\ d\psi/dt &= Q\sin\phi\sec\theta + R\cos\phi\sec\theta \end{aligned}\right\} \quad (7A)$$

Eqs. (7) or (7A) have been given previously by Frazer, Duncan, and Collar,[3] Goldstein,[5] and Hall.[1]

(5) *Small-Disturbance Motion Projections on Earth Axes*

Eqs. (7A) may be used together with Eqs. (5A) to obtain the components of airplane linear velocity in earth coordinates, starting from motions calculated by small-disturbance dynamic stability theory, using stability axes. Making the necessary assumptions,

$$\begin{aligned} U &= \mathfrak{V}_1 + u = \mathfrak{V}_1(1 + u') & \psi_1 &= 0 \\ V &= v = \mathfrak{V}_1\beta & \theta_1 &= \gamma_1 \\ W &= w = \mathfrak{V}_1\alpha & \phi_1 &= 0 \end{aligned}$$

From Eq. (7A),

$$\left.\begin{aligned} \phi &= \int p\,dt + (\tan\gamma_1)\int r\,dt \\ \theta &= \gamma_1 + \int q\,dt \\ \psi &= (\sec\gamma_1)\int r\,dt \end{aligned}\right\} \quad (8)$$

With the usual approximations for sines, cosines, and products of infinitesimals, Eqs. (5A) give

$$\left.\begin{aligned} V_X/\mathfrak{V}_1 &= (1 + u')\cos\gamma_1 + (\alpha - \textstyle\int q\,dt)\sin\gamma_1 \\ V_Y/\mathfrak{V}_1 &= \textstyle\int r\,dt + \beta \\ V_Z/\mathfrak{V}_1 &= -(1 + u')\sin\gamma_1 + (\alpha - \textstyle\int q\,dt)\cos\gamma_1 \end{aligned}\right\} \quad (9)$$

For the special case where $\gamma_1 = 0$, the quantity $\int r\,dt$ is not necessarily infinitesimal for small disturbances, and

$$\left.\begin{aligned} V_X/\mathfrak{V}_1 &= (1 + u')\cos\textstyle\int r\,dt - \beta\sin\int r\,dt \\ V_Y/\mathfrak{V}_1 &= (1 + u')\sin\textstyle\int r\,dt + \beta\cos\int r\,dt \\ V_Z/\mathfrak{V}_1 &= \alpha - \textstyle\int q\,dt \end{aligned}\right\} \quad (10)$$

(6) *Azimuth and Elevation Angles*

One of the airplane kinematics problems which may be treated conveniently with the matrix of transformation is that of the relationship between a maneuvering airplane and a line-of-sight having an arbitrary space orientation. If the angles between the sight-line (or sight-line-plus-lead) and fixed earth axes are ψ_s and θ_s (in succession), then the projections of a unit sight-line vector on the earth axes are, from Eq. (5A),

$$\left.\begin{aligned} X &= \cos\theta_s\cos\psi_s \\ Y &= \cos\theta_s\sin\psi_s \\ Z &= -\sin\theta_s \end{aligned}\right\} \quad (11)$$

Similarly, if the angles between the sight-line and the airplane axes are A and E (in succession), then the projections of the unit sight-line vector on airplane axes are

$$\left.\begin{aligned} x &= \cos E\cos A \\ y &= \cos E\sin A \\ z &= -\sin E \end{aligned}\right\} \quad (12)$$

Using Eqs. (3A), (11), and (12),

$$\left.\begin{aligned} A &= \tan^{-1}\left[\frac{\cos\theta_s\cos\psi_s(\cos\psi\sin\phi\sin\theta - \sin\psi\cos\phi) + \cos\theta_s\sin\psi_s(\sin\psi\sin\phi\sin\theta + \cos\psi\cos\phi) - \sin\theta_s\sin\phi\cos\theta}{\cos\theta_s\cos\psi_s\cos\theta\cos\psi + \cos\theta_s\sin\psi_s\cos\theta\sin\psi + \sin\theta_s\sin\theta}\right] \\ E &= -\sin^{-1}\left[\cos\theta_s\cos\psi_s(\cos\psi\cos\phi\sin\theta + \sin\psi\sin\phi) + \cos\theta_s\sin\psi_s(\sin\psi\cos\phi\sin\theta - \cos\psi\sin\phi) - \sin\theta_s\cos\theta\cos\phi\right] \end{aligned}\right\} \quad (13)$$

Useful approximations to Eqs. (13) may be obtained for the case of small angles except for the bank angle ϕ, in which case

$$\left.\begin{aligned} A &= (\psi_s - \psi)\cos\phi - (\theta_s - \theta)\sin\phi \\ E &= (\theta_s - \theta)\cos\phi + (\psi_s - \psi)\sin\phi \end{aligned}\right\} \quad (13A)$$

(7) *Airplane Stability and Body Axes*

As defined in Reference Axes and Symbols, stability axes are a special case of body axes in which the Z-axis is perpendicular to the relative wind in steady flight or at the start of a disturbed motion. Body axes are obtained from stability axes by rotation about the Y-axis equal to the steady flight angle of attack α_1. Thus, if $[L_B]$ is the matrix of transformation using generalized body axis orientation angles ψ_B, θ_B, and ϕ_B, and $[L]$ is the corresponding matrix using the stability axes orientation angles ψ, θ, and ϕ,

$$[L_B] = [\alpha_1]\,[L] \quad (14)$$

where
$$[\alpha_1] = \begin{bmatrix} \cos\alpha_1 & 0 & -\sin\alpha_1 \\ 0 & 1 & 0 \\ \sin\alpha_1 & 0 & \cos\alpha_1 \end{bmatrix} \quad (15)$$

Performing the indicated multiplication of Eq. (14) and equating terms on both sides, the following relationships between body axes and stability axes orientation angles are obtained:

$$\left.\begin{aligned} \sin\theta_B &= \cos\alpha_1\sin\theta + \sin\alpha_1\cos\phi\cos\theta \\ \sin\phi_B &= \sin\phi\cos\theta/\cos\theta_B \\ \sin\psi_B &= (\cos\alpha_1\cos\theta\sin\psi - \\ &\qquad \sin\alpha_1\sin\psi\cos\phi\sin\theta + \\ &\qquad \sin\alpha_1\cos\psi\sin\phi)/\cos\theta_B \end{aligned}\right\} \quad (16)$$

Note that the relationships between the orientation angles of any two arbitrary sets of body axes may also be obtained from Eq. (16).

(8) *Measurement of Airplane Orientation*

The principles previously applied to derive the general relationships of airplane kinematics may be applied as well to analyze the gimbal angles of free gyros used for measurement of airplane orientation. Since the orthogonal matrix of transformation $[L]$ of Eq. (2) is an operator representing a finite rotation, then if another matrix of transformation represents the same end rotation, the two matrices are equal (element for element). The second matrix is a gyro matrix, formed by functions of the gimbal angles.*

The bases of free gyros may be carried to any arbitrary orientations by three noninteracting successive rotations; about the gyro wheel spin axis, the inner gimbal axis, and the outer gimbal axis. The gyro matrix is formed similarly to Eq. (2), by three successive applications of Eq. (1) using angles about these axes. Only two cases are considered in this paper, the conventional vertical and directional free gyros. There are four additional possible arrangements of free gyros with orthogonal gimbals, and many other possible tilted-spin-axis free gyros, none of which are in common use. The conventional vertical and directional free gyros are defined as follows:

(1) Conventional vertical gyro—Spin axis vertical, outer gimbal axis directed along the X-axis (body axis).

(2) Conventional directional gyro—Spin axis level and having an arbitrary geographic heading (usually magnetic north), outer gimbal axis directed along Z-axis (body axis).

The positive directions of the gimbal angles G_i and G_o in each case corresponds to the positive senses of the airplane orientation angles measured. Thus for the vertical gyro, positive G_i corresponds to positive θ, and positive G_o corresponds to positive ϕ. For the directional gyro, positive G_o corresponds to positive ψ. According to these concepts and definitions, the gyro matrices for these two cases are

$$\left.\begin{aligned} [G]_V &= [G_o]\,[G_i]\,[G_s] \\ &= \begin{bmatrix} 1 & 0 & 0 \\ 0 & \cos G_o & \sin G_o \\ 0 & -\sin G_o & \cos G_o \end{bmatrix}\begin{bmatrix} \cos G_i & 0 & -\sin G_i \\ 0 & 1 & 0 \\ \sin G_i & 0 & \cos G_i \end{bmatrix}\begin{bmatrix} \cos G_s & \sin G_s & 0 \\ -\sin G_s & \cos G_s & 0 \\ 0 & 0 & 1 \end{bmatrix} \\ &= \begin{bmatrix} \cos G_i\cos G_s & \cos G_i\sin G_s & -\sin G_i \\ \sin G_o\sin G_i\cos G_s - \sin G_s\cos G_o & \sin G_s\sin G_i\sin G_o + \cos G_s\cos G_o & \sin G_o\cos G_i \\ \cos G_s\cos G_o\sin G_i + \sin G_s\sin G_o & \sin G_s\cos G_o\sin G_i - \cos G_s\sin G_o & \cos G_o\cos G_i \end{bmatrix} \end{aligned}\right\} \quad (17)$$

$$\left.\begin{aligned} [G]_D &= [G_o]\,[G_i]\,[G_s] \\ &= \begin{bmatrix} \cos G_o & \sin G_o & 0 \\ -\sin G_o & \cos G_o & 0 \\ 0 & 0 & 1 \end{bmatrix}\begin{bmatrix} \cos G_i & 0 & -\sin G_i \\ 0 & 1 & 0 \\ \sin G_i & 0 & \cos G_i \end{bmatrix}\begin{bmatrix} 1 & 0 & 0 \\ 0 & \cos G_s & \sin G_s \\ 0 & -\sin G_s & \cos G_s \end{bmatrix} \\ &= \begin{bmatrix} \cos G_o\cos G_i & \sin G_i\sin G_s\cos G_o + \sin G_o\cos G_s & -\cos G_o\sin G_i\cos G_s + \sin G_o\sin G_s \\ -\sin G_o\cos G_i & -\sin G_o\sin G_i\sin G_s + \cos G_o\cos G_s & \sin G_o\sin G_i\cos G_s + \cos G_o\sin G_s \\ \sin G_i & 0 & \cos G_i\cos G_s \end{bmatrix} \end{aligned}\right\} \quad (18)$$

* This procedure was suggested to the author by S. Fingerhood of the Sperry Gyroscope Company.

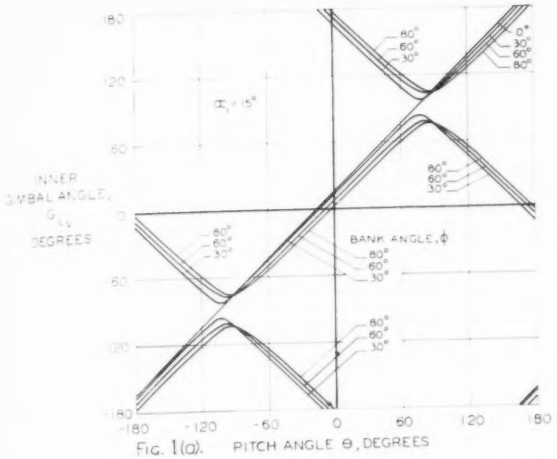

FIG. 1(a). PITCH ANGLE θ, DEGREES

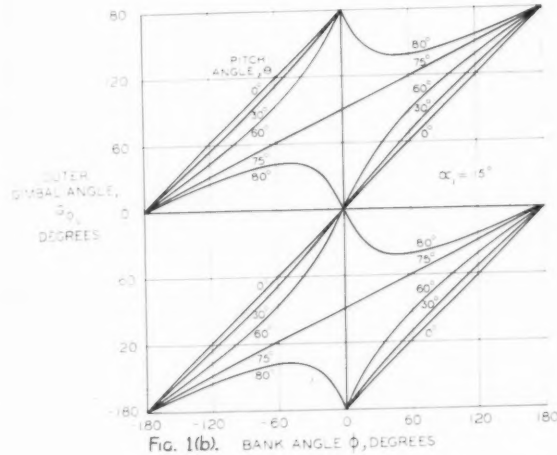

FIG. 1(b). BANK ANGLE ϕ, DEGREES

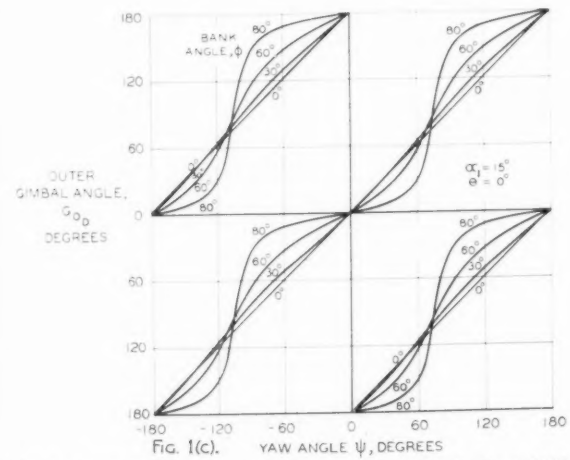

FIG. 1(c). YAW ANGLE ψ, DEGREES

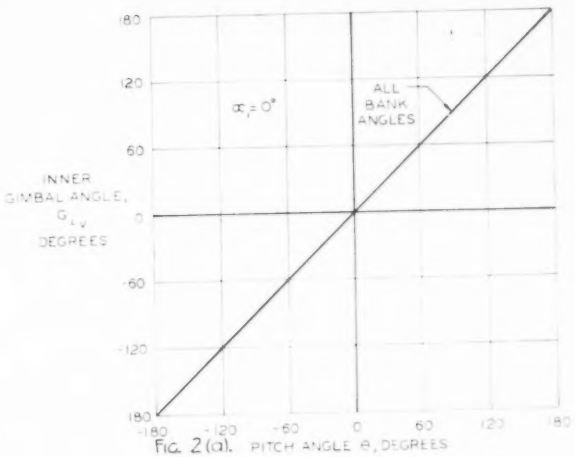

FIG. 2(a). PITCH ANGLE θ, DEGREES

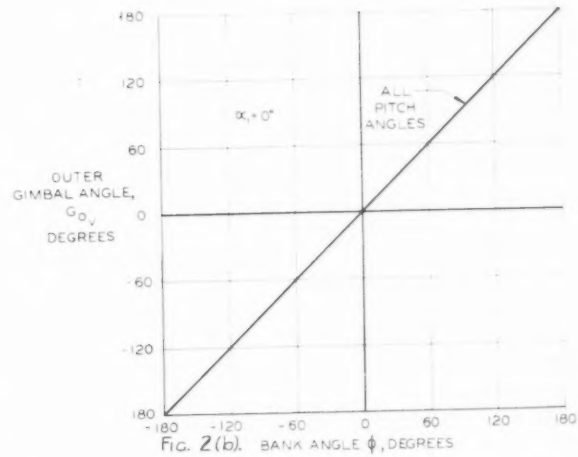

FIG. 2(b). BANK ANGLE ϕ, DEGREES

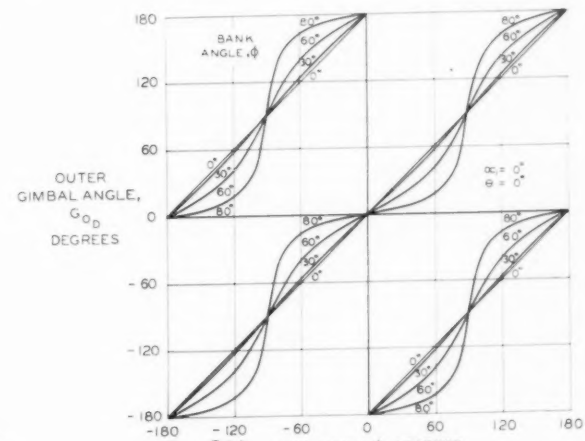

FIG. 2(c). YAW ANGLE ψ, DEGREES

FIG. 1. Gyro gimbal angles at a typical high angle of attack (15°), (a) vertical gyro inner gimbal angle, (b) vertical gyro outer gimbal angle, (c) directional gyro outer gimbal angle.

FIG. 2. Gyro gimbal angles at zero angle of attack, (a) vertical gyro inner gimbal angle, (b) vertical gyro outer gimbal angle, (c) directional gyro outer gimbal angle.

Equating corresponding elements of $[G]_V$ and $[G]_D$ to $[\alpha_1]$ $[L]$ of Eqs. (2) and (15) leads to the following gyro equations:

$$G_{i_V} = \sin^{-1}(\cos\alpha_1 \sin\theta + \sin\alpha_1 \cos\phi \cos\theta) \quad (19)$$

$$G_{o_V} = \tan^{-1}[\sin\phi \cos\theta/(\cos\alpha_1 \cos\phi \cos\theta - \sin\alpha_1 \sin\theta)] \quad (20)$$

$$G_{i_D} = \sin^{-1}[\cos\alpha_1(\cos\psi \cos\phi \sin\theta + \sin\psi \sin\phi) + \sin\alpha_1 \cos\psi \cos\theta] \quad (21)$$

$$G_{o_D} = \tan^{-1}\left[\frac{\sin\psi \cos\phi - \sin\phi \sin\theta \cos\psi}{\cos\alpha_1(\cos\theta \cos\psi) - \sin\alpha_1(\sin\psi \sin\phi + \cos\psi \cos\phi \sin\theta)}\right] \quad (22)$$

The angle α_1 in Eqs. (19) to (22) is the angle between the outer gimbal axis of the vertical gyro and the airplane's X-axis. α_1 is also the angle between the directional gyro outer gimbal axis and the airplane's Z-axis. If airplane stability axes are used, α_1 is the steady flight angle of attack of the vertical gyro outer gimbal axis or of the normal to the directional gyro outer gimbal axis.

Typical relationships between gimbal angles and airplane orientation angles for these gyros are shown in Figs. 1 and 2. Fig. 1 represents a case typical of either low-speed or maneuvering flight, where the angle of attack α_1 of the vertical gyro outer gimbal axis (and of the normal to the directional gyro outer gimbal axis) is a relatively large positive angle. Fig. 2 is typical of high-speed flight, where α_1 is small. It is evident from examination of these figures that direct readings of pitch and roll orientation angles are possible with the vertical gyro only when the outer gimbal axis angle of attack α_1 is zero. Also, direct readings of yaw are possible with the directional gyro when not only α_1 but also the bank angle ϕ are zero. The ambiguity (possible readings less than 180° apart) in pitch and roll angles for given gimbal angles, when α_1 is not zero, is overcome in an actual case by knowledge of the entire history of the maneuver. Finally, it should be noted that inner gimbal angles in the vicinity of $\pm 90°$ lead to "gimbal lock," rendering the gyro useless as an instrument in this range.

Conclusion

The orthogonal matrix of transformation has been shown to be a useful tool in developing kinematic relationships in airplane motion. A limited number of applications have been made in this paper, but other specialized applications have been made to the problems of gyro instrumentation and transformation of wind-tunnel data. In all cases, finite rotations are represented by matrices obeying the usual laws of matrix multiplication and equality. In this paper, the following kinematic relationships have been developed:

(1) Projections of a vector quantity (like velocity) from earth to airplane axes, or vice-versa.

(2) Relationships of angular velocities about airplane axes and orientation angle rates.

(3) Projections on earth axes of the small-disturbance motions calculated by classic dynamic stability theory.

(4) Azimuth and elevation angles of a target with relation to the axes of a tracking aircraft.

(5) Relationships of airplane stability and body axes orientations.

(6) Readings of conventional vertical and directional free gyros in terms of airplane orientation.

References

[1] Hall, A. C., *A Generalized Analogue Computer for Flight Simulation*, Trans. Amer. Inst. Elec. Engrs., Vol. 69, pp. 316, 320, 1950.

[2] Oswald, Telford W., *The Effect of Nonlinear Aerodynamic Characteristics on the Dynamic Response to a Sudden Change in Angle of Attack*, Journal of the Aeronautical Sciences, Vol. 19, No. 5, pp. 302–316, May, 1952.

[3] Frazer, R. A., Duncan, W. J., and Collar, A. R., *Elementary Matrices*, 1st Ed., pp. 251, 255, 284–287; Cambridge University Press, 1938.

[4] Durand, W. F., *Aerodynamic Theory*, 1st Ed., Vol. 5, p. 122; Julius Springer, Berlin, 1934.

[5] Goldstein, H., *Classical Mechanics*, 1st Ed., pp. 132–134; Addison-Wesley Press, 1950.

Notice to Contributors

Manuscripts submitted for publication *must* be double- or triple-spaced originals. There should be wide margins on both sides of the sheets and triple spacing around formulas to allow for the marking of directions for the printer.

Original drawings (jet black India ink on white paper or tracing cloth) should accompany the manuscript. *(Blueprints are not acceptable.)* Photographs *must* be on glossy white paper. The smallest lettering on 8- by 10-in. figures should be no less than 1/4 in. high.

Only the simplest formulas should be typewritten; all others should be carefully written in pen and ink. The difference between capital and lower-case letters and Greek symbols should be clearly distinguished.

See Inside Back Cover of this issue for further details

Minimum Weight Design of a Simply Supported Transversely Stiffened Plate Loaded in Shear*

MALCOLM F. SYMONDS†

University of California at Los Angeles and Northrop Aircraft, Inc.

SUMMARY

A method is developed and presented for the minimum weight design of a simply supported, transversely stiffened plate loaded in shear. It is assumed that the plate resists the ultimate load in an unbuckled or "shear resistant" state. In order to include the effects of plasticity, the curves are drawn for a given material, 24S-T3 aluminum alloy. Curves of the optimum plate shear stress, optimum critical shear stress coefficient, optimum area of stiffener, optimum average plate-stiffener shear stress, and optimum average plate-stiffener thickness are plotted against the structural index for three values of the ratio of stiffener spacing to plate depth.

For a given material, the most significant parameter affecting efficient design appears to be the ratio of stiffener spacing to beam depth. Minimum weight is obtained by using closely spaced stiffeners. The bending efficiency of the stiffener has a small but significant effect on the minimum weight.

Comparisons with other types of shear carrying members show that corrugated plate is more efficient at low values of the structural index. This seems to be analogous to a limiting case of very closely spaced stiffeners. For larger values of the structural index and for closely spaced stiffeners, the nonbuckling plate design is found to be more efficient than the "diagonal tension" type of design where the plate carries the ultimate load in a buckled condition between stiffeners.

SYMBOLS

A = cross-sectional area of stiffener, sq.in.
b = length of stiffener web, in.
C = a dimensionless shape factor measuring the bending efficiency of the stiffener cross section, $C = I/A^2$
d = stiffener spacing, in.
E = modulus of elasticity of plate, psi
E_s = modulus of elasticity of stiffener, psi
h = depth of plate, in.
I = effective moment of inertia of stiffener, in.^{4} $I \approx (I_o + I_x)/2$
I_o = moment of inertia of stiffener about stiffener centroid, in.^{4}
I_x = moment of inertia of stiffener about centroid of plate, in.^{4}
K = critical shear stress coefficient
N = $I/\eta dt^3$
n = ratio of length of stiffener flange to length of stiffener web
q = ultimate shear flow, lb./in.
t = plate thickness, in.
t_s = thickness of stiffener elements, in.
$\bar{t}$ = average plate-stiffener thickness, in. $\bar{t} = t + A/d$
η = plasticity coefficient used to reduce the modulus of elasticity in the plastic range
μ = Poisson's ratio
τ = critical shear stress in plate, psi
τ_y = shear yield stress, psi
$\bar{\tau}$ = average shear stress in plate-stiffener combination, psi
opt = subscript denoting optimum value
min = subscript denoting minimum value
ss = subscript denoting four edges simply supported

Received March 11, 1955.

* Based on a thesis submitted in partial satisfaction of the requirements for the degree of Master of Science in Engineering at the University of California at Los Angeles, June, 1954.

† Formerly, Graduate Student, University of California at Los Angeles, and Research Analyst "A," Structural Research and Development Group, Northrop Aircraft, Inc. Now, Structures Engineer, Hiller Helicopters.

(1) INTRODUCTION

THIS PAPER PRESENTS A METHOD for obtaining the minimum weight design of a simply supported, transversely stiffened plate loaded in shear. The plate is designed to carry the ultimate load in an unbuckled condition.

Methods have been developed[1–4] for the stability analysis of a flat plate with transverse stiffeners loaded in shear. However, these methods assume that the geometry of the structure is known and therefore give no direct information on the efficiency of various arrangements of the components. The problem of minimum weight design must be approached from a different standpoint.

In the general design problem the ultimate shear flow q (the shear load in pounds per inch) and the plate depth h are known quantities. These quantities define q/h, the structural index,[5] which is a measure of the loading intensity on the structure. The effects of the relative size of the structure can be eliminated by use of the structural index. The design problem is to determine the plate thickness, stiffener spacing, and stiffener size and shape which will carry the ultimate load with minimum weight. The effects of these variables are studied in this paper.

Stein and Fralich[1] and Bleich[2] discuss and evaluate work previously done on the stability of simply supported transversely stiffened plates loaded in shear. The stability analysis of Stein and Fralich is the most satisfactory, and their results are used in this paper as a basis for obtaining the minimum weight design.

(2) ANALYSIS AND OPTIMIZATION

(2.1) *Assumptions and Limitations*

(a) The plate is infinitely long. Stein and Fralich consider only infinitely long plates in their solution.[1] However, from a study of similar papers[3, 6] which in-

clude both finite and infinite plates, it is felt that the methods discussed in the present paper are applicable to any plate with four or more panels.

(b) The stiffeners have bending stiffness but zero torsional stiffness. The behavior of most open section stiffeners closely approximates this assumption.

(c) The stiffeners are identical and equally spaced.

(d) Post-buckling behavior of the plate between stiffeners is not considered. The structural efficiency of such "diagonal tension" panels has been considered by Kuhn.[7]

(2.2) *Material Properties*

The general methods developed in this paper apply to any material. However, in order to include the effects of inelastic behavior and also to present the results in a clear manner, a given material is considered. It is assumed that the plate and stiffeners are fabricated from 24S-T3 aluminum alloy. From reference 8, Table 3.111 (a):

Modulus of elasticity, $E = 10.5 \times 10^6$ psi
Tensile yield stress = 48,000 psi

The inelastic buckling theory for shear developed by Stowell[9] is used. The curve of inelastic buckling stress τ versus the fictitious "elastic" buckling stress τ/η is shown in Fig. 1. This curve is used in conjunction with Eq. (1) as explained in Section (2.3). The relationship between τ and the plasticity coefficient η is also plotted in Fig. 1.

A fictitious shear "yield" stress τ_y is obtained from the specified tensile yield stress. This shear "yield" stress is used in Fig. 1 as a reasonable cutoff value for the buckling shear stress in the plate. In other words, it is assumed that the shear stress in the plate cannot exceed the shear "yield" stress. The Mises yield condition[10] is used to obtain the approximate shear "yield" stress from the tensile yield stress:

$$\tau_y = 48{,}000/\sqrt{3} = 27{,}700 \text{ psi}$$

Other yield conditions such as the Tresca yield condition[10] or a yield condition based on a new engineering theory of plasticity developed by Shanley[11] could be used, but these would not appreciably affect the results.

The common assumption that Poisson's ratio $\mu = 0.30$ is made. The small increase of Poisson's ratio in the inelastic range[5] is neglected.

(2.3) *Stability Relationships*

Consider a simply supported, transversely stiffened plate loaded in shear (Fig. 2). Let q be the ultimate shear flow, h the beam depth, d the stiffener spacing, and t the plate thickness. The ultimate shear stress is $\tau = q/t$. For minimum weight the ultimate shear stress will equal the critical shear stress. The structure shown in Fig. 2 can buckle in two ways: local instability of the plate between stiffeners, and general instability of the plate-stiffener system where the buckle pattern includes a number of stiffeners. For minimum weight, both types of buckling occur simultaneously.

The critical shear stress is given by:

$$\tau/\eta = KE(t/h)^2 \tag{1}$$

where K, the critical shear stress coefficient, is plotted in Figs. 3, 4, and 5 as a function of $I/\eta dt^3$ for three values of the ratio of stiffener spacing to beam depth, $d/h = 1.0$, 0.5, and 0.2. Figs. 3, 4, and 5 are a modification of Fig. 1, reference 1. $I/\eta dt^3$ is a simplified form of the ratio of the flexural rigidity of the stiffener to the flexural rigidity of the plate, $12(1-\mu^2)E_sI/\eta Edt^3$. Since it is assumed that the plate and stiffeners are made of the same material, $E_s = E$. The plasticity coefficient η must be included in the denominator of $I/\eta dt^3$ due to the following physical concept. When a stiffened plate is loaded in shear, there is theoretically zero load in the stiffeners until the plate buckles. The plate-stiffener combination is designed to carry the shear load in an unbuckled condition. Therefore, when the shear stress in the plate is in the inelastic range, E is replaced by ηE but E_s remains elastic.

The fictitious "elastic" buckling stress τ/η is computed directly by using Eq. (1). Then the actual inelastic buckling stress τ is obtained as a function of τ/η from Fig. 1 for 24S-T3 aluminum alloy.

A third mode of instability, involving local deformation of the attached leg of the stiffener, is not considered in the theory of reference 1. This mode of buckling can be estimated by use of an empirical method presented in reference 7. Although the curves developed in the present paper consider instability of the plate between stiffeners and general instability of the plate-stiffener system as is done in reference 1, they do not preclude the possibility of local deformation of the attached leg of the stiffener if this leg is too thin. Thus, after the minimum weight design is obtained from the curves of this paper, which are based on moment of inertia considerations for the stiffener, the attached leg of the stiffener should be checked for local deformation by use of Eq. (32) and Fig. 12 of reference 7.

(2.4) *Optimum Relationships*

The minimum weight can be expressed as the minimum cross-sectional area or the minimum average thickness per inch of plate-stiffener system since the density is constant and also since the depth of beam h is constant for a particular design consideration.

The average thickness per inch of plate-stiffener system is:

$$\bar{t} = t + (A/d) \tag{2}$$

For a given value of the shear flow q, the plate thickness t varies inversely with respect to K [see Eq. (1)], while I and therefore A vary directly with K (see Figs. 3, 4, and 5). Thus the variation of $\bar{t}$ with respect to the design variables is rather complex.

The curves relating K to $I/\eta dt^3$ have abrupt changes in slope due to changes in the theoretical buckling patterns as developed by Stein and Fralich.[1] Therefore, the curves in Figs. 3, 4, and 5 cannot be represented

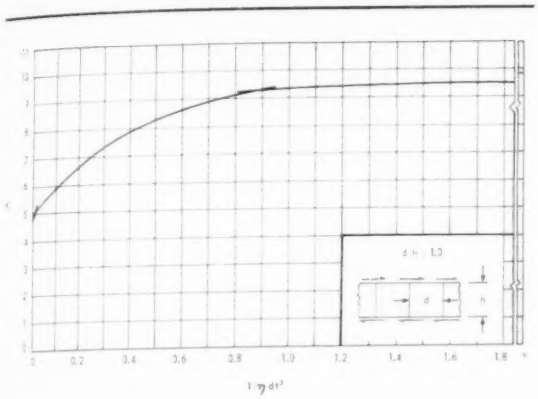

FIG. 1. Inelastic shear buckling curves, 24S-T3 aluminum alloy.

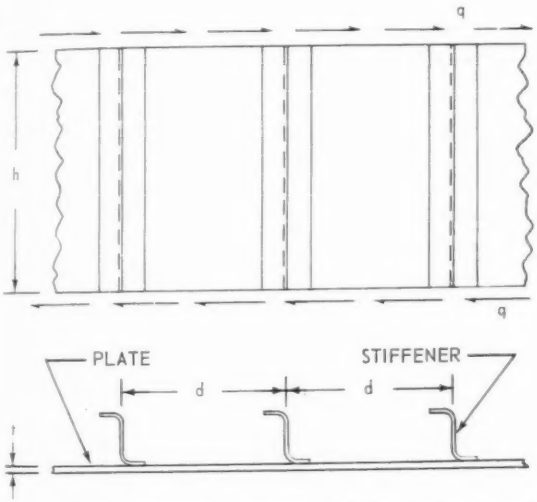

FIG. 2. Simply supported, transversely stiffened plate loaded in shear.

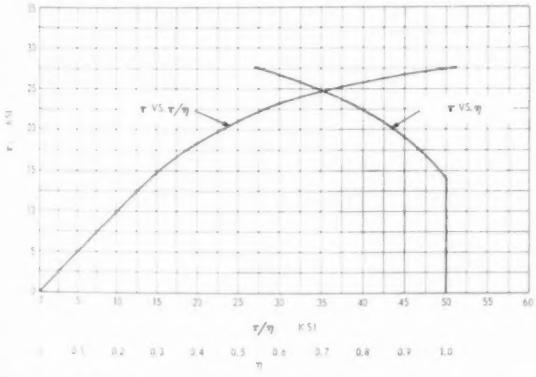

FIG. 3. Critical shear stress coefficient, K, for $d/h = 1.0$.

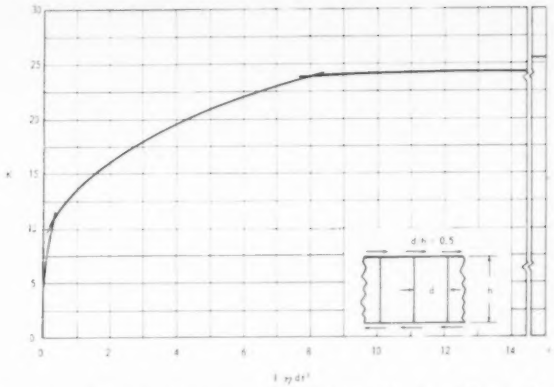

FIG. 4. Critical shear stress coefficient, K, for $d/h = 0.5$.

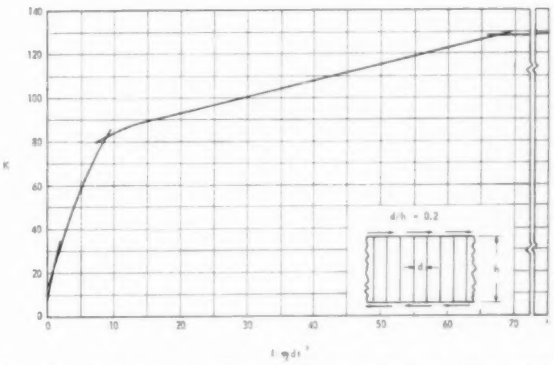

FIG. 5. Critical shear stress coefficient, K, for $d/h = 0.2$.

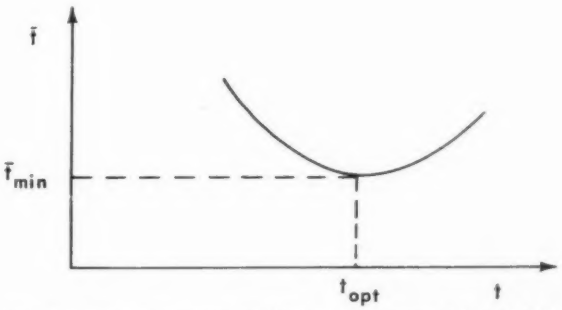

FIG. 6. Typical variation of $\bar{f}$ with t for a given q/h and d/h.

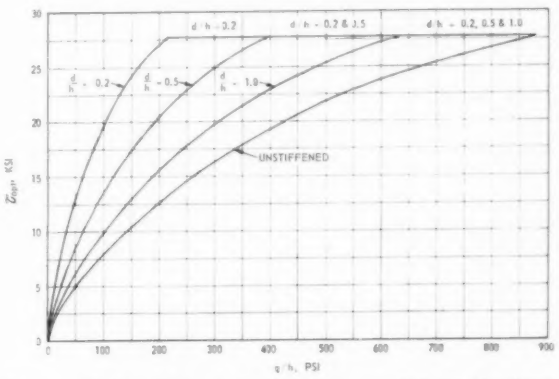

FIG. 7. Optimum plate shear stress, τ_{opt}, 24S-T3 aluminum alloy.

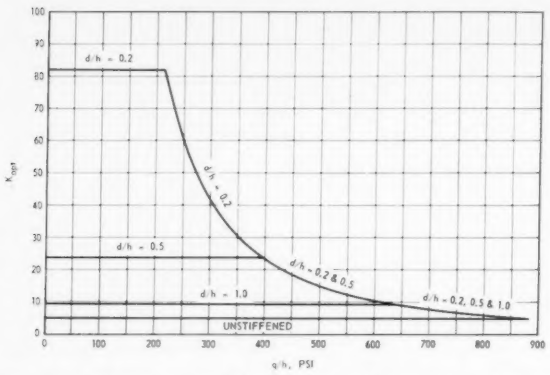

FIG. 8. Optimum critical shear stress coefficient, K_{opt}, 24S-T3 aluminum alloy.

analytically in a simple manner. Bleich[2] has fitted analytical expressions to these curves, but the expressions are extremely unwieldy and only approximately correct. An analytical minimization of the weight using empirical equations for these curves is thus out of the question, and the results would be of dubious validity.

In order to obtain information on the variation of $\bar{l}$ with the design parameters, a series of plate-stiffener combinations was designed for various values of the structural index. For given values of q/h and d/h, the plate thickness was varied until the minimum average thickness was obtained. These design tables are not presented in this paper since they are of value only with respect to the conclusions that are drawn from them. A typical plot of t versus $\bar{l}$ is shown in Fig. 6. When t is less than t_{opt}, the excess weight is due to the large moment of inertia of stiffener required to stabilize the plate. When t is greater than t_{opt}, the excess weight is obviously in the plate itself. It can be seen from Fig. 6 that a small variation in t from t_{opt} has an almost negligible effect on $\bar{l}_{min}$.

An important conclusion can be obtained from these systematic designs. As long as the optimum shear stress in the plate is less than the shear "yield" stress [as defined in Section (2.2)], there is a very narrow range of optimum values of K corresponding to t_{opt} for each value of d/h independent of the structural index q/h. These values of K_{opt} occurred at or extremely close to one of the sharp breaks in slope corresponding to a change in buckle pattern in the curves of Figs. 3, 4, and 5. For practical purposes, one value of K_{opt} corresponding to the sharp break in the curves for each value of d/h can be used, since $\bar{l}_{min}$ is almost constant in the range of t_{opt}. For each d/h, there is also an optimum value of $I/\eta dt^3$ corresponding to K_{opt} in Figs. 3, 4, and 5. These optimum relationships are presented in Table 1.

TABLE 1
Optimum Relationships for Minimum Weight

d/h	K_{opt}	$(I/\eta dt^3)_{opt}$
1.0	9.23	0.867
0.5	23.8	8.05
0.2	82.0	8.80

Table 1 does not apply when the optimum shear stress in the plate equals the shear "yield" stress. For this condition K_{opt} and therefore $(I/\eta dt^3)_{opt}$ decrease as the structural index increases. This relationship is developed in Section (2.5).

By fulfilling the requirements of Table 1, the optimum plate thickness and the optimum stiffener area can be obtained analytically. This is done in Sections (2.5) and (2.6). The overall optimization is then performed in Section (2.7).

(2.5) *Plate Optimization*

The plate buckling stress is given by Eq. (1). For minimum weight, the buckling stress is equal to the ultimate stress, $\tau = q/t$ or $t = q/\tau$. The plate thickness can be eliminated from Eq. (1) by substituting in $t = q/\tau$:

$$\tau/\eta = KE(q/\tau h)^2$$

Rearranging:

$$q/h = [\tau/(KE)^{1/2}]\,(\tau/\eta)^{1/2} \tag{3}$$

For each value of d/h, K_{opt} is a constant for τ_{opt} less than τ_y as shown in Table 1. Eq. (3) can be solved directly by assuming a value of τ_{opt}, reading the corresponding value of τ/η from Fig. 1 and calculating q/h for each d/h by inserting the proper value of K_{opt}. $E = 10.5 \times 10^6$ psi. By repeating this procedure for various values of τ_{opt}, the curves of τ_{opt} versus q/h for $d/h = 1.0$, 0.5, and 0.2 can be constructed and are shown in Fig. 7.

The curve for an infinitely long, simply supported, unstiffened plate is also included in Fig. 7 for comparative purposes. For this case, assuming $\mu = 0.30$, $K = 4.82$.[2, 4]

It can be seen from Fig. 7 that for a given value of q/h, τ_{opt} increases as d/h decreases, as long as τ_{opt} is less than τ_y. Since $t_{opt} = q/\tau_{opt}$, the optimum plate thickness decreases as d/h decreases.

The values of K_{opt} are constant for a given d/h only when τ_{opt} is less than τ_y. As shown in Fig. 7, τ_{opt} reaches τ_y at a definite value of q/h depending upon the d/h ratio. For larger values of q/h, $\tau_{opt} = \tau_y = 27{,}700$ psi. From Fig. 1, $\tau/\eta = 51{,}300$ psi. Inserting these values and $E = 10.5 \times 10^6$ psi into Eq. (3) and rearranging:

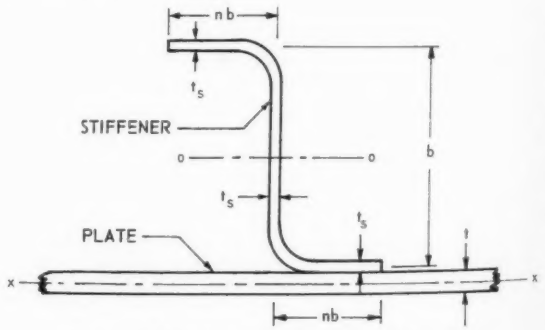

FIG. 9. Stiffener cross section attached to plate.

$$K_{opt} = 3{,}745{,}000/(q/h)^2 \qquad (4)$$

for $\tau_{opt} = \tau_y$.

The optimum values of the critical shear stress coefficient K are plotted in Fig. 8 for the entire range of the structural index by using Table 1 and Eq. (4).

The curves in Figs. 7 and 8 intersect at $q/h = 883$ psi. The physical significance of this is that if the structural index is larger than 883, stability is no longer a problem and strength requirements alone will govern the design. The minimum weight design for this case is obtained by using an unstiffened plate with a thickness $t = q/\tau_y$.

(2.6) *Stiffener Optimization*

Stein and Fralich assume that the stiffeners are symmetrical with respect to the middle plane of the plate in their stability analysis.[1] However, efficient design dictates placing the stiffeners on one side of the plate in order to obtain the required moment of inertia with the least area. The effective axis of bending of the stiffener will lie somewhere between the plate centroidal axis and the stiffener centroidal axis parallel to the plate, depending upon the ratio of the area of stiffener to the area of plate and the buckle pattern.

The actual position of the effective axis of bending of stiffeners located on only one side of a plate loaded in shear has not been theoretically obtained to the author's knowledge. Since the position of the effective axis of bending has a pronounced effect on the required area of stiffener, a method of approximating this position is necessary.

The effective axis of bending of longitudinal stiffeners located on one side of a plate under compression has been investigated by Seide.[12] Since reference 12 contains the only solution available for the problem of stiffeners located on one side of the plate, Seide's results were modified to obtain an approximate solution for plates loaded in shear. A study of the parameters involved in Eq. (4) of reference 12 led to the conclusion that the effective moment of inertia I for stiffeners on one side of a plate loaded in shear could be approximated by the average value of the stiffener moments of inertia about the stiffener centroid and the plate centroid:

$$I = (I_0 + I_z)/2 \qquad (5)$$

The value of I obtained from Eq. (5) is probably slightly conservative for most efficient designs where the area of stiffener is small compared to the area of plate (see Fig. 10).

The flexural rigidity required to prevent general instability of the plate-stiffener combination is expressed as a function of the effective moment of inertia of the stiffener. The minimum weight design is a function of the area of the stiffener. Therefore, a relationship between the effective moment of inertia and the area of the stiffener is needed. This relationship can be obtained by introducing a dimensionless shape factor C defined as follows:

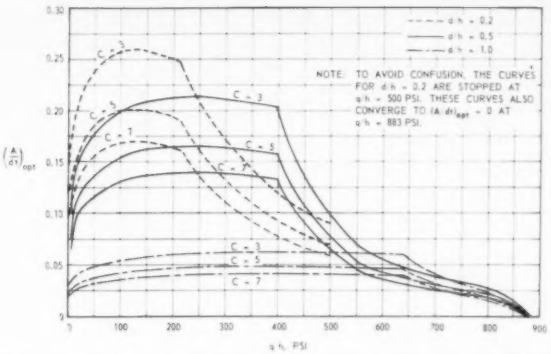

FIG. 10. Optimum stiffener area ratio, $(A/dt)_{opt}$, 24S-T3 aluminum alloy.

$$C = I/A^2 \qquad (6)$$

A practical shape of stiffener will be used in order to obtain an approximate idea of the range of C values encountered in design. A formed Z-section stiffener attached to one side of the plate is chosen, since it is probably as efficient as any other practical stiffener. An integral stiffener is more efficient since no attaching leg is necessary, but such stiffeners are not commonly used today. The thicknesses of all elements of the stiffener are assumed equal. For simplicity, the lengths of the two flanges are assumed equal. A sketch of the stiffener cross section attached to the plate is shown in Fig. 9. By using Eqs. (5) and (6), values of C are computed for $b/t_s = 20$, 30, and 40, and for $n = 0.3$, 0.4, and 0.5. The results are shown in Table 2. Since the parameters used in Table 2 cover the practical range of efficiently designed Z-section stiffeners, values of C equal to 3, 5, and 7 are chosen for use in the stiffener optimization.

It should be emphasized at this point that the method of minimum weight design developed in this paper is not restricted to Z-section stiffeners but can be applied to any shape stiffener by using the appropriate value of C. Z-section stiffeners are considered only because they are commonly used and are an efficient practical cross section. Also the effective moment of inertia I could be calculated by a method different from Eq. (5) if desired. The effect would be a change in the value of C for a given stiffener.

The stiffener optimization can now be performed. For convenience, let $N = I/\eta dt^3$. From Eq. (6), $I = CA^2$. Thus:

$$N = I/(\eta dt^3) = CA^2/(\eta dt^3) \qquad (7)$$

TABLE 2
Values of C for Z-Section Stiffeners

n	b/t_s	A/t_s^2	I/t_s^4	C
0.3	20	32	3,980	3.89
	30	48	12,830	5.57
	40	64	29,720	7.25
0.4	20	36	4,650	3.59
	30	54	15,000	5.15
	40	72	34,770	6.71
0.5	20	40	5,310	3.32
	30	60	17,170	4.77
	40	80	40,820	6.38

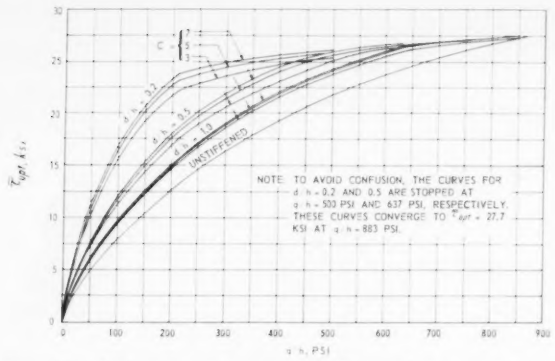
C
d/h = 0.2
d/h = 0.5
d/h = 1.0
UNSTIFFENED
NOTE: TO AVOID CONFUSION, THE CURVES FOR d/h = 0.2 AND 0.5 ARE STOPPED AT q/h = 500 PSI AND 637 PSI, RESPECTIVELY. THESE CURVES CONVERGE TO τ̄opt = 27.7 KSI AT q/h = 883 PSI.
τ̄opt, KSI
q/h, PSI

FIG. 11. Optimum average plate-stiffener shear stress, $\bar{\tau}_{opt}$, 24S-T3 aluminum alloy.

Substituting $t = q/\tau$ for one of the t's in Eq. (7) and multiplying both sides of Eq. (7) by h/d:

$$N(h/d) = (CA^2\tau/\eta dt^2 q)\,(h/d) = C(A/dt)^2\,[(\tau/\eta)/(q/h)] \quad (8)$$

Rearranging Eq. (8):

$$(A/dt)^2 = [N(h/d)\,(q/h)]/[C(\tau/\eta)] \quad (9)$$

For given values of q/h and d/h, values of $(A/dt)_{opt}$ can be obtained for various values of C by using Eq. (9) and the procedure explained below.

Procedure for solving Eq. (9):

(a) τ_{opt} less than τ_y:
  (1) Assume values of q/h, d/h, and C.
  (2) Obtain τ_{opt} from Fig. 7 for the values of q/h and d/h considered.
  (3) Obtain τ_{opt}/η from Fig. 1.
  (4) Obtain N_{opt} from Table 1 for the value of d/h considered.
  (5) Solve Eq. (9) for $(A/dt)_{opt}$.

(b) τ_{opt} equal to τ_y:
  (1) Assume values of q/h, d/h, and C.
  (2) If Fig. 7 shows that $\tau_{opt} = \tau_y = 27{,}700$ psi, then $\tau_{opt}/\eta = 51{,}300$ psi from Fig. 1.
  (3) Obtain K_{opt} from Fig. 8.
  (4) Obtain N_{opt} from Figs. 3, 4, or 5 for the values of K_{opt} and d/h under consideration.
  (5) Solve Eq. (9) for $(A/dt)_{opt}$.

A plot of Eq. (9) for the full range of the structural index is shown in Fig. 10.

(2.7) *Overall Optimization*

The average thickness of the plate-stiffener combination $\bar{t}$ is given by Eq. (2). The average shear stress in the plate-stiffener combination is expressed as:

$$\bar{\tau} = q/\bar{t} \quad (10)$$

The shear flow can also be written as $q = \tau t$. Substituting this value and Eq. (2) into Eq. (10):

$$\bar{\tau} = \tau t/[t + (A/d)] = \tau/[1 + (A/dt)] \quad (11)$$

For given values of q/h, d/h, and C, τ_{opt} is obtained from Fig. 7 and the corresponding value of $(A/dt)_{opt}$ is obtained from Fig. 10. $\bar{\tau}_{opt}$ is then found by substituting these values of τ_{opt} and $(A/dt)_{opt}$ into Eq. (11). A plot of the resulting values of $\bar{\tau}_{opt}$ is shown in Fig. 11.

$\bar{\tau}_{opt}$, not τ_{opt}, is a true measure of the structural efficiency of the plate-stiffener combination, since it includes the area of the stiffener. Therefore, when comparing the relative efficiency of different configurations, $\bar{\tau}_{opt}$ (Fig. 11) should be used. However for design it is usually more convenient to work directly in terms of τ_{opt} (Fig. 7) and $(A/dt)_{opt}$ (Fig. 10).

For weight estimation purposes, it is desirable to have curves showing the variation of $\bar{t}_{min}$ with the structural index. Such curves can be obtained from Fig. 11 by dividing values of the abscissa q/h by corresponding values of the ordinate $\bar{\tau}_{opt}$:

$$(q/h)\bar{\tau}_{opt} = (q/\bar{\tau}_{opt})/h = (\bar{t}/h)_{min} \quad (12)$$

These curves are plotted in Fig. 12.

(3) EXAMPLE

The use of the curves developed in this paper will be illustrated by an example.

Design Data:

Plate depth, $h = 10$ in.
Ultimate shear flow, $q = 2{,}000$ lb./in.
No restrictions on stiffener spacing d.

A Z-section stiffener will be used with $b/t_s = 20$ and $n = 0.5$. From Table 2, $C = 3.32$. The structural index is:

$$q/h = 2{,}000/10 = 200 \text{ psi}$$

First, a weight comparison of various stiffener spacings will be made. From Fig. 12:

Unstiffened: $\bar{t}/h = 0.0158$, $t = 0.158$ in.
Stiffened: $d/h = 1.0$, $\bar{t}/h = 0.01355$, $\bar{t} = 0.1355$ in.
Stiffened: $d/h = 0.5$, $\bar{t}/h = 0.0115$, $\bar{t} = 0.115$ in.
Stiffened: $d/h = 0.2$, $\bar{t}/h = 0.00915$, $\bar{t} = 0.0915$ in.

It can be seen that considerable weight savings can be obtained by using closely spaced stiffeners. However, fabrication or cost considerations might make wider spaced stiffeners more desirable. Therefore, for com-

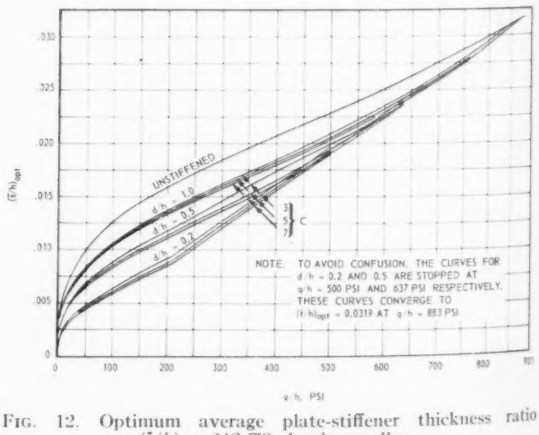
(t̄/h)opt
UNSTIFFENED
d/h = 1.0
d/h = 0.5
d/h = 0.2
C
NOTE: TO AVOID CONFUSION, THE CURVES FOR d/h = 0.2 AND 0.5 ARE STOPPED AT q/h = 500 PSI AND 637 PSI RESPECTIVELY. THESE CURVES CONVERGE TO (t̄/h)opt = 0.0319 AT q/h = 883 PSI.
q/h, PSI

FIG. 12. Optimum average plate-stiffener thickness ratio $(\bar{t}/h)_{opt}$, 24S-T3 aluminum alloy.

TABLE 3

Optimum Plate-Stiffener Designs, q = 2,000 lbs./in., h = 10 in., q/h = 200 psi, 24S-T3 Aluminum Alloy

d/h	d $(d/h)h$, in.	τ_{opt} Fig. 7, psi	t_{opt} q/τ_{opt}, in.	$(A/dt)_{opt}$ Fig. 10	A_{opt} $(A/dt)dt$, in.^{2}	$t_s\sqrt{A/40}$ (Table 2), in.	b $20t_s$, in.	nb $0.5b$, in.
1.0	10	15,550	0.1287	0.057	0.0734	0.0428	0.856	0.428
0.5	5	20,500	0.0975	0.200	0.0975	0.0494	0.988	0.494
0.2	2	27,050	0.0740	0.236	0.0349	0.0296	0.592	0.296

parative purposes, designs will be obtained for an unstiffened plate and for stiffened plates with d/h = 1.0, 0.5, and 0.2.

Unstiffened Plate:

For this case $\bar{t} = t$ and the design consists merely of using a plate with a thickness t = 0.158 in.

Stiffened Plate: See Table 3.

Scale drawings of the cross sections of the four designs are shown in Fig. 13 to give a visual idea of the relative sizes considered. Practical considerations that would affect the above idealized designs are briefly discussed in the following section.

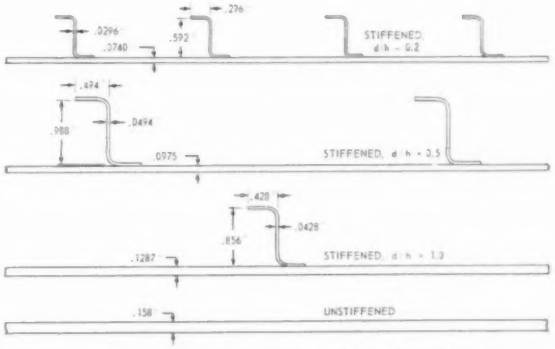

FIG. 13. Scale drawings of cross sections of optimum plate-stiffener combinations designed in Section (3). q = 2,000 lbs./in., h = 10 in., q/h = 200 psi, 24S-T3 aluminum alloy.

(4) Discussion and Comparisons

(4.1) Practical Considerations

There are many practical considerations that introduce nonoptimum weight into the plate-stiffener combinations. The use of standard plate thicknesses is one of these factors. When choosing a standard plate thickness, both the thickness above and the thickness below the optimum thickness should be considered. Since the required value of K varies with the plate thickness, Fig. 3, 4, or 5 should be used to obtain the required moment of inertia of stiffener to stabilize the standard plate thickness chosen.

The stiffeners designed in Section (3) would probably have to be modified slightly to obtain the required length of flange to allow for proper edge distance and clearance for the rivets attaching the stiffener to the plate.

Usually a minimum allowable plate thickness and stiffener thickness are specified in design requirements. If the required stiffener moment of inertia is small, minimum stiffener thickness requirements might make a simpler stiffener cross section, such as an angle, more efficient than a Z-section stiffener. The requirement of minimum length of attaching stiffener leg would also favor a simple angle section if the stiffener moment of inertia is small.

Since the above factors would be influenced by specific design requirements of various organizations, they will not be discussed in any further detail in this paper.

As discussed in Section (2.3), the minimum weight design should be checked for local deformation of the attached leg of the stiffener. A check of the stiffeners shown in Fig. 13 by the empirical method given in reference 7 reveals that local deformation of the attached leg is likely to occur before the design shear load is reached. Therefore, the thickness of the attached leg would probably have to be increased somewhat, and a weight penalty would be introduced. In effect, the stiffeners in the final design would have a lower C value than that chosen for the example.

(4.2) Importance and Effects of Design Variables

The stiffener spacing is the most important design variable affecting minimum weight. From an inspection of Fig. 12, it can be seen that minimum weight design is obtained by using closely spaced stiffeners. This is due to the fact that close stiffener spacing develops a high value of the optimum critical shear stress coefficient (Table 1) which in turn reduces the required plate thickness considerably for a given value of the structural index. Since about 75 to 95 per cent of the total weight of an optimum designed structure is in the plate [see Eq. (2) and Fig. 10], the importance of using closely spaced stiffeners is evident.

This paper considers only structural optimization for minimum weight. In many cases other factors such as minimum cost and ease of fabrication have an important effect on the optimum structural design. Thus in practical design a wider stiffener spacing might be chosen which would introduce a weight penalty. This excess weight can be easily calculated by using Fig. 12.

The bending efficiency of the stiffener has a relatively small effect on the minimum weight as can be seen from Fig. 12. However, all the Z-section stiffeners considered in this paper are reasonably efficient. If an inefficient stiffener cross section is chosen, say, an angle stiffener that has a C value of about 1, the effect of the bending efficiency would become a more important consideration.

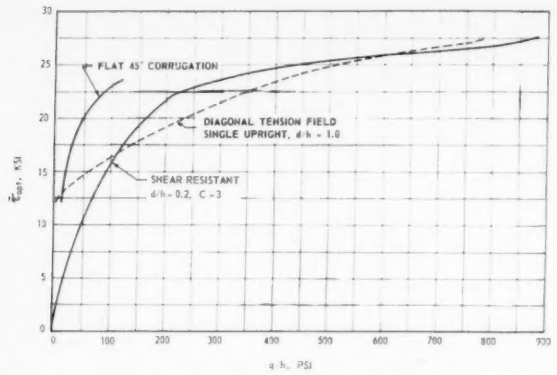

FIG. 14. Comparison of several types of shear carrying structures, 24S-T3 aluminum alloy.

(4.3) Comparisons with Other Types of Shear Carrying Structures

Two other types of efficient shear carrying structures are the corrugated shear panel and the diagonal tension field plate stiffener combination. Some data on the efficiency of 24S-T flat 45° corrugated shear panels are presented in Fig. 2.11 of reference 5. This curve is replotted in Fig. 14.

The diagonal tension field structure is composed of a flat plate with transverse stiffeners. The flat plate carries the ultimate shear flow in a buckled condition between stiffeners. This causes additional tensile stresses in the plates and compressive stresses in the stiffeners. The efficiency of such structures has been considered by Kuhn.[7] Kuhn concluded that the stiffener spacing ($d/h = 0.25$ or $d/h = 1.0$) on tension field structures has little effect on the optimum average shear stress for 24S-T3 aluminum alloy. He also found that single or double stiffeners are about equally efficient. For comparative purposes, the curve of $\bar{\tau}_{opt}$ for single uprights with $d/h = 1.0$ is replotted from Fig. 23(a) of reference 7 and presented in Fig. 14.

The curve of $\bar{\tau}_{opt}$ for $d/h = 0.2$ and $C = 3$ for the nonbuckling or "shear resistant" plate design developed in this paper is plotted in Fig. 14 for comparison with the aforementioned types of structure. It can be seen from Fig. 14 that for small values of the structural index, the corrugated shear panel is considerably more efficient than either of the other designs. The tension field structure is also more efficient than the shear resistant structure in this range. For larger values of the structural index, the shear resistant type of design is more efficient than the tension field type as long as closely spaced stiffeners are used. For very large values of the structural index, the tension field and shear resistant designs tend to compare fairly close. This is due to the fact that as the structural index increases, the tension field structure carries a larger percentage of the ultimate shear flow in the nonbuckled condition.

If the corrugated shear panel curve from Fig. 14 is superimposed on Fig. 11, it appears to be an upper bound to the efficiency of nonbuckling shear carrying structures. Since the trend of increased efficiency with closely spaced stiffeners is established in Fig. 11, the corrugated shear panel might be thought of as the limiting case of nonbuckling shear structures with very closely spaced stiffeners.

A comparison of the optimum stiffener area ratio for shear resistant structures (Fig. 10) with that for tension field structures [Fig. 23(a), reference 7] shows that for low values of the structural index the shear resistant structures have considerably smaller values of $(A/dt)_{opt}$. For larger values of the structural index, $(A/dt)_{opt}$ is about the same for both types of structure.

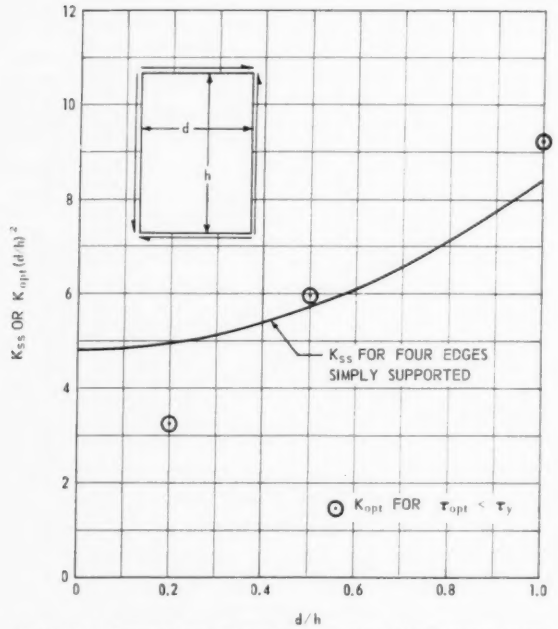

FIG. 15. Comparison of optimum critical shear stress coefficient, K_{opt}, with the critical shear stress coefficient for a panel with four edges simply supported, K_{ss}.

(4.4) Relative Efficiency of Designing Stiffeners to Divide Plate into Simply Supported Panels

A commonly used design assumption is that the stiffeners divide the plate into a series of simply supported panels. The critical shear stress is obtained as:

$$\tau/\eta = K_{ss}E\,(t/d)^2 \qquad (d \leq h) \qquad (13)$$

where K_{ss} is the critical shear stress coefficient for simply supported panels.[2, 4] K_{ss} is plotted in Fig. 15 as a function of d/h.

It is interesting to compare the value of K_{opt} shown in Table 1 with K_{ss} in Eq. (13). Since K_{opt} is used in Eq. (1), it must be multiplied by $(d/h)^2$ in order to compare directly with K_{ss} in Eq. (13). The comparison is shown in Fig. 15. It is seen that for $0.5 \leq d/h \leq 1.0$, the assumption of simply supported panels gives a design close to the minimum weight design. However, for closely spaced stiffeners, considerable nonoptimum weight is introduced if it is assumed that the stiffeners divide the plate into simply supported panels. If $\tau_{opt} = \tau_y$, K_{opt} decreases with increasing values of the

structural index as shown in Fig. 8. This would make the assumption of simply supported panels even more inefficient for closely spaced stiffeners.

The required moment of inertia of stiffener to divide the plate into simply supported panels is obtained by entering Figs. 3, 4, or 5 with $K_{ss}\,(h/d)^2$ where K_{ss} is obtained from Fig. 16.

(5) Conclusions

(a) A method is developed and presented for the minimum weight design of a simply supported, transversely stiffened plate loaded in shear. The plate carries the ultimate load in an unbuckled condition.

(b) Minimum weight design is obtained by using closely spaced stiffeners.

(c) For the ratios of stiffener spacing to plate depth considered (d/h = 0.2, 0.5, and 1.0), the plate contains approximately 75 to 95 per cent of the total weight for minimum weight design.

(d) Since the stiffeners contain a small percentage of the total weight, the bending efficiency of the stiffeners has a relatively small effect on the minimum weight design.

(e) Practical considerations, such as ease of fabrication or cost, might make wider stiffener spacings more desirable. This would involve a weight penalty that could be calculated by the methods developed in this paper.

(f) Comparisons with other types of shear carrying members show that corrugated plate is more efficient at low values of the structural index. This seems to be analogous to the limiting case of very closely spaced stiffeners. For larger values of the structural index and for closely spaced stiffeners, the nonbuckling plate design is found to be more efficient than the "diagonal tension" type of design.

(g) The commonly used assumption that the stiffeners divide the plate into a series of simply supported panels results in a design close to the minimum weight design for stiffeners spaced fairly wide apart ($0.5 \leq d/h \leq 1.0$). However, excess weight is introduced if this assumption is used for closely spaced stiffeners, where minimum weight design is obtained when the stiffeners provide considerably less than simple support for the panels between stiffeners.

References

[1] Stein, Manuel, and Fralich, Robert W., *Critical Shear Stress of Infinitely Long, Simply Supported Plate with Transverse Stiffeners*, NACA TN 1851, April, 1949.

[2] Bleich, F., *Buckling Strength of Metal Structures*, 1st Ed., Chap. XI; McGraw-Hill Book Company, Inc., New York, 1952.

[3] Wang, T. K., *Buckling of Transversely Stiffened Plates Under Shear*, Journal of Applied Mechanics, Vol. 14, No. 4, pp. A-269–A-274, December, 1947.

[4] Timoshenko, S., *Theory of Elastic Stability*, 1st Ed., Chap. VII; McGraw-Hill Book Company, Inc., New York, 1936.

[5] Shanley, F. R., *Weight-Strength Analysis of Aircraft Structures*, 1st Ed., Part I; McGraw-Hill Book Company, Inc., New York, 1952.

[6] Budiansky, Bernard, and Seide, Paul, *Compressive Buckling of Simply Supported Plates with Transverse Stiffeners*, NACA TN 1557, April, 1948.

[7] Kuhn, Paul, Peterson, James P., and Levin, L. Ross, *A Summary of Diagonal Tension, Part I—Methods of Analysis*, NACA TN 2661, May, 1952.

[8] Anon., *Strength of Metal Aircraft Elements*, ANC-5, Munitions Board Aircraft Committee, U.S. Government Printing Office, Washington, D. C., June, 1951.

[9] Stowell, E. Z., *Critical Shear Stress of an Infinitely Long Plate in the Plastic Region*, NACA TN 1681, August, 1948.

[10] Prager, William, and Hodge, Philip G., Jr., *Theory of Perfectly Plastic Solids*, Chap. 1; John Wiley & Sons, Inc., New York, 1951.

[11] Shanley, F. R., *An Engineering Theory of Plasticity*, (unpublished paper), February, 1954.

[12] Seide, Paul, *The Effect of Longitudinal Stiffeners Located on One Side of a Plate on the Compressive Buckling Stress of the Plate-Stiffener Combination*, NACA TN 2873, January, 1953.

Stability of a Flexible Helicopter Rotor Blade in Forward Flight

(Continued from page 670)

(4) Inclusion of a δ_3 hinge.

(5) Revision of the small angle assumption.

(6) When more basic knowledge about unsteady lift distribution on rotor blades is gained, it should be included, although it would probably not affect the results appreciably.

Since it was shown that a high-speed electronic computer was used successfully to obtain numerical solutions of the complicated equations, this device may be used to advantage in solving the more complicated equations that will result from inclusion of the above-mentioned refinements.

References

[1] Hohenemser, K., *Some Aerodynamic and Dynamic Problems of the Compound Rotary-Fixed-Wing Aircraft*, Eighth Annual Forum of the American Helicopter Society, Inc., p. 152, May, 1952.

[2] Glauert and Shone, RAE Report BA 1080, 1933.

[3] Bennett, J. A. J., *Rotary Wing Aircraft*, Aircraft Engineering, Vol. XII, No. 135, p. 139, May, 1940.

[4] Horvay, G., *Rotor Blade Flapping Motion*, Quarterly of Applied Mathematics, Vol. V, No. 2, p. 149, July, 1947.

[5] Parkus, H., *The Disturbed Flapping Motion of Helicopter Rotor Blades*, Journal of the Aeronautical Sciences, Vol. 15, No. 2, pp. 103–106, February, 1948.

[6] Flax, A. H., *The Bending of Rotor Blades*, Journal of the Aeronautical Sciences, Vol. 14, No. 1, pp. 42–50, January, 1947.

[7] Morse, P. M., and Feshbach, H., *Methods of Theoretical Physics*, Vol. I, Ch. 5; McGraw-Hill Book Company, Inc., New York, 1953.

[8] Draper, C. S., McKay, W., and Lees, S., *Instrument Engineering*, Vol. II, Ch. 20; McGraw-Hill Book Company, Inc., New York, 1953.

[9] Morduchow, M., *A Theoretical Analysis of Elastic Vibrations of Fixed Ended and Hinged Helicopter Blades in Hovering and Vertical Flight*, NACA TN 1999, January, 1950.

Readers' Forum

BRIEF REPORTS of investigations in the aeronautical sciences and discussions of papers published in the JOURNAL are presented in this special department. Entries must be restricted to a maximum of 1,300 words or the equivalent of one JOURNAL page including formulas and illustrations. Publication is completed as soon as possible after receipt of the material. The Editorial Committee does not hold itself responsible for the opinions expressed by the correspondents.

Contents

Comparison of Radiant and Conductive Heat Transfer in a Supersonic Wing ..... N. J. Hoff 694

The Effect of Shape on the Orthotropic Characteristics of a Rectangular Plate ..... Wasfi A. Hijab 696

Forced Convection of Heat from Cylinders at Low Reynolds Numbers ..... D. C. Collis 697

A Note on Transient Aerodynamic Heating ..... Eugene Covert and Frank Durgin 699

Inviscid Leading-Edge Effect in Hypersonic Flow ..... H. K. Cheng and A. J. Pallone 700

Supplementary Note on Turbulent Velocity Fluctuations ..... Heinrich B. Helmbold 702

Note on Photothermoelasticity ..... George Gerard and Arthur C. Gilbert 702

An Experimental Investigation of the Boundary-Layer Flow on a Rotating Flat Plate ..... Jerome Persh and A. Wiley Sherwood 703

On Linearized Transonic Flow Theory for Slender Bodies ..... John W. Miles 704

Erratum—"Subsonic Influence of Compressibility on the Pressure Distribution of a Profile" ..... F. S. Weinig 705

A Method for the Solution of an Eigenvalue Problem with a Complex Matrix ..... Ta Li 705

Notes on the Calculation of the Subsonic Downwash and Sidewash Angles Near Wings ..... Raymond F. Anderson 707

Comparison of Radiant and Conductive Heat Transfer in a Supersonic Wing

N. J. Hoff*

Head, Department of Aeronautical Engineering and Applied Mechanics, Polytechnic Institute of Brooklyn, Brooklyn, N.Y.

January 2, 1956

As the radiation of heat is proportional to the fourth power of the absolute temperature of the radiating body while conduction depends only on the gradient of the temperature but is independent of its absolute value, the problem of the simultaneous transfer of heat by the two processes is difficult to solve. The purpose of the present study is to establish the order of magnitude of the amount of heat transferred in a wing structure by each of the processes alone and to compare the results so obtained.

To provide a sufficiently simple model, the wing structure of Fig. 1 was devised; it was assumed to be infinitely long perpendicular to the plane of the figure. Originally, the structure had a uniform temperature T_0; at $t = 0$, the temperature of the coverplates was suddenly raised to T_c, and thereafter it was maintained at that uniform temperature.

According to the Stefan-Boltzmann law, the total heat emitted per unit time by a perfectly black surface of unit length perpendicular to the plane of the figure and of length dy in the y direction is

$$dq = \sigma dy\, T_c^4 \tag{1}$$

where T_c is the temperature of the coverplate and σ is Boltzmann's constant

$$\sigma = 0.174 \times 10^{-8} \text{ B.t.u./hr. ft.}^2 \text{ °F.}^4 \tag{2}$$

This heat is radiated in every direction in the half space faced by the surface. But as long as conditions are identical everywhere along the perpendicular to the plane of the figure, exactly as much heat is lost to other sections as is recovered from them.

* The author is indebted to Professor F. V. Pohle for checking his calculations.

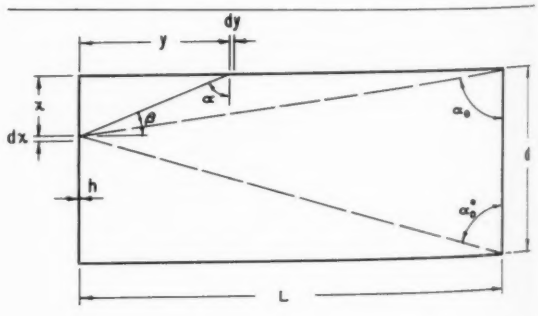

FIG 1

TABLE 1

Proportionality Factors at Eighth Points of Web

x/d =	0	1/8	1/4	3/8	1/2	5/8	3/4	7/8	1
$2 - \cos\alpha_0 - \cos\alpha_0^*$ =	1.553	1.537	1.5245	1.517	1.516	1.517	1.5245	1.537	1.553

It is permissible therefore to assume that the heat rays are parallel to the plane of the figure; this assumption of plane radiation greatly simplifies the calculations and at the same time leads to rigorous results.

Next it is assumed that Lambert's law holds[1]—that is, the radiating surface appears equally bright from every direction. Then the intensity of the radiation along a line subtending an angle α with the normal to the radiating surface is $k \cos\alpha$ if it is k along the surface normal. The total radiation emitted is

$$\int_{-\pi/2}^{+\pi/2} T_c^4\, dy\, k \cos\alpha\, d\alpha = 2kT_c^4 dy \tag{3}$$

As the right-hand members of Eqs. (1) and (3) must be equal, $k = \sigma/2$. The radiation reaching the area $1 \times dx$ is

$$dq_1 = (1/r)\, T_c^4 dy \times 1 \times k \cos\alpha\, dx \cos\beta \tag{4}$$

As at the same time the area $1 \times dx$, whose temperature is T, also radiates heat, the net gain in heat of area $1 \times dx$ is

$$dq_2 = (1/r)\,(T_c^4 - T^4) dx\, dy \cos\alpha \cos\beta \tag{5}$$

The net gain in heat of area $1 \times dx$ because of radiative heat exchange with the entire flange can be obtained through integration during which x is held constant and y is varied. Manipulations yield

$$dq_2 = \int_0^{\alpha_0} (T_c^4 - T^4) k\, dx \sin\alpha\, d\alpha = (T_c^4 - T^4) k\, dx \times (1 - \cos\alpha_0) \tag{6}$$

where

$$\alpha_0 = \tan^{-1}(L/x) \tag{7}$$

At the same time area $1 \times dx$ receives radiation from the lower coverplate. As the temperature of this coverplate is also maintained constant at T_c, the total gain in heat of area $1 \times dx$ is

$$dq_4 = k(T_c^4 - T^4) dx (2 - \cos\alpha_0 - \cos\alpha_0^*) \tag{8}$$

where

$$\alpha_0^* = \tan^{-1}[L/(d - x)] \tag{9}$$

For the time being, it is assumed that the radiation between the two shear webs is small as compared to the radiation just calculated and thus it can be neglected. It is also assumed that the heat conductivity of the material is zero. Under these conditions, the net gain in heat of the surface $1 \times dx$ increases the temperature of the material. Hence

$$dT/dt = dq_4/c\ \rho g h\, dx \tag{10}$$

where ρ is the density of the material and c its specific heat, g is the gravity constant and h the wall thickness of the shear web. Substitution from Eq. (8) yields the differential equation

$$dT/dt = D(T_c^4 - T^4) \tag{11}$$

with

$$D = (k/c\rho g h)(2 - \cos\alpha_0 - \cos\alpha_0^*) \tag{12}$$

In this equation, the variables can be separated

$$dT/(T_c^4 - T^4) = D\, dt \tag{13}$$

Integration gives

$$\frac{1}{4DT_c^3}\left(\log\frac{T_c + T}{T_c - T} + 2\tan^{-1}\frac{T}{T_c} = t + C\right) \tag{14}$$

where C is a constant of integration. If the initial condition is taken into account, one obtains

$$t = \frac{1}{4DT_c^3}\left[\log\left(\frac{1 + r}{1 + r_0}\frac{1 - r_0}{1 - r}\right) + 2(\tan^{-1} r - \tan^{-1} r_0)\right] \tag{15}$$

where

$$r = T/T_c \tag{16}$$

$$r_0 = T_0/T_c$$

In a numerical example, it was assumed that the wing section had an L/d ratio of 2, was built of steel, and had a web thickness of $^1/_{16}$ in. With

$$k = \sigma/2 = 0.87 \times 10^{-9}\ \text{B.t.u. hr.}^{-1}\ \text{ft.}^{-2}\ °\text{F.}^{-4}$$

$$\rho g = 0.283\ \text{lb. in.}^{-3}$$

$$c = 0.125\ \text{B.t.u. lb.}^{-1}\ °\text{F.}^{-1}$$

$$T_c = 1000°R$$

one obtains

$$(2 - \cos\alpha_0 - \cos\alpha_0^*)/4DT_c^3 = 5.48\ \text{min.}$$

The values of the numerator have been computed for the eighth points and are presented in Table 1.

It can be seen that the heat gain through radiation is almost uniform along the web of this particular box beam. This justifies the procedure of disregarding the radiative heat exchange between the webs. In the middle of the web, one has $^1/_4 DT_c^3 = 3.62$ min.

It was next assumed that the initial temperature of the box beam was −60°F. At $t = 0$, the coverplate temperature was assumed to be raised to some value between 340°F. and 1,340°F. and the time was calculated after which the middle of the web gained half as much in temperature as the coverplate. The results of the computations are given in Table 2. As $1/D$ is proportional to h, the time necessary to reach any particular temperature is increased by a factor f if the thickness of the web is increased by the same factor.

For the sake of comparison, the heat transfer by conduction from coverplate to web was also investigated. The material was assumed to have a finite conductivity. The thermal connection between coverplate and web was taken as perfect, and all radiant heat transfer was disregarded. The entire structure was assumed to be at the uniform temperature T_0 when $t < 0$; at $t = 0$, the temperature of the coverplate was suddenly raised to T_c, and it was maintained at that level thereafter. The solution for the temperature distribution in the web was taken from reference 2

$$T = T_0 + (T_c - T_0)\, erfc(x/2\sqrt{at}) \tag{17}$$

where a is the diffusivity of the material. For steel, its value is $a = 1.116$ in.^{2}/min. Eq. (17) was derived for the semi-infinite solid; but as heat penetrates slowly into the web, the temperature of its middle is little affected during the periods of heating here considered. Hence the interaction between the heat flowing from the two coverplates can be disregarded, Eq. (17) need not be modified, and the average temperature of the web can be calculated from the expression

$$T_{ave} = T_0 + (T_c - T_0)(2/d)\int_0^{d/2} erfc(x/2\sqrt{at})\, dx \tag{18}$$

Integration gives

$$T_{ave} = T_0 + (T_c - T_0)(2/d)\sqrt{at}\,[1.1284 - 2\, ierfc(d/4\sqrt{at})] \tag{19}$$

For the numerical example, d was taken as 8 in. The average web temperature was computed for the heating periods listed in Table 2. The results of the computations are presented in Table 3.

TABLE 2

Temperature Rise Because of Radiation

T_c °F.	340	540	740	940	1140	1340
ΔT_{middle} °F.	200	300	400	500	600	700
t min.	8.51	4.87	3.04	2.02	1.4	1.015

TABLE 3

Temperature Rise Because of Conduction

t min	8.51	4.87	3.04	2.02	1.4	1.015
T_c°F.	340	540	740	940	1140	1340
ΔT_{ave} °F.	264	361	390	412	419	418

If Table 3 is compared with Table 2, one can see that the rise in average temperature due to conduction is 1.32 times that due to radiation when $T_c = 340$°F.; but at $T_c = 1{,}340$°F., radiation transfers 1.67 times as much heat as does conduction. The effect of a change in the thickness of the web can be easily determined. From Eqs. (12) and (15), the time necessary to reach the temperature previously established increases in proportion to h when radiation alone is considered. On the other hand, in Eq. (19) the increase in temperature is proportional to the square root of the time if the second term in the brackets is disregarded. Hence, an increase in web thickness increases the share of conduction in the heat-transfer phenomenon.

REFERENCES

[1] Jakob, Max, *Heat Transfer*, p. 27; John Wiley and Sons, Vol. 1, 1949.

[2] Carslaw, H. S., and Jaeger, J. C., *Conduction of Heat in Solids*, p. 43; Clarendon Press, Oxford, 1947.

The Effect of Shape on the Orthotropic Characteristics of a Rectangular Plate*

Wasfi A. Hijab†

Department of Engineering Mechanics, College of Engineering, University of Florida, Gainesville, Fla.

February 2, 1956

SUMMARY

Timoshenko's method for the solution of the plane stress problem of an isotropic rectangular plate with a parabolic loading on two opposite sides is employed to solve its orthotropic analog. It is found that, while the stress distribution of a square or nearly square plate is determined to a significant degree by the elastic constants of the material, the elastic constants play a negligible role in determining the stress distribution of a plate whose width is small compared to its length. Thus, the distinction between orthotropic and isotropic materials tends to disappear in such structures as bars.

SYMBOLS

ϕ	=	stress function
S	=	maximum normal stress at the boundary
$c_1, c_2, c_3, \ldots$	=	parameters of assumed stress function
V	=	strain energy
V_0	=	strain energy per unit volume
$\sigma_x, \sigma_y, \tau_{xy}$	=	stress components
$\epsilon_x, \epsilon_y, \gamma_{xy}$	=	strain components
E_x, E_y, G_{xy}	=	Young's moduli and modulus of rigidity
ν_{xy}, ν_{yx}	=	Poisson's ratios

DISCUSSION

THE PROBLEM of an isotropic rectangular plate subjected to a parabolic loading on two opposite sides was solved by Timoshenko[1, 2] through the application of the Principle of Least Work as a minimization condition for the determination of the unknown parameters in an assumed stress function that satisfies the equations of equilibrium and the conditions at the boundary. The same method is to be applied to the orthotropic analog of the problem where the two axes of elastic symmetry coincide with the geometric axes.

The assumed stress function for the orthotropic problem is to be the same as Timoshenko's stress function for the isotropic case

$$\phi = (1/2)S\,y^2\,[1 - (y^2/6\,b^2)] + (x^2 - a^2)^2\,(y^2 - b^2)^2\,(c_1 + c_2x^2 + c_3y^2 + \ldots) \quad (1)$$

c_1, c_2, c_3, etc., are the unknown parameters to be determined from the minimum conditions

$$\partial V/\partial c_1 = 0, \quad \partial V/\partial c_2 = 0, \quad \partial V/\partial c_3 = 0, \quad \text{etc.}$$

Obviously, the above stress function satisfies the equations of equilibrium if, as usual, the stress components are taken to be

$$\sigma_x = \partial^2\phi/\partial y^2, \quad \sigma_y = \partial^2\phi/\partial x^2, \quad \tau_{xy} = -\partial^2\phi/\partial x\,\partial y$$

Also, ϕ satisfies the conditions at the boundary

for $x = \pm a$ $\quad \sigma_x = S(1 - y^2/b^2)$ and $\tau_{xy} = 0$

for $y = \pm b$ $\quad \sigma_y = 0$ and $\tau_{xy} = 0$

Hooke's Law for an orthotropic plate in a state of plane stress assumes the form

$$\left.\begin{aligned} \epsilon_x &= s_{11}\sigma_x + s_{12}\sigma_y \\ \epsilon_y &= s_{12}\sigma_x + s_{22}\sigma_y \\ \gamma_{xy} &= s_{33}\tau_{xy} \end{aligned}\right\} \quad (2)$$

where $s_{11} = 1/E_x, \qquad s_{22} = 1/E_y$

$$s_{12} = -\nu_{xy}/E_x = -\nu_{yx}/E_y, \qquad s_{33} = 1/G_{xy}$$

The strain energy per unit volume for a system in plane stress is

$$V_0 = (1/2)\,(\sigma_x\epsilon_x + \sigma_y\epsilon_y + \tau_{xy}\gamma_{xy})$$

Hence, by Eq. (2),

$$V = 1/2 \iint (s_{11}\sigma_x^2 + 2\,s_{12}\sigma_x\sigma_y + s_{22}\sigma_y^2 + s_{33}\tau_{xy}^2)\,dx\,dy \quad (3)$$

If we now calculate the stress components from the assumed stress function—Eq. (1), substitute these stress components into the expression for the strain energy—Eq. (3), carry out the double integration, get the derivative of the strain energy with respect to each of the parameters, and equate each of these derivatives to zero, we then arrive at the following set of linear equations in the three parameters that were kept in the assumed stress function:

$$\left.\begin{aligned} &c_1\left(\frac{64}{7} + \frac{256}{49}\,n\,r^2 + \frac{64}{7}\,m\,r^4\right) + c_2\,a^2\left(\frac{64}{77} + \frac{64}{49}\,m\,r^4\right) + c_3\,a^2\left(\frac{64}{49}\,r^2 + \frac{64}{77}\,m\,r^6\right) = \frac{S}{a^4b^2} \\ &c_1\left(\frac{64}{11} + \frac{64}{7}\,m\,r^4\right) + c_2\,a^2\left(\frac{192}{143} + \frac{256}{77}\,n\,r^2 + \frac{192}{7}\,m\,r^4\right) + c_3\,a^2\left(\frac{64}{77}\,r^2 + \frac{64}{77}\,m\,r^6\right) = \frac{S}{a^4b^2} \\ &c_1\left(\frac{64}{7} + \frac{64}{11}\,m\,r^4\right) + c_2\,a^2\left(\frac{64}{77} + \frac{64}{77}\,m\,r^4\right) + c_3\,a^2\left(\frac{192}{7}\,r^2 + \frac{256}{77}\,n\,r^4 + \frac{192}{143}\,m\,r^6\right) = \frac{S}{a^4b^2} \end{aligned}\right\} \quad (4)$$

where

$$m = \frac{s_{22}}{s_{11}}, \quad n = \frac{2\,s_{12} + s_{33}}{2\,s_{11}}, \quad r = \frac{b}{a}$$

REDUCTION TO THE ISOTROPIC CASE

The isotropic plate is a special case of the orthotropic one in which

$$s_{11} = s_{22}, \qquad s_{12} = -(\nu/E)$$

and $\qquad s_{33} = 1/G = 2\,(1 + \nu)/E$

From the above relations it is easily seen that

$$m = n = 1 \quad (5)$$

If Eq. (5) is substituted into Eq. (4), we arrive at Timoshenko's solution for the isotropic plate.

* The author wishes to acknowledge his indebtedness to Dr. C. B. Smith, Department of Mathematics, University of Florida, for proposing the problem.

† Assistant in Research.

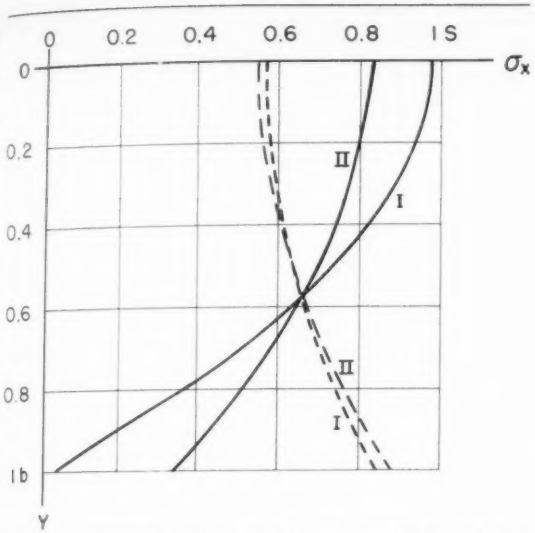

FIG. 1. Distribution of σ_x on the cross section $x = 0$ of a square plate (continuous) and a narrow plate, $a = 10\ b$ (dashed). Curves I, orthotropic; curves II, isotropic.

CONCLUSION

Looking at Eq. (4), we note that the first term in each coefficient of all the parameters is independent of the elastic constants of the material, while the remaining terms are not; we also note that these remaining terms which involve the elastic constants are, at the same time, terms which include high or higher powers of the dimensions ratio r. Thus, we arrive at the following conclusion: in a square plate, or a nearly square plate such that the ratio r is nearly equal to unity, the elastic constants of the material determine to a significant degree the kind of stress distribution that develops in the plate; while, in a plate where r is small compared to unity, the influence of the elastic constants is negligible and the distinction between orthotropic and isotropic materials tends to disappear.

NUMERICAL ILLUSTRATION

Fig. 1 illustrates the above conclusion for the case of a particular orthotropic material—sitka spruce. The elastic constants of the material make $m = 22.3$ and $n = 7.12$. The illustrations are based on numerical calculations of a one-parameter solution. Thus, the figure shows how, while there is a marked difference in the stress distributions of an orthotropic and an isotropic square plate (continuous curves), the corresponding distributions of a narrow plate (dashed curves) are almost identical.

REFERENCES

[1] Timoshenko, S., *Approximate Solution of Two-Dimensional Elastic Problems*, Philosophical Magazine, Vol. 47, pp. 1095–1104, 1924.

[2] Timoshenko, S., and Goodier, J. N., *Theory of Elasticity*, 2nd Ed., pp. 169–170, McGraw-Hill Book Company, Inc., New York, 1951.

Forced Convection of Heat from Cylinders at Low Reynolds Numbers

D. C. Collis

Aeronautical Research Laboratories, Department of Supply, Australia

February 12, 1956

AN INVESTIGATION OF forced convection heat transfer to an air stream of low turbulence level has been carried out on cylindrical wires ranging from 0.00012 to 0.0021 in. in diameter for temperature differences from 30° to 320°C. and air speeds normal to the wire of up to 140 ft. per sec. This range of variables is of particular interest in hot-wire anemometry.

TABLE 1

	$0.02 < Re < 44$	$44 < Re < 140$
m	0.17	0.17
n	0.45	0.51
A	0.24	0
B	0.56	0.48

After correcting for metallic conduction and molecular effects, a widely valid law for forced convection from wires of aspect ratio greater than 10^3 was obtained. If the Nusselt number Nu and the Reynolds Number Re are evaluated at the arithmetic mean absolute temperature T_m of the cylinder temperature T_w and the ambient temperature T_a, then the following relation holds, with the constants taking the values shown in Table 1:

$$Nu(T_m/T_a)^{-m} = A + BRe^n \qquad (1)$$

The sudden change in the values of the constants at $Re = 44$ (approximately) is due to the onset of eddy shedding, while the upper limit of $Re = 140$ was simply set by the scope of the measurements. Deviation from this law occurs quite suddenly at low Reynolds Numbers when buoyancy effects become important. For Reynolds Numbers less than 0.1, buoyancy is negligible provided $Re > Gr^{1/3}$ where Gr is the Grashof number, both quantities in this case being evaluated at ambient temperature. Thus, the minimum velocity which can be measured with a hot-wire anemometer varies as $(T_w - T_a)^{1/3}$ and is independent of the wire diameter. The experimental results from which the above conclusions are derived are presented in Fig. 1.

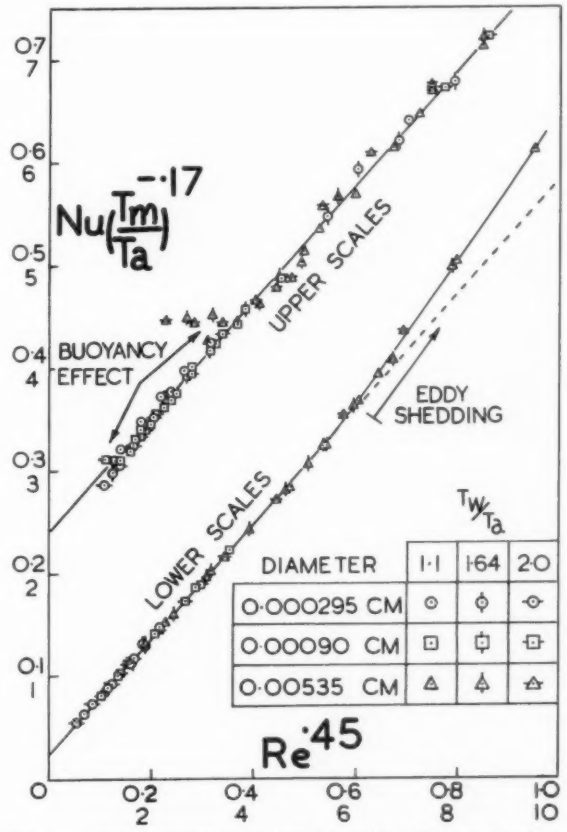

FIG. 1. Forced convection at low Reynolds Numbers, showing effect of buoyancy and eddy shedding.

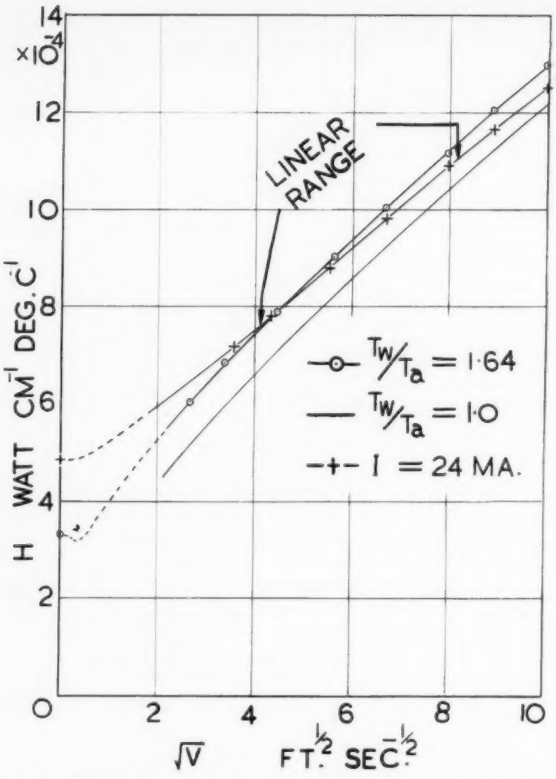

FIG. 2. Comparison of constant-resistance and constant-current calibration curves for hot wires, showing linear range of latter.

For the abscissa, $Re^{0.45}$ was chosen since it gives a linear plot for most of the Reynolds Number range.

Molecular effects enter through the discontinuity of temperature in the air at the surface of the wire. An adequate correction can be obtained by calculating the "temperature jump" using a formula derived from kinetic theory[1] and computing the Nusselt number on the basis of the temperature difference outside the region of discontinuity. If the ratio of mean free path to wire diameter be denoted by K, then the effect of temperature jump on Nusselt number is less than 1 per cent if $K.Nu < 0.005$.

No significant deviation from Eq. (1) due to three-dimensional effects other than metallic conduction has been found for aspect ratios ranging from about 10^3 to 10^4. For aspect ratios less than about 10^3, three-dimensional effects become progressively more evident but cannot generally be predicted accurately because of the variable influence of the wire support geometry. The main effect is on the constants A and B, the power of Re remaining sensibly constant.

For practical application of the heat-transfer relation, it is convenient to expand into dimensional form. For an electrically heated wire with a power input I^2R, the relation between heat loss and velocity, in the absence of eddy shedding, can be written in the form

$$(I^2R)/(T_w - T_a) = A[1 + 0.00164(T_w - T_a)] + B[1 + 0.00025(T_w - T_a)]\,V^{0.45} \quad (2)$$

where A and B now include the various factors which remain constant in hot-wire anemometry and V is the velocity of the air stream. This relation should be compared with the classical equation of King[2] which has been the universal basis for hot-wire anemometry—namely,

$$(I^2R)/(T_w - T_a) = A[1 + \gamma(T_w - T_a)] + B[1 + \delta(T_w - T_a)]\,V^{1/2} \quad (3)$$

in which King's experimental values of the temperature coefficients are $\gamma = 0.00114$ and $\delta = 0.00008$. The important difference is that, in the new relation, Eq. (2), the velocity appears to the 0.45 power instead of to the 1/2 power as in King's equation. The temperature coefficients are also both significantly greater. Despite the long standing of King's law, the disagreement displayed here is not particularly surprising. King's theoretical treatment of the problem is clearly unsatisfactory, and analysis of experimental results has hitherto not been so exacting as it might be. Some published measurements do indicate a deviation from the law in $V^{1/2}$, and extrapolation of these to evaluate A and the two temperature coefficients is inevitably an uncertain process and scarcely justifiable.

Some comments on the application of Eqs. (2) and (3) to hot-wire anemometry are required. When employing King's equation, Eq. (3), the temperature coefficient δ may usually be neglected, and it has also become common practice to neglect the much larger coefficient γ. That the latter omission can lead to important errors in the measurement of turbulence was shown by Betchov[3] in an elaborate analysis incorporating both the temperature coefficient γ and the effect of conduction of heat along the wire. In 1951, the writer[4] observed appreciable discrepancies between the apparent sensitivity of hot wires calibrated respectively by the constant-current and constant-resistance methods, but Betchov's analysis was held to be inapplicable as the calibration curves were inconsistent with King's law itself. The discrepancies were completely resolved by using Eq. (2). More recently, Ruetenik[5] has relied upon the temperature dependence of King's constant A to account for similar discrepancies, but he was only partially successful. The basic investigation of heat transfer reported here requires a complete analysis to take into account the modified dependence of heat transfer on velocity, the greater value of the temperature coefficients, and the effect of temperature discontinuity. The temperature coefficient of the velocity term is generally not negligible and predominates for $Re > 10$, although, for very fine wires, the temperature discontinuity effect tends to obscure this.

Fortunately, it is generally possible to choose the operating conditions of hot wires so that these complications can be circumvented. In the case of a hot wire operated at constant current, there is always a fairly wide range of velocity for which the two effects—(1) the temperature dependence of the heat-transfer rate per unit length l, namely $H = (I^2R)/[l(T_w - T_a)]$, and (2) the departure from the dependence on $V^{1/2}$—are such that H varies very nearly linearly with $V^{1/2}$; in other words, Eq. (3) can be applied in this range with $\delta = \gamma = 0$. This remains true even for cases where there is appreciable metallic conduction and temperature jump. The point is illustrated by means of Fig. 2. The constant temperature curves clearly show the departure from dependence on $V^{1/2}$, while the constant current curve exhibits a marked linear range centered about a point of inflexion. The operating point of a wire can be determined either experimentally or by computing the point of inflexion using Eq. (2).

REFERENCES

[1] **Kennard, E. H.**, *Kinetic Theory of Gases;* McGraw-Hill Book Company, Inc., New York and London, 1938.

[2] **King, L. V.**, *On the Convection of Heat from Small Cylinders in a Stream of Fluid. Determination of Convection Constants of Small Platinum Wires with Application to Hot-Wire Anemometry*, Phil. Trans. Roy. Soc. (London), Ser. A., Vol. 214, pp. 373–432, 1914.

[3] **Betchov, R.**, *Non-Linear Theory of the Hot-Wire Anemometer* (in French), Proc. Kon. Ned. Akad. Wet., Vol. 52, No. 3, pp. 195–207, 1949. (Translated as NACA TM 1346.)

[4] **Collis, D. C.**, *An Investigation of Technique for Measuring Velocity and Pressure Fluctuations in Turbulent Flow with Some Experiments on the Decay of Isotropic Turbulence*, thesis presented for degree of Ph.D., University of Manchester, January, 1952.

[5] **Ruetenik, J. R.**, *The Effect of the Temperature Dependence of King's "Constant" A on the Hot-Wire Sensitivity Coefficient*, Journal of the Aeronautical Sciences, Vol. 22, No. 7, pp. 502–503, July, 1955.

A Note on Transient Aerodynamic Heating*

Eugene Covert and Frank Durgin
Aeronautical Engineers, Naval Supersonic Laboratory, Massachusetts Institute of Technology
February 7, 1956

CURRENTLY, THERE IS a great interest in heat-transfer problems in aeronautics as is evidenced by the frequency with which reports and articles on this subject appear. The early contributors to this subject dealt, naturally enough, with restricted cases. Recently, Tribus and Klein[1] have summarized most of the solutions to the problem of heat transfer through a laminar boundary layer with arbitrary surface temperature distributions. These solutions enable one not only to calculate the variation in surface temperature but also to account for the interaction of the material, whose properties are assumed constant, with the surface temperature distribution. It is the purpose of this note to outline a general method of carrying out this calculation. We include also some results which indicate that the method can be applied to the problem of calculating the temperature response of a hemisphere that has been subjected to a step function in velocity. Since our calculations provide a means of finding the temperature within the body as well as on the surface, we do not make the thin-skin assumption of Bryson and Edwards.[2] We do, however, retain their assumption of a quasi-steady boundary layer.

Before formulating the solution to this problem, it is convenient to normalize the temperature by letting

$$\psi(\bar{r}, t) = [T(\bar{r}, t) - T(\bar{r}_1, 0)]/[T_0 - T(\bar{r}_1, 0)] \tag{1}$$

where

$\bar{r}$ = position vector of any point in the body
$\bar{r}_1$ = position vector of the coldest point in the body at time $t = 0$
t = time
T = temperature in the body
T_0 = maximum value of stagnation temperature
ψ = normalized temperature variable

It is clear that the denominator of the right-hand side of Eq. (1) is the largest possible temperature difference that can occur, hence ψ varies at most between zero and unity. Now, if the diffusivity of the material is defined as

$$a^2 = k_m/(\rho_m C) = \text{const} \tag{2}$$

where

k_m = material conductivity
ρ_m = material mass density
C = material specific heat

then the differential equation which governs the distribution of ψ in the body is the diffusion equation

$$\nabla^2\psi = (1/a^2)\cdot(\partial\psi/\partial t) \tag{3}$$

The initial temperature distribution is given as $\psi(r, 0)$, and the boundary conditions are

$$\partial\psi/\partial n = q/\{k_m[T_0 - T(r_1, 0)]\} \tag{4}$$

on the outer boundary, and

$$\partial\psi/\partial n = 0 \tag{5}$$

on the inner boundary, where

n = the normal to the boundary positive outwards
q = heat transfer positive to the wall

The inner boundary condition precludes the possibility of free convection—i.e., this mode of heat transfer is assumed negligible in comparison to the forced convection on the outer surface. The error due to this assumption will be discussed later.

* This research was supported in whole or in part by the USAF under Contract No. AF 33(616)-2107, monitored by the WADC.

If we consider the interior of the body as source-free, then the application of Green's Theorem to Eq. (3) gives the solution as

$$\psi(\bar{r}, t) = \frac{1}{4\pi}\int_0^t\int_{S_0} G(\bar{r}, \bar{r}_0, t-\tau)\,\frac{\partial\psi(\bar{r}_0, \tau)}{\partial n_0}\,dS_0 d\tau + \frac{1}{4\pi a^2}\int_{V_0}\psi(\bar{r}_0, 0)\,G(\bar{r}, \bar{r}_0, t)\,dV_0 \tag{6}$$

where

G = a suitable Green's function
S_0 = surface boundary
V_0 = volume enclosed in S_0

It should be observed that, in the integration with respect to time, care should be taken to include singularities at $\lim_{\longleftarrow 0}(t + \epsilon)$.

Now, using the results of reference 1 applied to the stagnation point of a hemisphere or some similar form of Lighthill's solution, we find that

$$\frac{\partial\psi}{\partial n} = \frac{q(\psi)}{k_m[T_0 - T(\bar{r}, 0)]} = -0.555\sqrt{3}\,k_a P_r^{1/3}\,\frac{\sqrt{Re_D}}{k_m D}\times \frac{\theta R^{1/3}}{3^{1/3}}\int_0^x \frac{d[\psi(x_1, t) - \psi_r(x, t)]}{(x - x_1)^{1/3}}\Bigg|_{x\,=\,(R\theta^3/3)} \tag{7}$$

where

k_a = air conductivity
P_r = Prandtl Number
D = sphere diameter
θ = angular position on sphere, measured from stagnation point in radians
Re_D = Reynolds Number based on the diameter and, if flow is supersonic, conditions after the normal shock
$\psi_r(\theta, t)$ = recovery temperature

Now we substitute for $\partial\psi/\partial n$ into Eq. (6) and let $\bar{r} \rightarrow \bar{r}_0$ which gives us an integral equation for the temperature at the surface of the sphere. Once this equation is solved for $\psi(\bar{r}_0, t)$, then this Eq. (6) may now be integrated to give the normalized temperature distribution in the body. The critical part of the calculation is the inversion of the transform of the solution of the integral equation, for it is well known that the diffusion Eq. (3) represents the propagation of temperature into a body when the surface conditions are specified.

The details of the approximate solution are not given here; however, the asymptotic form of the normalized temperature distribution on the outer surface of a hemisphere subjected to a step input in velocity is

$$\psi(\bar{r}_0, t) = 0.992\{1 - e^{-[\beta/2(3)^{1/3}]t}\} + \frac{T_0}{T_0 - T(\bar{r}_1, 0)}\times \left[-0.05\sqrt{P_r}\,\theta^2(1 - e^{-.691\beta t}) + 0.0058\,\theta^3(1 - e^{-.75\beta t})\right] \tag{8}$$

where

$$\beta = \frac{4a^2}{b}\left[1.35\,\frac{k_a}{k_w}\,\frac{P_r^{1/3}\sqrt{Re_D}}{D}\right] = [4/(\rho_m C_m b D)]\,(1.35\,k_a P_r^{1/3}\sqrt{Re})$$

b = shell thickness

This approximation is accurate to terms of order (b/R).[2]

An experimental check on Eq. (8) was made in the NSL supersonic wind tunnel. The test was conducted on a dielectric hemisphere at a Mach Number of 3.01, a total pressure of 12.2 psia, and a total temperature of 75°F. The dielectric proved a convenient material, for the walls could be made thin enough to allow use of the asymptotic forms of the required eigenfunctions and yet provide sufficient material for instrumentation, while the time constant remained large enough to be measured easily. The temperature was measured by recording the output of copper-constantin thermocouples on a Bristol Wide Strip Chart recorder. This recorder had a step response time, for

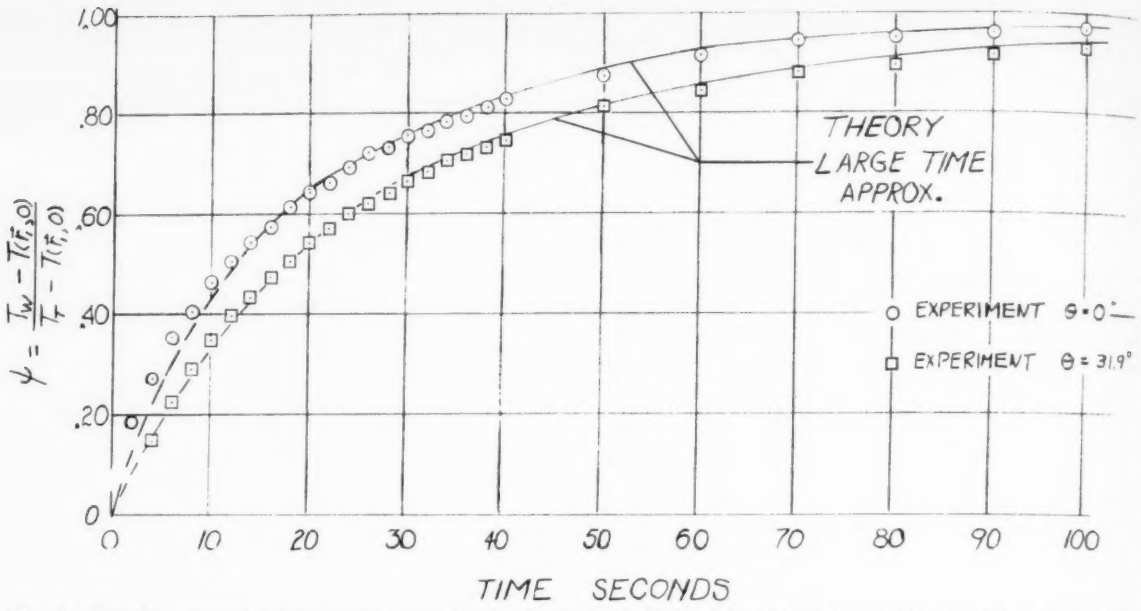

FIG. 1. Transient temperature response to a step function in velocity. Dielectric hemisphere 0.1 in. thick; 4.5 in. in diameter; $T_0 = 75°F.$; $P_0 = 12.2$ psia; $M = 3.01$.

small inputs, of about 0.2 sec. The accuracy of the thermocouple, Bristol system is estimated to be 0.5°F.

The step function was simulated by the use of a close-fitting dry-ice cap that was placed on the hemisphere. This cap was allowed to blow off after the tunnel was started and total pressure and temperature were stabilized and after the hemisphere had reached a uniform temperature that was essentially dry-ice temperature. This simple scheme seemed to approximate the step very closely.

The results of the measurement are shown in Fig. 1 for two positions on the hemisphere together with the calculations based on Eq. (8). This figure shows that the asymptotic time variation can be predicted by the theory since at large times the quasi-steady boundary-layer assumption is valid. While the "time constant" is well represented, there is a systematic difference in the level of about 1 per cent between the calculations and the measurement. Some crude calculations indicate that this systematic error can be attributed primarily to free convection on the inside of the sphere.

We conclude that the solution to the integral equation is satisfactory, and, hence, the calculation of the interior temperature to within approximately 1 per cent (or so) is reduced to integration.

The extension of arbitrary velocity variation can be made, in principle at least, by changing the time variable in Eqs. (6) and (7) to

$$\lambda = \int_0^t \beta(t)\, dt \tag{9}$$

Once this substitution is made, the solution of the integral equation can be carried out without unusual trouble although the algebra may become quite burdensome.

REFERENCES

[1] Tribus, Myron, and Klein, John, *Forced Convection Through a Laminar Boundary Layer with Arbitrary Temperature Variation*, Journal of the Aeronautical Sciences, Vol. 22, No. 1, p. 62, January, 1955.

[2] Bryson, A. E., and Edwards, R. H., *The Effect of Nonuniform Surface Temperature on the Transient Aerodynamic Heating of Thin-Skinned Bodies*, Journal of the Aeronautical Sciences, Vol. 19, No. 7, pp. 471–475, July, 1952.

Inviscid Leading-Edge Effect in Hypersonic Flow*

H. K. Cheng and A. J. Pallone†
Aerodynamics Section, Bell Aircraft Corporation, Buffalo, N.Y.
February 20, 1956

CURRENT INTEREST IN the problem of inviscid-viscous interaction has led to the realization of the significant effect of the leading-edge thickness in hypersonic flow.[1–4] The purpose of this note is to give an account of the downstream influence of the blunt leading edge on the basis of the hypersonic small perturbation theory.[5]

Experimental data furnished by the recent work of Hammitt and Bogdonoff for high Mach Numbers indicate clearly that the leading-edge thickness plays an important role in determining the downstream flow field (see data reproduced in Figs. 1 and 2).[6] In order to estimate the downstream influence of a blunt leading edge in an inviscid hypersonic flow, a preliminary analysis applying the method of characteristics[7, 8] was carried out for the case of a flat plate with a circular leading edge. The shock shape and the sonic line in the nose region was determined by means of the Moeckel theory, and a *straight* sonic line was assumed.[9] In the absence of a more appropriate method, it was felt, at the time, that this would suffice to yield qualitative results. Under the specialization of the values of the free-stream Mach Number $M \simeq 14$ and the specific heat ratio $\gamma = 7/5$, the analysis was carried out from the leading edge to a station about 20 thicknesses downstream; the pressure distribution was obtained. It appears clearly from the results, as presented in Fig. 3, that the pressure variation over a considerable extent downstream of the edge may be approximated by a power law as $\Delta P/P_\infty \sim (x/d)^{-\kappa}$ where the power κ comes very closely to the value 2/3. In fact, the same law with the power 2/3 fits also quite well into the correlated experimental data of reference 6 for

* In the course of preparation of this note, Dr. Lester Lees, California Institute of Technology, informed the writers that he had arrived at a similar result in a more general treatment of the problem, and the work will probably be published shortly.

† Now on leave as Research Associate, Aeronautical Laboratory, Polytechnic Institute of Brooklyn, Freeport, L.I., N.Y.

the higher Reynolds Numbers which were reproduced in Fig. 1 and which were obtained for Helium ($\gamma = 5/3$) at different hypersonic Mach Numbers with different nose shape. The regularity revealed in both experimental results and the characteristics solution, based on a set of tentative initial conditions at the leading edge, points to the fact that, downstream of the leading edge, a *similar solution* may exist and that it is quite independent of the flow details at the immediate vicinity of the leading edge.

Previously, the problem of a cylindrical blast wave produced by an instantaneous energy release has been treated by Lin.[10] This problem was identified, on the basis of the hypersonic small perturbation theory after Hayes,[5] as that pertaining to a transient flow field in a transverse plane containing the *wake* of a traveling object, such as a meteor. It is apparent that the problem of present interest is also identifiable as one of a similar kind—namely, the problem of a *plane* blast wave resulting from instantaneous energy release.

The mathematical solution of the latter problem has been obtained under the assumptions of one-dimensional adiabatic (particleisentropic) flow of an ideal gas and infinite shock strength, in a similar manner as references 10 and 11.* There are many features of resemblance in the solutions of the plane blast wave and of that with cylindrical symmetry. The pressure decay and shock layer growth, however, obey different laws, the former being $P \sim t^{-2/3}$ (instead of t^{-1}), the latter $\delta \sim t^{2/3}$ (instead of $t^{1/2}$).

Thus, it appears that a picture of the transient flow field behind a blunt leading edge at very high Mach Number can be obtained in that the energy is being released in the form of nose drag. Because of the vanishing of velocity near the plane where the blast wave was initially set off and the symmetry in pressure and density with respect to it, the similar solution obtained corresponds to the case of a *flat plate* or that involving an idealized wake. Let U be the free-stream velocity and x the distance downstream of the leading edge. Putting x/U for the time and U/M for the speed of sound, one arrives, from the blast wave solution, at a plate pressure formula obeying the two-third power law:

$$P_w/P_\infty \backsimeq (\text{constant})k^{2/3}\, M^2(x/d)^{-2/3} \tag{1}$$

where d is a reference length, say the leading-edge thickness, and k the "nose drag" coefficient defined as

$$k \equiv 2E/[(1/2)\rho_\infty U^2 d] \tag{2}$$

The value E, to be sure, is the energy released (per unit depth chordwise) to the transverse flow field by the nose and is therefore given, in the symmetrical case, directly by one half the value of nose drag D—i.e., $2E = DU/U = D$. The constant of proportionality in Eq. (1), according to the calculated results, is 0.169 for $\gamma = 5/3$ and 0.112 for $\gamma = 7/5$. The corresponding shock shape is given simply by the equation

$$\delta/d \backsimeq (\text{constant})k^{1/3}(x/d)^{2/3} \tag{3}$$

which is independent of the Mach Number. The constant which appears above is 0.90 for $\gamma = 5/3$ and 0.89 for $\gamma = 7/5$.

These results, obtained under the assumption of infinite shock strength, can only be taken as the leading term in an *asymptotic* development of the exact solution for sufficiently high Mach Number [large value of $M(d\delta/dx)$] and for sufficiently downstream (small value of $d\delta/dx$). For, in comparing the present result with the pressure data of reference 6 (Fig. 1) and that in Fig. 3, it is found that the validity of the above results can be extended to a wider range covering the weaker effect further downstream, by taking the pressure P_w in Eq. (1) to be the pressure increment $\Delta P = P_w - P_\infty$. This step, though irrelevant in the derivation of Eq. (1) on the basis of infinite Mach Number and thus extremely high pressure, should actually be justified by carrying out the successive developments in a similar manner as Stewartson.[11] The theoretical curve drawn in Fig. 1 is determined with an assumed value of the nose drag coefficient $k = 2.0$ for the almost-square type of leading edge employed in the test series of reference 6; the theoretical curve for the shock shape which appears in Fig. 2 is computed according to the *same* value of k; while the theoretical curve in Fig. 3 is based on a value of $k = 11/9$, resulting from integration of the pressure drag around the circular leading edge with a "Newtonian type" pressure distribution.

It is noted that the energy dependence in the blunt leading-edge effect seems to be consistent with the observation that there was no significant difference between the square and the round leading edges as reported in reference 6. The vanishing density on the plate predicted by the simplified theoretical

* Drs. I. Imai and S. C. Lin pointed out that the similar solution for the problem of blast wave in one, two, and three dimensions had been obtained by A. Sakurai.[12] The writer's computation gives a pressure on the wall which is about 10 per cent lower than the value in reference 12.

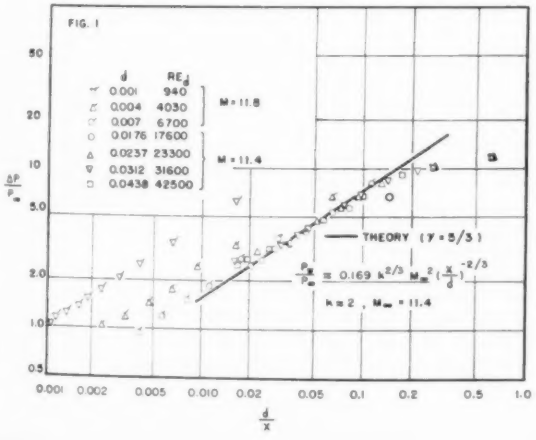

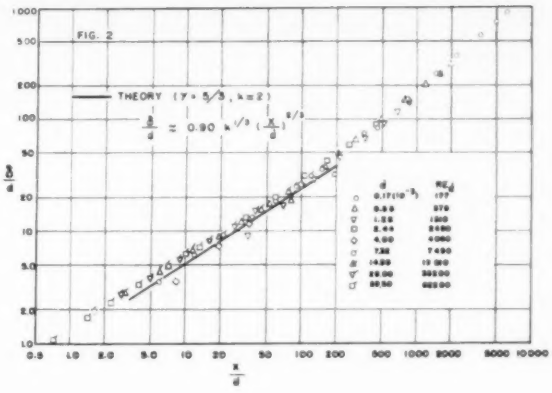

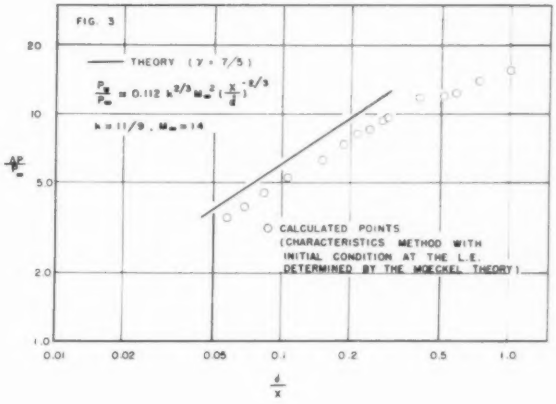
FIG. 3
THEORY (γ = 7/5)
k = 11/9 , M∞ = 14
CALCULATED POINTS
(CHARACTERISTICS METHOD WITH
INITIAL CONDITION AT THE L.E.
DETERMINED BY THE MOECKEL THEORY)

model with an instantaneous energy release also agrees with the attainment of very low density over the test model, as indicated by the interferogram.[6]

It can be seen that the approximation is not uniformly valid, especially because of the simplified description of the energy release; the above example does demonstrate, however, the possibility for inclusion of the blunt leading-edge (or nose) effect into a consistent treatment, under the framework of small perturbation theory, of hypersonic airfoils, and of slender bodies. Further remarks and results will be given in separate notes.

References

[1] Ferri, A., and Libby, P., *Note on an Interaction Between the Boundary Layer and the Inviscid Flow*, Readers' Forum, Journal of the Aeronautical Sciences, Vol. 21, No. 2, p. 130, February, 1954.

[2] Bertram, M. H., *Viscous and Leading-Edge Thickness Effects on the Pressures on the Surface of a Flat Plate in Hypersonic Flow*, Readers' Forum, Journal of the Aeronautical Sciences, Vol. 21, No. 6, pp. 430–431, June, 1954.

[3] Bogdonoff, S. M., and Hammitt, A. G., *Fluid Dynamic Effects at Speeds from M = 11 to 15*, Journal of the Aeronautical Sciences, Vol. 23, No. 2, pp. 108–116, February, 1956.

[4] Lees, L., *Hypersonic Flow*, paper presented at the Fifth International Aeronautical Conference, June 20, 1955. IAS Preprint No. 554.

[5] Hayes, W. D., *On Hypersonic Similitude*, Quart. Appl. Math., Vol. 5, pp. 105–106, 1947.

[6] Hammitt, A. G., and Bogdonoff, S. M., *Hypersonic Studies of the Leading Edge Effect on the Flow over a Flat Plate*. Paper presented at the 25th Annual Anniversary Meeting of American Rocket Society, November 14–18, 1955.

[7] Ferri, A., *The Method of Characteristics, General Theory of High Speed Aerodynamics*, pp. 583–670, Princeton University Press, 1954.

[8] Isenberg, J. S., *The Method of Characteristics in Compressible Flow*, Pt. I, USAF Tech. Rep. F-TR-1173A, December, 1947.

[9] Moeckel, W. E., *Approximate Method for Predicting Form and Location of Detached Shock Wave Ahead of Plane or Axially Symmetric Bodies*, NACA TW 1921, July, 1949.

[10] Lin, S. C., *Cylindrical Shock Wave Produced by Instantaneous Energy Release*, Jour. Appl. Physics, Vol. 25, No. 1, pp. 654–657, January, 1954.

[11] Stewartson, K., *On the Motion of a Flat Plate at High Speed in a Viscous Compressible Fluid, I. Impulsive Motion*, Proc. Camb. Phil. Soc., Vol. 51, Part 1, p. 202, January, 1955.

[12] Sakurai, A., *On the Propagation and Structure of the Blast Wave, I.* Jour. Phys. Soc. Japan, Vol. 8, No. 5, pp. 662–669, October, 1953.

Supplementary Note on Turbulent Velocity Fluctuations

Heinrich B. Helmbold

Research Scientist, Fairchild Engine and Airplane Corporation, Hagerstown, Md.

February 21, 1956

COMMON FEATURES of fully developed turbulent flow in pipes and plane boundary layers with zero pressure gradient were discussed in a former note on velocity fluctuations in equilibrium turbulent shear flow along solid boundaries.[1] This information is now completed by observations on the equilibrium turbulent flow in a two-dimensional radial diffuser of 2° wall-divergence angle.[2]

(a) As a result of the *adverse pressure gradient* the turbulent velocity field is no longer isotropic in the diffuser plane of symmetry. The x-component of the velocity fluctuations exceeds the y- and z-components which are equal in the plane of symmetry,

$$u_1' > v_1' = w_1'$$

These quantities are root-mean-square values of the velocity-fluctuation components, $u' = \sqrt{\overline{u^2}}$, etc.; the subscript 1 denotes the symmetry plane. The components are interconnected by the relationship

$$w' = \sqrt{(v_1'/u_1')u'v'} \qquad (1)$$

within the range $0.05 < \eta < 1.0$ where η denotes the nondimensional distance from the wall, referred to the half-width of the diffuser. In the special case of reference 2, $v_1'/u_1' = 0.75$. With *zero pressure gradient*, $u_1' = v_1' = w_1'$ or $v_1'/u_1' = 1$, and Eq. (1) simplifies to $w' = \sqrt{u'v'}$ as observed on pipe and flat plate.[1] Thus, Eq. (1) covers all hitherto known cases of equilibrium turbulent shear flow along longitudinally straight solid boundaries. If the ratio v'/u' is known as a function of η, this equation gives a complete description of the distribution of turbulent energy over the three components. The structure of Eq. (1) suggests to consider $[1 - (v_1'^2/u_1'^2)]u^2$ as representing longitudinal fluctuation energy bound by the adverse pressure gradient and $(v_1'^2/u_1'^2)\overline{u^2}$ as representing longitudinal fluctuation energy left free for interaction with the other components $\overline{v^2}$ and $\overline{w^2}$. Note that the factor v_1'/u_1' representing the effect of the pressure gradient in Eq. (1) is independent of η.

(b) Within the small range $0.09 < \eta < 0.25$, the velocity ratio v'/u' is still approximately the same as with the pipe and flat plate:

$$v'/u' = k + 0.37\sqrt{\eta} \qquad (2)$$

The constant $k = 0.41$ does not differ much from its value for zero pressure gradient ($k = 0.44 \pm 0.01$).

(c) If u' is replaced by its active portion $(v_1'/u_1')u'$, a reduced shear correlation coefficient is obtained:

$$\overline{uv}/[(v_1'/u_1')u'v'] = 0.45 \qquad (3)$$

within the range $0.05 < \eta < 0.5$. With zero pressure gradient, this coefficient is 0.46 for the parallel channel,[3] 0.42 for the pipe, 0.50 for the plane boundary layer within the range $0.1 < \eta < 0.3$ where all these flows are strictly comparable.

(d) Turbulent velocity data in wall proximity for different types of equilibrium turbulent flow are brought more closely together if, again, u' is replaced by its active portion and $(v_1'/u_1')u'$ + U_τ is plotted as a function of $U_\tau\, y/\nu$ (U_τ denotes the shear stress velocity). The maximum of this function occurs at $U_\tau\, y/\nu \approx 16$ and is about 2.6 for the 2° radial diffuser and the pipe, 2.5 for the parallel channel.

The observations described under (c) and (d) support the conclusion drawn under (a) that an adverse pressure gradient inactivates a certain portion of longitudinal turbulent energy with respect to its interaction with the transversal energy components.

References

[1] Helmbold, H. B., *Note on Velocity Fluctuations in Equilibrium Turbulent Shear Flow Along Solid Boundaries*, Readers' Forum, Journal of the Aeronautical Sciences, Vol. 22, No. 7, pp. 513–514, July, 1955.

[2] Ruetenik, T. R., and Corrsin, L., *Equilibrium Turbulent Flow in a Slightly Divergent Channel*, 50 Jahre Grenzschichtforschung, p. 446; H. Görtler and W. Tollmien, Braunschweig, 1955.

[3] Laufer, J., *Investigation of Turbulent Flow in a Two-Dimensional Channel*, NACA TR 1053, 1951.

Note on Photothermoelasticity*

George Gerard and Arthur C. Gilbert

Research Division, College of Engineering, New York University

February 22, 1956

RECENTLY PUBLISHED analytical work has indicated that, because of aerodynamic heating, aircraft structures may experience significant thermal stresses. Such calculations are necessarily based on idealized representations of wing structures. Consequently, considerable interest centers on experimental verification of the transient temperature distributions and resulting thermal stresses predicted by the available theories.

The use of strain-gage techniques is somewhat involved at elevated temperatures and, moreover, does not afford a complete view of the stress field at a particular time. Consequently, we

* Sponsored by the United States Air Force through the Office of Scientific Research, Air Research and Development Command.

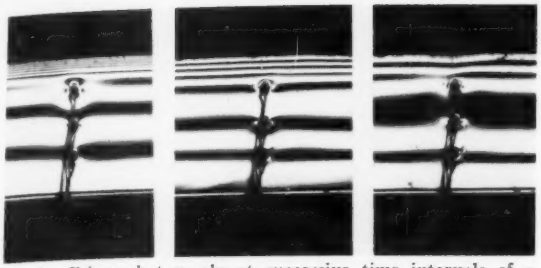

FIG. 1. Fringe photographs at successive time intervals of a beam with a temperature gradient applied to the upper surface.

have been investigating the use of photoelastic techniques to determine thermal stresses arising from transient temperature gradients.

Since photoelastic materials generally creep when exposed to elevated temperatures, the temperature gradient in our technique is established by refrigeration. Specifically, for the beam shown in Fig. 1, a temperature gradient was applied to the upper surface of the beam, and fringe photographs were taken of the model in the polariscope at successive time intervals. The three inclusions appearing in each photograph are thermocouples used to monitor the temperature distribution.

In Fig. 1, the left-hand picture was taken at the time of maximum fringe order. As the temperature gradients became less severe, the fringe order decreased as shown in the other pictures in Fig. 1.

We are currently investigating the photothermoelastic technique in considerable detail and expect to study built-up wing structures under representative thermal and static loading conditions.

An Experimental Investigation of the Boundary-Layer Flow on a Rotating Flat Plate

Jerome Persh* and A. Wiley Sherwood†
Aeronautical Engineering Department, University of Maryland, College Park, Md.
March 14, 1956

AN EXPERIMENTAL INVESTIGATION of the boundary-layer flow on a rotating flat plate is presently in progress at the University of Maryland. The purpose of this note is to provide a description of the experimental apparatus and also to report on the experimental results so far accumulated.

A photograph of the experimental apparatus used for the present investigation is shown in Fig. 1. The survey rake shown installed was not used for any of the measurements reported herein. The flat plate which is mounted on the test stand is 8 ft. in span and has a chord of about $1^1/_2$ ft. This plate is a solid piece of aluminum $1^1/_2$ in. thick with 30° bevels on the leading and trailing edges. The top surface, which is the test surface, is finished to a mirror-like surface but is not entirely free from scratches and slight depressions. However, all of the experimental data reported herein were obtained in a region free of these possible sources of disturbances. The plate is rotated by a 2-hp. d.c. motor which turns the 4-in. hollow steel shaft through a belt and pulley system. This can be seen in Fig. 1. At present, the useful speed range of the apparatus is from about 200 to 300 r.p.m., which corresponds to a free-stream velocity range at the quarter-span plane of about 40 to 70 ft./sec. The lower and upper limits of this speed range are dictated by the range of the manometer system used. Boundary-layer velocity profiles are measured with fixed survey rakes. The survey rakes are fitted into holes drilled through the blade in three chordwise and three spanwise planes. Only measurements in chordwise planes 2 and 3 ft. from the hub have been made so far. It is intended to survey the boundary layer at all positions for which holes have been provided.

The pressures are led from the survey rake along the underside of the plate with plastic tubes which are securely fastened to avoid flapping. The plastic tubes enter the hollow shaft through a common hole and are led downward and out individual holes in the shaft to the manometer tubes. Fig. 1 shows the manometer tube arrangement. This consists of twelve U-tubes fastened to the shaft at the upper and lower ends with steel belts. The region between the fastening belts on the shaft has been relieved slightly so that ozalid paper may be inserted around the shaft behind the tubes. This sensitized paper is exposed to strong light for about a minute using the carbon arc arrangement shown in Fig. 1, after a steady speed has been reached.

Each of the impact pressure tubes on the survey rakes is connected to one leg of a U-tube. The other leg is connected to a common static-pressure orifice near the pressure rake. This arrangement compensates for centrifugal-force effects in the pressure tubing. A static-pressure tube on the survey rake was used to check whether or not the slightly inboard position of the common static-pressure orifice is sufficient to induce some centrifugal-force effect on the data. None was found, however, at any of the stations investigated.

Initial boundary-layer pressure measurements made along the quarter-span plane indicate a rather thick separated region near the leading edge, with subsequent reattachment at the two downstream locations. A survey of the wake into which the leading edge was advancing was made slightly ahead of the leading edge. This survey indicated that the velocity deficiency (about 1/2 free-stream velocity) occurs in the plane of the test surface. This is probably responsible for the flow separation near the leading edge. It is difficult, from the measurements

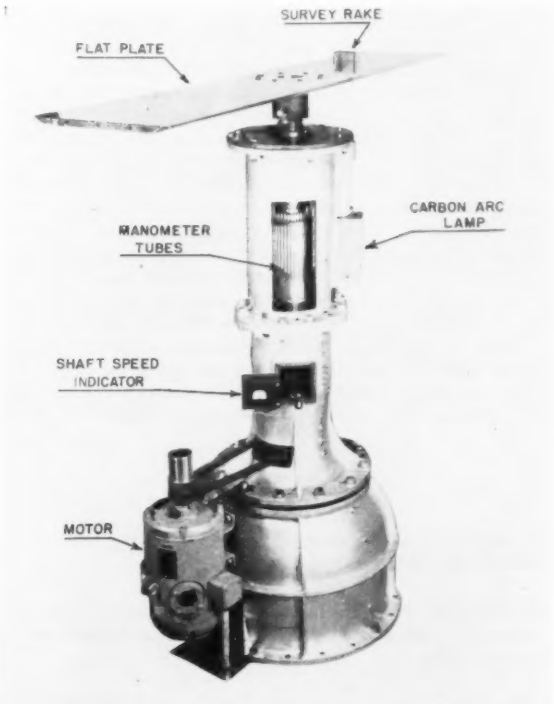

FIG. 1. Photograph of test apparatus.

* Physicist, Naval Ordnance Laboratory, Silver Spring, Md. This work was done on a part-time basis for the Aeronautical Engineering Department, University of Maryland.
† Professor of Aerodynamics.

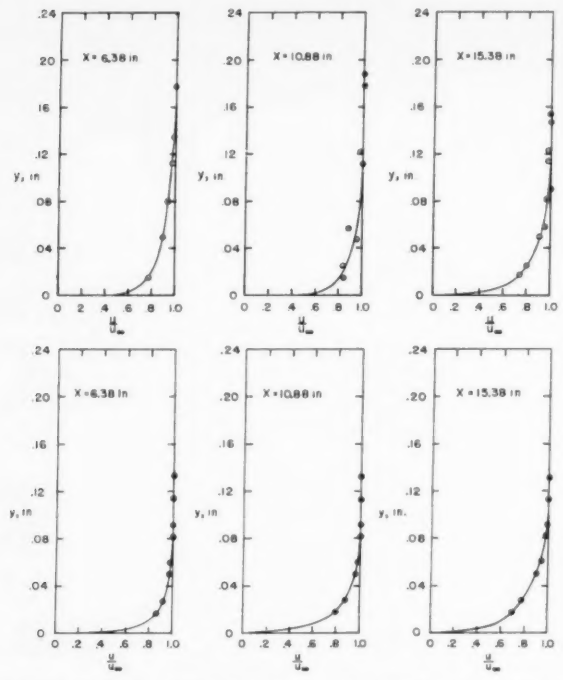

FIG. 2. (*Top*). Boundary-layer velocity profiles in a chordwise plane 2 ft. from axis of rotation. (*Bottom*). Boundary-layer velocity profiles in a chordwise plane 3 ft. from axis of rotation.

made, to determine the precise initial separation and reattachment points, but it may be surmised that separation occurred very close to the leading edge and that the boundary layer reattached between the first and second survey stations. All measured boundary-layer profiles were of the turbulent type.

The first attempt to eliminate the separated region consisted of attaching an extension to the leading edge which was a carefully sharpened piece of sheet aluminum about 2 in. in chord and bent downward in a circular arc such that the leading edge was 1/4 in. below the plane of the test surface. This extension, which can be seen in Fig. 1, reduced the separated region but did not eliminate it entirely. The next effort to remove the separated region consisted of attaching to the trailing edge creating the wake, a flat flap, 2 in. in chord, depressed to an angle of about 40°. This step removed the separated region entirely, and a conventional set of turbulent boundary-layer profiles were measured at all of the chordwise locations. These are shown in Fig. 2 for a representative free-stream velocity of about 60 ft./sec. Further efforts were made to establish a laminar boundary layer on the plate by increasing the length of the trailing-edge flap to 4 and 6 in., respectively. No noticeable difference in the velocity profiles on the blade was observed, however. From this investigation, it does not appear feasible to establish a laminar boundary layer on a surface which rotates such that the leading edge advances into a wake or region of velocity deficiency.

On Linearized Transonic Flow Theory for Slender Bodies

John W. Miles
Professor of Engineering, University of California, Los Angeles
March 20, 1956

MAEDER AND THOMMEN,[1] following Oswatitsch, recently have presented linearized approximations to the velocity potentials of thin airfoils and slender bodies in transonic flow. The present writer, having considered a similar approximation for slender bodies (*vide infra*), believes that the following criticisms should be noted.*

(1) The differential equation obtained by assuming ϕ_{xx} to be constant in the nonlinear term $\phi_x\phi_{xx}$ is everywhere parabolic when $M_\infty = 1$, whereas in reality it should be parabolic only on the sonic line.

(2) The asymptotic solution for three-dimensional flow at $M_\infty = 1$ presumably should approximate that obtained by Guderley and Yoshihara,[2] and the responsibility of satisfactorily explaining deviations therefrom should rest with the more approximate theory. There appears to be no possibility of achieving the correct asymptotic solution at $M_\infty = 1$ with a completely linearized theory.

(3) The solution at sufficiently large distances from the body when $M_\infty \neq 1$ should be governed by the linearized equation (with the term in $\phi_x\phi_{xx}$ becoming negligible); however, there exists an intermediate region in which nonlinear effects are decisive, even though a linearized approximation again becomes valid in the neighborhood of the (three-dimensional) body.

(4) A plot of the pressure distribution over a slender body of revolution is (to the eye) rather insensitive to the term $b(x)$ in the slender body approximation $\phi = a(x) \ln r + b(x)$; the integrated drag, however, is extremely sensitive to variations in $b(x)$ and, therefore, to the conditions at large distances from the body.

(5) A simple expression for the derivative with respect to M_∞ of the drag coefficient of an *expanding* body at $M_\infty = 1$ has been given by Liepmann and Bryson[3] and provides either a test on an approximate theory or a method for evaluating one undetermined (but independent of M_∞) parameter. The results of Maeder and Thommen render this derivative identically zero for a cone-cylinder.

The writer's derivation of results equivalent to those of Maeder and Thommen was motivated by his previous study[4] of accelerated bodies in transonic flow and by the observation that the sonic singularity in linearized theory may be avoided by assuming a dissipative medium, such that the wave equation for the velocity potential ϕ assumes the form

$$a^2\nabla^2\phi = (D^2\phi/Dt^2) + 2\epsilon(U/l)(D\phi/Dt) \tag{1}$$

where a and U are the sonic and flight speeds, respectively, and the *small* constant ϵ is the logarithmic decrement for a harmonic disturbance of wave length l or, more generally, simply a measure of the dissipation over a characteristic length l (ϵ, although introduced in a rather more arbitrary fashion, is equivalent to Maeder and Thommen's K). The corresponding, slender body solution for a pointed body of revolution of cross-sectional distribution $S(x)$ in supersonic flow is given by (using Ward's technique[5])

$$\phi(x, r) = a(x) \ln r + b(x) \tag{2}$$

$$a(x) = S'(x)/2\pi \tag{3}$$

$$b(x) = 1/2\int_0^x \{a'(\xi) + e^{-\mu x}(\partial/\partial\xi)\,[e^{\mu\xi}a(\xi)]\,\ln\,[B/2(x-\xi)]d\xi\} \tag{4}$$

$$B = (M_\infty^2 - 1)^{1/2}, \qquad \mu = \epsilon\,|\,M_\infty - 1\,|^{-1} \tag{5}$$

with a rather similar result for subsonic flow. We have referred all dimensions to the characteristic length l and the flight speed U and have replaced B^2 by $2|\,M_\infty - 1\,|$ in the transonic parameter μ.

* Addendum: Drs. Maeder and Thommen have replied to some of these criticisms in private correspondence and have informed the writer that they will be considered in a future paper on the subject.

The foregoing representation had anticipated that the arbitrary parameter ϵ might be evaluated for an expanding body through Liepmann and Bryson's result[3]

$$\frac{\partial C_D}{\partial B^2}_{B^2=0} = \frac{2}{(\gamma + 1)} \tag{6}$$

where C_D is the drag coefficient (referred to base area), and γ is the specific heat ratio. The result of Eq. (4), unfortunately, gives a value of zero for the left-hand side of Eq. (6) when applied to the important specific example of a cone-cylinder, so that we are compelled to conclude that the formulation of Eqs. (1)–(5) is quite unsatisfactory for *nonsmooth* bodies.

Disregarding this last objection for the moment, we find that for *smooth, pointed* bodies [so that $a(0) = a(1) = 0$] the transonic drag may be exhibited in the form

$$D = D_1 + |M_\infty - 1|^{-1}(M_\infty - 1)D_2(\epsilon/|M_\infty - 1|) \tag{7}$$

$$D_1 = \pi q \int_0^1 \int_0^1 a'(x)a'(\xi) \ln \left|\frac{1}{x - \xi}\right| d\xi\, dx \tag{8}$$

$$D_2(\mu) = 2\pi q \int_0^1 e^{-\mu x} a'(x)\, dx \int_0^x \ln\left(\frac{1}{x - \xi}\right) \frac{\partial}{\partial \xi} [e^{\mu\xi} a(\xi)] d\xi \tag{9}$$

where D_1 is one half the supersonic drag—i.e., $D \to 2\ D_1$ if $|M_\infty - 1| >> \epsilon$. The calculation of D_2 may be expedited by noting that

$$\frac{\partial D_2}{\partial \mu} = -\frac{\pi q}{\mu} \int_0^1 \int_0^1 a'(x)a'(\xi)e^{-\mu|x-\xi|}\, d\xi dx \tag{10}$$

We remark that the drag given by Eq. (7) is an antisymmetric (with respect to D_1) and (by virtue of the definite sign of $\partial D_2/\partial\mu$) monotonically increasing function of $M_\infty - 1$; consequently it does not exhibit a transonic peak.

If the criterion of Eq. (6) is imposed on Eq. (10), we obtain

$$\epsilon = \frac{\pi(\gamma + 1)}{2S_1} \int_0^1 a'^2(x)\, dx \tag{11}$$

for smooth, expanding bodies of base area S_1. This evaluation appears more satisfying than Maeder and Thommen's proposal to use the value of ϕ_{xx} at an arbitrary point on the body at $M_\infty = 0$, but the end results remain open to all of the objections cited above—especially the fact that the criterion of Eq. (6) fails to yield a value of ϵ for nonsmooth bodies.

We conclude by remarking that an approximate sonic drag theory,[6] based on a match between the slender body and Guderley-Yoshihara solutions along the sonic line, yields sonic drag coefficients for smooth expanding bodies that are very much less than D_1. It is true that this theory also involves arbitrary parameters and, although apparently satisfactory for sharp-shouldered bodies such as a cone-cylinder, requires further confirmation for smooth bodies; nevertheless, the assumptions made appear sufficiently reliable to justify the inference that values of the sonic drag (for smooth bodies) as high as D_1 are rather improbable.

References

[1] Maeder, P. F., and Thommen, H. U., *Some Results of Linearized Transonic Flow about Slender Airfoils and Bodies of Revolution*, Journal of the Aeronautical Sciences, Vol. 23, No. 2, pp. 187–188, February, 1956.

[2] Guderley, G., and Yoshihara, H., *An Axial-Symmetric Transonic Flow Pattern*, Quart. Appl. Math., Vol. 4, No. 4, pp. 333–339, April, 1951.

[3] Liepmann, H., and Bryson, A. E., *Transonic Flow Past Wedge Sections*, Journal of the Aeronautical Sciences, Vol 17, No. 12, pp. 745–755, December, 1950.

[4] Miles, J. W., *On the Transonic Drag of Accelerated Bodies*, Journal of the Aeronautical Sciences, Vol. 21, No. 9, pp. 644–645, September, 1954.

[5] Ward, G. N., *Supersonic Flow Past Slender Pointed Bodies*, Quart. Jour. Mech. and Appl. Math., Vol. 2, pp. 75–97, 1949.

[6] Miles, J. W., *On the Sonic Drag of a Slender Body*, Journal of the Aeronautical Sciences, Vol. 23, No. 2, pp. 146–154, February, 1956.

Erratum—"Subsonic Influence of Compressibility on the Pressure Distribution of a Profile"[1]

F. S. Weinig
Aerodynamicist, Component Development Section, AGT Development Dept., General Electric Company, Cincinnati

April 11, 1956

In Eq. (15), the term in the denominator should read:

$1 + \sqrt{1 - M_\infty{}^2}$ instead of $1 - \sqrt{1 - M_\infty{}^2}$

Reference

[1] Weinig, F. S., Journal of the Aeronautical Sciences, Readers' Forum, Vol. 23, No. 3, pp. 279–281, March, 1956.

A Method for the Solution of an Eigenvalue Problem with a Complex Matrix

Ta Li
Design Specialist, Dynamics Group, Convair, A Division of General Dynamics Corporation, San Diego, Calif.

January 21, 1956

Summary

A complex eigenvalue problem is reduced to the solution of a polynomial equation, the coefficients of which can be easily computed according to a simple rule suitable for digital computers.

Introduction

Since the high-speed computer is available, the solution of a polynomial equation can be achieved much more rapidly than the solution of its corresponding determinantal equation. However, in most physical and engineering problems, the basic equations are determinantal. Different methods for expanding these determinantal equations into polynomial equations were given in the summarizing paper of Wayland.[1] Wayland pointed out that, in spite of the fact that much effort had been spent in developing techniques to avoid expansion into polynomial form, this very technique frequently proved to be most economical of effort.

The main problem of expansion is to reduce the eigenvalue problems to the Frobenius Standard Form. This was done by Danielewsky[2] through repeated matrix multiplication and elimination and by Samuelson[3] through successive differentiation and elimination.

The present writer reduces the eigenvalue problem to the Frobenius form by one simple matrix transformation. The actual computation of the matrix of transformation is by no means necessary. The elements in the Frobenius matrix are given by a system of linear equations with coefficients computed according to a simple rule. It is clear that the accuracy of the eigenvalues will depend upon the accuracy of the solutions of the linear system.

Analysis

Let

$$A = \begin{bmatrix} a_{11} \ldots a_{1n} \\ \ldots\ldots \\ a_{n1} \ldots a_{nn} \end{bmatrix} \tag{1}$$

be a matrix with complex elements of which not all are zero.

We are interested in the eigenvalues of the matrix equation

$$(A - \lambda I)X = 0 \tag{2}$$

It is obvious that for every nonsingular matrix B, $B^{-1}AB$ has the same eigenvalues as A. Writing

$$B^{-1}X = Y \tag{3}$$

the eigenvalue problem

$$(B^{-1}AB - \lambda I)Y = 0 \tag{4}$$

is identical with Eq. (2) by virtue of Eq. (3).

To solve Eq. (2) we will consider the Frobenius Standard Matrix.

$$C = \begin{bmatrix} 0 & 0 & 0 \ldots 0 & -a_1 \\ 1 & 0 & 0 \ldots 0 & -a_2 \\ 0 & 1 & 0 \ldots 0 & -a_3 \\ . & . & \ldots\ldots & . \\ 0 & 0 & 0 \ldots 1 & -a_n \end{bmatrix} \tag{5}$$

The eigenvalues of this matrix are identical with the roots of the polynomial equation

$$a_1 + a_2\lambda + \ldots + a_n\lambda^{n-1} + \lambda^n = 0 \tag{6}$$

Let us write

$$B = \begin{bmatrix} x_1 & \xi_{12} \ldots \xi_{1n} \\ x_2 & \xi_{22} \ldots \xi_{2n} \\ . & \ldots\ldots \\ x_n & \xi_{n2} \ldots \xi_{nn} \end{bmatrix} \tag{7}$$

and solve the equation

$$AB = BC \tag{8}$$

subject to the condition $|B| \neq 0$.

From Eq. (8) we obtain

$$\xi_{i2} = \sum_{\nu_1=1}^{n} a_{i\nu_1} x_{\nu_1} \tag{9}$$

$$\xi_{i,(j+1)} = \sum_{\nu_j=1}^{n} a_{i\nu_j}\, \xi_{\nu_j, j} \tag{10}$$

where $\quad i = 1, 2, \ldots, n; \qquad j = 2, 3, \ldots, n-1 \tag{11}$

Written in detail we find

$$\xi_{i3} = \sum_{\nu_2=1}^{n} a_{i\nu_2} \sum_{\nu_1=1}^{n} a_{\nu_2\nu_1}\, x_{\nu_1} \tag{12}$$

$$\sum_{\nu_{n-1}=1}^{n} a_{i\nu_{n-1}} \sum_{\nu_{n-2}=1}^{n} a_{\nu_{n-1}\nu_{n-2}} \cdots \sum_{\nu_1=1}^{n} a_{\nu_2\nu_1}\, x_{\nu_1} \tag{13}$$

A comparison of the elements in the last column of both matrix products in Eq. (8) reveals

$$\sum_{\nu_1=1}^{n} a_{i\nu_1}\, \xi_{\nu_1 n} = -a_i x_i - \sum_{k=2}^{n} a_k\, \xi_{ik} \tag{14}$$

Substituting Eqs. (9)–(13) into Eq. (14), we obtain

$$\left.\begin{aligned} \sum_{\nu=1}^{n} f_{i\nu}(a_1, a_2, \ldots, a_n)x_\nu &= 0 \\ i &= 1, 2, 3, \ldots, n \end{aligned}\right\} \tag{15}$$

where $f_{i\nu}(a_1, a_2, \ldots, a_n)$ are linear functions of $a_1, a_2, \ldots, a_n$.

Choosing

$$\left.\begin{aligned} f_{1\nu}(a_1, a_2, \ldots, a_n) &= 0 \\ \nu &= 1, 2, \ldots, n \end{aligned}\right\} \tag{16}$$

we find a set of values $a_1, a_2, \ldots, a_n$. We will prove that these are the coefficients of Eq. (6).

Denoting the values found above by $a_1^{(1)}, a_2^{(1)}, \ldots, a_n^{(1)}$ and substituting them into the coefficients of the following equations

$$\left.\begin{aligned} \sum_{\nu=1}^{n} f_{i\nu}(a_1, a_2, \ldots, a_n)x_\nu &= 0 \\ i &= 2, 3, \ldots, n \end{aligned}\right\} \tag{17}$$

we obtain $n - 1$ equations for n unknowns. Let the rank of matrix

$$\begin{bmatrix} f_{21} \ldots f_{2n} \\ \ldots\ldots \\ f_{n1} \ldots f_{nn} \end{bmatrix} \qquad \text{for } a_\nu = a_\nu^{(1)}$$

be $r < n$ then $k = n - r$ of the unknowns, say $x_1, x_2, \ldots, x_k$ can be chosen arbitrarily. Consequently, the determinant of B is a polynomial $P(x_1, x_2, \ldots, x_k)$ in $x_1, x_2, \ldots, x_k$. It is obvious that there are infinitely many choices for $x_1, x_2, \ldots, x_k$ such that $P \neq 0$.

Using such a set $x_1, x_2, \ldots, x_k$ to form the matrix B, our eigenvalue problem is reduced to the solution of the polynomial equation

$$a_1^{(1)} + a_2^{(1)}\lambda + \ldots + a_n^{(1)}\lambda^{n-1} + \lambda^n = 0 \tag{18}$$

Now suppose we have made a second choice by equating

$$\left.\begin{aligned} f_{2\nu}(a_1, a_2, \ldots, a_n) &= 0 \\ \nu &= 1, 2, \ldots, n \end{aligned}\right\} \tag{19}$$

and thus obtained another set of values

$$a_\nu = a_\nu^{(2)} \qquad \nu = 1, 2, 3, \ldots, n$$

By the same process used above, we can find a set of values $x_1, x_2, \ldots, x_n$ such that $|B| \neq 0$, and our problem is reduced to the solution of

$$a_1^{(2)} + a_2^{(2)}\lambda + \ldots + a_n^{(2)}\lambda^{n-1} + \lambda^n = 0 \tag{20}$$

Since the eigenvalues of A are independent of the nonsingular matrix, B, Eqs. (17) and (19) must have the same roots. This demands the equality of the corresponding coefficients of the two polynomials. Hence we have

$$a_\nu^{(1)} = a_\nu^{(2)} \qquad \nu = 1, 2, 3, \ldots, n \tag{21}$$

which shows that our process leads to the same polynomial Eq. (6) no matter which value of i, $i = 1, 2, 3, \ldots, n$ is taken to determine $a_1, a_2, \ldots, a_n$ by setting

$$\left.\begin{aligned} f_{i\nu}(a_1, a_2, \ldots, a_n) &= 0 \\ \nu &= 1, 2, \ldots, n \end{aligned}\right\} \tag{22}$$

The solution of Eq. (6) determines the eigenvalues of Eq. (2)

Example

In case $\quad A = \begin{bmatrix} a_{11} & a_{12} \\ a_{21} & a_{22} \end{bmatrix}$

we take $\quad B = \begin{bmatrix} x_1 & \xi_{12} \\ x_2 & \xi_{22} \end{bmatrix}$

and find

$$\xi_{12} = a_{11}x_1 + a_{12}x_2$$
$$\xi_{22} = a_{21}x_1 + a_{22}x_2$$

Eqs. (16) become

$$\left.\begin{aligned} f_{11} &= -a_1 - a_{11}a_2 - a_{11}^2 - a_{12}a_{21} = 0 \\ f_{12} &= \quad - a_2 \quad - a_{11} \quad - a_{22} \quad = 0 \end{aligned}\right\} \tag{a}$$

while Eqs. (19) take the forms

$$\left.\begin{aligned} f_{21} &= \quad a_2 + a_{11} \quad + a_{22} \quad = 0 \\ f_{22} &= a_1 + a_{22}a_2 + a_{12}a_{21} + a_{22}^2 = 0 \end{aligned}\right\} \tag{b}$$

Both systems (a) and (b) have the same solution

$$a_2 = -(a_{11} + a_{22})$$
$$a_1 = a_{11}a_{22} - a_{12}a_{21}$$

and the eigenvalue problem is reduced to the solution of the equation

$$(a_{11}a_{22} - a_{12}a_{21}) - (a_{11} + a_{22})\lambda + \lambda^2 = 0$$

References

[1] Wayland, Harold, *Expansion of Determinantal Equations*, Quarterly of Applied Mathematics, Vol. II, No. 4, pp. 277–306, January, 1945.

[2] Danielewsky, A., Trans. Mosc. Math. Soc., Vol. 44, 1937.

[3] Samuelson, P. A., *A Method of Determining Explicitly the Coefficients of the Characteristic Equation*, The Annals of Math. Statistics, Vol. XIII, pp. 424–429, 1942.

[4] Leppert, E. L., Jr., *A Fraction Series Solution for Characteristic Values Useful in Some Problems of Airplane Dynamics*, Journal of the Aeronautical Sciences, Vol. 22, No. 5, pp. 326–328, May, 1955.

Notes on the Calculation of the Subsonic Downwash and Sidewash Angles Near Wings

Raymond F. Anderson*
Aerodynamicist, The Radioplane Company, Van Nuys, Calif.
March 21, 1956

Symbols

sV	= semispan of a "U" vortex
x	= longitudinal coordinate from origin; positive aft, negative forward
y	= lateral coordinate from origin
x_i, y_i; x_l, y_l	= induced angle point and vortex center coordinates, respectively
Δx	= $x_i - x_l$, $\Delta y = y_i - y_l$ (F is the same for $-y$ as for $+y$)
Δz	= "vertical" (normal) distance between the vortex centers and an induced angle point, positive downward
$\Delta x_V, \Delta y_V, \Delta z_V$	= dimensionless distances in terms of sV
w	= component of induced velocity parallel to the z-axis, positive downward
v	= component of induced velocity parallel to the y-axis, positive toward right wing tip
F, G	= vertical and lateral induced velocity factors, respectively. B, R, and L as subscripts to w, v, F, and G indicate the separate effects of the bound, left trailing and right trailing vortices, respectively
$\epsilon_B, \epsilon_R, \epsilon_L$	= vertical induced angles due to the bound, right trailing and left trailing parts of a U vortex, respectively
$\epsilon^\circ, \beta^\circ$	= wing vertical and lateral induced angles in degrees, *angles without a superscript are in radians*
m	= number of vortex centers per chord
$\bar{n}$	= a spanwise station, $\bar{1}$, $\bar{2}$, etc.
C_L	= wing lift coefficient
β_R, β_L	= lateral induced angles due to the right and left trailing parts of a U vortex

Discussion

The "vertical" and lateral induced angles behind a wing at a distance of about one semispan or more may often be found with sufficient accuracy for aircraft design use by replacing the wing with a lifting line.

However, if induced angles are needed above or below a wing, say at a distance of the order of one-tenth semispan, then the vortices should be distributed chordwise as well as spanwise to obtain good accuracy. A distribution of U-shaped vortices is indicated by the vortex centers in Fig. 1 for an arbitrary wing. The chordwise strengths of the vortices are taken equal for convenience in calculation.

A typical point at which the vertical and lateral induced angles are to be calculated is shown beneath the outer part of the right wing.

The induced velocity due to a "U" vortex may be found from Δx, Δy, and Δz[1]. With conversion to the present notation, the vertical induced velocities due to the bound, right trailing and left trailing vortices are

$$w_B = \frac{K}{4\pi s_V} F_B, \qquad w_R = \frac{K}{4\pi s_V} F_R, \qquad w_L = \frac{K}{4\pi s_V} F_L$$

where

$$F_B = \left(\frac{\Delta x_V}{\Delta x_V^2 + \Delta z_V^2}\right)\left[\frac{\Delta y_V + 1}{\sqrt{\Delta x_V^2 + \Delta z_V^2 + (\Delta y_V + 1)^2}} - \frac{\Delta y_V - 1}{\sqrt{\Delta x_V^2 + \Delta z_V^2 + (\Delta y_V - 1)^2}}\right]$$

$$F_R = \left[-\frac{\Delta y_V - 1}{\Delta z_V^2 + (\Delta y_V - 1)^2}\right] \times \left[1 + \frac{\Delta x_V}{\sqrt{\Delta x_V^2 + \Delta z_V^2 + (\Delta y_V - 1)^2}}\right]$$

$$F_L = \left[\frac{\Delta y_V + 1}{\Delta z_V^2 + (\Delta y_V + 1)^2}\right] \times \left[1 + \frac{\Delta x_V}{\sqrt{\Delta x_V^2 + \Delta z_V^2 + (\Delta y_V + 1)^2}}\right]$$

With the vertical induced angle in radians given by w/V, the induced angles due to the three components of vertical induced velocity become

$$\epsilon_B = \frac{K}{4\pi V s_V} F_B, \qquad \epsilon_R = \frac{K}{4\pi V s_V}, \qquad \epsilon_L = \frac{K}{4\pi V s_V}, \qquad \text{radians}$$

The increment of induced angle due to a "U" vortex is found from the sum of the components as

$$\Delta\epsilon = \epsilon_B + \epsilon_R + \epsilon_L = \frac{K}{4\pi V s_V} F$$

where

$$F = F_B + F_R + F_L$$

The circulation, K, is related to the increment of lift produced by a "U" vortex from $\Delta l = 2 s_V \rho V K$. The corresponding increment of section lift coefficient is

$$\Delta c_l = \frac{\Delta l}{(\rho/2) V^2 (2 s_V c)} = \frac{2K}{Vc}$$

where c is the local chord. The increment Δc_l is related to the section lift coefficient c_l by $\Delta c_l = c_l/m$, so that $K = c_l V c/2m$. Then $\Delta\epsilon = (c_l c/8\pi m s_V) F$. With the introduction of $b = A\bar{c}$, where A is the aspect ratio and $\bar{c}$ is the mean chord $\Delta\epsilon$ is

$$\Delta\epsilon = \frac{c_l c}{8\pi m A \bar{c}} \frac{b}{s_V} F$$

The load coefficient at a spanwise station $\bar{n}$ is designated as $L_{\bar{n}} = (c_l c/C_L \bar{c})_{\bar{n}}$. Also the angle, ϵ, due to all the vortices is given by $\epsilon = \Sigma\Delta\epsilon$. With conversion to degrees the final equation for the vertical induced angle of a wing in terms of its lift coefficient becomes

$$\epsilon/C_L = (57.3/8\pi A)\ (b/s_V) \sum [(L_n/m)(F)_{n,m}]$$

In actual use it is convenient to number the vortex centers as indicated in Fig. 1. With three chordwise points the vertical induced angle becomes

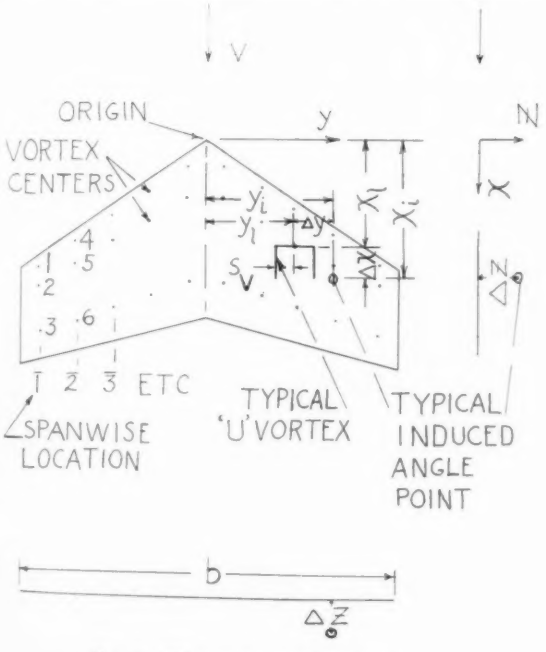

Fig. 1. Wing and vortex locations.

* Now, Research Engineer, Lockheed Missile Systems Division, Lockheed Aircraft Corp.

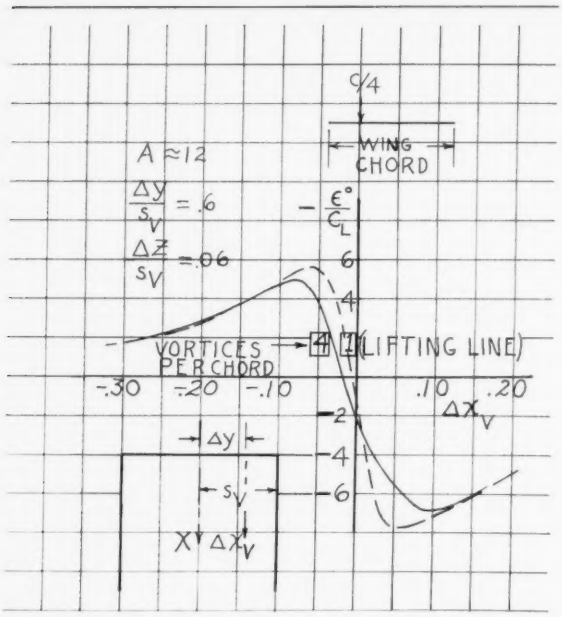

FIG. 2. Longitudinal variation of vertical induced angle for a wing with uniform lift distribution.

$$(\epsilon^\circ/C_L) = (57.3/8\pi A)(b/3s_V)[L_{\bar{1}}(F_1 + F_2 + F_3) + L_{\bar{2}}(F_4 + F_5 + F_6) + \ldots]$$

where $L_{\bar{1}}$ is the load coefficient at spanwise station $\bar{1}$ (Fig. 1) and F_1 is the factor calculated for vortex center number 1, etc.

Turning now to the lateral induced flow, the lateral induced velocity may be found from Δx, Δy, and Δz.[1] With conversion to the present notation, the lateral induced velocities of a "U" vortex due to the bound, right and left vortices are

$$v_B = 0, \qquad v_R = (K/4\pi s_V)G_R, \qquad v_L = (K/4\pi s_V)G_L$$

where

$$G_R = \{\Delta z_V/[\Delta z_V^2 + (\Delta y_V - 1)^2]\} \times \{1 + [\Delta x_V/\sqrt{\Delta x_V^2 + \Delta z_V^2 + (\Delta y_V - 1)^2}]\}$$

$$G_L = \{-\Delta z_V/[\Delta z_V^2 + (\Delta y_V + 1)^2]\} \times \{1 + [\Delta x_V/\sqrt{\Delta x_V^2 + \Delta z_V^2 + (\Delta y_V + 1)^2}]\}$$

With the lateral induced angle in radians given by v/V, the induced angle components are

$$\beta_R = (K/4\pi V s_V)G_R, \qquad \beta_L = (K/4\pi V s_V)G_L$$

and the total angle increment due to a unit vortex is

$$\Delta\beta = \beta_R + \beta_L = \frac{K}{4\pi V s_V} G$$

where $G = G_R + G_L$.

Following the procedure for the vertical induced angle, the lateral induced angle due to all the unit vortices is given by

$$\frac{\beta^\circ}{C_L} = \frac{57.3}{8\pi A}\frac{b}{s_V}\sum\left[\frac{L_{\bar{n}}}{m}(G)_{\bar{n},m}\right] = \frac{57.3}{8\pi A}\frac{b}{3s_V} \times [L_{\bar{1}}(G_1 + G_2 + G_3) + \ldots]$$

The first relation is general and the second applies to three chordwise points.

The foregoing formulas may be used to compare the effect of taking one and several vortices per chord. The simplest case is a wing with a hypothetical uniform lift distribution. For such a wing, a comparison of the longitudinal distribution of vertical induced angles for one and four chordwise points is shown in Fig. 2. The conditions are $\Delta y_V = 0.6$, $\Delta Z_V = 0.06$ and $A = 12$. There is little effect on the upwash far ahead of the wing and on the downwash well behind it, but there is an appreciable effect near the wing. Additional comparisons are needed for wings with vortices distributed spanwise as well as chordwise.

If several spanwise locations and chordwise points are used, the labor of calculating F can be reduced if the tabulated values[2] can be used. The tabulated values are given for even integral values of Δy_V (2, 4, etc.). Such values can be obtained by locating a vortex center on an induced angle point. The required vortex semispan and number of spanwise stations can then be found.

The effect of compressibility on the distribution of induced angles may be taken into account by application of the Prandtl-Glauert rule.

The formulas that have been given are of value for calculating the flow angularity near wings. The vertical induced angles so calculated may be considered to be those due to a lifting flat plate.

REFERENCES

[1] Glauert, H., *The Elements of Airfoil and Airscrew Theory*, p. 158; Cambridge University Press, Cambridge, England, 1926.

[2] Diederich, F. W., *Charts and Tables for Use in Calculations of Downwash of Wings of Arbitrary Planform*, NACA TN 2353, May, 1951.

International Congress of Applied Mechanics

Brussels, Belgium, September 5–13, 1956

The National Science Foundation is planning to assist a limited number of engineers and scientists to attend the 9th International Congress of Applied Mechanics in Brussels. Applications for these international travel grants should be submitted to the National Science Foundation, Washington 25, D.C., not later than August 1, 1956.

/ V, the in-

L

angle, the
s given by

$G_3) + \ldots]$

s to three

ne effect of
est case is a
For such a
of vertical
own in Fig.
$A = 12$.
ing and on
iable effect
wings with

re used, the
values[3] can
gral values
locating a
red vortex
e found.
of induced
ne Prandtl-

calculating
l angles so
lifting flat

. 158; Cam-

of Downwash